AFRL-VA-WP-TR-1999-3052

DEVELOPMENT OF THE AERODYNAMIC/AEROSERVOELASTIC MODULES IN ASTROS

VOLUME 4: ZAERO THEORETICAL MANUAL (F33615-96-C-3217)

P.C. CHEN
D. SARHADDI
D.D. LIU

ZONA Technology, Inc.
7430 E. Stetson Drive, Ste 205
Scottsdale, AZ 85251

FEBRUARY 1999

FINAL REPORT FOR PERIOD SEPTEMBER 1996 – SEPTEMBER 1998

Approved for public release; distribution unlimited

19991115 092

AIR VEHICLES DIRECTORATE
AIR FORCE RESEARCH LABORATORY
AIR FORCE MATERIEL COMMAND
WRIGHT-PATTERSON AIR FORCE BASE, OH 45433-7542

DTIC QUALITY INSPECTED 4

NOTICE

USING GOVERNMENT DRAWINGS, SPECIFICATIONS, OR OTHER DATA INCLUDED IN THIS DOCUMENT FOR ANY PURPOSE OTHER THAN GOVERNMENT PROCUREMENT DOES NOT IN ANY WAY OBLIGATE THE UNITED STATES GOVERNMENT. THE FACT THAT THE GOVERNMENT FORMULATED OR SUPPLIED THE DRAWINGS, SPECIFICATIONS, OR OTHER DATA DOES NOT LICENSE THE HOLDER OR ANY OTHER PERSON OR CORPORATION; OR CONVEY ANY RIGHTS OR PERMISSION TO MANUFACTURE, USE, OR SELL ANY PATENTED INVENTION THAT MAY BR RELATED TO THEM.

THIS REPORT IS RELEASEABLE TO THE NATIONAL TECHNICAL INFORMATION SERVICE (NTIS). AT NTIS, IT WILL BE AVAILABLE TO THE GENERAL PUBLIC, INCLUDING FOREIGN NATIONS.

THIS TECHNICAL REPORT HAS BEEN REVIEWED AND IS APPROVED FOR PUBLICATION.

VICTORIA A. TISCHLER
Aerospace Engineer
Design and Analysis Branch

VIPPERLA B. VENKAYYA
Leader, Multidisciplinary Design
Design & Analysis Branch

Nelson D. Wolf
NELSON D. WOLF, Chief
Design and Analysis Branch
Structures Division

IF YOUR ADDRESS HAS CHANGED, IF YOU WISH TO BE REMOVED FROM OUR MAILING LIST, OR IF THE ADDRESSEE IS NO LONGER EMPLOYED BY YOUR ORGANIZATION, PLEASE NOTIFY AFRL/VASD BLDG 45, 2130 8TH STREET, SUITE 1, WRIGHT-PATTERSON AFB OH 45433-7542 TO HELP MAINTAIN A CURRENT MAILING LIST.

COPIES OF THIS REPORT SHOULD NOT BE RETURNED UNLESS RETURN IS REQUIRED BY SECURITY CONSIDERATIONS, CONTRACTUAL OBLIGATIONS, OR NOTICE ON A SPECIFIED DOCUMENT.

REPORT DOCUMENTATION PAGE

Form Approved
OMB No. 0704-0188

Public reporting burden for this collection of information is estimated to average 1 hour per response, including the time for reviewing instructions, searching existing data sources, gathering and maintaining the data needed, and completing and reviewing the collection of information. Send comments regarding this burden estimate or any other aspect of this collection of information, including suggestions for reducing this burden, to Washington Headquarters Services, Directorate for information Operations and Reports, 1215 Jefferson Davis Highway, Suite 1204, Arlington, VA 22202-4302, and to the Office of Management and Budget, Paperwork Reduction Project (0704-0188), Washington, DC 20503.

1. AGENCY USE ONLY (*Leave Blank*)	2. REPORT DATE FEBRUARY 04, 1999	3. REPORT TYPE AND DATES COVERED FINAL 24 SEP 1996 – 24 SEP 1998

4. TITLE AND SUBTITLE

DEVELOPMENT OF THE AERODYNAMIC/AEROSERVOELASTIC MODULES IN ASTROS
VOLUME 4 – ZAERO THEORETICAL MANUAL

5. FUNDING NUMBERS

C:	F09603-95-D-0175
PE:	65520F
PR:	STTR
TA:	41
WU:	00

6. AUTHOR(S)

P. C. Chen, D.D. Liu and D. Sarhaddi
ZONA Technology, Inc.

7. PERFORMING ORGANIZATION NAME(S) AND ADDRESS(ES)

ZONA Technology, Inc.
7434 E. Stetson Drive, Suite 205
Scottsdale, AZ 85251
Tel 602-945-9988 / Fax 602-945-6588

8. PERFORMING ORGANIZATION REPORT NUMBER

ZONA 99-11D

9. SPONSORING/MONITORING AGENCY(S) AND ADDRESS(ES)

Air Vehicles Directorate
Air Force Research Laboratory
Air Force Materiel Command
Wright-Patterson Air Force Base, Oh 45433-7542
POC: Dr V. B. Venkayya, AFRL/VASD, 937-255-2582

10. SPONSORING/MONITORING AGENCY REPORT NUMBER

AFRL-VA-WP-TR-1999-3052

11. SUPPLEMENTARY NOTES

12a. DISTRIBUTION/AVAILABILITY STATEMENT

APPROVED FOR PUBLIC RELEASE; DISTRIBUTION UNLIMITED

12b. DISTRIBUTION CODE

13. ABSTRACT (*Maximum 200 words*)

This report is a part of the documentations which describe the complete development of an STTR Phase II effort entitled, "Development of the Aerodynamic/Aeroservoelastic Modules in ASTROS." This report is one of four manuals that comprise the final report. The remaining reports consist of the ZAERO User's Manual (Volume I), the ZAERO Programmer's Manual (Volume II) and the ZAERO Applications Manual (Volume III).

ASTROS* is the seamless integration of the ZAERO module into ASTROS. As an aerodynamic enhancement to ASTROS, ZAERO is the ZONA aerodynamic module, unified for all Mach number ranges.

This theoretical manual presents the theoretical formulations of the ZONA6, ZTAIC, ZONA7, and ZONA7U methods that comprise the aeroelastic engineering modules of ZAERO. Other areas covered include the following: fundamentals of aeroelasticity, the Unified Aerodynamic Influence Coefficient (AIC) matrix generation, the spline methods for spline matrix generation and solution techniques for flutter analysis.

14. SUBJECT TERMS

Multidisciplinary Optimization, ZAERO Module, ASTROS*, Subsonic-Transonic-Supersonic-Hypersonic Aerodynamics, Aeroelasity, Aeroservoelasticity, Flutter

15. NUMBER OF PAGES
158

16. PRICE CODE

17. SECURITY CLASSIFICATION OF REPORT	18. SECURITY CLASSIFICATION OF THIS PAGE	19. SECURITY CLASSIFICATION OF THIS ABSTRACT	20. LIMITATION OF ABSTRACT
UNCLASSIFIED	UNCLASSIFIED	UNCLASSIFIED	SAR

TABLE OF CONTENTS

Page

1.0 INTRODUCTION 1

1.1 Overview 1
1.2 ZAERO/UAIC: A Unified AIC Based Aerodynamic Module 3
1.3 ZAERO/UAIC and ASE modules in ASTROS 7
1.4 Other New ZAERO modules in ASTROS: AGM, 3D Spline and Flutter ... 8

2.0 AEROELASTICITY FOUNDATION OF ZAERO 11

2.1 Fundamental of Aeroelasticity 11
2.2 Unified *AIC* of ZAERO 14
2.3 Functionality of the Spline Matrix 16
2.4 Impact of Q(*ik*) on Flutter Solution Technique 17

3.0 ZONA6 / ZONA7: UNSTEADY SUBSONIC / SUPERSONIC AERODYNAMICS FOR WING-BODYAIRCRAFT CONFIGURATIONS WITH EXTERNAL STORES 20

3.1 Backgrounds of ZONA6 and ZONA7 20
3.2 Integral Equations of the Linearized Small Disturbance Equation 34
3.3 Unsteady Boundary Condition and Unsteady Pressure Coefficients 38
3.4 Paneling Scheme for Aircraft Configuration 40
3.5 Discretization of the Source and Doublet Integrals 42
3.6 Matrix Equations for the Solution of Unsteady Pressure 44
3.7 Construction of Aerodynamic Influence Coefficient (*AIC)* Matrix 47
3.8 J-Set and K-Set Aerodynamic Degrees of Freedom for *AIC* Matrix 49
3.9 Body Wake Effect 50
3.10 Technique of Minimizing Spurious Waves for Supersonic Body Boxes 56
3.11 Super-Inclined Boxes and Inlet Boxes 61
3.12 Treatment of Engine Inlets 62

4.0 ZTAIC: UNSTEADY TRANSONIC AERODYNAMICS WITH STEADY PRESSURE INPUT 64

4.1 Background of ZTAIC 65
4.2 The Chordwise Mean Flow and Spanwise Phase Correction Procedure 72
4.3 The Inverse Airfoil Design (IAF2) Scheme 74
4.4 Frequency-Domain Pressure Coefficient by Indicial Method 76
4.5 Modal Aerodynamic Influence Coefficient (MAIC) Matrix 78

TABLE OF CONTENTS (cont.)

Page

5.0 ZONA7U: UNIFIED HYPERSONIC / SUPERSONIC UNSTEADY AERODYNAMICS FOR WING-BODY AIRCRAFT CONFIGURATION 81

5.1 Background of ZONA7U 81
5.2 Review of Piston Theory 88
5.3 Hypersonic Similarity for Thickness Effects 92
5.4 Unified Supersonic/Hypersonic Lifting Surface Method of ZONA7U 93
5.5 *AIC* Matrix of ZONA7U for Hypersonic Wing-Body Configuration 95

6.0 SPLINE METHODS FOR SPLINE MATRIX GENERATION 96

6.1 The Infinite Plate Spline (IPS) Method 97
6.2 The Thin-Plate Spline (TPS) Method 104
6.3 The Beam Spline Method 107
6.4 The Rigid-Body Attachment (RBA) Method 115
6.5 Matrix Assembly of the Total Spline Matrix 117

7.0 FLUTTER SOLUTION METHODS 118

7.1 The K-Method 119
7.2 The P-K Method 122
7.3 The g-Method 125

REFERENCES 141

LIST OF FIGURES

Figure		Page
1.1	Computational Aeroelasticity: A Global Strategy	2
1.2	Computational Aeroelasticity for MDO Applications	2
1.3	ZAERO/UAIC: A Unified AIC Based Aerodynamic Module	4
1.4	ZAERO/UAIC Module	4
1.5	The Aerodynamic Geometry Module (AGM) of ZAERO	8
1.6	The 3D Spline Module of ZAERO	9
2.1	Aeroelastic Functional Diagram	12
2.2	Typical Panel Model of a Wing-Body Configuration	15
3.1	Comparison of Computed Unsteady Pressures for Plunging M=1.25 and k=2.0	21
3.2	Comparison of Computed Unsteady Pressures for a Pitching Flat Plate About the Leading Edge at M=1.25 and k=2.0	21
3.3	Aerodynamic Modeling of F-18 Wing	21
3.4	Effects on Panels on Computed Pressures for an F-18 Wing with an Oscillating Leading Edge Flap at 58.8% Span, M=1.1 and k=4.0	22
3.5	Real and Imaginary Part of the Lift on the Main Wing due to Pitch of the Canard, M=1.054	22
3.6	Paneling Scheme for a 70° Delta Wing	23
3.7	Computed and Measured Flutter Speeds vs. Mach Number	23
3.8	Comparison of Ratios of Flutter Frequency vs. Mach Number	23

LIST OF FIGURES (cont.)

Figure		Page
3.9	In-Phase and Out-of-Phase Pressure Coefficients for a Bolic-Ogive in First Bending Mode at $M=2.5$ and Reduced Frequency $k=1.0$.	24
3.10	Static Loading About the Fuselage-Wing Junctions	24
3.11	Paneling Model for the Underwing Store Configuration: Northrop F-5 Wing Plus Underwing Pylon, Launcher, Missile Body with Four Aft Fins	25
3.12	Unsteady Normal Force and Pitching Moment for the Underwing Store Configuration With and Without the Missile Body Oscillating about 50% Root Chord at $M_\infty = 1.1$ and 1.35 and Reduced Frequency $k = 0.1$	25
3.13	Unsteady Side Force and Yawing Moment for the Complete Underwing Store Configuration With and Without the Missile Body and Launcher Oscillating about 50% Root Chord at $M_\infty = 1.1$ and 1.35 and Reduced Frequency $k = 0.1$	26
3.14	Unsteady Spanwise Normal Force and Pitching Moment for the Clean F-5 Wing and the Underwing Store Configuration at $M_\infty = 1.35$ and Reduced Frequency $k = 0.1$	26
3.15	Static Loading of NACA Wing-Body Configuration; $M = 0.6$ and $\alpha = 4°$	27
3.16	NLR Wing-Tip-Tank Configuration Showing Paneling Scheme	27
3.17	Steady Pressure Distribution Along the Tip-Tank of NLR Wing-Tip-Tank Configuration; $M = 0.45$ and $\alpha = 4°$: a) $\theta = 292.5°$ and b) $\theta = 67.5°$	28
3.18	Unsteady Pressure Distribution Along the Tip-Tank of NLR Wing-Tip-Tank Configuration; $M = 0.45$, $\alpha = 0°$, $k = 0.305$, $\bar{x}_o = 0.15\ c_R$, and $\theta = 202.5°$	28
3.19	Unsteady Normal Load Distribution Along the Tip-Tank of NLR Wing-Tip-Tank Configuration; $M = 0.45$, $\alpha = 0°$, $k = 0.305$ and $\bar{x}_o = 0.15\ c_R$,	28

LIST OF FIGURES (cont.)

Figure Page

3.20 Generalized Aerodynamic Forces C_{L_α} (=Q_{12}/S) versus Reduced Frequency k: $AR = 20$, Rectangular Wing ($M = 0.0, x_o = 0.5c$); a) Panel Number = 10 x 10, b) Panel Number = 10 x 40 29

3.21 Effects of Panel Numbers on GAF C_{L_α} and C_{M_α}: $AR = 20$; Rectangular Wing ($M = 0.0, k = 10, x_o = 0.5c$) 30

3.22 Typical Paneling Scheme 30

3.23 Effects of Sweptback Angle on C_{L_α} and C_{M_α} ($M = 0.8, k = 0.0, x_o = 0.5c$) 31

3.24 In-Phase Pressures on Two Spanwise Stations: 70° Delta Wing ($M = 0.8, k = 0.0, x_o = 0.5c$) 32

3.25 Out-of Phase Pressures on Two Spanwise Stations: 70° Delta Wing ($M = 0.8, k = 0.5, x_o = 0.5c$) 33

3.26 Out-of Phase Pressures on Two Spanwise Stations: 70° Delta Wing ($M = 0.8, k = 10.0, x_o = 0.5c$ 33

3.27 Effects of Panel Numbers on C_{L_α} and C_{M_α}: 70° Flat Delta Wing ($M = 0.8, k = 10.0, x_o = 0.5c$) 34

3.28 Surface definition of configuration and wake 37

3.29 Aircraft Components Showing Body and Wing Segment/Box 41

3.30 Flow Chart of Computation and Calculation Procedure for Unsteady Pressures 47

3.31 Comparison of Surface Pressure Distribution for a Blunt Body ($L_B/d = 5$) at $\alpha = 0°$, M = 0 and Base Pressure $C_{P_{base}} = -0.169$ 51

3.32 Computer Wake Shape for a Blunt Body at M = 0 and $\alpha = 0°$; a Meridian-Plane View 53

LIST OF FIGURES (cont.)

Figure		Page
3.33	Unsteady Pressure Distribution Along the Tip-Tank of NLR Wing-Tip-Tank Configuration; $M = 0.45$, $\alpha = 0°$, $k = 0.305$, $\bar{x}_o = 0.15\, c_R$, and $\theta = 202.5°$	54
3.34	NLR Wing-Tip-Tank-Pylon-Store Configuration Showing Paneling Scheme	54
3.35	Steady Pressure Distribution Along the Store of NLR Wing-Tip-Tank-Pylon-Store Configuration; $M = 0.45$ and $\alpha = 0°$: a) $\theta = 90°$, b) $\theta = 180°$ and c) $\theta = 270°$	55
3.36	Unsteady Pressure Distribution Along the Tip-Tank of NLR Wing-Tip-Tank Configuration at a) $\theta = 157.5°$ and b) $\theta = 292.5°$; $M = 0.45$, $\alpha = 0°$, $k = 0.305$ and $\bar{x}_o = 0.15\, c_R$,	56
3.37	Cone-Cylinder-Cone at $M = 2.0$ and $\alpha = 0°$ Using ZONA7 without Wave Minimization	57
3.38	Opposite Points from the Panel Having the Same x_{lower}	57
3.39	Propagation of Spurious Wave generated by the Real Geometry Corner	59
3.40	Cone-Cylinder-Cone at $M = 2.0$ and $\alpha = 0°$ Using ZONA7 with Wave Minimization	61
3.41	Superinclined Box a) on Engine Inlet, b) on Thick Body	62
4.1	Flow Chart of ZTAIC Computation Procedure	66
4.2	The Lessing Wing a) Configuration, b) Magnitude of the First Bending, c) Phase Angle (in °) of the First Bending, $M = 0.9$, $k = 0.13$	68
4.3	LANN Wing Comparison of In-Phase and Out-of Phase Pressures at Two Spanwise Locations: Pitching Oscillation About 62% Root-Chord at M=0.82, k=0.205	69
4.4	Northrop F-5 Wing with Oscillation Flap: Comparison of In-Phase and Out-of Phase Pressures with Hinge Line at 82% Chord at Sections 1 and 3, $M = 0.9$, $k = 0.274$	70

LIST OF FIGURES (cont.)

Figure		Page
4.5	Comparison of Flutter Speed and Frequency of 445.6 Weakened Wing at $M = 0.678$, 0.90 and 0.95	71
4.6	Comparison of Flutter Speed and Frequency of 445.6 Solid Wing at $M = 0.90$ and 0.95	71
4.7	Steady Pressure Inputs and Equivalent Airfoil Outputs at various Spanwise Locations (□ upper surface, Δ lower surface, —— presents TES data):	75
	a) LANN Wing at Mean Incidence $\propto_0 = 0.62°$, $M_\infty = 0.82$ (NLR Measured Data);	
	b) Northrop F-5 Wing at Mean Incidence $\propto_0 = 0°$, $M_\infty = 0.90$ (NLR Measured Data);	
	c) Northrop F-5 Wing at Mean Incidence $\propto_0 = 0°$, $M_\infty = 0.95$ (XTRAN3S-Ames Input)	
5.1	Stability Derivatives for an oscillating Wedge vs. Reduced Frequency: ($M = 3.0$, $h = 0.5c$, $\sigma = 10°$)	82
5.2	Damping-in-pitch $C_{m_{\dot{\theta}}}$ vs. Semiwedge Angle, $h = 0.5c$: $M =$ a) 5.0, b) 10.0	83
5.3	Stiffness Derivative C_{m_θ} and Damping-in-pitch Derivatives $C_{m_{\dot{\theta}}}$ vs. Semiwedge Angle, $h = 0.5c$: $M =$ a) 5.0, b) 10.0	83
5.4	Oscillating Panels Mounted on a Wedge with Semi-Wedge Angle $\sigma = 2°$	84
5.5	Effect of Reduced Frequency on Generalized Aerodynamic Forces for Oscillating Panels ($M = 5.0$, $\sigma = 2°$, $N = 2$)	85
5.6	Paneling Scheme of SAAB Canard-Wing	85
5.7	GAF Q_{12} of SAAB Canard-Wing vs. Mach Number: Mode 1 Wing Plunging and Mode 2 Canard Pitching about Midchord	86

LIST OF FIGURES (cont.)

Figure		Page
5.8	Flutter Speeds and Flutter Frequencies:	87
	a) vs. Mach Number Predicted by Various Methods: 70° Delta Wing with and without Thickness	
	b) for a 15° Swept Untapered Wing ($M = 1.3$ and 3.0)	
5.9	Surface Pressure of a Wedge According to Various Supersonic/Hypersonic Models: $\tau = \tan 10°$; $\gamma = 1.4$	89
5.10	Oscillating Leading-Edge Flap of a Thin Wedge Airfoil: $\sigma = 2°$	94
5.11	Unsteady Pressure Distribution for an Oscillating Leading Edge Flap with Hinge Line at Quarter Chord: ($M = 2.4$, $k = 0.5$, $\sigma = 3°$)	95
6.1	Spline Axis Coordinate System a) Spline Axis Along the Elastic Axis of Wing-Like Component, b) Spline Axis Along the Center Line of Body-Like Component	108
7.1	AGARD 445.6 *K*-Method Flutter Results (ZONA6), $M = 0.9$, $\rho = 0.000193$ slug/ft^3	121
7.2	AGARD 445.6 *P-K* Method Flutter Results (ZONA6), $M = 0.9$, $\rho = 0.000193$ slug/ft^3	123
7.3	Jet Transport Wing at M=0.0 at Sea Level using: a) *K-Method*, b) *P-K Method*	124
7.4	Generalized Aerodynamic Forces vs. Reduced Frequency of the 15° Sweptback Wing at $M = 0.45$, 4 Modes	129
7.5	*V*-g and *V-f* Diagrams of the 15° Sweptback Wing at $M = 0.45$	130
7.6	Search History of the Reduced Frequency-Sweep Technique at $V = 500$ ft/sec, a) Imaginary Damping and b) Real Damping	131

LIST OF FIGURES (cont.)

Figure		Page
7.7	Search History of the Reduced Frequency-Sweep Technique at $V = 600$ ft/sec	132
7.8	V-g and V-f Diagrams of the BAH Wing, $M = 0.0$, 10 Modes	133
7.9	Generalized Forces of 2 D.O.F. Airfoil, C.G. @ 37% Chord (HA145A1), $M = 0.0$, 2 Modes	134
7.10	2 D.O.F. Airfoil, C.G. @ 37% Chord (HA145A1), $M = 0.0$, 2 Modes	135
7.11	Damping and Frequency vs. Velocity of 2 D.O.F. Airfoil, C.G. @ 37% Chord (HA145A1), $M = 0.0$, 2 Modes	135
7.12	Damping and Frequency vs. Velocity of 2 D.O.F. Airfoil, C.G. @ 45% Chord (HA145A2), $M = 0.0$, 2 Modes	136
7.13	Damping and Frequency vs. Velocity of 3 D.O.F. Airfoil, C.G. @ 37% Chord (HA145A2), $M = 0.0$, 3 Modes	137
7.14	Damping and Frequency vs. Velocity of 3 D.O.F. Airfoil, C.G. @ 45% Chord (HA145A2), $M = 0.0$, 3 Modes	138
7.15	Johnson Configuration Generalized Aerodynamic Forces, M=0.84, 17 Modes	138
7.16	Damping and Frequency vs. Velocity of Johnson Configuration, M = 0.84, 17 Modes	139

FOREWORD

This final report is submitted in fulfillment of CDRL CLIN 0001, Data Item A001, Title: Scientific and Technical Reports of a Small Business Technology Transfer (STTR) Phase II contract No. F33615-96-C-3217 entitled, "Development of the Aerodynamic/Aeroservoelastic Modules in ASTROS," covering the performance period from 24 September 1996 to 24 September 1998.

This work is the second phase of a continuing two-phase STTR contract supported by AFRL/Wright-Patterson. The first phase STTR contract No. F33615-95-C-3219 entitled, "Enhancement of the Aeroservoelastic Capability in ASTROS," was completed in May 1996 and published as WL-TR-96-3119.

Both STTR Phase I and Phase II contracts are performed by the same ZONA Team in which ZONA Technology, Inc. is the prime contractor, whereby the team members include: the University of Oklahoma (OU), Universal Analytics, Inc. (UAI), and Technion (I.T.T.).

This final report consists of eight volumes, these are:

*ASTROS**
Volume I - ZAERO User's Manual
Volume II - ZAERO Programmer's Manual
Volume III - ZAERO Application Manual
Volume IV - ZAERO Theoretical Manual

ASTROServo
Volume I - Aeroservoelastic Discipline in ASTROS, User's Manual
Volume II - Aeroservoelastic Discipline in ASTROS, Programmer's Manual
Volume III - Aeroservoelastic Discipline in ASTROS, Application Manual
Volume IV - Aeroservoelastic Discipline in ASTROS, Theoretical Manual

This document (Vol. IV) is a Theoretical Manual of the ZAERO module, seamlessly integrated into ASTROS (called ASTROS*). The contributors are: P.C. Chen, D.D. Liu and D. Sarhaddi of ZONA Technology, Inc.

At AFRL/Wright-Patterson, Capt. Gerald Andersen is the contract monitor and Dr. V.B. Venkayya is the initiator of the whole STTR effort. The technical advice and assistance received from Mr. Doug Niell of The MacNeal Schwendler Corporation, Dr. V.B. Venkayya and others from AFRL during the course of the present phase on the development of ASTROS* are gratefully acknowledged.

1.0 INTRODUCTION

Supported by AFRL/VA under a three-year STTR contractual effort, ZONA Technology has successfully completed the seamless-integration of the ZAERO module with ASTROS (Automated Structural Optimization Systems). ZONA Technology (ZONA) and its team members: University of Oklahoma, Universal Analytics, Inc. and Technion, have further validated and tested the ZAERO/ASTROS (called ASTROS*). Utilizing ZAERO, ZONA and Technion have developed an Aeroservoelastic (ASE) module for ASTROS* during the contractual period (called ASTROServo).

ZAERO is ZONA's unsteady/steady aerodynamic program that contains four essential modules, namely: the AGM (Aerodynamic Geometry Module), the 3D Spline Module, the UAIC (Unified Aerodynamic Influence Coefficient Module) and the Flutter Module. Central in ZAERO is the UAIC module, which renders ZAERO applicable to complex aircraft configurations covering all Mach numbers ranging from subsonic, transonic, supersonic to hypersonic flight regimes.

The functionality of ZAERO is to provide ASTROS a much improved aerodynamic module which, as opposed to the existing DLM/CPM and USSAERO codes, unifies all Mach number and generates high-fidelity wing-body configurated aerodynamics for advanced aeroelastic analysis/design applications in an ASTROS/MDO environment. Thus, when interfaced with the ASE module, ZAERO/ASTROS or ASTROS* can perform aircraft design/analysis with additional aeroservoelastic constraints.

In this section, we will briefly describe:

- *Overview*
- *ZAERO/UAIC: A Unified AIC-Based Aerodynamic Module*
- *ZAERO/UAIC and ASE Modules in ASTROS*
- *Other new ZAERO modules in ASTROS: AGM, 3D Spline and Flutter*

1.1 Overview

For modern aeroelastic methodology, preference to the Computational Fluid Dynamics (CFD) methods or the Aerodynamic Influence Coefficient (AIC) methods for aeroelastic applications has been the subject of much discussion. Here, we refer to both methodologies as a part of computational aeroelasticity. In general, our concept of computational aeroelasticity consists of Aeroelastic Modeling Methodology, which includes AIC methods, structural FEM, spline methods and flutter solution methods, etc., and Aeroelastic Simulation Methodology, which includes CFD methods, closely-coupled CFD/CSD interfacing method, etc. (Figs 1.1, 1.2). In our estimation, there should exist little conflict in the choice of these two methodologies if we are directed towards a holistic approach for aeroelastic applications. Rather, they should compliment each other if their practices could follow the proposed global strategy as shown in Figs 1.1 and 1.2.

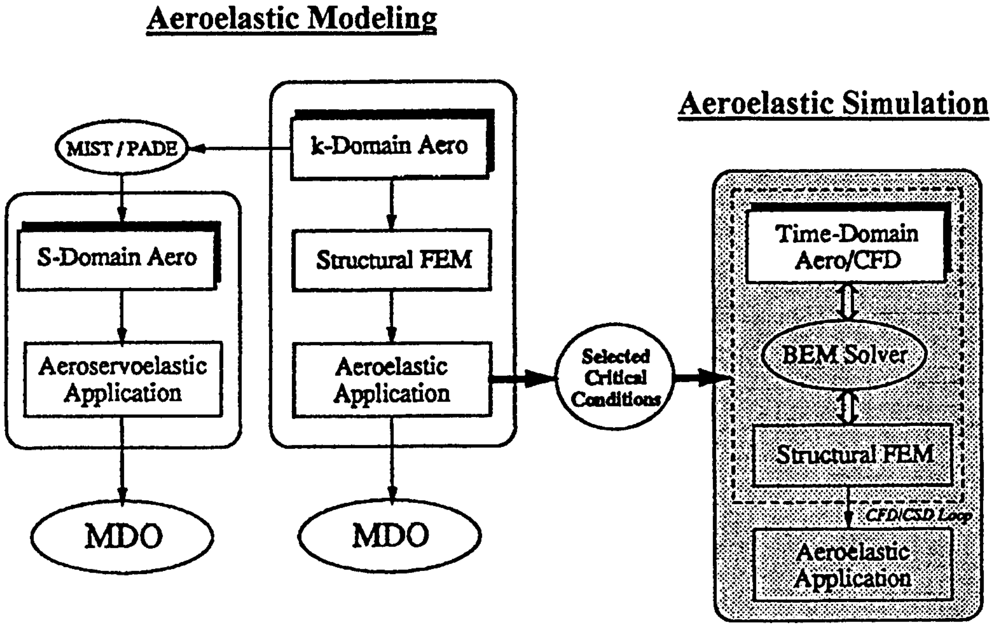
Aeroelastic Modeling
Aeroelastic Simulation
MIST / PADE
k-Domain Aero
S-Domain Aero
Structural FEM
Aeroservoelastic Application
Aeroelastic Application
Selected Critical Conditions
Time-Domain Aero/CFD
BEM Solver
Structural FEM
CFD/CSD Loop
Aeroelastic Application
MDO
MDO

Fig 1.1 Computational Aeroelasticity: A Global Strategy

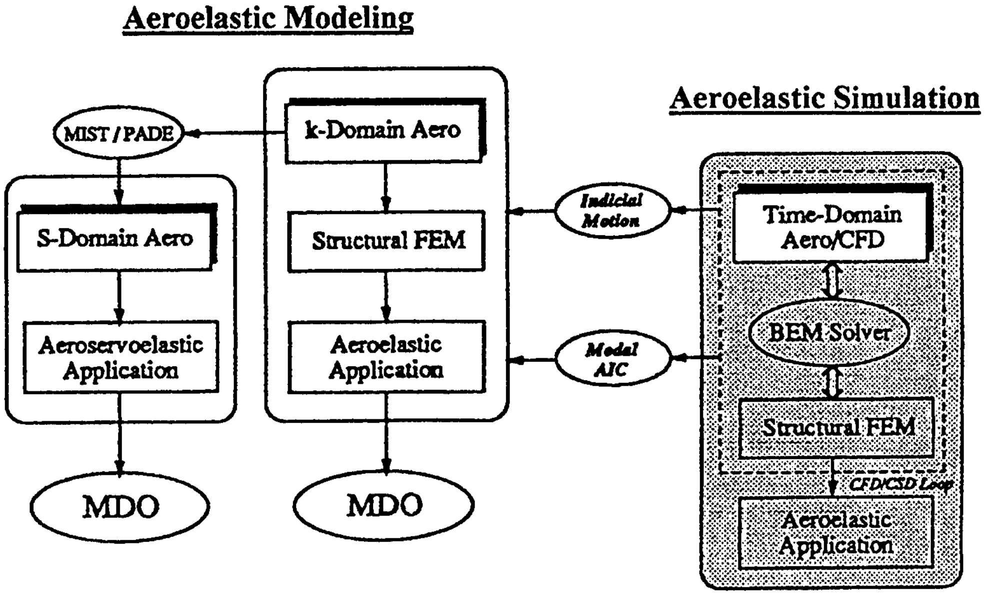
Aeroelastic Modeling
Aeroelastic Simulation
MIST / PADE
k-Domain Aero
S-Domain Aero
Structural FEM
Aeroservoelastic Application
Aeroelastic Application
Indicial Motion
Modal AIC
Time-Domain Aero/CFD
BEM Solver
Structural FEM
CFD/CSD Loop
Aeroelastic Application
MDO
MDO

Fig 1.2 Computational Aeroelasticity for MDO Applications

While both methodologies can cope with configurations of complex geometry in high fidelity, AIC methods can provide expedient amplitude-perturbed eigen solutions in the k-domain and the s-domain. Rapid flutter solutions can be readily obtained by several standard flutter methods. For this reason, AIC methods are preferred by industries.

Moreover, application of AIC methods to aeroservoelasticity and the Multidisciplinary Design Optimization (MDO) environment is straightforward. In terms of aeroelastic applications, they should provide selected critical conditions for CFD methods to fine tune the unsteady aerodynamics in a confined flow regime, thus saving substantial computing effort in search of potential flutter solutions.

On the other hand, the utilization of CFD methods is to link up with a structural FEM via a closely-coupled CFD/CSD interfacing, such as the BEM solver (Ref 1.5), as indicated in Figs 1.1 and 1.2. Clearly, CFD methods are required when more accurate solutions become mandatory in a flow regime where nonlinearity dominates (e.g. thick wing in supercritical flow, high-angle-of-attack flow with vortex dynamics).

For classical-flutter predictions, the flow nonlinearity could be linearized through a robust indicial method routine in conjunction with a proposed modal AIC method. In this way, CFD solutions could be carried over to the k-domain for its subsequent participation to aeroservoelasticity and MDO applications. For applications in static aeroelasticity, the proposed modal AIC method can be an expedient means in utilizing CFD solutions to generate a flexibility correction to the measured rigid load. *Therefore, it is clear that an effective AIC method with sufficiently high-fidelity modeling capability remains to be the backbone of computational aeroelasticity.*

Towards this end, a Unified Aerodynamic Influence Coefficient (UAIC) method for arbitrary wing-body configurations has been developed that covers the complete flight regime of subsonic, transonic, supersonic and hypersonic Mach numbers. This unsteady/steady UAIC methodology has been further established as a computer module, known as the ZAERO/UAIC module. The ZAERO/UAIC module is a stand-alone aerodynamic module, which can be interfaced with existing FEM programs such as NASTRAN and ASTROS. Under a two-year AFRL/Wright Lab contractual support, a seamless integration of the ZAERO/UAIC module into ASTROS is successfully completed. Fig 1.3 shows the integrated ASTROS/ZAERO program architecture. This theoretical manual attempts to describe the theoretical formulations of ZAERO, with special emphasis on UAIC formulation and its applications in each flow regime.

1.2 ZAERO/UAIC: A Unified AIC Based Aerodynamic Module

The ZAERO/UAIC module consists of four major unsteady aerodynamics codes that jointly cover the complete domain of all Mach number ranges, namely ZONA7U (formerly ZONA51U), ZONA6, ZONA7 and ZTAIC. As can be seen in Fig 1.4, the aero modules currently integrated within MSC/NASTRAN and ASTROS only have the purely subsonic and supersonic capabilities.

The development of the ZAERO module has been the major endeavor of ZONA Technology in the last decade. The following is a brief account for the capability of the computer codes within the ZAERO module.

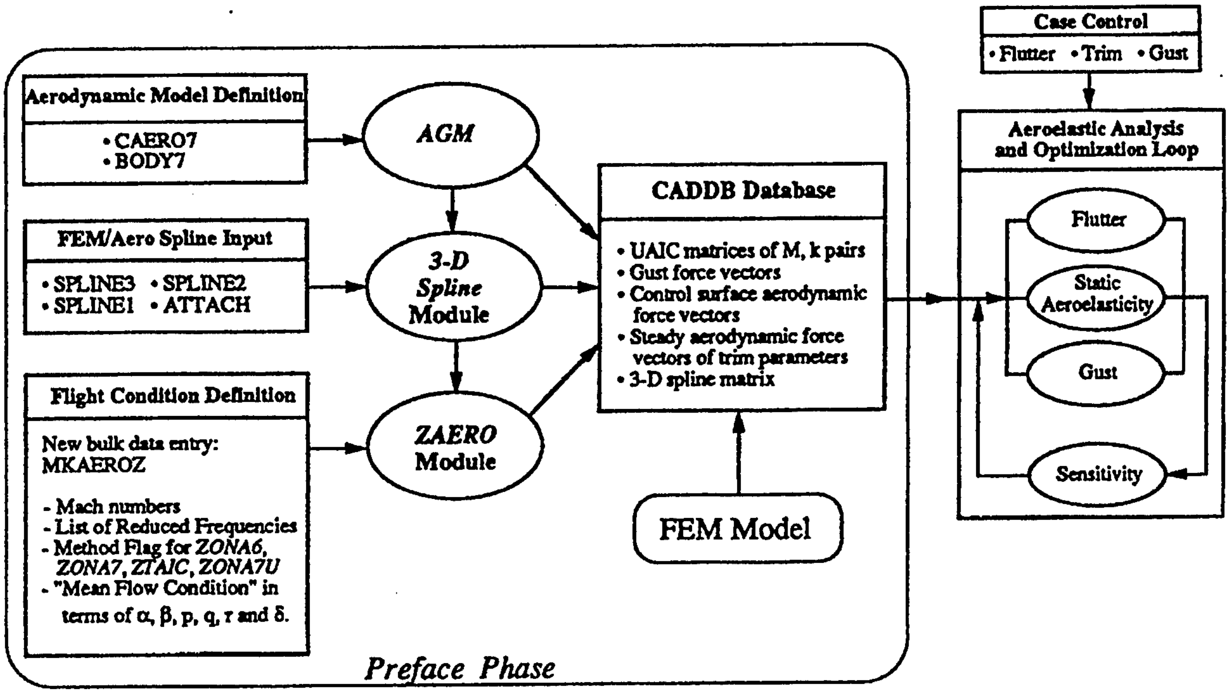
Case Control
• Flutter • Trim • Gust
Aerodynamic Model Definition
• CAERO7
• BODY7
AGM
FEM/Aero Spline Input
• SPLINE3 • SPLINE2
• SPLINE1 • ATTACH
3-D Spline Module
Flight Condition Definition
New bulk data entry: MKAEROZ
- Mach numbers
- List of Reduced Frequencies
- Method Flag for ZONA6, ZONA7, ZTAIC, ZONA7U
- "Mean Flow Condition" in terms of α, β, p, q, r and δ.
ZAERO Module
CADDB Database
• UAIC matrices of M, k pairs
• Gust force vectors
• Control surface aerodynamic force vectors
• Steady aerodynamic force vectors of trim parameters
• 3-D spline matrix
FEM Model
Aeroelastic Analysis and Optimization Loop
Flutter
Static Aeroelasticity
Gust
Sensitivity
Preface Phase

Fig 1.3 ASTROS/ZAERO Program Architecture

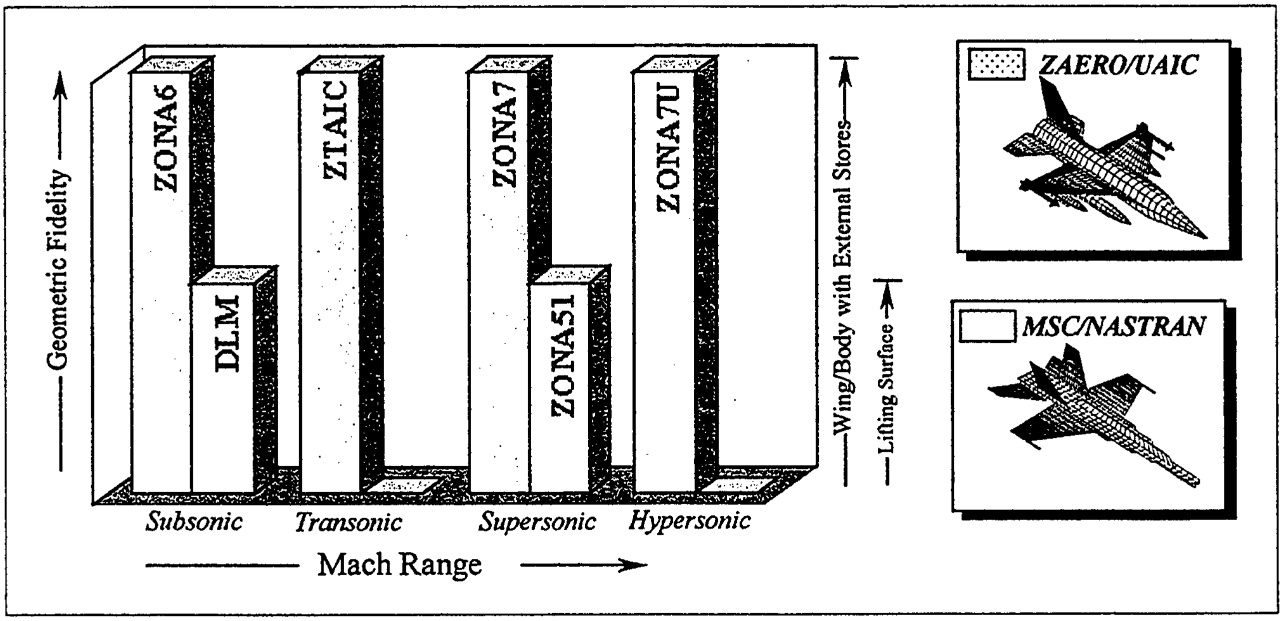
Geometric Fidelity
ZONA6
DLM
ZTAIC
ZONA7
ZONA51
ZONA7U
Wing/Body with External Stores
Lifting Surface
Subsonic
Transonic
Supersonic
Hypersonic
Mach Range
ZAERO/UAIC
MSC/NASTRAN

Fig 1.4 ZAERO/UAIC Module

ZONA6/ZONA7: Generates Unsteady Subsonic/Supersonic Aerodynamics for Aircraft Configurations with External Stores

Prior to 1990, all unsteady aerodynamic methods for aeroelastic computations were based on low-order lifting-surface models (e.g. DLM, Refs 1.6, 1.7). The low-order formulation of these lifting-surface methods renders input complexity in dealing with general planform configurations. Most importantly, the aerodynamic effects due to the presence of bodies and due to wing-body interference were largely ignored. Meanwhile, the coupled external-store wing flutter, a problem that is of frequent concern to modern aeroelasticians, can no longer be resolved by lifting surface modeling alone. For this reason, development of methods such as ZONA6 and ZONA7 are mandatory (Refs 1.8, 1.9).

The main features of ZONA6 and ZONA7 include:

- ZONA6 generates steady/unsteady subsonic aerodynamics for wing-body/aircraft configurations with external stores/nacelles including the body-wake effect.
- ZONA6 is based on a higher-order panel formulation for lifting surfaces than the Doublet Lattice Method (DLM). Cases studied confirm the ZONA6 robustness over the DLM.
- Panel formulation of ZONA7 for lifting surface is identical to that of ZONA51 – now the industrial standard method for supersonic flutter analysis in MSC/NASTRAN.
- ZONA6 and ZONA7 can model any combinations of planar/nonplanar lifting surfaces with arbitrary bodies such as fuselage, stores, tip missiles, or their combinations.
- High-order paneling of ZONA6 and ZONA7 allows high-fidelity modeling of complex aircraft with arbitrary stores/tip missile arrangement.

For further details in the background, application examples and theoretical formulation of ZONA6 and ZONA7, the reader is referred to Section 3.0.

ZTAIC: Generates Unsteady Transonic Aerodynamics for Lifting Surface Systems

Since 1985, ZONA has been following up on the development of the Transonic Strip (TES) Method (Refs 1.10, 1.11) for unsteady flow computations of arbitrary wing planforms. The TES method consists of two consecutive steps, to a given nonlinear Transonic Small Disturbance Code such as ZTRAN, namely the chordwise mean flow correction and the spanwise phase correction. The spanwise correction procedure is further enhanced by a recently uncovered generalized relation obtained according to Oyibos' separability principle.

Based on the TES concept, ZONA's Transonic Aerodynamic Influence Coefficient (ZTAIC) method is developed to fully automate the computation procedure resulting in a modal-based AIC matrix (Ref 1.12). The computation procedure requires direct pressure input from a set of computed or measured data. Otherwise, it does not require airfoil shape or grid generation for a given planform. Meanwhile, all the mean-flow shock jumps are properly included in the resulting unsteady aerodynamics through the AIC formulation. The unsteady pressures can readily be solved on the surfaces of a lifting surface system according to the following modal-based AIC formulation, i.e.

$$\{\Delta C_P\} = [MAIC]\ \{h\}$$

where $[MAIC] = [\Delta C_P \cdot (\phi^T \phi)^{-1} \phi^T]$, ϕ is the base-line modes. ΔC_{P_b} is the computed pressure due to ϕ, and h is the given modes which expressed in terms of ϕ.

The main features of ZTAIC include:

- ZTAIC generates unsteady transonic modal AIC using externally-provided steady mean pressure.
- ZTAIC adopts steady pressure input (provided by measurement or CFD), whereby:
  - no grid generation is required, and
  - the correct unsteady shock strength and position are ensured.
- The modal AIC of ZATIC as an archival data entity allows:
  - repetitive aeroelastic analysis and structure design.
  - the ease of application of the *K* / *P-K* / *g* methods for flutter analysis.
- ZTAIC is readily integrated with ZONA6 as a unified subsonic/transonic AIC method for complex aircraft configurations.
- Additional input to ZONA6 amounts to only the provided steady pressure data.

For further details in the background, application examples and theoretical formulation of ZTAIC, the reader is referred to Section 4.0.

ZONA7U: Generates Unified Unsteady Hypersonic/Supersonic Aero-dynamics for Lifting Surface Systems and Wing-body Configurations

A Unified Supersonic/Hypersonic Lifting Surface Method has been developed recently (Refs 1.13, 1.14). This method combines the Supersonic Lifting Surface Theory (such as ZONA51, Ref 1.15) with a nonlinear thickness correction matrix E_{ij}, based on a composite third-order theory, which is rendered uniformly valid throughout the hypersonic/supersonic regime, i.e.

$$\{\Delta C_P\} = [D + \mu E]^{-1}\ \{w\}$$

where D is the linear supersonic downwash matrix provided by ZONA51 and μ is a switching function that operates on the nonlinear thickness matrix E for compression and expansion waves. This correction matrix takes the flow nonlinearity as well as the flow rotationality due to shock waves into account, which covers both the Mach-wave and Newtonian limits. For aeroelastic applications, ZONA51U has been applied to various wing planforms with thickness distributions. Superseding ZONA51U, ZONA7U integrates ZONA51U into ZONA7 in that the lifting surfaces are subject to unified hypersonic/supersonic aerodynamics.

The main features of ZONA7U include:

- ZONA7U generates unified hypersonic and supersonic steady/unsteady aerodynamics for wing-body/aircraft configurations with external stores/nacelles.
- Nonlinear thickness effects of ZONA7U yields good agreement with Euler solution and test data.
- Steady solutions approach linear and Newtonial limits.
- Confirms hypersonic Mach independent principle.
- Results/formulation are superior to Unsteady Linear Theory and Piston Theory.
- ZONA7U usually results in more conservative flutter boundaries than other methods.
- Unified with ZONA7 and is therefore applicable to all Mach numbers > 1.0.
- Additional input to ZONA7 amounts to only wing root to wing tip sectional thickness profiles.

For further details in the background, application examples and theoretical formulation of ZONA7U, the reader is referred to Section 5.0.

1.3 ZAERO/UAIC and ASE Modules in ASTROS

According to the ASTROS/ZAERO program architecture (Fig 1.3), database entities (such as MAIC) generated by the ZAERO module are computed during the ASTROS preface phase and need not be recomputed in the ASTROS analysis/optimization loop. Meanwhile, computation of the ZAERO module is triggered by the new bulk data entry MKAEROZ which specifies the Mach number, reduced frequencies, method flags and the mean flow conditions.

The development of an aeroservoelasticity (ASE) module, based on the ZAERO/UAIC aerodynamics, and its integration with ASTROS has been completed. The ASE module will facilitate the inclusion of multi-input multi-output (MIMO) control system effects on the dynamic stability and response in the ASTROS multidisciplinary analysis and design optimization software package. Its overall capabilities include:

- Provide closed-loop robust stability analysis.
- Add continuous gust response capabilities.
- Allow the inclusion of stability and gust-response constraints in structural design optimization.
- Allow the inclusion of user-defined control parameters of a given control law in the multidisciplinary optimization process.
- Export an efficient state-space representation of the aeroservoelastic system for subsequent analysis and control synthesis with commercially available tools such as MATLAB and MATRIX x.

ASE mandates the s-domain aerodynamics as a base, which can be obtained from the k-domain aerodynamics by means of several rational approximation methods. Among existing methods the minimum-state approach (MIST) is selected here because it offers significant savings in the number of added states with little or no penalty in the accuracy of modeling the aerodynamic forces. The minimum-state approach converts the generalized aerodynamic forces $Q(i\omega)$ to $Q(s)$ in the following form:

$$\bar{Q}(s) = \bar{A}_0 + \bar{A}_1 \frac{sb}{V} + \bar{A}_2 \left(\frac{sb}{V}\right)^2 + \bar{D}\,\bar{F}^{-1}(s)\,\bar{E}\left(\frac{sb}{V}\right)$$

where $\overline{F}(s) = \frac{sb}{V} I - R$ and $\overline{A}_i$ are the real-value approximation matrices, $\boldsymbol{R}$ is a diagonal matrix with distinct negative terms representing the aerodynamic lags, and $\overline{D}$ and $\overline{E}$ are aerodynamic coupling matrices between the modal and aerodynamic states.

For further details in the background, application examples and theoretical formulation of the ASE module utilizing ZAERO/UAIC, the reader is referred to Ref 1.16, 1.17 and 1.18.

1.4 Other New ZAERO Modules in ASTROS: AGM, 3D Spline and Flutter

ZAERO also includes three other new modules in ASTROS (Fig 1.4). These are: the Aerodynamic Geometry Module (AGM), the 3D Spline Module and the Flutter Module. The essential features of these modules are briefly described as follows.

Aerodynamic Geometry Module (AGM)

The AGM module is capable of modeling any full aircraft configuration with stores and/or nacelles. A complex aircraft configuration can be represented by the AGM module by means of wing-like and body-like definitions. Any modifications to the AGM module, such as input geometry enhancements, will have minimal impact on other general modules.

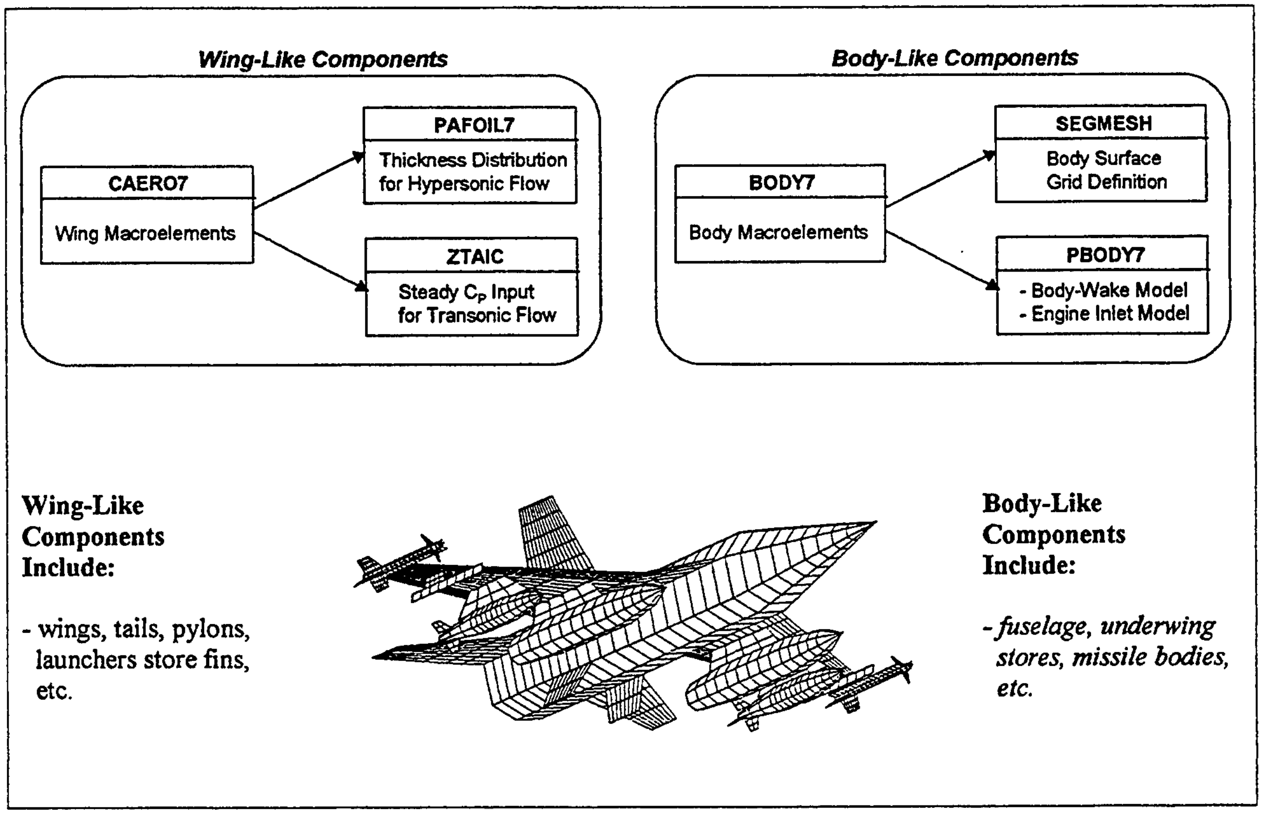
Wing-Like Components
CAERO7
Wing Macroelements
PAFOIL7
Thickness Distribution for Hypersonic Flow
ZTAIC
Steady C_p Input for Transonic Flow
Body-Like Components
BODY7
Body Macroelements
SEGMESH
Body Surface Grid Definition
PBODY7
- Body-Wake Model
- Engine Inlet Model
Wing-Like Components Include:
- wings, tails, pylons, launchers store fins, etc.
Body-Like Components Include:
- fuselage, underwing stores, missile bodies, etc.

Fig 1.5 The Aerodynamic Geometry Module (AGM) of ZAERO

3D Spline Module

The 3D Spline module establishes the displacement/force transferal between the structural Finite Element Method (FEM) model and the ZAERO aerodynamic model. It consists of four spline methods that jointly assemble a spline matrix. These four spline methods include: (a) Thin Plate Spline; (b) Infinite Plate Spline; (c) Beam Spline and (d) Rigid Body Attachment methods. The spline matrix provides the x, y and z displacements and slopes in three dimensions at all aerodynamic grids.

FEM Model **Aerodynamic Model**

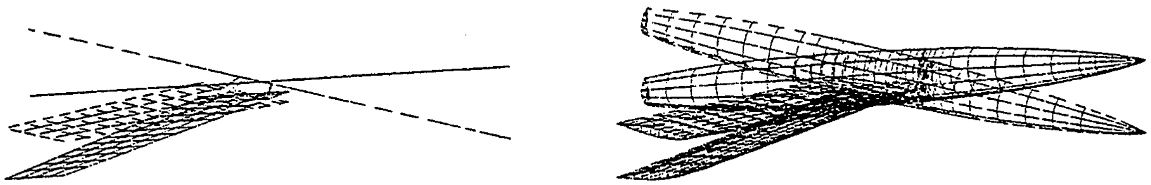

Rigid Body Pitch Mode

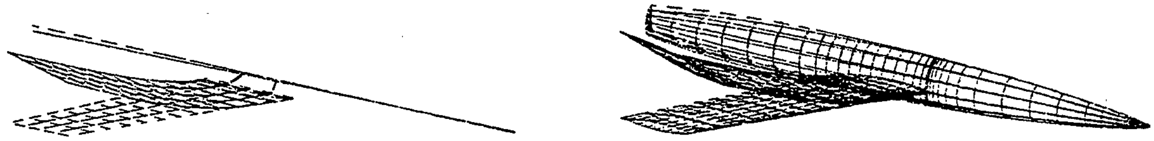

First Wing Bending Mode

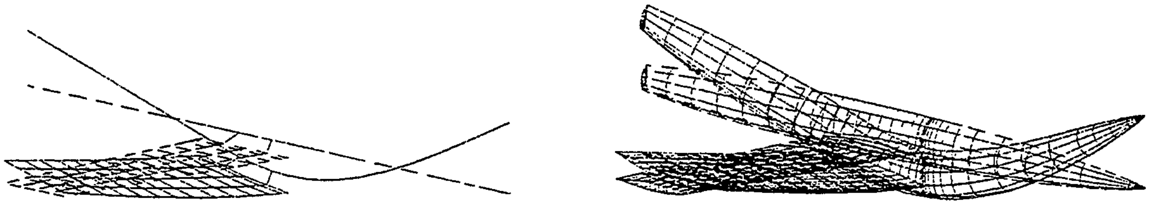

First Body Bending Mode

NACA L51F07 Wing-Body Configuration with Three Structural Modes.

Fig 1.6 The 3D Spline Module of ZAERO

Flutter Module

The ZAERO flutter module contains two flutter solution techniques: the *K*-method and the *P-K* method. The *K*-method is a new contribution of ZAERO to ASTROS. For further details on the background and the theoretical formulation of the 3D Spline Module and the Flutter Module, the reader is referred to Sections 6.0 and 7.0, respectively.

Lastly, we remark that in parallel to seamlessly integrated ZAERO and ASE modules in ASTROS, the stand-alone ZAERO and ASE modules are being developed which should be readily interfaced with other systems such as NASTRAN.

2.0 AEROELASTICITY FOUNDATION OF ZAERO

In this section, we will discuss:

- *fundamentals of aeroelasticity.*
- *aeroelastic matrix equations of ZAERO for flutter analysis.*
- *three disciplines that are required to generate the aeroelastic matrix equations, namely the structural finite element method, the unsteady aerodynamic methods, and spline methods.*

Since the structural finite element method (FEM) is a well-established methodology, no detailed description of the formulation for the generation of the structural matrices will be given. For the unsteady aerodynamic methods, the concepts of amplitude linearization, modal approach and frequency-domain formulation for the generation of Aerodynamic Influence Coefficient (*AIC*), leading to an eigenvalue problem for the flutter analysis, will be discussed in detail.

2.1 Fundamentals of Aeroelasticity

Aeroelastic response of flight vehicle is a result of the mutual interaction of inertial and elastic structural forces, aerodynamic forces induced by the static or dynamic deformation of the structure, and external disturbance forces. The equation of motion of the aeroelastic system in terms of discrete system can be derived based on the equilibrium condition of these forces, i.e.:

$$\overline{\mathbf{M}}\,\ddot{\mathbf{x}}(t) + \overline{\mathbf{K}}\,\mathbf{x}(t) = \mathbf{F}(t) \qquad (2.1)$$

where $\overline{\mathbf{M}}$ and $\overline{\mathbf{K}}$ are the mass and stiffness matrices generated by the structural finite element method. $\mathbf{x}(t)$ is the structural deformation.

The structural damping matrix is excluded in Eq 2.1 for simplicity, but it can be easily included. In Eq 2.1, the terms $\overline{\mathbf{M}}\,\ddot{\mathbf{x}}(t)$ and $\overline{\mathbf{K}}\,\mathbf{x}(t)$ are the inertial and elastic structural forces, respectively, whereas $\mathbf{F}(t)$ represents the aerodynamic forces applied on the structure. $\mathbf{F}(t)$ can be generally split into two parts; the aerodynamic forces induced by the structural deformation $\mathbf{F}_a(\mathbf{x})$ and the external forces $\mathbf{F}_e(t)$, i.e.:

$$\mathbf{F}(t) = \mathbf{F}_a(\mathbf{x}) + \mathbf{F}_e(t) \qquad (2.2)$$

The external forces $\mathbf{F}_e(t)$ are usually provided. Typical example of $\mathbf{F}_e(t)$ is the continuous atmospheric turbulence or impulsive-type gusts. The generation of $\mathbf{F}_a(\mathbf{x})$ normally relies on the theoretical prediction that requires the unsteady aerodynamic computations. Since $\mathbf{F}_a(\mathbf{x})$ depends on the structural deformation $\mathbf{x}(t)$, the relationship can be interpreted as an aerodynamic feedback. Fig 2.1 presents a functional diagram that illustrates the aeroelastic interaction of these structural and aerodynamic forces.

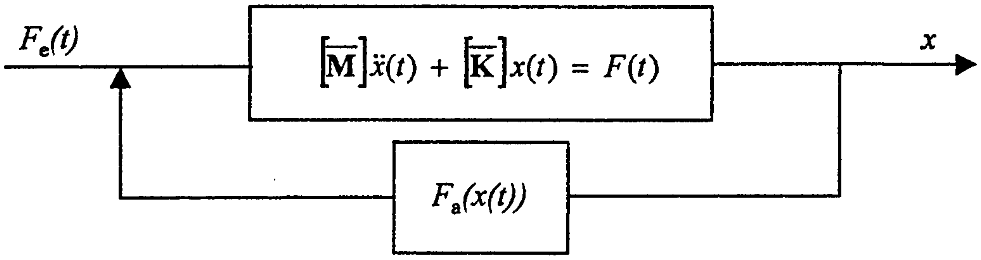

Fig 2.1 Aeroelastic Functional Diagram

Without the aerodynamic feedback, Fig 2.1 reduces to an open-loop forced-structural vibration system whose response amplitude is usually finite. With the inclusion of $\mathbf{F}_a(\mathbf{x})$, Fig 2.1 represents a closed-loop dynamic response problem which can be expressed by the following equation:

$$\overline{\mathbf{M}}\ddot{\mathbf{x}}(t) + \overline{\mathbf{K}}\mathbf{x}(t) - \mathbf{F}_a(\mathbf{x}) = \mathbf{F}_e(t) \tag{2.3}$$

Eq 2.3 is obtained by combining Eq 2.1 and Eq 2.2. The left hand side of Eq 2.3 is in fact a closed-loop aeroelastic system which can be self-excited in nature. This gives rise a stability problem of the closed-loop aeroelastic system known as flutter. Flutter analysis usually involves the search of the structural stability boundary of an aircraft structure in terms of its flight speed and altitude or the corresponding dynamic pressure. If $\mathbf{F}_a(\mathbf{x})$ is a nonlinear function with respect to $\mathbf{x}(t)$, the flutter analysis must be performed by a time-marching procedure solving the following equation:

$$\overline{\mathbf{M}}\ddot{\mathbf{x}}(t) + \overline{\mathbf{K}}\mathbf{x}(t) - \mathbf{F}_a(\mathbf{x}) = 0 \tag{2.4}$$

with initial condition of $\mathbf{x}(0)$ and $\dot{\mathbf{x}}(0)$ being specified at $t = 0$.

The stability boundary of the aeroelastic system is then determined by examining the decay or growth of the structural response $\mathbf{x}(t)$ with respect to the flight speed. This time-marching computational procedure is rather costly since it generally requires a nonlinear time-domain unsteady aerodynamic method known as the Computational Fluid Dynamics (CFD) method. However, the conventional industrial practice of flutter analysis is to recast Eq 2.4 into a set of linear systems and to determine the flutter boundary by solving the complex eigenvalues of the linear systems. Such a procedure involves the assumption of amplitude linearization. The amplitude linearization states that the aerodynamic response varies linearly with respect to the amplitude of the structure deformation in a given aircraft motion if the amplitude is sufficiently small at all times.

Since flutter analysis is a dynamic aeroelastic stability problem, the required amplitude for determining such a stability boundary can be assumed to be mathematically infinitesimal. This follows that the amplitude linearization assumption could recast Eq 2.4 into an eigenvalue problem for flutter analysis. In this case, the aerodynamic system can be approximated by a linear system for which an aerodynamic transfer function can be defined. This transfer function relates the aerodynamic feedback $\mathbf{F}_a(\mathbf{x})$ to the structural deformation $\mathbf{x}(t)$ by means of the following convolution integral, i.e.:

$$\mathbf{F}_a(\mathbf{x}) = \int_0^t q_\infty \, \mathbf{H}\left(\frac{V}{L}(t-\tau) \right) \mathbf{x}(\tau) \, d\tau \tag{2.5}$$

where:

$q_\infty \mathbf{H}$	represents the aerodynamic transfer function
q_∞	is the dynamic pressure.
L	is the reference length and is generally defined as:
$L = \frac{c}{2}$	where c is the reference chord

and:

V	is the velocity of undisturbed flow.

The Laplace domain counterpart of Eq 2.5 is simply:

$$\mathbf{F}_a(\mathbf{x}(s)) = q_\infty \, \overline{\mathbf{H}}\left(\frac{sL}{V}\right) \mathbf{x}(s) \tag{2.6}$$

where:

$\overline{\mathbf{H}}$	is the Laplace domain counterpart of $\mathbf{H}$

With Eq 2.6 at hand, Eq 2.4 can be readily transformed into the Laplace domain and results in an eigenvalue problem in terms of s. This reads:

$$\left[s^2 \, \overline{\mathbf{M}} + \overline{\mathbf{K}} - q_\infty \, \overline{\mathbf{H}}\left(\frac{sL}{V}\right) \right] \mathbf{x}(s) = 0 \tag{2.7}$$

Since the finite element model of aircraft structure normally contains a large amount of degrees of freedom, the size of the mass and stiffness matrices are usually very large. Hence, solving the eigenvalue problem of Eq 2.7 directly would be computationally costly. To circumvent this problem, one introduces the "*modal approach*" which can be expressed as:

$$\mathbf{x} = \mathbf{\Phi} \, \mathbf{q} \tag{2.8}$$

where $\mathbf{\Phi}$ is the modal matrix whose columns contain the lower order natural modes. Normally, no more than ten numbers of the lowest natural modes are sufficient for the flutter analysis of a wing structure. For the whole aircraft structure, fifty natural modes are usually sufficient. $\mathbf{q}$ is the so-called generalized coordinates which are the eigenvectors to be determined.

The rationale of the modal approach is based on the premises that the critical flutter modes are usually due to the coupling of the lower order structural modes. Thus, the structural deformation of the flutter mode can be sufficiently represented by the superposition of lower order modes.

Substituting Eq 2.8 into Eq 2.7 and pre-multiplying Eq 2.7 with Φ^T yield the dynamic (or the flutter) equation:

$$\left[s^2 \mathbf{M} + \mathbf{K} - q_\infty \mathbf{Q}\left(\frac{sL}{V}\right) \right] \mathbf{q} = 0 \tag{2.9}$$

where:

$$\mathbf{M} = \Phi^T \overline{\mathbf{M}} \, \Phi \quad \text{is the generalized mass matrix} \tag{2.10}$$

$$\mathbf{K} = \Phi^T \overline{\mathbf{K}} \, \Phi \quad \text{is the generalized stiffness matrix} \tag{2.11}$$

and:

$$\mathbf{Q}\left(\frac{sL}{V}\right) = \Phi^T \overline{\mathbf{H}}\left(\frac{sL}{V}\right) \Phi \quad \text{is the generalized aerodynamic forces matrix.} \tag{2.12}$$

Since the size of the matrices in Eq 2.9 is in the order of number of modes, the modal approach provide a reduced size of the eigenvalue problem for the flutter analysis that is expressed in the generalized coordinates. Solving such a reduced size eigenvalue problem is computationally much more efficient than that of Eq 2.7. Eq 2.9 is generally referred as the classical flutter matrix equation.

The above discussion shows that reducing the time-domain, generally non-linear flutter equation (Eq 2.4) to the classical flutter matrix equation (Eq 2.9) lies in the availability of the aerodynamic transfer function. However, the generation of aerodynamic transfer functions in the Laplace domain by solving unsteady aerodynamics can be a very complicated procedure. For this reason, unsteady aerodynamic methods are often formulated in the frequency domain by assuming simple harmonic motion. The frequency-domain aerodynamic transfer function in matrix form is called the *Aerodynamic Influence Coefficient (AIC) matrix*. In fact, the major functionality of ZAERO is to generate such *AIC* matrices for the aircraft configuration. This will be briefly discussed in the following section.

2.2 Unified *AIC* of ZAERO

Four unsteady aerodynamic methods are incorporated in ZAERO, namely ZONA6, ZONA7, ZTAIC and ZONA7U that jointly generate the *AIC* matrices covering the complete domain of Mach number range. Theses ZAERO generated *AIC* matrices are called the *unified AIC* for their unified feature in Mach number range.

ZONA6 and ZONA7 solve the integral equations due to the respective unsteady linearized small-disturbance subsonic and supersonic equations for general aircraft configurations. The integral equation is formulated in the reduced frequency domain which is in the context of the simple harmonic motion. The reduced frequency, denoted as *k*, is a fundamental unsteady aerodynamic parameter defined as:

$$k = \frac{\omega L}{V} \tag{2.13}$$

where:

ω is the harmonic oscillatory frequency.

Panel method is adopted by ZONA6 and ZONA7 to solve the integral equations. The panel method requires the aircraft configuration to be discretized into many small panels. Each panel is defined as "aerodynamic box". Fig 2.2 shows a typical panel model of a wing-body configuration.

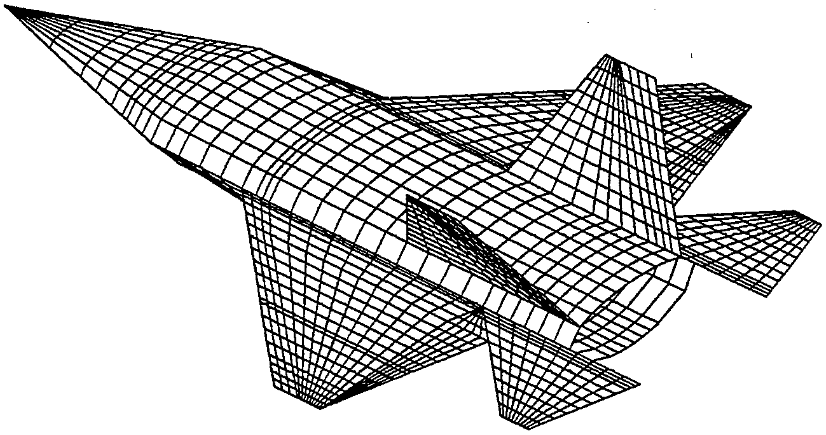

Fig 2.2 Typical panel model of a wing-body configuration

Each aerodynamic box contains a control point where the boundary condition is imposed. According to the panel model, the integral equation is then approximated by the summarization of elementary integrals associated with each aerodynamic boxes. The assembly of the elementary integral solutions gives a matrix whose coefficients represent the aerodynamic influence of aerodynamic boxes to control points. This matrix is called the *Aerodynamic Influence Coefficient (AIC) matrix* which relates the structural deformation to the aerodynamic forces by:

$$\mathbf{F}_{\mathrm{h}} = q_{\infty}\left[\,AIC(ik)\,\right]\mathbf{h} \tag{2.14}$$

where:

$\mathbf{h}$ is the structural deformation defined at the aerodynamic boxes

$\mathbf{F}_{\mathrm{h}}$ is the resultant aerodynamic forces at the aerodynamic boxes due to $\mathbf{h}$.

Comparing Eq 2.4 with Eq 2.6, one can see that q_∞ [*AIC*(*ik*)] is indeed the aerodynamic transfer function, except that:

- *AIC* matrix is computed in the reduced-frequency domain (*k*-domain) rather than the Laplace domain.
- *AIC* matrix is computed based on the panel model which is, in general, considerably different from its respective structural finite element model. This gives rise the problem of displacement and force transferal between these two models. These issues can be resolved by a spline matrix that relates or interpolates the displacements at structural finite element grid points to those at aerodynamic panel model. The derivation of spline matrix will be discussed later. The detailed theoretical background of ZONA6 and ZONA7 is discussed in Section 3.

The ZTAIC method computes the unsteady aerodynamics for transonic flows. It requires the steady pressure distribution input from the users. ZTAIC utilizes an inverse design method for airfoil design by solving the transonic small-disturbance equation. These airfoil sections produce the steady pressure distribution that matches input steady pressure. Unsteady pressure coefficients on the airfoil sections are then computed by solving the unsteady transonic small disturbance equation. These unsteady pressure coefficients are used to correct the linear unsteady pressure computed by ZONA6 for the transonic shock effects. At the end, ZTAIC employs a modal *AIC* approach to reconstruct the *AIC* matrix computed by ZONA6, leading to a transonic *AIC* matrix. For detailed theoretical description, see Section 4 for the formulation of the ZTAIC method.

ZONA7U is a unified supersonic/hypersonic unsteady aerodynamic method. This method combines the supersonic lifting surface aerodynamics of ZONA7 with a nonlinear correction matrix based on Donov & Linnell's uniformly-valid, high-order Hypersonic/Supersonic Scheme. This correction matrix takes the flow nonlinearity as well as the flow rotationality due to oscillatory shock waves into an account, which covers both the Mach wave and Newtonian limits. The only additional input for ZONA7U is the sectional airfoil thickness distribution. ZONA7U generates the *AIC* matrix that is in the same form of that of ZONA7.

The detailed theoretical formulations of ZONA7U is discussed in Section 5.

2.3 Functionality of the Spline Matrix

The problem of data transferal between the panel model and the structural finite element model usually amounts to the displacement transferal from the structural grid points to the aerodynamic control points of the panel model and that of the forces from the aerodynamic control points to structural grid points. ZAERO provides a spline module which generates a spline matrix **G** such that:

$$\mathbf{h} = \mathbf{G}\,\mathbf{x} \tag{2.15}$$

Note that **h** is defined by the aerodynamic control points whereas **x** by the structural finite element grid points. Four methods are incorporated in the spline module, namely the beam spline method, infinite plate spline method, thin-plate spline method and rigid-body attachment method. These four spline methods jointly construct the spline matrix **G** for the displacement transferal. The detail formulations of these four spline methods are discussed in Section 6.

Once the spline matrix **G** is generated, the force transferal from the aerodynamic control points to structural grid points can be performed accordingly:

$$\mathbf{F}_a = \mathbf{G}^T \mathbf{F}_h \tag{2.16}$$

Eq 2.16 is derived based on the principle of virtual work. Since the forces at aerodynamic boxes $\mathbf{F}_h$ and their structurally equivalent values $\mathbf{F}_a$ must do the same virtual work in their respective displacements, we have:

$$\delta\mathbf{h}^T \mathbf{F}_h = \delta\mathbf{x}^T \mathbf{F}_a \tag{2.17}$$

where:

$\delta\mathbf{h}$ and $\delta\mathbf{x}$ are virtual displacements.

Substituting Eq 2.15 into the left-hand side of Eq 2.17 and upon rearranging, yields:

$$\delta\mathbf{x}^T \left(\mathbf{F}_a - \mathbf{G}^T \mathbf{F}_h \right) = 0 \tag{2.18}$$

Because of the arbitrariness of the virtual deflection, i.e. $\delta\mathbf{x} \neq 0$, the terms in the bracket of Eq 2.18 must vanish, which leads to Eq 2.16. With Eq 2.15 and Eq 2.16 at hand, the aerodynamic feedback acting at the structural grid points can be obtained. Combining Eq 2.14 and Eq 2.15 and substituting the resultant equation into Eq 2.16 yield:

$$\mathbf{F}_a = q_\infty \mathbf{G}^T \left[AIC(ik) \right] \mathbf{G}\ \mathbf{x} \tag{2.19}$$

Again, note the similarity between Eq 2.19 and Eq 2.6. The generalized aerodynamic forces matrix in the *k*-domain can be obtained and computed by applying the modal approach:

$$\mathbf{Q}(ik) = \mathbf{\Phi}^T \mathbf{G}^T \left[AIC(ik) \right] \mathbf{G}\, \mathbf{\Phi} \tag{2.20}$$

The *k*-domain **Q**(*ik*) results from the reduction to the simple harmonic motion (frequency domain) from the transient motion (Laplace domain) introduced previously in the unsteady aerodynamic formulation. The impact of *k*-domain **Q**(*ik*) on the solution technique required to solve the classical flutter matrix equation will be discussed in the following section:

2.4 Impact of Q(*ik*) on Flutter Solution Technique

The reduction to the harmonic motion introduced in the previous unsteady aerodynamic formulation indicates that the *k*-domain **Q**(*ik*) is valid only for steady state response of the structure. This also implies that the flutter solution is valid only at the flutter boundary where damping of the aeroelastic system is zero. Since the generalized aerodynamic forces matrix is available only in the frequency domain, the frequency-domain counterpart of Eq 2.9 can be obtained by replacing $\mathbf{Q}(\frac{sL}{V})$ by $\mathbf{Q}(ik)$ and s by $i\omega$. This gives:

$$[-\omega^2 \mathbf{M} + \mathbf{K} - q_\infty \mathbf{Q}(ik)]\, \mathbf{q} = 0 \tag{2.21}$$

As a stability measure, an artificial structural damping is added to Eq 2.21:

$$[-\omega^2 \mathbf{M} + (1 + ig_s)\mathbf{K} - q_\infty \mathbf{Q}(ik)]\mathbf{q} = 0 \tag{2.22}$$

where:

g_s is the added artificial structural damping.

Eq 2.22 is the so-called *K*-method flutter equation. It is mathematically consistent with the assumption of simple harmonic motion introduced in the unsteady aerodynamic formulation. But its predicted damping is only an artifice used to seek out the flutter point and cannot be interpreted as having a physical significance as a measure of decay rate of the aeroelastic response.

While the *K*-method flutter equation is capable providing the prediction of the flutter boundary, e.g. flutter speed at zero damping, it is often desired to have a reliable damping prediction to detect the aeroelastic characteristics at sub-critical flight speeds. The predicted damping values at sub-critical flight speeds can serve as a guideline for conducting wind tunnel or flight flutter tests. It is for this reason that the *P-K* method is widely adopted by aeroelasticians as the primary tool for finding flutter solutions. In Eq 2.9, the *P-K* method replaces the Laplace domain generalized aerodynamic forces matrix $\mathbf{Q}(\frac{sL}{V})$ by $\mathbf{Q}(ik)$; and it further defines a non-dimensional Laplace parameter p such that:

$$p = \frac{sL}{V} = (\gamma k + ik) \tag{2.23}$$

where:

γ is the transient decay rate coefficient,

In this way, Eq 2.9 becomes:

$$\left[\left(\frac{V^2}{L^2}\right)\mathbf{M}\,p^2 + \mathbf{K} - q_\infty \mathbf{Q}(ik)\right]\mathbf{q} = 0 \tag{2.24}$$

For a given $\mathbf{Q}(ik)$, the *P-K* method solves the complex eigenvalues of Eq 2.24 in terms of p. Eq 2.24 is solved at several given values of V and q_∞, for complex eigenvalues p associated with modes of interest. This is accomplished by an iterative procedure that matches the reduced frequency k to the imaginary part of p for every structural mode.

Strictly speaking, the *P-K* method is mathematically inconsistent because **Q**(*ik*) is obtained by the simplification of simple harmonic motion (or by applying the Fourier Transform) but other terms in Eq 2.24 are associated with the transient motion (or by applying the Laplace Transform). However, it is generally believed that the *P-K* method is a good approximation method in finding the rate-of-decay type of solution. The rationale for the *P-K* method is that for simple harmonic motion with slowly increasing or decreasing amplitude, the generalized aerodynamic force based on constant amplitude are good approximations.

The detailed formulations and the solution technique of the *K*-method and the *P-K* method will be discussed in Section 7. In Section 7, a newly developed flutter solution method developed by ZONA Technology called the *g*-method will also be presented. The *g*-method includes a first order damping term in the flutter equation that is rigorously derived from the Laplace-domain aerodynamics. The *g*-method generalizes the *K*-method and the *P-K* method and could provide unlimited roots of the flutter equation. The extra roots obtained by the *g*-method are associated with the aerodynamic lag root which could not be otherwise obtained by the two methods. The superiority and the physical significance of the *g*-method will also be discussed in Section 7.

3.0 ZONA6 / ZONA7: UNSTEADY SUBSONIC / SUPERSONIC AERODYNAMICS FOR WING-BODY AIRCRAFT CONFIGURATIONS WITH EXTERNAL STORES

ZONA6 and ZONA7 solve the respective unsteady three-dimensional linearized small-disturbance potential equations of subsonic and supersonic aerodynamics. Their unique feature lies in the capability of modeling realistic configurations such as an aircraft/wing-body combination including external stores or nacelles. In this section, we will discuss:

- *Background of ZONA6 and ZONA7.*
- *Derivations of unsteady boundary condition and pressure coefficient.*
- *Derivations of the unsteady linearized small-disturbance equations and their corresponding integral equations.*
- *Formulation of panel method employed by ZONA6 and ZONA7 for solving the integral equations.*
- *Generation of their Aerodynamic Influence Coefficient (AIC) matrices.*
- *Treatments of body-wake effect in subsonic flow.*
- *Treatments of inlet boxes and superinclined aerodynamic boxes in supersonic flow.*

3.1 Backgrounds of ZONA6 and ZONA7

Since 1985, ZONA has been devoting its R&D effort to the development of unsteady aerodynamic methods for aeroelastic applications. The first ZONA software product for supersonic lifting surface unsteady aerodynamics is the ZONA51 code. ZONA51 employs the acceleration-potential approach for thin-wing type of lifting surfaces (Ref 3.1). This acceleration-potential approach is the outgrowth from the Harmonic Gradient Method (HGM) developed by Chen and Liu in 1985 (Ref 3.2). Today, ZONA51 is the industrial standard method for supersonic lifting surface unsteady aerodynamics in MSC/NASTRAN - Aero Option II (Ref 3.3).

In Figs 3.1 and 3.2, computed results of Re(ΔC_p) and Im(ΔC_p) of a flat plate undergoing plunging and pitching motion about the leading edge are presented. It can be seen that the results computed by ZONA51 are in better agreement with Jordan's exact solution (Ref 3.4) than that of HGM. The close agreement with Jordan's result near the trailing edge is attributed to an exact treatment of linearized pressure in the acceleration-potential formulation of ZONA51.

At the National Aeronautical Establishment (NAER) Canada, Lee (Ref 3.5) has performed a comparative study on computed pressures for an oscillating leading-edge flap on the F-18 wing at 58.8% span and at $M = 1.1$ and reduced frequency $k = 4.0$ (see Fig 3.3). Two computer codes are used: the ZONA51 code and the SPIP code (Ref 3.6).

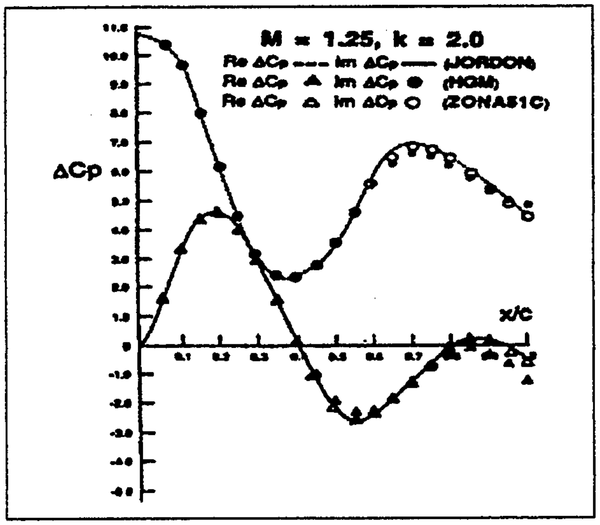

Fig 3.1 Comparison of Computed Unsteady Pressures for a Plunging $M = 1.25$ and $k = 2.0$

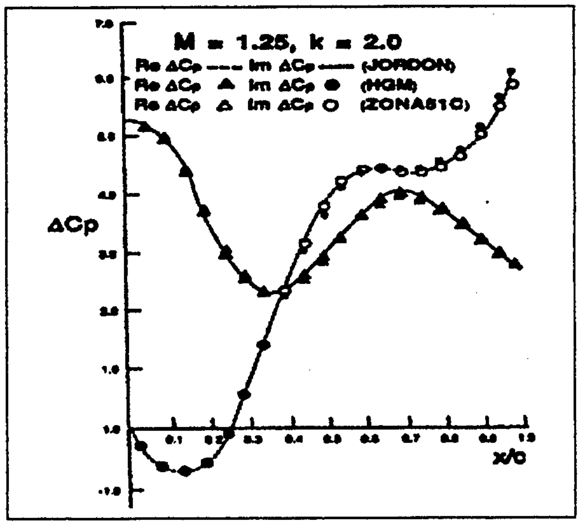

Fig 3.2 Comparison of Computed Unsteady Pressures for a Pitching Flat Plate About the Leading Edge at $M = 1.25$ and $k = 2.0$

In Fig 3.4, computed results show that the expected pressure jump at the hinge line is well predicted by ZONA51 using 126 panels. The results obtained by the SPIP code, however, depend on the number of quadrature points chosen where no pressure jump across the hinge line is seen until more quadrature points are used.

Johnson et al. (Ref 3.7) performed as supersonic unsteady aerodynamic computation for the Viggen Idealization (Ref 3.8) using ZONA51 option in MSC/NASTRAN. The canard is slightly above the wing plane by a distance of 0.1 length units. The generalized force $Q_{1,2}$ shown is the lift coefficient of the wing due to a unit rotation of the canard about its midchord.

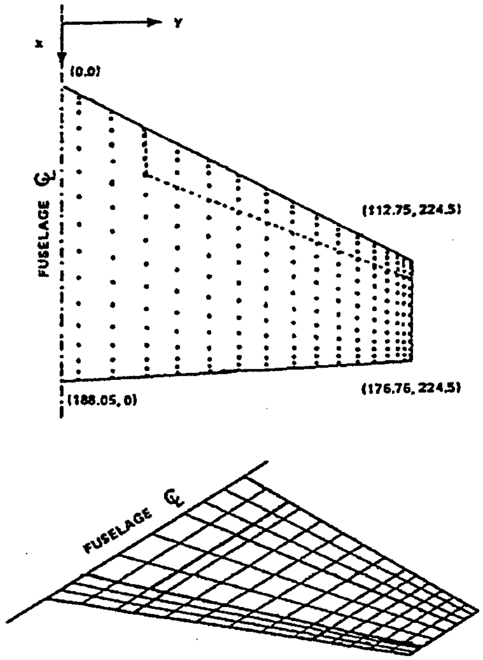

Fig 3.3 Aerodynamic Modeling of F-18 Wing

The lift coefficient is obtained by dividing the generalized force by the dynamic pressure and the square of the wing span (1.20 units). As shown in Ref 3.6, the wing lift is calculated by considering two rigid-body modes of motion, the first being the wing alone undergoing unit plunging, and the second being unit canard rotation. The reduced frequency is based on a reference semichord of 1.00 unit. The results are shown in Fig 3.5 and almost coincide with the NLR SPNLRI-CP (Ref 3.9) results up to the high reduced frequency of $k = 5.0$.

To verify convergence, two aerodynamic element ("box") idealizations were considered. In the first, the canard was divided into 8 equal width strips with 8 equal chordwise divisions, and the wing was divided into 12 equal width strips and 12 equal chordwise divisions, giving a total of 208 boxes. In the second idealization, the equal divisions were 10 x 10 on the canard and 20 x 20 on the wing for a total of 500 boxes. The two sets of results agreed within plotting accuracy and are not distinguished in Fig 3.5.

Stark's Characteristic Box Method (CHB; Ref 3.10) results are also shown in Fig 3.5. It can be seen that the CHB results agree with the NLR SPNLRI-CP and ZONA51 results only at low reduced frequencies ($k < 1$). At higher reduced frequencies, the CHB results give considerable discrepancy compared to these of the other two methods.

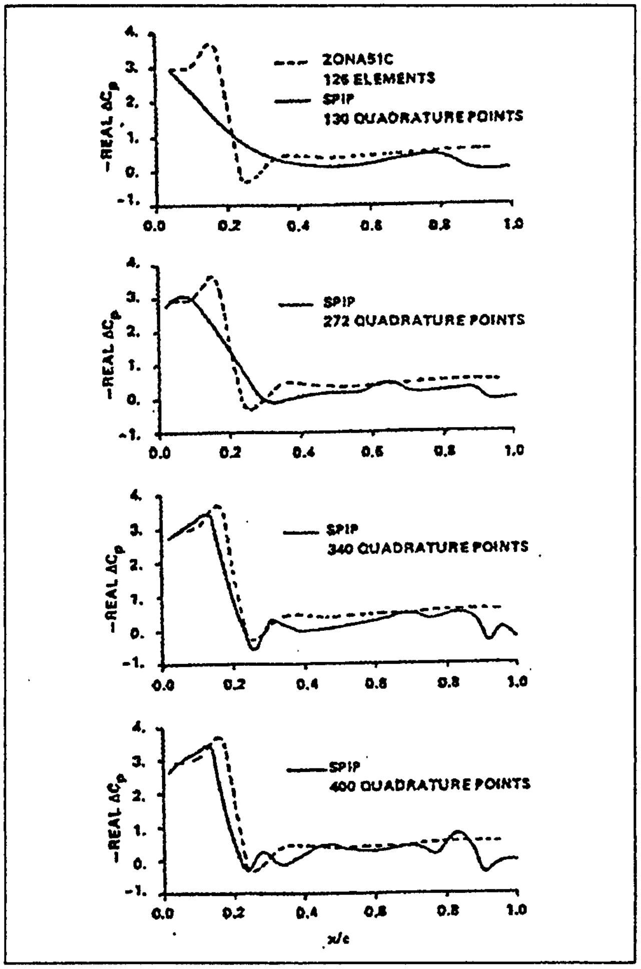

Fig 3.4 Effects on Panels on Computed Pressures for an F-18 Wing with an Oscillating Leading-Edge Flap at 58.8% span, $M = 1.1$ and $k = 4.0$

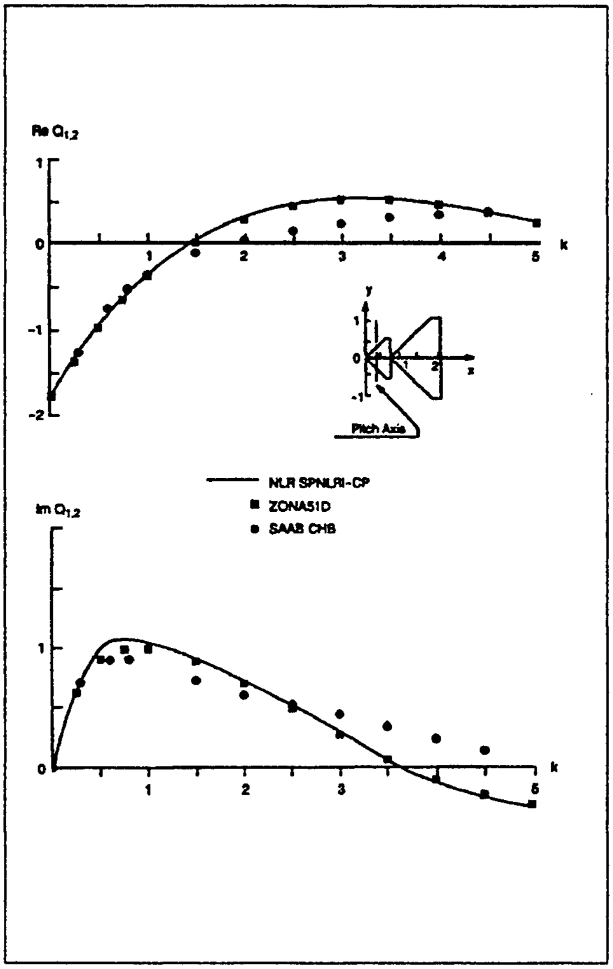

Fig 3.5 Real and Imaginary Part of the Lift on the Main Wing Due to Pitch of the Canard, $M = 1.054$

In order to demonstrate the capability of ZONA51 for supersonic flutter analysis, a 70° swept delta wing (model 1A) in this series is selected for comparison with the existing flutter results. The planform is subdivided into 100 panels as shown in Fig 3.6. Four modes are used in the present flutter analysis.

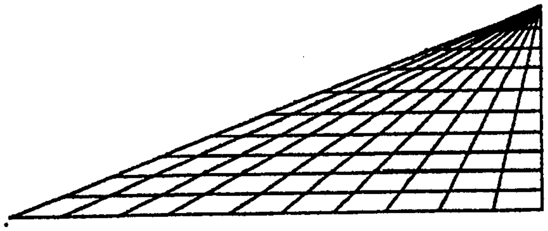

Fig 3.6 Paneling Scheme for a 70° Delta Wing

A set of flutter points were obtained for seven Mach numbers ($M = 1.01$, 1.19, 1.30, 1.64, 2.0, 2.25 and 3.0) using ZONA51. Throughout the supersonic Mach number range considered, ZONA51 appears to yield the best correlation with experimental data among all supersonic methods shown here; these include FAST (Ref 3.11), ACUNN (Ref 3.12), Piston Theory (second order) (Ref 3.13) and CAP-TSD (Ref 3.14) (Figs 3.7, 3.8). Overall, ZONA51 predicts slightly lower values in the flutter frequency ratio ω_f / ω_2 (ω_2 is the natural frequency of mode 2) than the obtained experimental data.

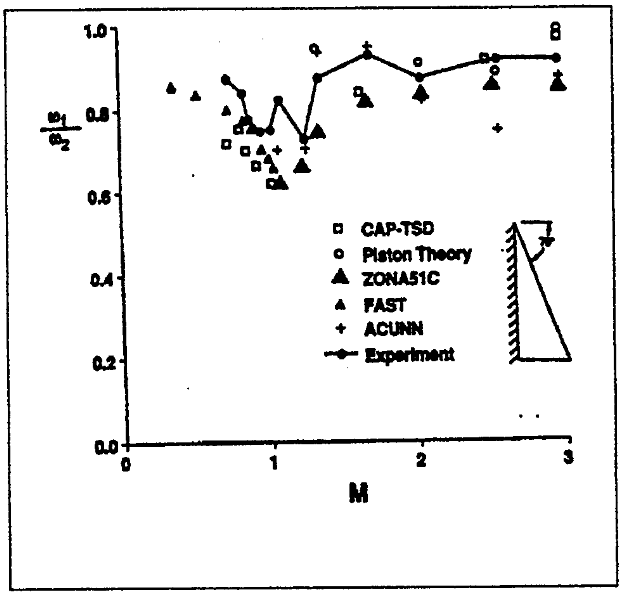

Fig 3.7 Computed and Measured Flutter Speeds vs. Mach Number

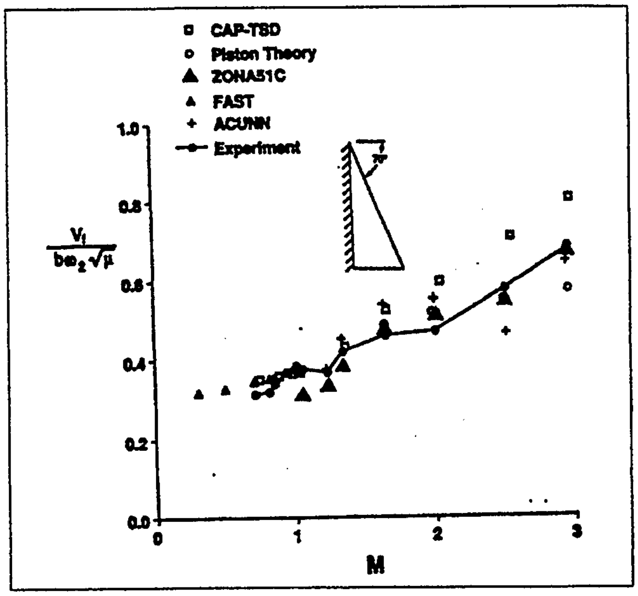

Fig 3.8 Comparison of Ratios of Flutter Frequency vs. Mach Number

ZONA7 (Ref 3.15) generalizes ZONA51 for the wing-body configuration. Its lifting surface method is identical to ZONA51. But its body aerodynamic capability enables ZONA7 to model realistic aircraft configuration including the external stores. To verify ZONA7 on body-alone configuration, a 10% thick ogive body performing oscillation in a first bending model is selected (Fig 3.9). Complete agreement is found between the HPP (Ref 3.16) results and the present results in this high reduced-frequency case ($k = 1.0$).

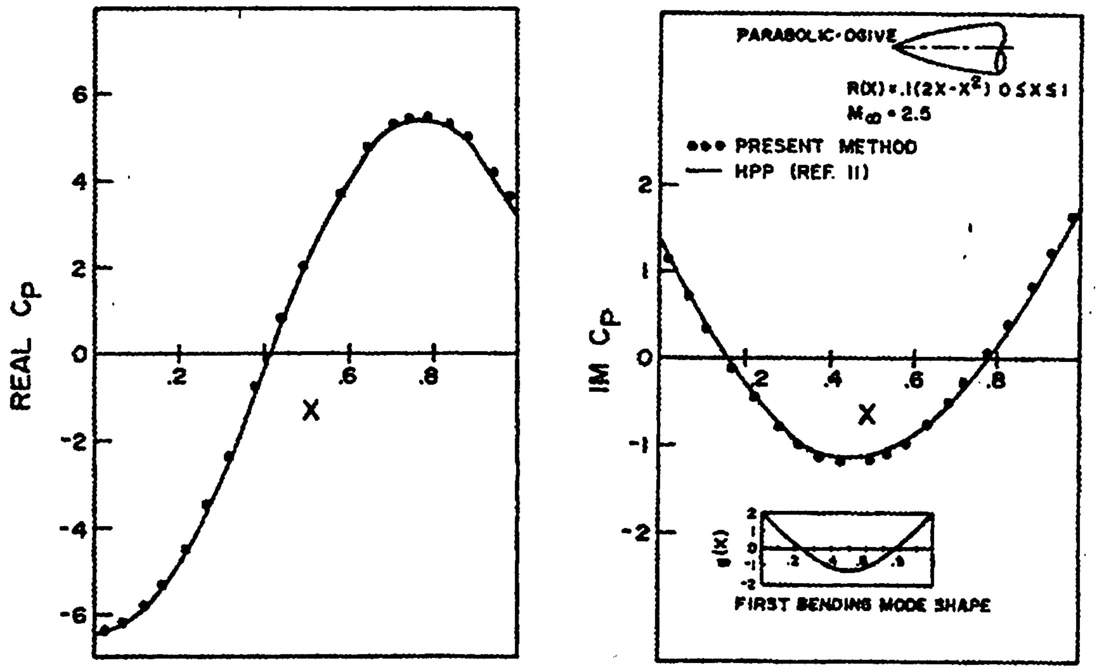

Fig 3.9 In-Phase and Out-Of-Phase Pressure Coefficients for a Bolic-Ogive in First Bending Mode at $M_\infty = 2.5$ and Reduced Frequency $k = 1.0$

For the case of wing-body configuration in steady flow, longitudinal loadings ($C_n d / d_{\max}$) over a 10% thick body with and without a tapered wing ($AR = 4.0$ and taper ratio = 0.6) are presented in Fig 3.10.

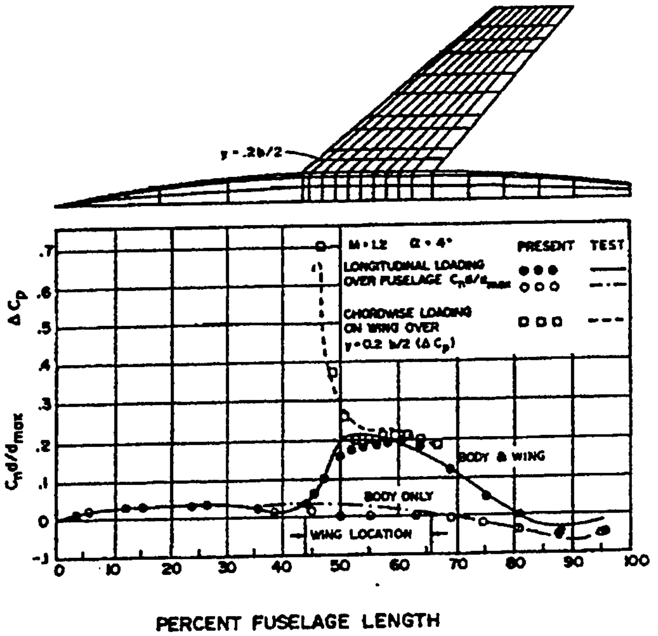

Fig 3.10 Static Loadings About the Fuselage-Wing Junctions

No interference effect is noted in the first 40% of the body length, as expected. A bump-like loading along 40-85% body length is observed as a result of the presence of the tapered wing. In addition, lifting pressure distribution along the wing chord is also plotted at the 20% semispanwise location. Good agreement is found between the computed and measured results (Ref 3.17). Thus, the steady aerodynamic option of the ZONA7 method is validated by means of this present interference example.

For wing-store configuration, an NLR wind-tunnel test configuration constructed with an F-5 wing plus an underwing store is modeled by 112 body panels representing the missile body, 72 wing panels for the launcher and 24 panels for the four aft fins (Fig 3.11). The complete configuration is in pitching oscillation about 50% root chord at a circular frequency f = 10 Hz, and at two Mach numbers, M = 1.1 and 1.35.

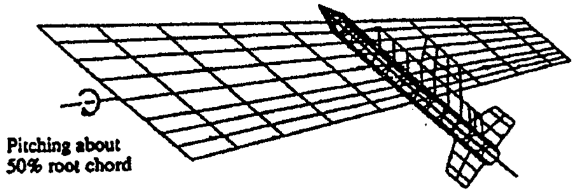

Fig 3.11 Paneling Model for the Underwing Store Configuration: Northrop F-5 Wing Plus Underwing Pylon, Launcher, Missile Body with Four Aft Fins

Figs 3.12-3.14 present the comparisons of the NLR measured data and the present computed results are presented.

Fig 3.12 presents the unsteady normal forces and pitching moments on the underwing store system of two different combinations: 1) the pylon plus launcher ($P + L$), and 2) in addition to 1), a missile body with four aft fins ($P + L + MB + AW$). The in-phase (real) part of the computed normal forces and pitching moments for both cases correlated well with the measured data, while all out-of-phase (imaginary) parts remain insignificantly small.

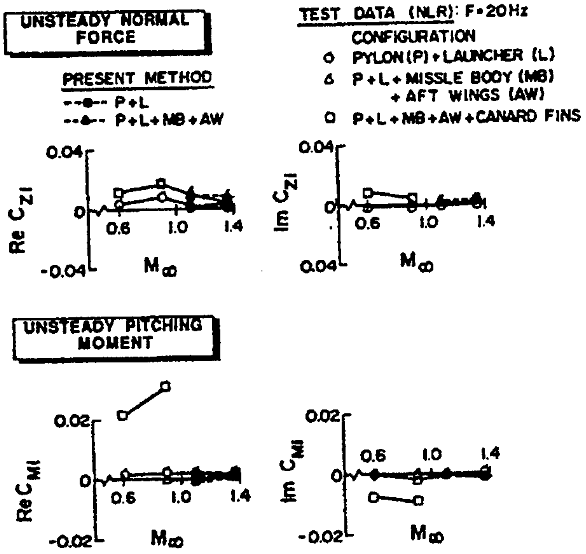

Fig 3.12 Unsteady Normal Force and Pitching Moment for the Underwing Store Configuration With and Without the Missile Body Oscillating about 50% Root Chord at M_∞ = 1.1 and 1.35 and Reduced Frequency k = 0.1

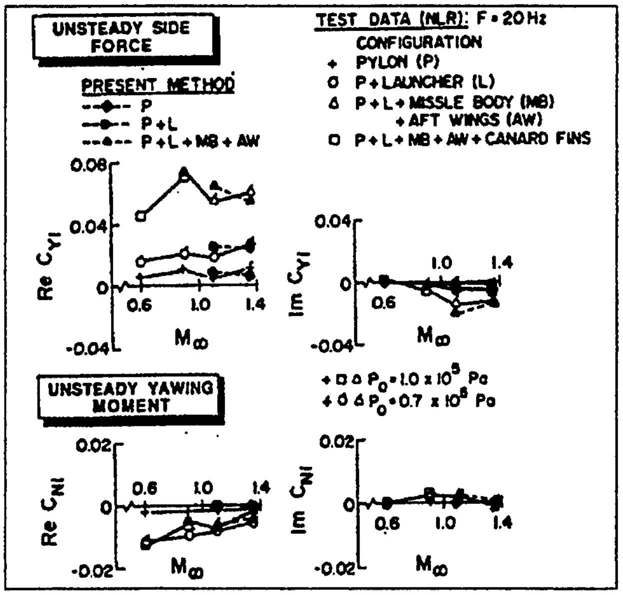

Fig 3.13 Unsteady Side Force and Yawing Moment for the Complete Underwing Store Configuration With and Without the Missile Body and Launcher Oscillating about 50% Root Chord at $M_\infty = 1.1$ and 1.35 and Reduced Frequency $k = 0.1$

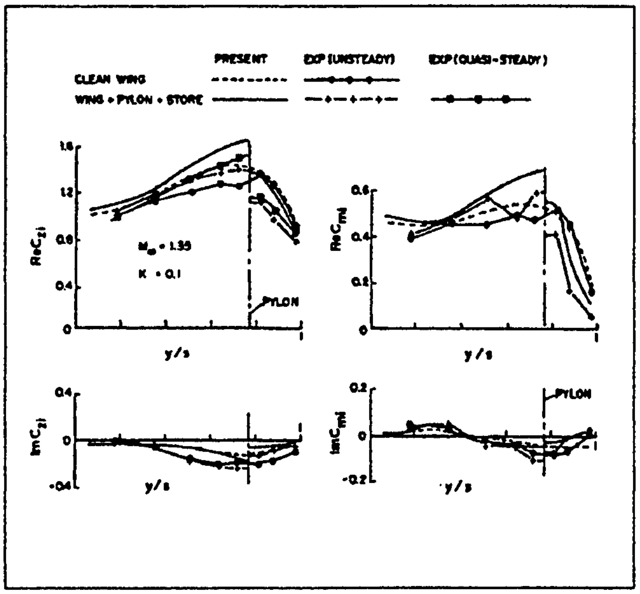

Fig 3.14 Unsteady Spanwise Normal Force and Pitching Moment for the Clean F-5 Wing and the Underwing Store Configuration at $M_\infty = 1.35$ and Reduced Frequency $k = 0.1$

Fig 3.13 presents the side forces and yawing moments on the underwing store systems in three different combinations: 1) pylon alone (*P*); 2) pylon and launcher (*P* + *L*); and 3) in addition to 2), a missile body with four aft fins (*P* + *L* + *MB* + *AW*). Both measured data and computed results show increases in the in-phase normal forces (positive for outboard direction) with the addition of the system from 1) to 3), whereas a decreasing trend is observed for the out-of-phase parts. The unsteady yawing moments on the system are relatively small. The computed results also show that the added missile with fins to the system contributes most to the in-phase moment (positive body apex pointing inboard).

In Fig 3.14, the integrated spanwise unsteady normal forces and pitching moments along the F-5 wing under the influence of the complete underwing store system are plotted against those of the clean-wing case according to the computed results and the test data. It seen that the computed forces and moments predict the same trend as the measured data showing a finite discontinuity across the pylon location. The computed results tend to overestimate the in-phase forces and moments and underestimate the out-of-phase forces and moments in comparison with the measured data.

However, these discrepancies may be caused by the uncertainties in the measured unsteady data as mentioned in Ref 3.18. Meanwhile, NLR also provided the measured quasisteady data, which is supposedly more reliable for the in-phase forces. Better agreement in trend between the quasisteady data and the computed results is found for this case.

ZONA6 (Ref 3.19) is the subsonic counterpart of ZONA7 except that includes the important body-wake effects for fuselage and stores. For wing-body configuration in steady flow, the static loading of the same fuselage-wing configuration depicted in Fig 3.10 is now computed by ZONA6 at $M = 0.6$, $\alpha = 4°$. Fig 3.15 shows an excellent agreement found between ZONA6 results and the measured data.

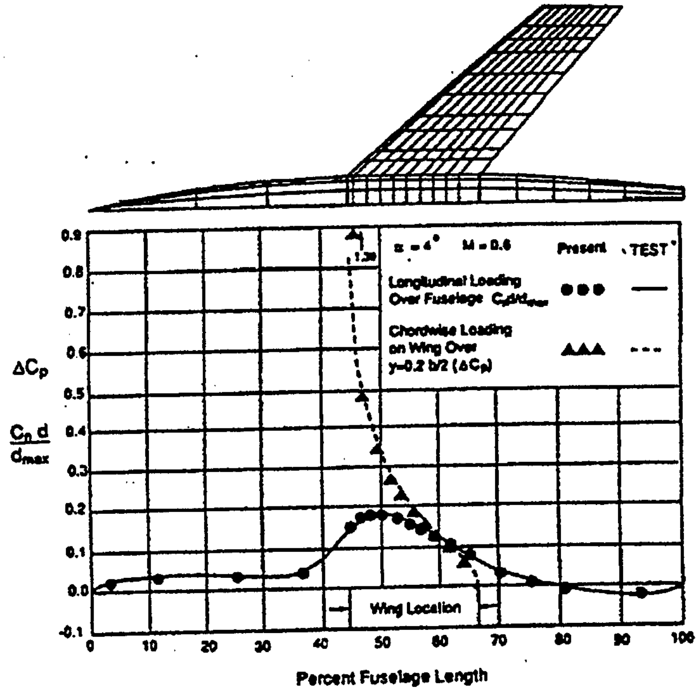

Fig 3.15 Static Loading of NACA Wing-Body Configuration; $M = 0.6$ and $\alpha = 4°$

Figs 3.16 – 3.19 present a series of computed results by ZONA6 in comparison with NLR measured and analysis data for an NLR modeled wing-tip-store configuration (Ref 3.20).

Based on the configuration and the paneling scheme shown in Fig 3.16, the computed steady pressure coefficients along the tip-tank at two azimuthal angles, 1) $\theta = 292.5°$ and 2) $\theta = 67.5°$, are presented in Fig 3.17. The present results appear to be in good agreement with each other and with NLR's computed and measured data.

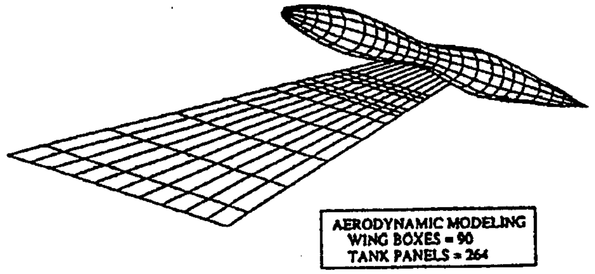

Fig 3.16 NLR Wing-Tip-Tank Configuration Showing Paneling Scheme

Fig 3.18 presents the unsteady pressures along tip-tank at an azimuthal angle $\theta = 202.5°$. It is seen that the present results are in good agreement with the NLR measured data. The present in-phase C_p without wake appears to deteriorate towards the tail of the tip-tank, whereas that with wake appears to correlate best with the measured data. This is expected, because the flow is known to separate at the rear in this case. For the out-of-phase C_p, the NLR computed results show a discrepancy with the measured data starting from the midbody.

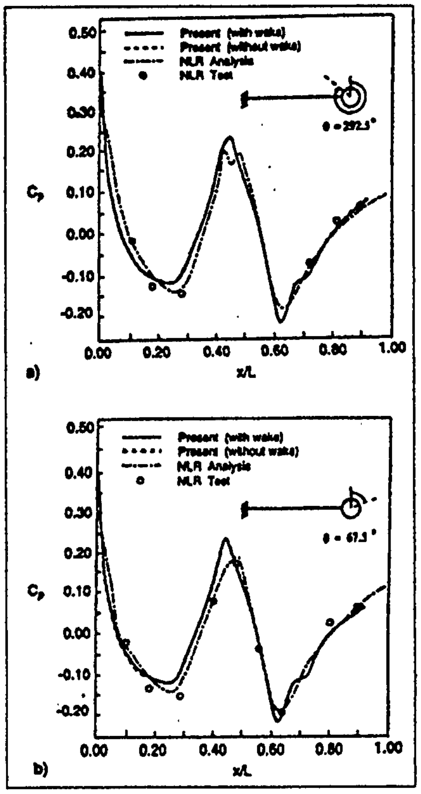

Fig 3.17 Steady Pressure Distribution Along the Tip-Tank of NLR Wing-Tip-Tank Configuration;
$M = 0.45$ and $\alpha = 4°$:
a) $\theta = 292.5°$ and b) $\theta = 67.5°$

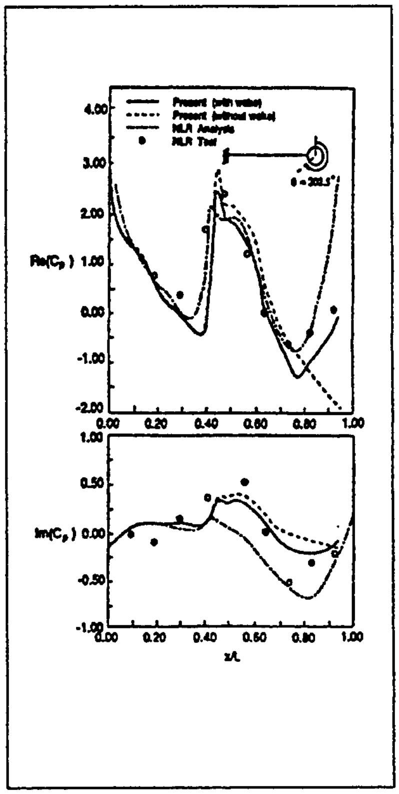

Fig 3.18 Unsteady Pressure Distribution Along the Tip-Tank of NLR Wing-Tip-Tank Configuration;
$M = 0.45$, $\alpha = 0°$, $k = 0.305$,
$\bar{x}_o = 0.15\, c_R$, and $\theta = 202.5°$

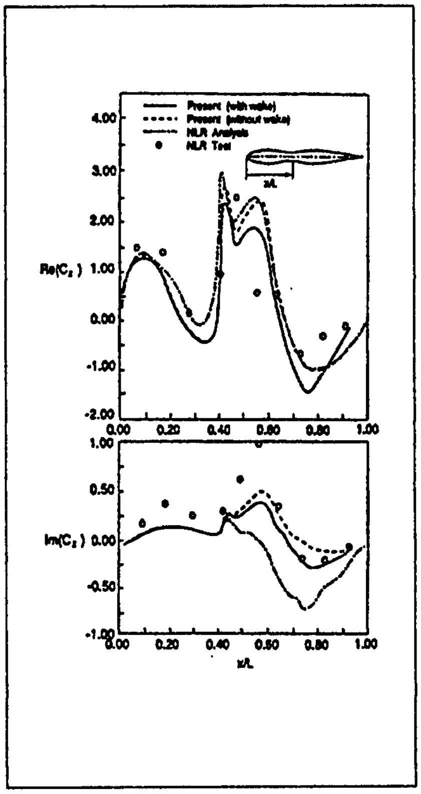

Fig 3.19 Unsteady Normal Load Distribution Along the Tip-Tank of NLR Wing-Tip-Tank Configuration;
$M = 0.45$, $\alpha = 0°$, $k = 0.305$
and $\bar{x}_o = 0.15\, c_R$,

Fig 3.19 presents the unsteady normal load C_z along the tip-tank. It is seen that the present predicted values of the in-phase and out-of-phase C_z are in better agreement with the measured data than those of NLR, particularly for the cases with the wake model. In addition, the NLR's out-of-phase result show considerable departure from the measured data.

It should also be noted that ZONA6's lifting surface method adopts a higher order paneling scheme than the Doublet Lattice Method (DLM) (Ref 3.21), in that the later only considers a line distribution on each aerodynamic box. It is found that the high order paneling scheme is of importance for the robustness of the unsteady lifting surface methods (Ref 3.22). In order to demonstrate this, two wing planforms are selected for comparison of the present results and DLM results. These planforms include a rectangular wing of aspect ratio 20 at $M = 0.0$ and a 70° delta wing at $M = 0.8$. The main objective in the present cases studied is to display the ease of utilization of a high-order panel code such as ZONA6 as opposed to that of DLM. For all cases considered (Figs 3.20-3.27), a commonly-practiced paneling scheme, as shown in Fig 3.22, the spanwise panel cut N_y is provided by equal cut along the span whereas the chordwise panel cut

N_x by lines that connects the equally-divided points along the root chord and tip chord. It will be shown that ZONA6 is less sensitive to the paneling scheme than DLM, hence a more robust code. No attempt is made to select other paneling schemes for further investigation of this issue.

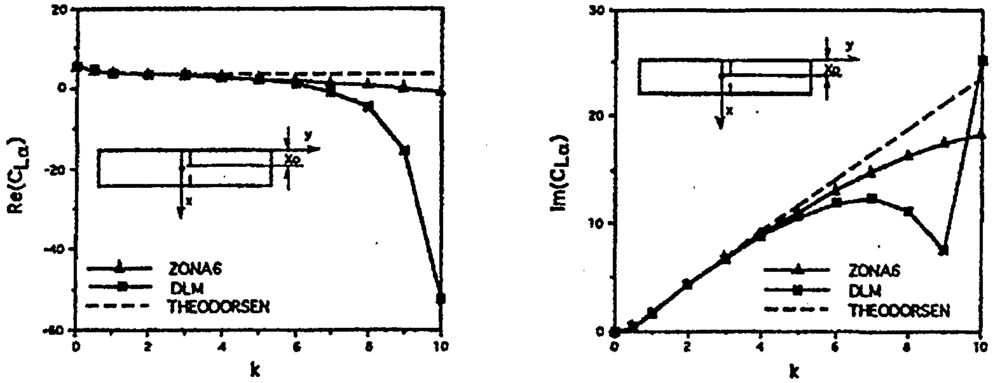

(a) 10 x 10

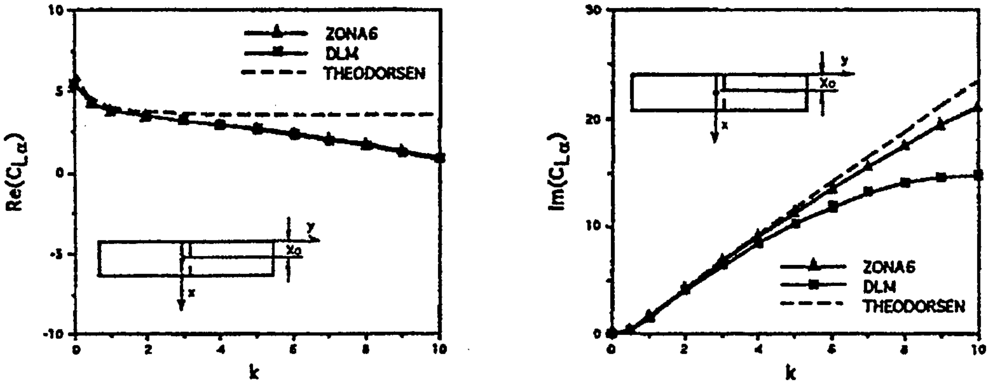

(b) 10 x 40

Fig 3.20 Generalized Aerodynamic Forces C_{L_α} (=Q_{12}/S) versus Reduced Frequency k:
$AR = 20$, Rectangular Wing ($M = 0.0, x_o = 0.5c$);
a) Panel Number = 10 x 10, b) Panel Number = 10 x 40

Rectangular Wing of AR = 20

Fig 3.20 presents the ZONA6 and DLM results in terms of generalized aerodynamic forces (GAF) versus reduced frequencies K for a rectangular wing of AR = 20.0 pitching about 50% chord. Two paneling schemes are adopted: N_x x N_y = 10 x 10 (Fig 3.20a) and N_x x N_y = 10 x 40 (Fig 3.20b). It can be seen that for the 10 x 10 case the DLM results depart from the Theodorsen's exact theory (Ref 3.23) exponentially for k = 0.3, while the ZONA6 results maintains an acceptable range. For the 10 x 40 case, the error of ZONA6 results are further reduced as one would expect. However, large discrepancy still exists in the imaginary part of C_{L_α} between DLM and Theodorsen's theory.

According to the MSC/NASTRAN manual (Ref 3.3), the chordwise panel number is linearly proportional to reduced frequency k. For obtaining a valid result, DLM requires that $k = 0.08\ N_x$, for N_x at least equal to or greater than four. This is to say that for N_x = 10 the valid limit for k is around 1.0, and for $k = 10$, N_x has to be over 100. For a rectangular wing, the spanwise panel number N_y can be expressed as:

$$N_y = \left(\frac{AR}{2\,\Delta AR}\right) N_x$$

where AR and ΔAR are the aspect ratio of wing and panel, respectively. If ΔAR is bounded by 3.0, N_y should be at least over 400. It is clear that all these tedious numerical restrictions are a result of the low orderness of DLM. By contrast, ZONA6 removes all these restrictions and can be applied readily with the present paneling scheme. A further study of these methods in the effect of the panel number on C_{L_α} and C_{M_α} results is shown in Fig 3.21. It is seen that the DLM result is very sensitive to the spanwise panel cut if N_y is below 20 and it converges very slowly to Theodorsen's solution. On the other hand, ZONA6 results approach Theodorsen's solution asymptotically as the panel number increases.

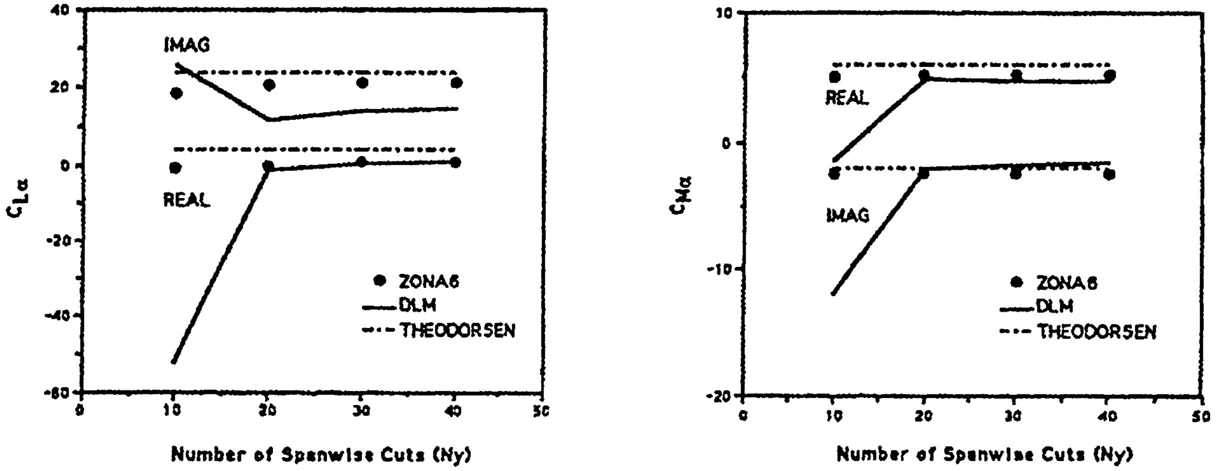

Fig 3.21 Effects of Panel Numbers on GAF C_{L_α} and C_{M_α} :
$AR = 20$; Rectangular Wing ($M = 0.0$, $k = 10$, $x_o = 0.5c$)

Slender Delta Wings

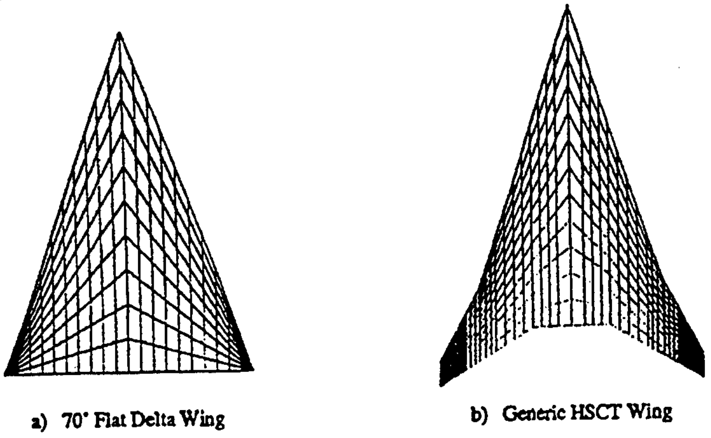
a) 70° Flat Delta Wing

b) Generic HSCT Wing

Fig 3.22 Typical Paneling Scheme

The slender delta wing family belongs to another planform category that, with the present paneling scheme (see Fig 3.22), DLM would have difficulty in producing satisfactory results. For a tapered or delta wing planform, N_y can be generalized to:

$$\Delta AR_i = \left(\frac{N_x}{2N_y}\right)\left(\frac{c}{c_i}\right)AR$$

where ΔAR_i is the panel aspect ratio of the ith strip and c_i is the corresponding local chord length. Hence, the ratio of ΔAR_i on two strips is inversely proportional to their local chord lengths. For a 70° delta wing with a 10 x 10 panel cut (Fig 3.22), the aspect ratio of the outboard strip at the tip section, would amount to 17 times that of an inboard strip at the second station. This condition would probably be too stringent a condition for DLM to be applicable.

The effect of swept angle on the steady C_{L_α} and C_{M_α} for a slender wing is presented in Fig 3.23 at $M = 0.8$. With a 10 x 10 panel cut for a slender delta wing, it seen that ZONA6 result correctly approaches Miles' asymptotic slender-wing limit (Ref 3.24), whereas DLM would not do so.

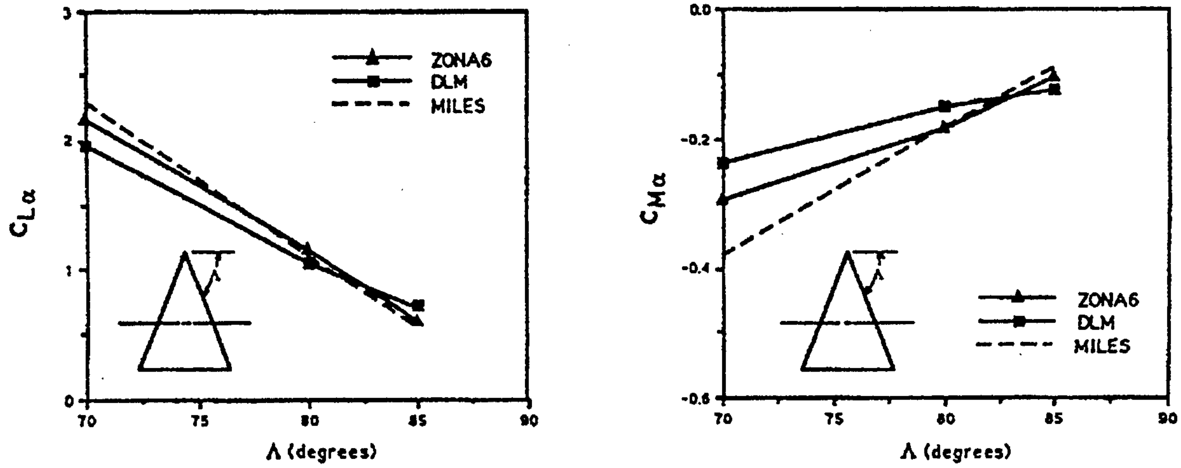

Fig 3.23 Effects of Sweptback Angle on C_{L_α} and C_{M_α} ($M = 0.8, k = 0.0, x_o = 0.5c$)

70° Delta Wing

A thorough numerical study has been conducted on a 70° delta wing in pitching about its midchord at $M = 0.8$. The unsteady pressures, forces and moments are computed at various spanwise locations based on DLM and ZONA6. Figs 3.24, 3.25 and 3.26 present the pressure distribution on two spanwise stations at 15% half span (station 2) and 95% half span (station 10) at reduced frequencies $k = 0.0$, 0.5 and 10.0, respectively. Two paneling schemes are used, one with 10 x 10 cut, the other 40 x 10 cut. Several observations on the computed pressures in these figures are in order:

- All ZONA6 results are valid showing consistent improvement in pressure details as the panel number increases.
- Almost all DLM results are invalid except at station 2 with a 10 x 10 cut, corresponding to a panel aspect ratio of 0.43. It should be noted that the panel aspect ratio for all other cases are greater than unity.
- The DLM pressures tend to converge to the ZONA6 pressures toward the aft wing portions at station 2. The reason for this is not clear. Perhaps the skewness of the upstream panels might also attribute to the solution breakdown.

An obvious remedy to use DLM is to adopt a different paneling scheme from the present one. This then would amount to establishing another set of numerical restrictions. But all these could be avoided if one uses ZONA6 instead.

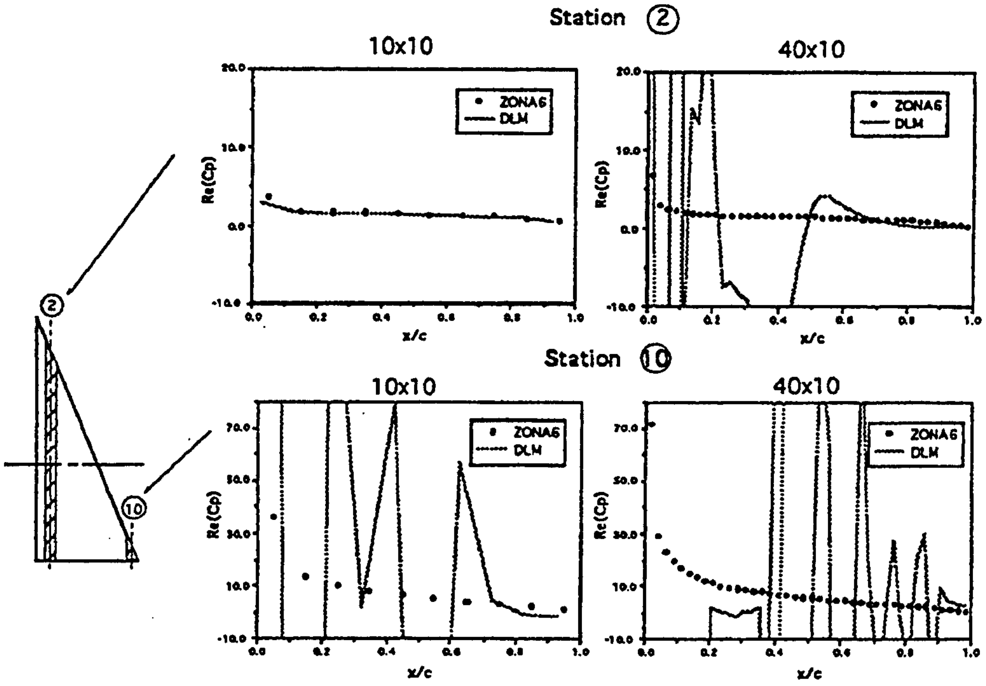

Fig 3.24 In-Phase Pressures on Two Spanwise Stations:
70° Delta Wing ($M = 0.8$, $k = 0.0$, $x_o = 0.5c$)

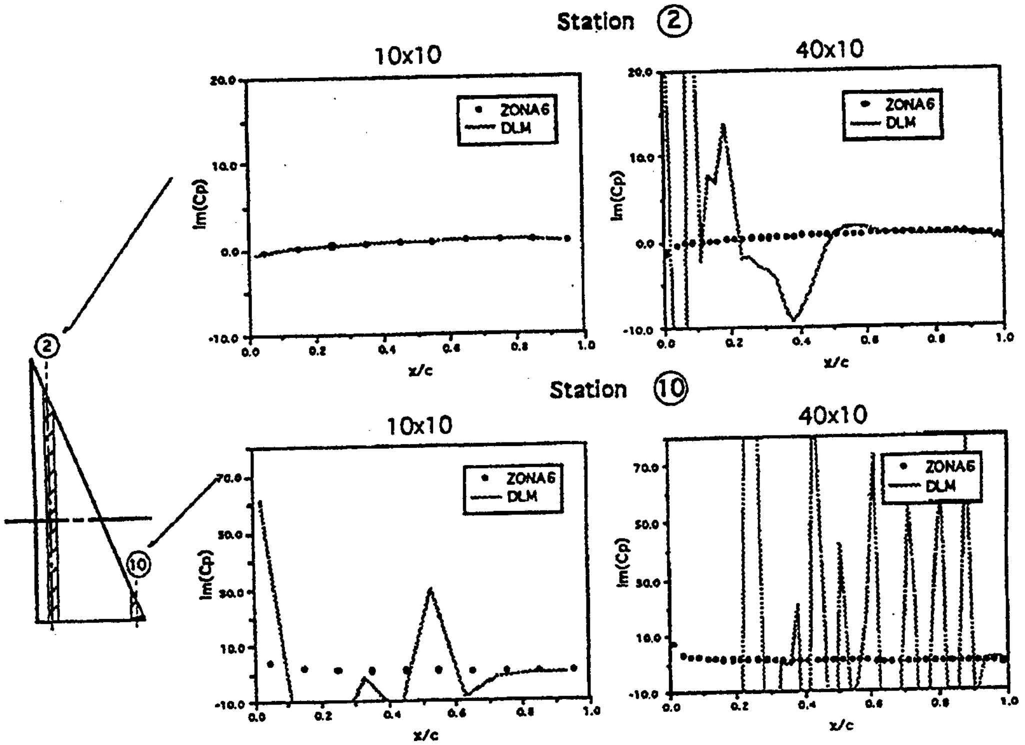

Fig 3.25 Out-of Phase Pressures on Two Spanwise Stations: 70° Delta Wing ($M = 0.8$, $k = 0.5$, $x_o = 0.5c$)

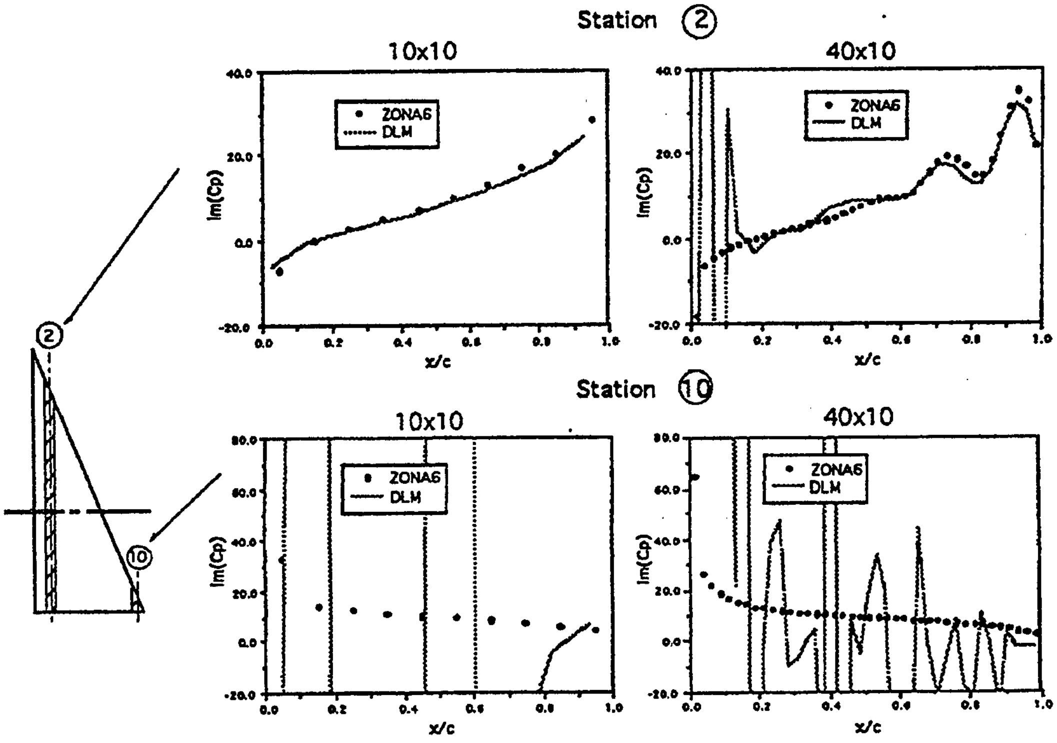

Fig 3.26 Out-of Phase Pressures on Two Spanwise Stations: 70° Delta Wing ($M = 0.8$, $k = 10.0$, $x_o = 0.5c$

Lastly, Fig 3.27 presents the effect of the panel number on the generalized aerodynamic forces C_{L_α} and C_{M_α}. It is seen that ZONA6 results consistently approach to a converged solution as the chordwise panel number N_x increases, whereas the results of DLM fail to do so.

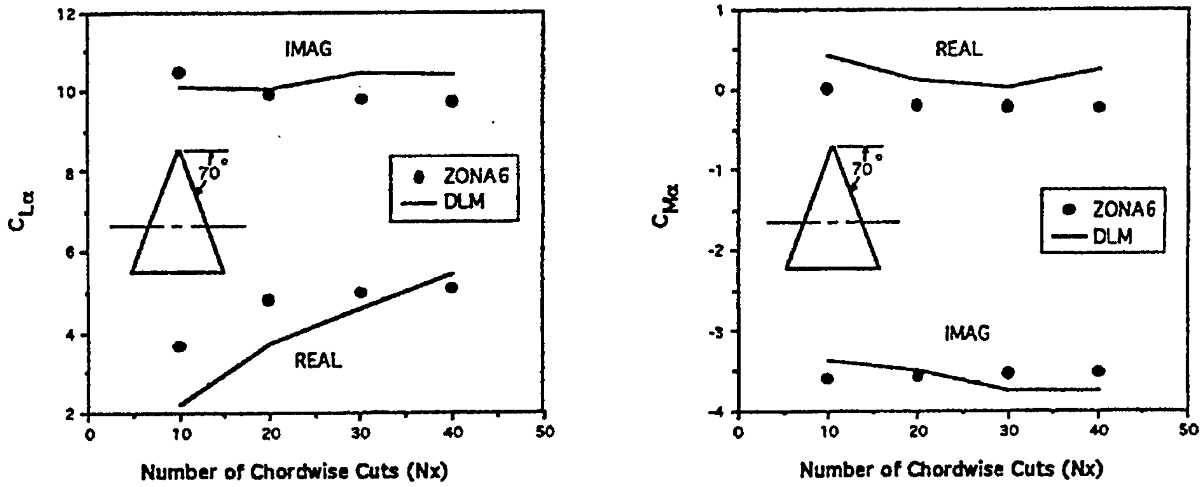

Fig 3.27 Effects of Panel Numbers on C_{L_α} and C_{M_α}:
70° Flat Delta Wing ($M = 0.8$, $k = 10.0$, $x_o = 0.5c$)

3.2 Integral Equations of the Linearized Small Disturbance Equation

ZONA6 and ZONA7 solve the linearized small disturbance equation that reads:

$$\left(1 - M_\infty^2\right) \Phi_{xx} + \Phi_{yy} + \Phi_{zz} - 2 M_\infty^2 \Phi_{xt} - M_\infty^2 \Phi_{tt} = 0 \tag{3.1}$$

where:

M_∞ is the freestream Mach number

and:

$$\Phi = \phi_o + \phi_1 \quad \text{is the total velocity potential.} \tag{3.2}$$

Eq 3.2 shows that the total potential Φ consists of two parts; the steady potential ϕ_0 as well as the unsteady potential ϕ_1 where ϕ_o is of the order of wing thickness and ϕ_1 is of the order of oscillatory amplitude due to the structural modes. For stability analysis the amplitude of the structural oscillation is assumed to be smaller than wing thickness or at all times, i.e.

$$\phi_1 << \phi_o \tag{3.3}$$

Substituting Eq 3.2 into Eq 3.1 and collecting the like-order terms yield the equations for ϕ_1 and ϕ_o:

$$\left(1 - M_\infty^2\right) \phi_{oxx} + \phi_{oyy} + \phi_{ozz} = 0 \tag{3.4}$$

$$\left(1 - M_\infty^2\right) \phi_{1xx} + \phi_{1yy} + \phi_{1zz} - M_\infty^2 \phi_{1tt} - 2 M_\infty^2 \phi_{1xt} = 0 \tag{3.5}$$

Eqs 3.4 and 3.5 are the steady and unsteady linearized small disturbance equations respectively. The steady and unsteady potentials are decoupled in these equations because Eq 3.1 is a linear equation. Solving the steady and unsteady flows requires Eqs 3.4 and 3.5 to be subjected to their respective steady and unsteady boundary conditions. The solution techniques for solving the time-domain unsteady linearized small disturbance equation (Eq 3.5) have been presented by Morino and Tseng (Ref 3.25) for subsonic flow and Freedman and Tseng (Ref 3.26) for supersonic flow by a time domain Green's function approach. However, such a time domain Green's function approach is complex and costly in computation. Also, insufficient unsteady results were presented in their work for proper assessment of the applicability to aeroelastic analysis.

Consider an aircraft of interest performs a simple harmonic motion, the unsteady potential ϕ_1 generated can be expressed in a reduced form:

$$\phi_1 = \phi \, e^{i\omega t} \tag{3.6}$$

where:

ω is oscillation frequency

ϕ is the reduced frequency-domain potential.

Let:

$$x' = L \beta x , \qquad y' = L y , \qquad z' = L z \tag{3.7}$$

where:

L is the reference length (3.8)

and:

$$\beta = \sqrt{\left|1 - M_\infty^2\right|} \tag{3.9}$$

Introducing the so-called modified potential $\bar{\phi}$ such that:

$$\phi = \bar{\phi} \, e^{i \lambda M_\infty x'} \tag{3.10}$$

where:

$$\lambda = \frac{k\,M_\infty}{\beta} \quad \text{is the so-called compressible reduced frequency} \tag{3.11}$$

and:

$$k = \frac{\omega\,L}{V} \quad \text{is the reduced frequency.} \tag{3.12}$$

One can transform Eq 3.5 into:

$$\bar{\phi}_{x'x'} + \mu\,\bar{\phi}_{y'y'} + \mu\,\bar{\phi}_{z'z'} + \lambda^2\,\bar{\phi} = 0 \tag{3.13}$$

where:

$$\mu = 1 \qquad \text{for} \qquad M_\infty < 1 \tag{3.14}$$

$$\mu = -1 \qquad \text{for} \qquad M_\infty > 1 \tag{3.15}$$

Applying Green's theorem to Eq 3.13, an integral solution can be obtained in terms of the unsteady source and doublet singularity distributions σ and $\Delta\phi$ over the surface S of the configuration of interest. Transforming this integral solution back to an expression for ϕ, one obtains:

$$\begin{aligned}\phi(x_o, y_o, z_o) = &-\frac{1}{E\pi}\iint_S \sigma(x, y, z)\ e^{i\lambda M_\infty \xi}\ K\,dS \\ &+\frac{1}{E\pi}\iint_{S+W} \Delta\phi(x, y, z)\ e^{i\lambda M_\infty \xi}\ \frac{\partial}{\partial n}\,K\,dS\end{aligned} \tag{3.16}$$

where:

x_o, y_o, z_o	are the field points (to be influenced)	
x, y, z	are the sending points (from the sources and doublets)	
$E = 4$	for	$M_\infty < 1$
$E = 2$	for	$M_\infty > 1$
σ	is the unsteady source singularity distribution	
$\Delta\phi$	is the unsteady doublet singularity distribution	
$\frac{\partial}{\partial n} = \vec{n}\cdot\vec{\nabla}$,	$\vec{n}$ is the out-normal vector	
K	is the Kernel function	

$$K = \frac{e^{-i\lambda R}}{R} \qquad \text{for} \qquad M < 1 \qquad \text{(Subsonic Kernel)}$$

$$K = \frac{\cos(\lambda R)}{R} \qquad \text{for} \qquad M > 1 \qquad \text{(Supersonic Kernel)} \tag{3.17}$$

$$R = \sqrt{\xi^2 + \mu\,\eta^2 + \mu\,\zeta^2} \tag{3.18}$$

and:

$$\xi = \left(\frac{x - x_o}{\beta L}\right), \qquad \eta = \left(\frac{y - y_o}{L}\right), \qquad \zeta = \left(\frac{z - z_o}{L}\right) \tag{3.19}$$

The integral associated with the unsteady source singularity is defined over the surface of the configuration S, where S can be expressed as:

$$S(x, y, z, t) = 0 \tag{3.20}$$

whereas the unsteady doublet singularity over the configuration and the wake surfaces $S + W$. The surface of a typical wing section and its associated wake surface are shown in Fig 3.28.

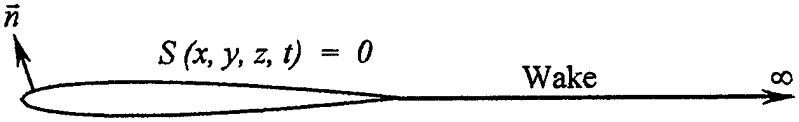

Fig 3.28 Surface definition of configuration and wake

The vector $\vec{n}$ shown in Fig 3.28 represents the out-normed vector of S and can be expressed as:

$$\vec{n} = \frac{\vec{\nabla} S_o}{\left|\vec{\nabla} S_o\right|} = n_x \vec{i} + n_y \vec{j} + n_z \vec{k} \tag{3.21}$$

where n_x, n_y and n_z are the components of $\vec{n}$ along x, y and z directions, respectively.

For solving the integral equation in Eq 3.16, ZONA6 and ZONA7 adopt the so-called panel method whose formulation will be discussed in a later section.

3.3 Unsteady Boundary Condition and Pressure Coefficients

The inviscid fluid flow boundary condition requires the flow to be tangential only to a moving body at all times, i.e.:

$$\frac{\partial S}{\partial t} + \vec{V} \cdot \nabla S = 0 \qquad \text{at} \quad S(x, y, z, t) = 0 \tag{3.22}$$

where S is the body surface defined in a wind-fixed coordinate system and $\vec{V}$ is the flow velocity.

Eq 3.22 is the generic equation for all tangency conditions desired for elastic wing planforms of unsteady motions. For elastic bodies performing unsteady motion, however, Eq 3.22 is found to be unsuitable. Attempts in the past (Ref 3.20) to derive the body tangency condition using Eq 3.22 in fact failed to produce useful results. By useful results, it is meant to arrive a set of second order terms to account for the body thickness effect in addition to the slender body boundary condition. Benneker, Roos and Zwaan (Ref 3.20) has derived such a wind-fixed boundary condition. But their boundary condition contains several second-order *singular* terms, all associated with the second derivative of the mean-flow potential. It appears that no clear resolution was stated in Ref 3.20 as to the remedy of the singular terms.

In their extensive analysis, Garcia-Fogeda and Liu (Ref 3.27) suggested an approach to adopt the body-fixed coordinate system that could totally circumvent the singularity problem. The flow tangency condition under this system reads:

$$\left(\vec{V} - \vec{V}_{\mathrm{B}}\right) \cdot \nabla S = 0 \qquad \text{at} \quad S = 0 \tag{3.23a}$$

where $\vec{V}_{\mathrm{B}}$ is the velocity due to body surface motion. This approach results in all regular second-order terms. The usefulness of the boundary condition and the resulting C_P expression (will be shown later), have been ascertained and adopted by much of ZONA's subsequent works in unsteady subsonic and supersonic aerodynamics for bodies and wing-body configurations (Refs 3.28, 3.29).

Garcia-Fogeda and Liu started from Eq 3.23a and obtained the following equation for an arbitrary elastic body in harmonic motion with given modes, i.e.:

$$\vec{\nabla}\phi \cdot \vec{n} = \mathbf{F}_{\mathrm{B}} \tag{3.23b}$$

where $\vec{\nabla}\phi = (u, v, w)$ is the unsteady perturbation velocity vector due to the harmonic motion, and:

$$\mathbf{F}_{\mathrm{B}} = n_{\mathrm{x}}\,(h_{\mathrm{x}}'\,u_{\mathrm{o}} + i\,k\,h_{\mathrm{x}}) + n_{\mathrm{y}}\,(h_{\mathrm{y}}' + i\,k\,h_{\mathrm{y}}) + n_{\mathrm{z}}\,(h_{\mathrm{z}}' + i\,k\,h_{\mathrm{z}}) \tag{3.24}$$

is the so-called "downwash function" on arbitrary bodies,

where:

h_x, h_y and h_z are the components of the modes with respect to the reference length L along x, y and z directions, respectively

u_o is the steady perturbation velocity components in the x direction

$(\ )'$ is the differential operator with respect to $\left(\frac{x}{L}\right)$.

For a flat plate type lifting surface, i.e. $n_x = 0$, Eq 3.24 is reduced to the familiar boundary condition:

$$\vec{\nabla}\varphi \cdot \vec{n} = \mathbf{F}_W \qquad \text{at} \quad S = 0 \tag{3.25}$$

where:

$$\mathbf{F}_W = \mathbf{h}_W' + i\,k\,\mathbf{h}_W \tag{3.26}$$

is the so-called "downwash function" on flat-plate type of lifting surface,

and:

$$\mathbf{h}_W = n_y\, h_y + n_z\, h_z \tag{3.27}$$

Comparing $\mathbf{F}_W$ to $\mathbf{F}_B$, one can see that indeed Eq 3.25 is a special case of Eq 3.23. Also, while the unsteady boundary condition of lifting surfaces is totally uncoupled from the steady flow influence, the unsteady boundary condition of arbitrary body includes the steady (mean) flow component u_o. Computing the steady flow components requires the solution of the steady small disturbance equation (Eq 3.4) with the well-known steady boundary condition:

$$\vec{\nabla}\phi_o \cdot \vec{n} = -(\vec{V} \cdot \vec{n}) \tag{3.28}$$

where $\vec{V}$ is the free-stream velocity vector.

Based on the work of Garcia-Fogeda and Liu (Ref 3.27), the unsteady pressure coefficient on the body expressed in the body-fixed coordinate reads:

$$\begin{aligned} C_p = -2\, C_o \Big(& (1+u_o)(u+h_x' u_o + h_y' u_o) + v_o v + w_o w \\ & + h_z' w_o + h_y' v_o + i\,k(\phi + h_x u_o + h_y v_o + h_z w_o)\Big) \end{aligned} \tag{3.29}$$

where:

$$C_o = \left[1 - \frac{\gamma-1}{2} M_\infty^2 \left(2u_o + u_o^2 + v_o^2 + w_o^2\right)\right]^{\frac{1}{\gamma-1}} \tag{3.30}$$

u_o, v_o and w_o are the steady perturbation velocity components

ϕ, u, v and w are the unsteady perturbation potential and velocity components

γ is the specific heat ratio

For a flat-plate type lifting surface at zero angle of attack, the steady perturbation velocity components are zeros, i.e. $u_o = v_o = w_o = 0$. Eq 3.29 is the reduced to the well-known pressure coefficient expression of lifting surfaces:

$$C_p = -2\,(u + ik\phi) \tag{3.31}$$

However, the conventional pressure coefficient of lifting surface is an expression in terms of the difference of pressure between its lower and upper surfaces. Expressing Eq 3.31 in terms of pressure difference on the mean surface gives:

$$\Delta C_p = -2\,(\Delta u + ik\Delta\phi) = -2\left(\frac{\partial\Delta\phi}{\partial x} + ik\Delta\phi\right) \tag{3.32}$$

where $\Delta(\cdot)$ denotes the difference between the lower and upper surfaces of $(\cdot)$.

It should be remarked that the unsteady pressure C_p for arbitrary bodies Eq 3.29 involves coupling terms with the perturbation velocities of the steady mean flow, which brings in the thickness effects. By contrast, the unsteady pressure ΔC_p for lifting surface (Eq 3.32) is uncoupled from the steady mean flow terms.

3.4 Paneling Scheme for Aircraft Configurations

The surface of an aircraft configuration is broadly divided into two categories: the body-like components and wing-like components (see Fig 3.29). The body-like components (BLC) consists of fuselage, external stores, tiptanks, etc. Each BLC is divided into *NG* number of segments by x = constant cuts. Each segments consists of *NR* x *NQ* number of surface boxes, all of which are flat panel elements. That is, each segment is subdivided into *NR* rings by *NR*+1 cross sections, obtained by cutting the segment with x = constant planes. Next, a circumferential (radial) cut is applied to this same segment yielding *NQ* boxes on each ring. There are *NQ*+1 circumferential points to define the *NQ* boxes. The order of these *NQ*+1 points begins from the bottom meridian counting in the clockwise direction looking downstream. Let *NB* represent the number of boxes of the total body-like components for an aircraft, and let *NBODY* denote the number of body-like components. Thus, *NB* can be expressed as:

$$NB = \sum_{i=1}^{NBODY} \sum_{j=1}^{NG_i} (NR_{ij} \times NQ_{ij}) \tag{3.33}$$

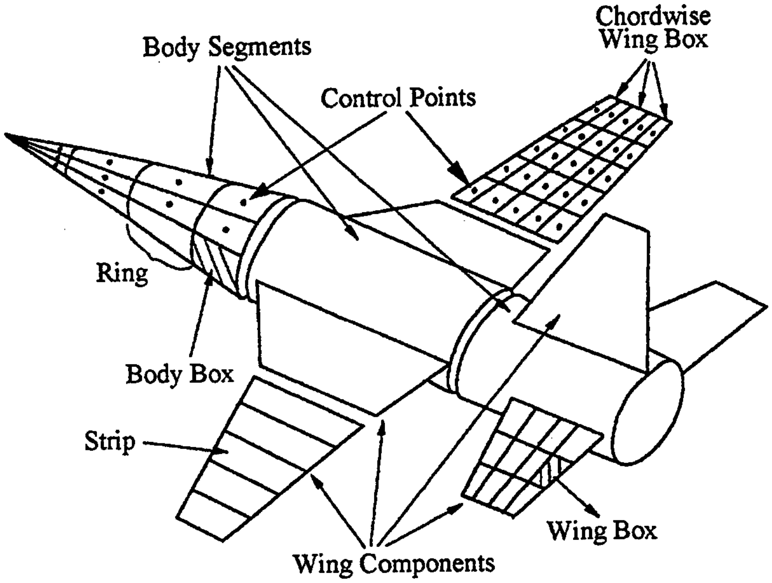

Fig 3.29 Aircraft Components Showing Body and Wing Segment/Box

The wing-like components (WLC) consists of thin surfaces whose spanwise cross section can be represented by airfoil-like thickness distribution such as wings, canard, fins, pylons, launchers, etc. A wing component is defined by a lifting surface enclosed by a straight leading, trailing and two side edges. Each wing component is then divided into *NS* streamwise strips by *NS*+1 lines parallel to the x-axis called "spanwise divisions", and each strip is subdivided into *NC* chordwise trapezoidal boxes by *NC*+1 spanwise lines called "chordwise divisions". Let *NW* be the number of boxes of the total WLC of an aircraft, and let *NWING* denote the number of wing segments. Then *NW* can be expressed as:

$$NW = \sum_{i=1}^{NWING} NS_i \times NC_i \tag{3.34}$$

It should be noted that for unsteady linear aerodynamics the thickness effects of the thin lifting surfaces are of first order. This is to say that for the wing-like components there is no requirement of modeling the thickness distribution on the lifting surfaces. Thus, all wing-like components are assumed to be flat plate in the present paneling scheme. Since source singularity is usually used to simulate the thickness effects whereas doublet singularity to generate lift, the flat-plate type of lifting surfaces require no source singularity and only the doublet singularity is distributed on the mean-plate of the wing-like components and their associated wake surfaces. On the other hand, the present panel scheme for bodies takes up a simplified formulation in which only the source singularity is distributed on the body-like components. This will greatly simplify the effort for deriving the solutions of the source and doublet integrals. With this paneling scheme, Eq 3.16 becomes:

$$\phi(x_o, y_o, z_o) = \phi_W(x_o, y_o, z_o) + \phi_B(x_o, y_o, z_o) \tag{3.35}$$

where:

$$\phi_W = \frac{1}{E\pi} \iint_{\text{wing + wake}} \Delta\phi(x, y, z)\, e^{i\lambda M_\infty \xi} \frac{\partial}{\partial n} K\, dS \tag{3.36}$$

is the potential influence due to the wing-like components

and:

$$\phi_B = -\frac{1}{E\pi} \iint_{\text{body}} \sigma(x, y, z)\, e^{i\lambda M_\infty \xi}\, K\, dS \tag{3.37}$$

is the potential due to the body-like components

The derivations of ϕ_W and ϕ_B solution are discussed on the next section.

3.5 Discretization of the Source and Doublet Integrals

Doublet singularity distribution on the wing-like components and their associated wake surfaces implies that the panel modeling is required not only for the wing-like components but also for the wake surfaces. This will greatly increase the modeling effort due to the large domain of the wake surface that starts from the wing trailing edge and extends to downstream infinity. To circumvent this problem, one introduces the acceleration potential ψ which is directly proportional to a perturbation pressure field related to the potential ϕ by:

$$\psi = \frac{\partial \Delta\phi}{\partial x} + ik\Delta\phi \tag{3.38}$$

Comparing Eq 3.38 with Eq 3.32 results:

$$\Delta C_p = -2\psi = -2\left(\frac{\partial \Delta\phi}{\partial x} + ik\Delta\phi\right) \tag{3.39}$$

Eq 3.39 establishes a transformation from the unsteady doublet singularity $\Delta\phi$ to the pressure coefficient difference ΔC_p. Applying this transformation to Eq 3.36 gives:

$$\phi_W(x_o, y_o, z_o) = \frac{\beta}{2E\pi} \iint_{\text{wing}} \Delta C_p(x, y, z)\, e^{-ik\beta\xi}\, \overline{K}(\xi, \eta, \zeta)\, dS \tag{3.40}$$

where:

$$\overline{K} = -\int_x^{\xi} e^{i\frac{k}{\beta}\tau} \frac{\partial K}{\partial n}\, d\tau \tag{3.41}$$

and:

$$X = -\infty \qquad \text{for } M < 1$$

$$X = \sqrt{\eta^2 + \zeta^2} \qquad \text{for } M > 1$$

Since the wake surface cannot sustain force, i.e. $\Delta C_p = 0$ on wake surface, the integral equation of ϕ_W (Eq 3.40) is applied on the mean-plane of the wing components only. The integral on wake surface vanishes automatically. Therefore, with the acceleration potential transformation, the integral equation of ϕ_W is expressed directly in terms of ΔC_p and requires no panel modeling of the wake surface.

Based on the paneling scheme depicted in Fig 3.29, the integrals of Eqs 3.37 and 3.40 can be discretized into many elementary Kernel integrals associated with each aerodynamic box. On each aerodynamic box, a constant singularity distributed is assumed. For the ith control point located either on the wing or body box, its perturbation potential ϕ can be approximated by:

$$\phi(x_o, y_o, z_o) = \sum_{j=1}^{NB} \phi_{B_{ij}} \sigma_j + \sum_{j=1}^{NW} \phi_{W_{ij}} \Delta C_{p_j} \tag{3.42}$$

$$(\ i = 1, 2, \ldots, NB+NW\ )$$

where:

$$\phi_{B_{ij}} = -\frac{1}{E\pi} \iint_{\Delta\xi_{ij}\,\Delta\eta_{ij}} e^{-i\lambda M_\infty \xi}\ K\ d\xi\ dn \tag{3.43}$$

is the elementary source Kernel integral representing the potential influence coefficient at the ith control point due to the jth body box

$$\phi_{W_{ij}} = \frac{\beta}{2E\pi} \iint_{\Delta\eta_{ij}\,\Delta\xi_{ij}} e^{-ik\beta\xi}\ \overline{K}\ d\eta\ d\xi \tag{3.44}$$

is the elementary pressure Kernel integral representing the potential influence coefficient at the ith control point due the jth wing box

σ_j is the unknown source strength of the jth body box

ΔC_{p_j} is the unknown pressure jump on the jth wing box

$\Delta\xi_{ij}$ and $\Delta\eta_{ij}$ represent the boundary of the jth box relative to the ith control point

Likewise, the unsteady perturbation velocities u_i, v_i, w_i, can be expressed as:

$$(u_i, v_i, w_i) = \sum_{j=1}^{NB} (u_{\mathrm{B}_{ij}}, v_{\mathrm{B}_{ij}}, w_{\mathrm{B}_{ij}})\, \sigma_j + \sum_{j=1}^{NW} (u_{\mathrm{W}_{ij}}, v_{\mathrm{W}_{ij}}, w_{\mathrm{W}_{ij}})\, \Delta C_{\mathrm{p}_j} \tag{3.45}$$

$$(i = 1, 2, \ldots, NB+NW)$$

where:

$$(u_{\mathrm{B}_{ij}}, v_{\mathrm{B}_{ij}}, w_{\mathrm{B}_{ij}}) = -\frac{1}{E\pi} \iint_{\Delta\xi_{ij}\,\Delta\eta_{ij}} \vec{\nabla} \left\{ \mathrm{e}^{i\lambda M_\infty \xi} K \right\} d\xi \, d\eta \tag{3.46}$$

and:

$$(u_{\mathrm{W}_{ij}}, v_{\mathrm{W}_{ij}}, w_{\mathrm{W}_{ij}}) = \frac{\beta}{2E\pi} \iint_{\Delta\eta_{ij}\,\Delta\xi_{ij}} \vec{\nabla} \left\{ \mathrm{e}^{ik\beta\xi} \overline{K} \right\} d\eta \, d\xi \tag{3.47}$$

are the velocity influence coefficients at the ith control point due to the jth wing box

The potential and velocity influence coefficients of the body box and the wing box are obtained by solving the elementary kernel integrals (Eq 3.44) and the elementary pressure kernel integrals (Eq 3.45) respectively. The detailed derivations of the solutions of these integrals can be found in Refs 3.2, 3.15 and 3.19.

3.6 Matrix Equations for the Solution of Unsteady Pressure

Applying Eqs 3.42 and 3.43 at *NB+NW* number of control points, one can construct the influence coefficient matrices *PIC*, *UIC*, *VIC* and *WIC* as:

$$\{\phi\} = [PIC] \begin{Bmatrix} \sigma \\ \Delta C_{\mathrm{p}} \end{Bmatrix}$$

$$\{\mathbf{u}\} = [UIC] \begin{Bmatrix} \sigma \\ \Delta C_{\mathrm{p}} \end{Bmatrix}$$

$$\{\mathbf{v}\} = [VIC] \begin{Bmatrix} \sigma \\ \Delta C_{\mathrm{p}} \end{Bmatrix}$$

$$\{\mathbf{w}\} = [WIC] \begin{Bmatrix} \sigma \\ \Delta C_{\mathrm{p}} \end{Bmatrix} \tag{3.48}$$

where $\{\phi\}$, $\{\mathbf{u}\}$, $\{\mathbf{v}\}$ and $\{\mathbf{w}\}$ are the perturbation potential and velocities of all control points, and:

$$[PIC] = \begin{bmatrix} (\phi_B)_{BB} & (\phi_W)_{WB} \\ (\phi_B)_{BW} & (\phi_W)_{WW} \end{bmatrix}$$ is the potential influence coefficient matrix,

$$[UIC] = \begin{bmatrix} (u_B)_{BB} & (u_W)_{WB} \\ (u_B)_{BW} & (u_W)_{WW} \end{bmatrix}, \qquad [VIC] = \begin{bmatrix} (v_B)_{BB} & (v_W)_{WB} \\ (v_B)_{BW} & (v_W)_{WW} \end{bmatrix},$$

$$[WIC] = \begin{bmatrix} (w_B)_{BB} & (w_W)_{WB} \\ (w_B)_{BW} & (w_W)_{WW} \end{bmatrix}$$

are the velocity influence coefficient matrices, (3.49)

and:

$(\ )_{BB}$ is the influence at the body control points due to the body boxes
$(\ )_{BW}$ is the influence at the wing control points due to the body boxes
$(\ )_{WB}$ is the influence at the body control points due to the wing boxes
$(\ )_{WW}$ is the influence at the wing control points due to the wing boxes

Applying the boundary conditions of the wing boxes (Eq 3.27) and the body boxes (Eq 3.24) gives:

$$[NIC] \begin{Bmatrix} \sigma \\ \Delta C_p \end{Bmatrix} = \begin{Bmatrix} \mathbf{F}_B \\ \mathbf{F}_W \end{Bmatrix} \tag{3.49a}$$

where:

$$\begin{aligned} [NIC] &= \vec{u} \cdot \vec{n} \\ &= [n_x][UIC] + [n_y][VIC] + [n_z][WIC] \end{aligned}$$

is an $(NB+NW)$ by $(NB+NW)$ square matrix and is named Normal Velocity Influence Coefficient Matrix

$$\vec{u} = (u, v, w)$$

is unsteady velocities on wing-body

Inverting $[NIC]$ gives the singularity strengths of the body and the wing boxes, i.e.:

$$\begin{Bmatrix} \sigma \\ \Delta C_p \end{Bmatrix} = [NIC]^{-1} \begin{Bmatrix} \mathbf{F}_B \\ \mathbf{F}_W \end{Bmatrix} \tag{3.50}$$

For a given set of downwash functions $\mathbf{F}_W$ and $\mathbf{F}_B$, unknown strengths σ's and ΔC_p's can be solved from Eq 3.50. Once σ's and ΔC_p's are known, the perturbation potential and velocities

$\{\phi\}$, $\{\mathbf{u}\}$, $\{\mathbf{v}\}$ and $\{\mathbf{w}\}$ can be evaluated according to Eq 3.48. Consequently, the unsteady pressure coefficient on body boxes can be calculated according to Eq 3.29.

Notice that the boundary condition and pressure coefficient of the body boxes involve the steady perturbation velocities u_o, v_o and w_o. To evaluate them form Eq 3.50, it is required to solve the steady aerodynamics of the body. Now, the unsteady Kernel functions of Eq 3.17 can be readily reduced to its counterpart in the zero frequency limit. Thus, the influence coefficient matrices of the steady aerodynamics can adopt directly from these of the unsteady aerodynamics by setting $k = 0$. The steady perturbation velocities can then be obtained by applying the steady boundary condition presented in Eq 3.28.

Fig 3.30 presents the solution procedure in obtaining the unsteady pressure coefficients on wing and body boxes. This procedure is proceeded as follows:

- Solve for steady perturbation velocities u_o, v_o and w_o.
- Construct Influence Coefficient matrices $[UIC]$, $[VIC]$, $[WIC]$, $[PIC]$ and $[NIC]$ according to Eq 3.49. Note that this step takes up most of the computation time in ZONA6/ZONA7. However, being independent of the mode shape, they can be obtained and saved once and for all for a given M and k pair.
- Construct Downwash functions $\mathbf{F}_{\mathrm{B}_i}$ and $\mathbf{F}_{\mathrm{W}_i}$ of Eqs 3.24 and 3.26; perform matrix decomposition on $[NIC]$ and solve for σ and ΔC_p from Eq 3.50.
- Compute unsteady velocities u, v and w and unsteady potential ϕ according to Eq 3.48.
- Compute unsteady pressure C_p on body according to Eq 3.29.

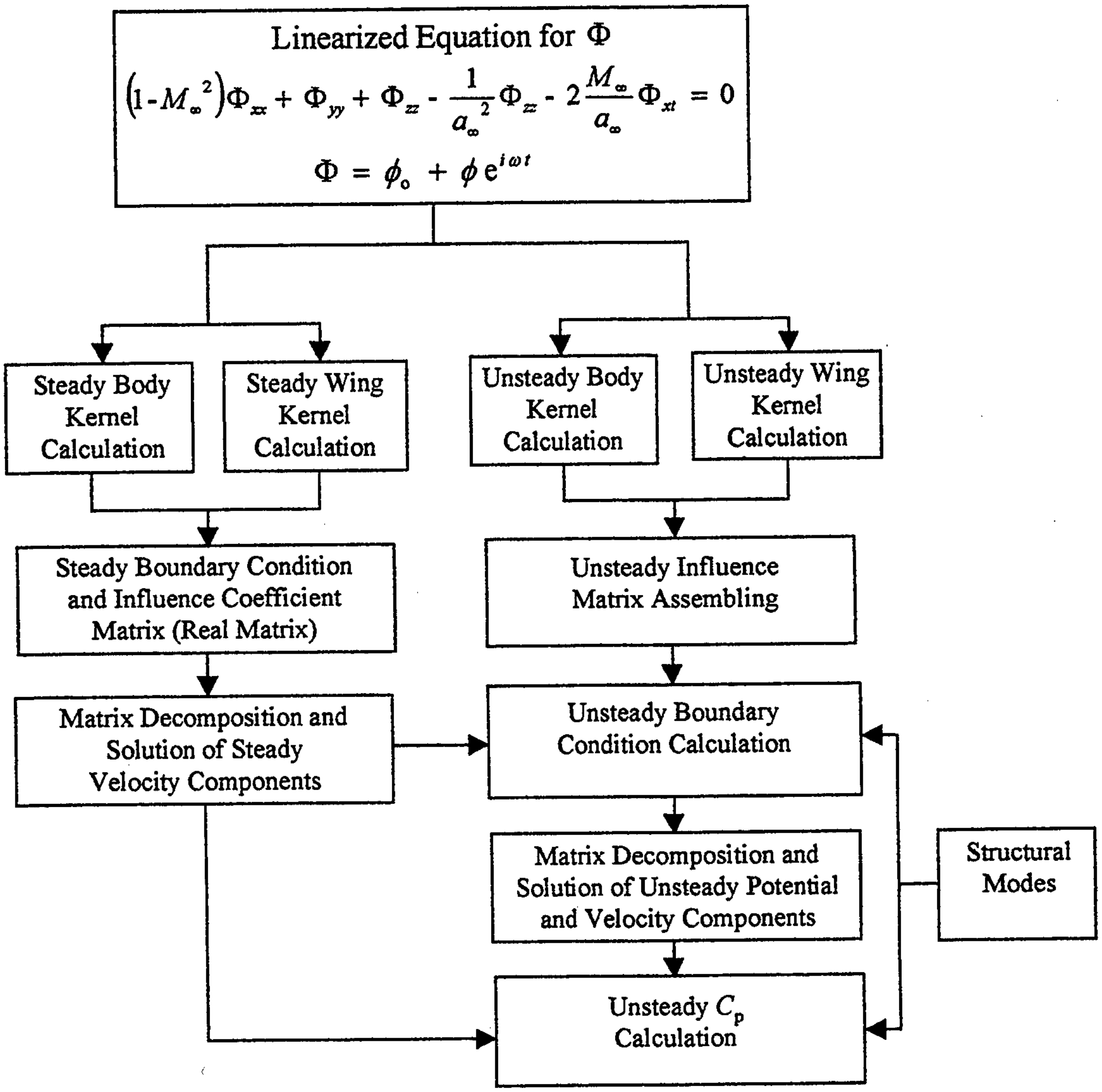
Linearized Equation for Φ
$\left(1-M_\infty^2\right)\Phi_{xx} + \Phi_{yy} + \Phi_{zz} - \frac{1}{a_\infty^2}\Phi_{zz} - 2\frac{M_\infty}{a_\infty}\Phi_{xt} = 0$
$\Phi = \phi_o + \phi e^{i\omega t}$
Steady Body Kernel Calculation
Steady Wing Kernel Calculation
Unsteady Body Kernel Calculation
Unsteady Wing Kernel Calculation
Steady Boundary Condition and Influence Coefficient Matrix (Real Matrix)
Unsteady Influence Matrix Assembling
Matrix Decomposition and Solution of Steady Velocity Components
Unsteady Boundary Condition Calculation
Matrix Decomposition and Solution of Unsteady Potential and Velocity Components
Structural Modes
Unsteady C_p Calculation

Fig 3.30 Flow Chart of Computation and Calculation Procedure for Unsteady Pressures

3.7 Construction of Aerodynamic Influence Coefficient (*AIC*) Matrix

The flow chart shown in Fig 3.30 gives a step-by-step computational procedure for unsteady pressure calculation, but it does not provide the *AIC* matrix to directly relate the given structural mode shape to the unsteady aerodynamic forces. To construct an *AIC* matrix for the wing-like components is rather straightforward. The force acting normal to the wing boxes can be obtained by multiplying the area of the wing boxes to the unsteady pressure on wing boxes. This gives:

$$\{\mathbf{L}_{\text{wing}}\} = q_\infty \left[\mathbf{0} \quad \mathbf{A}_w\right] [NIC]^{-1} \begin{Bmatrix} \mathbf{F}_B \\ \mathbf{F}_W \end{Bmatrix} \tag{3.51}$$

where:

$$[NIC] = \begin{bmatrix} [NIC]_{\mathrm{BB}} & [NIC]_{\mathrm{WB}} \\ [NIC]_{\mathrm{BW}} & [NIC]_{\mathrm{WW}} \end{bmatrix}$$

is the normal velocity influence coefficient matrix

q_∞ is the dynamic pressure

$\mathbf{A}_{\mathrm{W}}$ is a diagonal matrix containing the area of the wing boxes

L_{wing} is the normal force vector on wing boxes

The normal forces on the body-like components are more complicated that that of the wing-like components. Rewriting Eq 3.29 in matrix form and multiplying the body box area give:

$$\begin{aligned} \{\mathbf{L}_{\mathrm{body}}\} &= q_\infty\, [\mathbf{A}_{\mathrm{B}}]\, \{C_{\mathrm{p}}\} \\ &= q_\infty\, [[\mathbf{B}_{\mathrm{BB}}]\ [\mathbf{B}_{\mathrm{WB}}]]\, [NIC]^{-1} \begin{Bmatrix} \mathbf{F}_{\mathrm{B}} \\ \mathbf{F}_{\mathrm{W}} \end{Bmatrix} + \{\mathbf{d}\} \end{aligned} \tag{3.52}$$

where:

$\mathbf{A}_{\mathrm{B}}$ is a diagonal matrix containing the area of the body boxes

$\mathbf{L}_{\mathrm{body}}$ is the normal force vector on the body boxes

$$\begin{aligned} [[\mathbf{B}_{\mathrm{BB}}]\ [\mathbf{B}_{\mathrm{WB}}]] = [\mathbf{A}_{\mathrm{B}}]\, [-2C_{\mathrm{o}}]\, \big[\, [1+u_{\mathrm{o}}]\, [[UIC_{\mathrm{BB}}]\ \ [UIC_{\mathrm{WB}}]] \\ + [v_{\mathrm{o}}]\, [[VIC_{\mathrm{BB}}]\ \ [VIC_{\mathrm{WB}}]] \\ + [w_{\mathrm{o}}]\, [[WIC_{\mathrm{BB}}]\ \ [WIC_{\mathrm{WB}}]] \\ + [ik]\, [[PIC_{\mathrm{BB}}]\ \ [PIC_{\mathrm{WB}}]]\, \big] \end{aligned} \tag{3.53}$$

where **d** contains the terms in Eq 3.29 associated with the given mode shapes,

$$\begin{aligned} \{\mathbf{d}\} = -2\, \mathbf{A}_{\mathrm{B}}\, C_{\mathrm{o}}\, [\, (1+u_{\mathrm{o}})\,(h_{\mathrm{x}}'\, u_{\mathrm{o}} + h_{\mathrm{y}}'\, u_{\mathrm{o}}) + h_{\mathrm{z}}'\, w_{\mathrm{o}} + h_{\mathrm{y}}'\, v_{\mathrm{o}} \\ + ik(h_{\mathrm{x}}\, u_{\mathrm{o}} + h_{\mathrm{y}}\, v_{\mathrm{o}} + h_{\mathrm{z}}\, w_{\mathrm{o}})\,] \end{aligned} \tag{3.54}$$

Combining Eqs 3.51 and 3.54 gives:

$$\begin{Bmatrix} \mathbf{L}_{\mathrm{body}} \\ \mathbf{L}_{\mathrm{wing}} \end{Bmatrix} = q_\infty\, [NIC]^{-1} \begin{Bmatrix} \mathbf{F}_{\mathrm{B}} \\ \mathbf{F}_{\mathrm{W}} \end{Bmatrix} + \begin{Bmatrix} \mathbf{d} \\ \mathbf{0} \end{Bmatrix} \tag{3.55}$$

where:

$$\left[\bar{\mathbf{B}}\right] = \begin{bmatrix} [\mathbf{B}_{\mathrm{BB}}] & [\mathbf{B}_{\mathrm{WB}}] \\ [\,\mathbf{0}\,] & [\mathbf{A}_{\mathrm{W}}] \end{bmatrix} \tag{3.56}$$

Eq 3.55 establishes a relationship between the boundary condition of box and wing components (Eqs 3.24 and 3.25) to the normal forces on the box and wing boxes. However, it is desirable to express Eq 3.55 in the standard format of *AIC* matrix equation as:

$$\{\mathbf{L}_{\mathrm{h}}\} = q_{\infty}\, [AIC]\, \{\mathbf{h}\} \tag{3.57}$$

where **h** and $\mathbf{L}_{\mathrm{h}}$ represents respectively expression for the mode shapes and force vectors on the body and wing boxes.

To derive the Eq 3.57 from Eq 3.55, it is required to introduce the *J-set* and *K-set* degrees of freedom of the aerodynamic boxes. This will be discussed next.

3.8 J-Set and K-Set Aerodynamic Degrees of Freedom for *AIC* Matrix

The *J-set* aerodynamic degrees of freedom (d.o.f.) is simply the number of aerodynamic boxes. For instance, the size of vectors and matrices in Eq 3.55 are all in the order of *J-set* d.o.f., i.e.:

$$J\text{-}set\ d.o.f. = NB + NW \tag{3.58}$$

By examining the boundary conditions of the body and wing boxes, it can be realized that mode shapes h in Eq 3.57 contains six components on each aerodynamic box, namely $h_{\mathrm{x}}, h_{\mathrm{y}}, h_{\mathrm{z}}, h'_{\mathrm{x}}, h'_{\mathrm{y}}$ and h'_{z}. This implies that the size of h is in the order of 6 x *J-set*. Defining *K-set* = 6 x *J-set* as:

$$K\text{-}set = 6 \times J\text{-}set = 6 \times (NB+NW) \tag{3.59}$$

gives the mode shapes **h** as:

$$\{\mathbf{h}\}_{K\text{-set}} = \left\{ \begin{matrix} \vdots \\ \left\{ \begin{matrix} h_{\mathrm{x}} \\ h_{\mathrm{y}} \\ h_{\mathrm{z}} \\ h'_{\mathrm{x}} \\ h'_{\mathrm{y}} \\ h'_{\mathrm{z}} \end{matrix} \right\}_i \\ \vdots \end{matrix} \right\} \tag{3.60}$$

where i denotes the ith *J-set* d.o.f., and $(\cdot)'$ represents the derivative of $(\cdot)$ with respect to $\left(\dfrac{x}{L}\right)$.

Rewriting the vectors $\{\mathbf{F}_B\}$ and $\{\mathbf{d}\}$ in Eq 3.55 in matrix forms, one can redefine Eq 3.55 as:

$$\left\{\begin{matrix}\mathbf{L}_{\text{body}}\\ \mathbf{L}_{\text{wing}}\end{matrix}\right\} = q_\infty \left[\left[\bar{\mathbf{B}}\right][NIC]^{-1}\left[\bar{\mathbf{F}}\right] + \left[\bar{\mathbf{D}}\right]\right]\{\mathbf{h}\} \tag{3.61}$$

where $\bar{\mathbf{F}}$ and $\bar{\mathbf{D}}$ are the *K-set* by *J-set* complex matrices containing the steady velocity components u_o, v_o and w_o and the normal vector components n_x, n_y and n_z as well as the reduced frequency k.

In general, the force at each grid point of the structural finite element method has six components; forces and moments along the x, y and z directions. In order to be compatible with the structural finite element method, it is required to convert the normal force vector in Eq 3.61 to the three force components (F_x, F_y, F_z) and the three moment components (M_x, M_y, M_z) along the x, y and z directions. This can be done by:

$$\{\mathbf{F}_h\} = \left\{\begin{matrix}\vdots\\ \left\{\begin{matrix}F_x\\F_y\\F_z\\M_x\\M_y\\M_z\end{matrix}\right\}_i\\ \vdots\end{matrix}\right\} = \begin{bmatrix}\vdots & \vdots & 0 & \vdots & \vdots\\ \vdots & \vdots & \left\{\begin{matrix}n_x\\n_y\\n_z\\0\\0\\0\end{matrix}\right\}_i & \vdots & \vdots\\ \vdots & \vdots & 0 & \vdots & \vdots\end{bmatrix}\left\{\begin{matrix}\mathbf{L}_{\text{body}}\\ \mathbf{L}_{\text{wing}}\end{matrix}\right\} \tag{3.62}$$

Combining Eqs 3.61 and 3.62 gives:

$$\{\mathbf{L}_h\} = q_\infty\,[AIC]\,\{\mathbf{h}\} \tag{3.63}$$

Finally, we have derived a *K-set* by *K-set* square *AIC* matrix that directly relates the structural mode shapes to the aerodynamic forces. It should be noted that the structural mode shape $\{\mathbf{h}\}$ in Eq 3.62 is defined at the aerodynamic boxes. Transferring the structural mode shapes from the structural finite element grid points to the aerodynamic boxes requires the generation of a spline matrix. This will be discussed in Section 6.

3.9 Body Wake Effect

The wake generated by flow separation at the tail section or behind the base of a body-like component has considerable influence to the wing-body or body-alone aerodynamics. ZAERO provides a non-iterative approach for the body wake modeling. Fig 3.31 presents the comparisons of the ZONA6 results with and without the wake modeling with the experimental pressure distributions along the blunt-base body in incompressible flow.

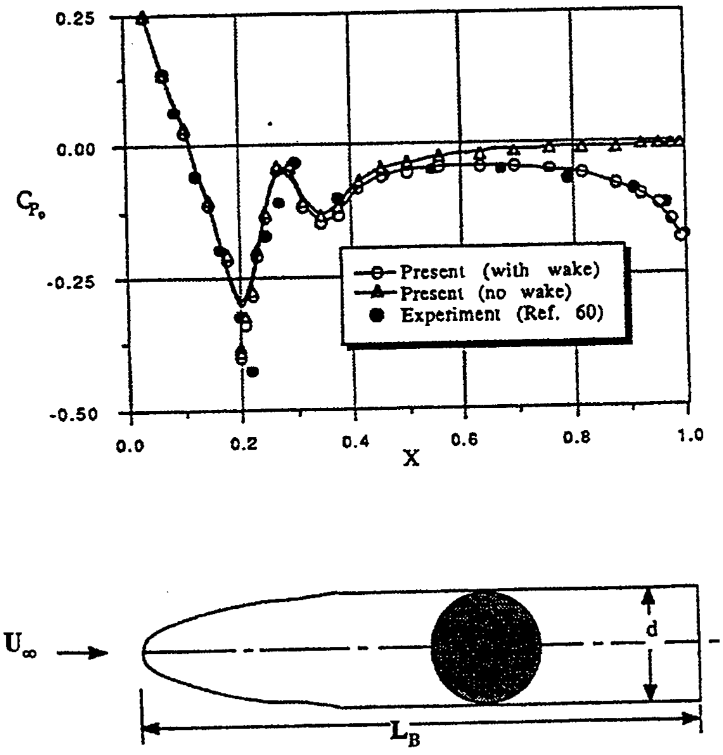

Fig 3.31 Comparison of Surface Pressure Distribution for a Blunt Body ($L_B/d = 5$) at $\alpha = 0°$, M = 0 and Base Pressure $C_{p_{base}} = -0.169$

It is seen that the present (no wake) result begins to deviate from the measured data at a forebody portion of 0.3 L_B, where L_B is the body length. By contrast, the present (with wake) result shows remarkably close agreement with measured data. This comparison clearly demonstrates the importance of the body wake modeling for accurate aerodynamic prediction.

This non-iterative body wake modeling requires a given base pressure coefficient $C_{p_{base}}$ a priori. Therefore, the pressure of the adjacent boxes to the body base is given by $C_p = C_{p_{base}}$. Imbedded singularities are placed in the assigned proximity of the body base regime to simulate the exterior wake flow. For steady flow the imbedded singularity is a source, whereas for unsteady flow it is a doublet. Next, the constant pressure condition is imposed at the body base. This boundary condition can be expressed as:

$$C_{p_o} = C_{p_{base}} \quad \text{and} \quad C_p = 0 \quad \text{at} \quad S(x=L_B,b,z)=0 \tag{3.64}$$

where C_{p_o} and C_p are the steady and unsteady pressure, respectively.

The combination of this constant pressure condition and the steady and unsteady boundary conditions yields a compact expression in terms of the velocities, the mode shape and its derivative, i.e.:

$$a\,\phi = b\,\phi_o \tag{3.65}$$

where a and b are both scalar operators.

$$a = \vec{V}_o \cdot \vec{\nabla} + ik$$

$$b = \frac{d\vec{c}}{dx} \cdot \vec{\nabla} + ik\vec{c} \cdot \vec{\nabla}$$

$\vec{c}$ is a function of the mode shape

ϕ_o and ϕ are the steady and unsteady potential due to the imbedded singularity, respectively.

The location of the imbedded source and the imbedded doublet are placed along the extended body axis at $x = L_B + q_s$ and $x = L_B + q_d$, respectively, in the region near the base. The values of q_s and q_d are, in general, related to the wake length which is yet to be solved as part of the solution, ordinarily, to be solved through an iteration procedure. However, our experience showed that empirical guidelines can be set up in which q_s can be confined to a width of $0.2 \sim 0.4\ L_B$ and q_d of $o.05 \sim 0.15\ L_B$ for any circular blunt base (L_B being the body length). By numerical experiment, it is found that the converged solutions are rather insensitive to the precise location q_s and q_d as long as they are placed within the width given. Fig 3.32 shows the side views of the computed base-flow of a blunt body, according to the present no-wake and the present with-wake model. The direction and the length of the arrows indicate the flow direction and the velocity magnitude, respectively. As expected, the no-wake flowfield velocities appear to be nearly uniform showing their immediate return to the freestream condition. It can be seen that the present wake model appears to closely simulate the wake profile. The dashed line is indeed the dividing streamline which defines the wake closure, or the computed wake shape. It is clearly shown that the stagnation point at the end of the wake is automatically captured by the present calculation. The computed wake flow is only physically meaningful in the outer wake flow region, whereas, the computed flow inside the wake is of no physical significance.

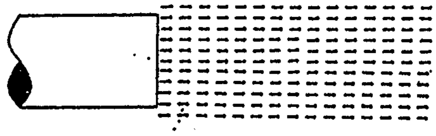

a) without wake model

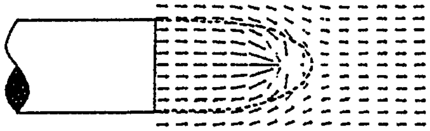

b) with wake model

Fig 3.32 Computer Wake Shape for a Blunt Body at M = 0 and α = 0°; a Meridian-Plane View

With the boundary condition expressed in Eq 3.65 for body wake effects, the unknown strength of the source singularity σ on body boxes, ΔC_p on wing boxes, and the imbedded wake singularity μ_{wake} can be solved by the following *NIC* matrix equation:

$$\begin{bmatrix} [NIC]_{BB} & [NIC]_{BW} & [NIC]_{B\text{-wake}} \\ [NIC]_{WB} & [NIC]_{WW} & [NIC]_{W\text{-wake}} \\ (a\phi)_{wake\text{-}B} & (a\phi)_{wake\text{-}W} & (a\phi)_{wake\text{-}wake} \end{bmatrix} \begin{Bmatrix} \sigma \\ \Delta C_p \\ \mu_{wake} \end{Bmatrix} = \begin{Bmatrix} \mathbf{F}_B \\ \mathbf{F}_W \\ b\,\phi_o \end{Bmatrix} \tag{3.66}$$

where:

$[NIC]_{B\text{-wake}}$ and $[NIC]_{W\text{-wake}}$ represent the *NIC* induced on the body and wing boxes by the wake singularity.

$(a\phi)_{wake\text{-}B}$, $(a\phi)_{wake\text{-}W}$ and $(a\phi)_{wake\text{-}wake}$ are the constant pressure condition imposed on the body boxes, wing boxes and the wake singularity, respectively.

Once the unknowns σ, ΔC_p and μ_{wake} are solved from Eq 3.66, the unsteady potential ϕ and velocities u, v and w can be obtained from Eq 3.48.

Fig 3.33 presents the unsteady pressures along the tip-tank of the *NLR* wing-tip-tank-pylon-store configuration (Fig 3.34) at an azimuthal angle $\theta = 202.5°$. The body wake effects on the wing-body configuration can be clearly seen in the ZONA6 results using the with- and without-wake models.

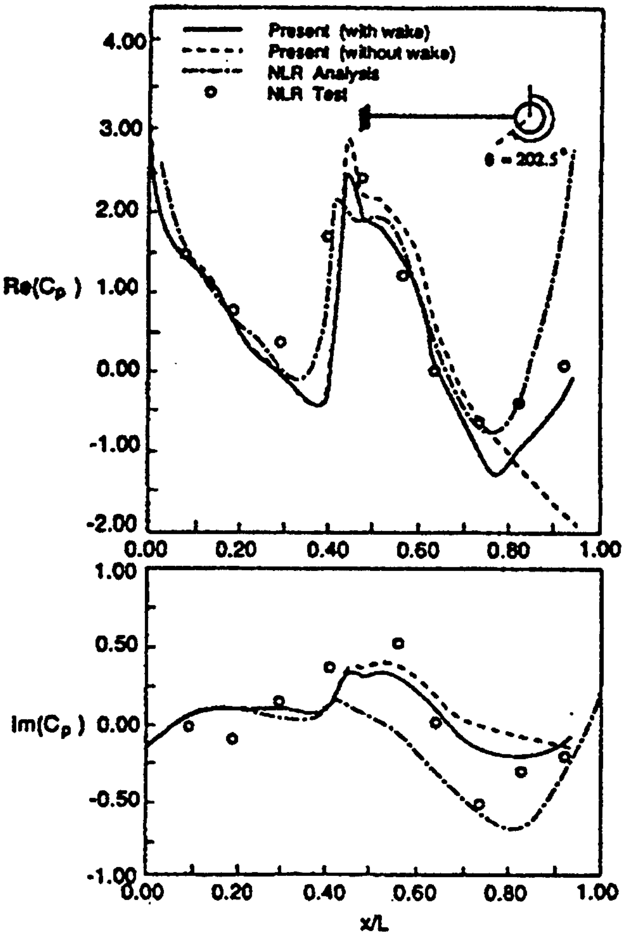

Fig 3.33 Unsteady Pressure Distribution Along the Tip-Tank of NLR Wing-Tip-Tank Configuration; $M = 0.45$, $\alpha = 0°$, $k = 0.305$, $\bar{x}_0 = 0.15\, c_R$, and $\theta = 202.5°$

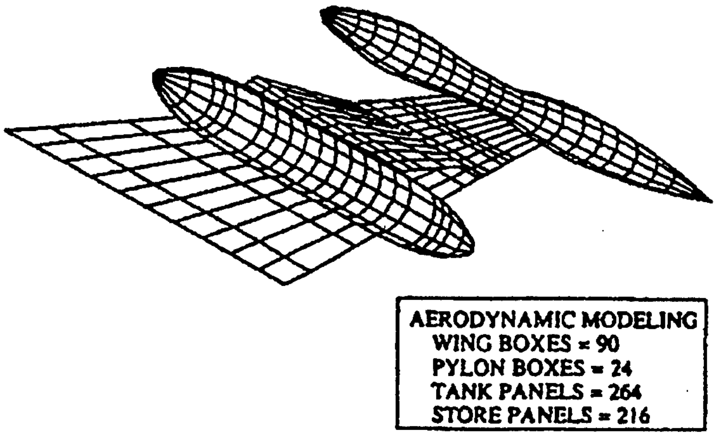
AERODYNAMIC MODELING
WING BOXES = 90
PYLON BOXES = 24
TANK PANELS = 264
STORE PANELS = 216

Fig 3.34 NLR Wing-Tip-Tank-Pylon-Store Configuration Showing Paneling Scheme

It is seen that the present no-wake in-phase C_p appears to deteriorate towards the tail of the tip-tank, whereas, that with wake appears to correlate best with the *NLR* measurements. This is expected, because the flow is known to separate at the rear in this case, according to Ref 3.20. For the out-of-phase C_p, the *NLR* computed results (Ref 3.20) show a discrepancy with the measurement starting from the mid body.

The computed steady pressure distribution along the store at three azimuthal angles, namely, $\theta = 90$, 180 and 270°, are presented in Fig 3.35. The solution with wake is seen to have better agreement with the measured data that without a wake. This leads one to believe that the flow might have separated at the body tail in this experiment, although no such information was supplied in Ref 3.20.

Fig 3.36 presents the unsteady pressure distributions along the store at two azimuthal angles: 1) $\theta = 157.5°$ and 2) $\theta = 292.5°$. From the present computed results, it is seen that adding the wing-tip-tank-pylon has altered the unsteady pressure distributions on the store substantially. In all cases, the present results with or without wake are in good agreement with the measured data. In particular, the solution with wake seems to show better agreement that the no-wake solution for the in-phase C_p, and there the solution also shows a trailing-edge peak due to pylon-store interaction (at $\theta = 292.5°$).

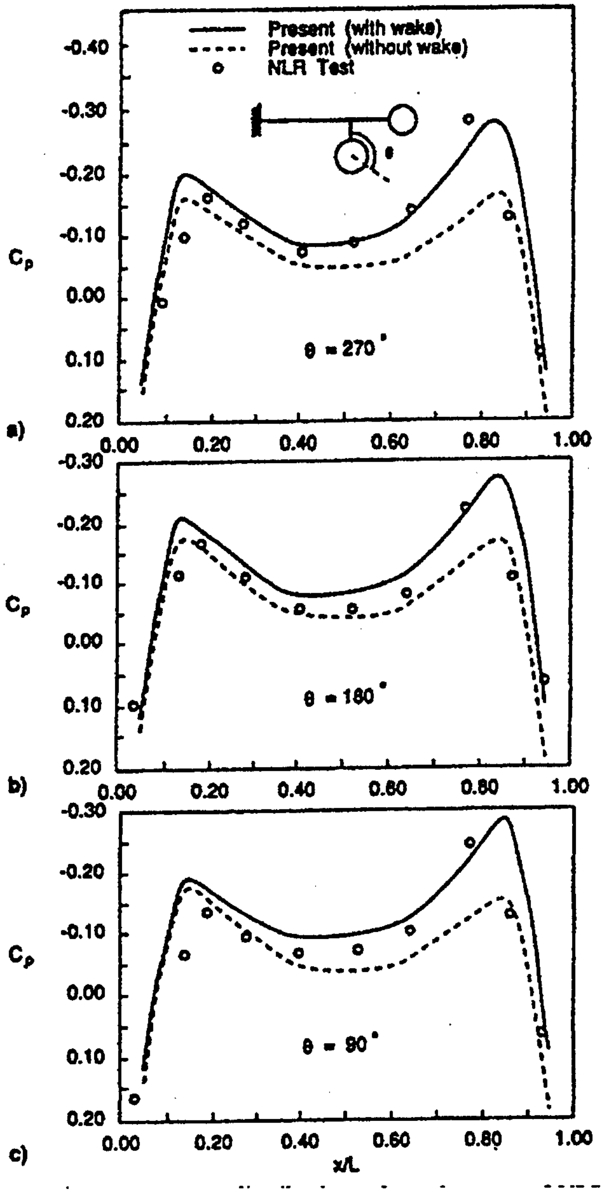

Fig 3.35 Steady Pressure Distribution Along the Store of NLR Wing-Tip-Tank-Pylon-Store Configuration; $M = 0.45$ and $\alpha = 0°$: a) $\theta = 90°$, b) $\theta = 180°$ and c) $\theta = 270°$

On the other hand, *NLR*'s computed results in the out-of-phase C_p indicates a solution departure from the measured data starting from the mid body section, and further deteriorates towards the body tail. By contrast, it is seen that both present solutions results in much better agreement with the measured data, especially near the body tail.

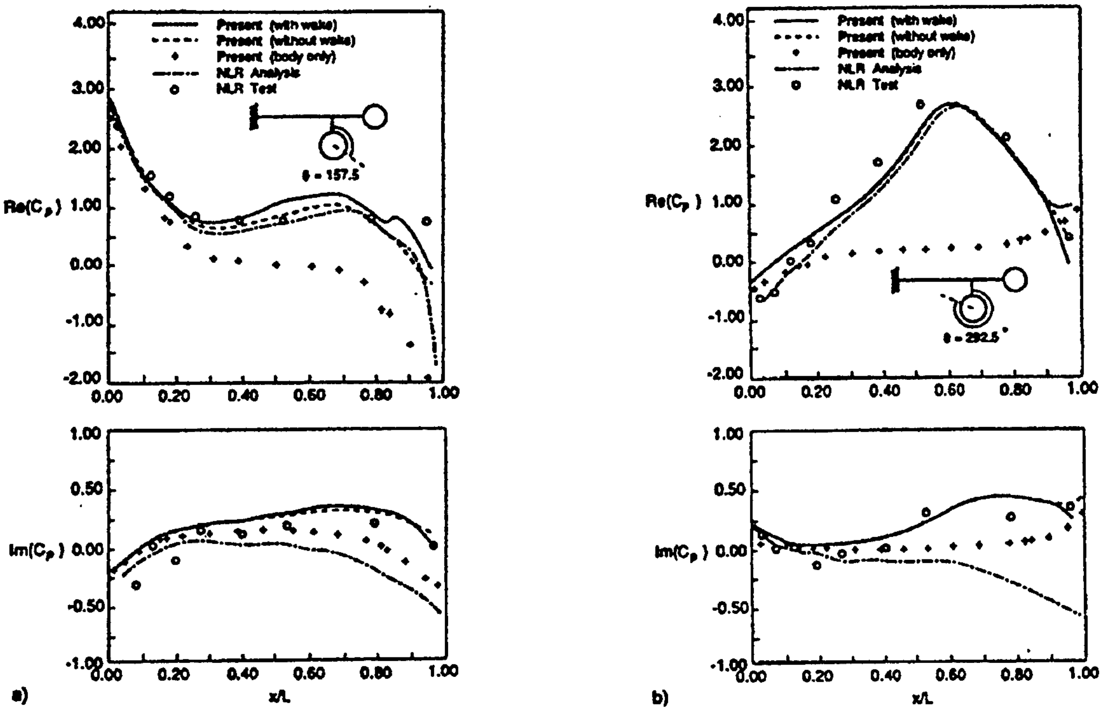

Fig 3.36 Unsteady Pressure Distribution Along the Tip-Tank of NLR Wing-Tip-Tank Configuration at a) $\theta = 157.5°$ and b) $\theta = 292.5°$; $M = 0.45$, $\alpha = 0°$, $k = 0.305$ and $\bar{x}_0 = 0.15\, c_R$,

3.10 Technique of Minimizing Spurious Waves for Supersonic Body Boxes

High order panel methods usually adopt the quadratic singularity distribution on the body boxes (e.g. PANAIR, Ref 3.30). By comparison, the constant source singularity distribution on the ZONA6/7 body boxes should be considered as a low order panel approach for body unsteady aerodynamics. For steady supersonic flow over a body, it is found that these constant source singularities on body boxes could generate the nonphysical internal Mach waves or "spurious" Mach waves inside the body-like components. These spurious Mach waves tend to accumulate as they propagate downstream within a closed body. As a result, this accumulation of waves often destabilize the external flow solutions and hence generate large error in the solution over the aft part of a closed body. This problem can be clearly seen in Fig 3.37 for a supersonic flow over a cone-cylinder-cone body. In contrast to the exact solution of Karman-Moore (Ref 3.31), the uncorrected ZONA7 solution (without wave minimization) deteriorates to the extent that the solution at the aft-cone becomes totally unacceptable.

To examine how the spurious waves are generated in supersonic flow, first consider a point *P* located on the *x*-*z* plane shown in Fig 3.38.

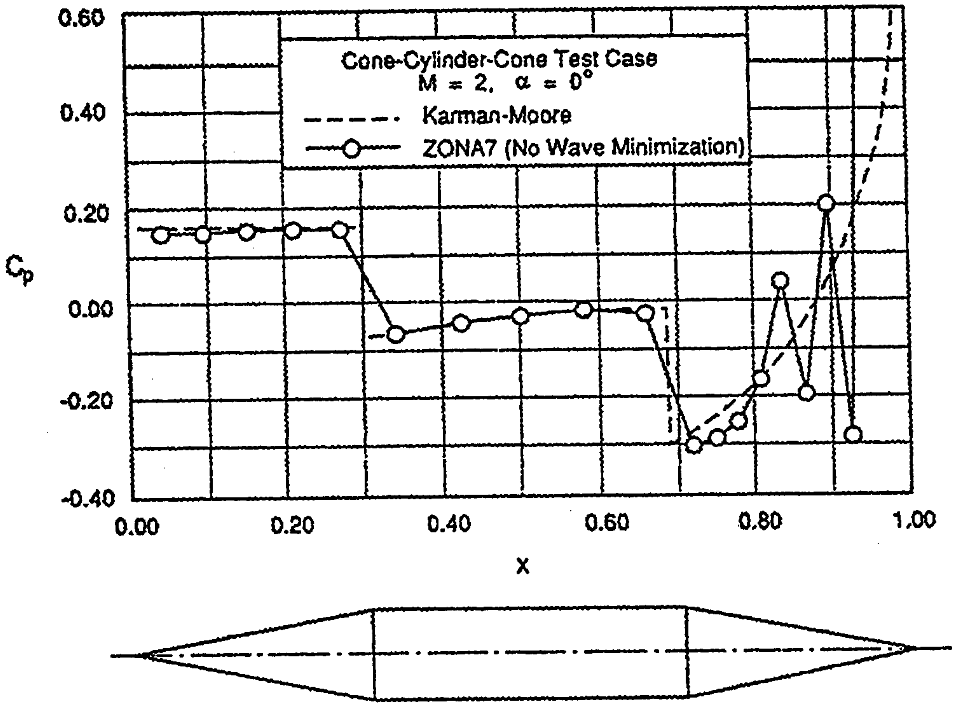

Fig 3.37 Cone-Cylinder-Cone at $M = 2.0$ and $\alpha = 0°$ Using ZONA7 without Wave Minimization

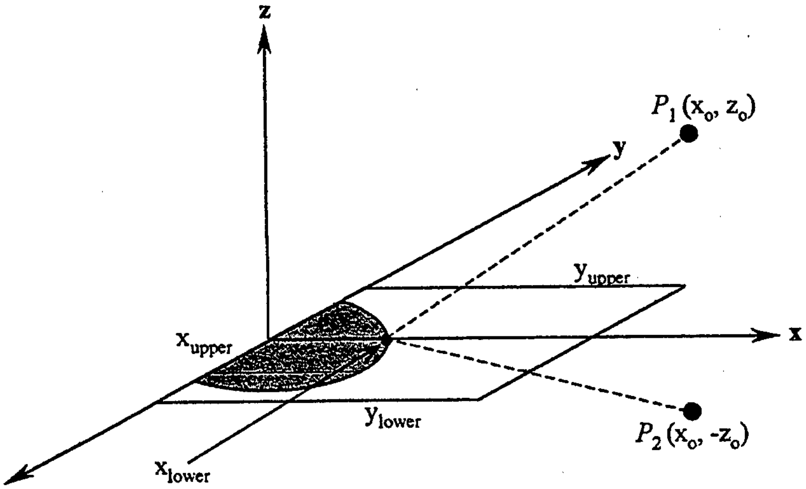
z
y
x
$P_1 (x_o, z_o)$
$P_2 (x_o, -z_o)$
y_{upper}
y_{lower}
x_{upper}
x_{lower}

Fig 3.38 Opposite Points from the Panel Having the Same x_{lower}

The steady normal perturbation velocity at P, $\frac{\partial \phi_o}{\partial z_o}$, from the body box (assuming a unit strength source singularity is distributed on the box) at $M_\infty = \sqrt{2}$ reads:

$$
\begin{aligned}
2\pi \frac{\partial \phi_o}{\partial z_o} &= \frac{\partial}{\partial z_o} \int_{x_{\mathrm{lower}}}^{x_{\mathrm{upper}}} \int_{y_{\mathrm{lower}}}^{y_{\mathrm{upper}}} \frac{1}{\sqrt{\xi^2 - \eta^2 - \zeta^2}}\, dy \\
&= \frac{\partial}{\partial z_o} \int_{x_{\mathrm{lower}}}^{x_{\mathrm{upper}}} - \sin^{-1} \frac{\eta}{\sqrt{\xi^2 - \zeta^2}} \Bigg|_{y_{\mathrm{lower}}}^{y_{\mathrm{upper}}} dx
\end{aligned}
\tag{3.67}
$$

where:

$$\xi = x_o - x, \quad \eta = y_o - y \quad \text{and} \quad \zeta = z_o - z$$

and x_{upper}, x_{lower}, y_{upper} and y_{lower} denote the boundary of the body box.

Eq 3.67 is the steady supersonic source integral of the body box obtained by setting $k = 0$ and $\beta = 1$ in Eq 3.37. If the body box has a large width so that y_{upper} and y_{lower} are located forward outside of the forward Mach cone emitted from P, the integration limits of Eq 3.67 is the intersection of the forward Mach cone $R = 0$ and the panel $z = 0$, i.e.:

$$y = \mp \sqrt{(x_o - x) - z_o^2} \qquad \text{at a particular } x \tag{3.68}$$

Therefore, the integrand of Eq 3.67 has the value of:

$$- \left[\sin^{-1} \frac{\sqrt{(x_o - x)^2 - z_o^2}}{\sqrt{(x_o - x)^2 - z_o^2}} + \sin^{-1} \frac{\sqrt{(x_o - x)^2 - z_o^2}}{\sqrt{(x_o - x)^2 - z_o^2}} \right] = -\pi \tag{3.69}$$

The upper limit of the x integral is at the panel's leading edge, i.e. $x_{\mathrm{upper}} = 0$. However, based on Eq 3.68 for $y = 0$, one can conclude that $x_{\mathrm{lower}} = x_o - |z_o|$. This proves that for two points located opposite of the panel with the same x location, they have the same value of x_{lower}.

Therefore, Eq 3.68 is resulted as:

$$
\begin{aligned}
2\pi \frac{\partial \phi_o}{\partial z_o} &= \frac{\partial}{\partial z_o} [x_{\mathrm{upper}} - x_{\mathrm{lower}}]\,(-\pi) \\
&= -\mathit{sign}(z_o)\,\pi
\end{aligned}
\tag{3.70}
$$

Eq 3.70 shows that for a point P located above the box (point P_1 in Fig 3.38), it receives a constant perturbation velocity $\frac{\partial \phi_o}{\partial z_o} = -\frac{1}{2}$ whereas a point P located below the box (point P_2 in

Fig 3.38), it receives $\frac{\partial \phi_o}{\partial z_o} = \frac{1}{2}$. It also proves that constant source panel generates a jump of $\frac{\partial \phi_o}{\partial z_o}$ across the box from $z_o = 0^-$ to $z_o = 0^+$.

To conclude the above discussion, consider a point on the $x - z$ plane travels along the x direction. This point receives no perturbation from the box until its forward Mach cone hits the box leading edge. For example, at the canopy sill line (Fig 3.39), a finite jump of perturbation velocity occurs (i.e. $\frac{\partial \phi_o}{\partial z_o} = \pm \frac{1}{2}$, sign selection depends on the upper or lower Mach cone). In other words, the leading edge of the body box generates two waves; the outer wave goes over the upper side and the inner wave goes under/to the lower side of the box. The outer (exterior) wave generated from the leading edge of the box propagates into the exterior flowfield and actually forms part of the required "physical" linearized supersonic exterior flow solution. However, the inner (internal) wave generates a set of inner wave train within the interior domain of the body. It is this inner wave train that creates the spurious velocity discontinuities which is responsible for the solution deterioration at the aft-cone.

ZONA6 and ZONA7 approximate a body surface by a set of fairly small boxes that are approximately contiguous and "flat" in curvature. Clearly, if such a geometric discretization is coupled with discontinuous singularity distribution such as constant source strength, then the amount of cancellation of the spurious waves between boxes must depend on the differences between their source strengths. For flat boxes with constant source, to keep such strength difference small requires the change in streamwise geometric slope between adjacent boxes to be kept small. This requirement sets the size criteria for box discretization which should minimize the undesirable spurious velocity discontinuities to be generated in the external flowfields. Without wave minimization, ZONA7 usually works well only for bodies with a simplified body model, in which the actual geometry of the body should be smoothed out. For engine inlets, they should be sealed and smoothed out as well.

Next, consider a body with a realistic geometry corner representing a canopy sill line as shown in Fig 3.39. The canopy sill line generates a set of strong Mach waves hence results in a larger jump in source strengths between the two adjacent, dividing the boxes.

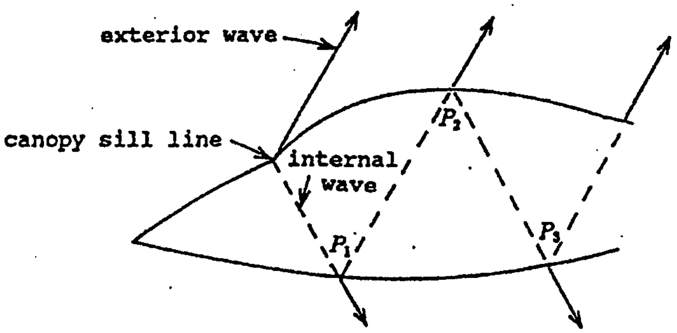

Fig 3.39 Propagation of Spurious Wave generated by the Real Geometry Corner

When the internal wave hits point P_1, the panel at P_1 must produce a jump in source strength in order to overcome the velocity discontinuity generated by the internal wave. In turn, it produces another internal wave (also another exterior wave) which travels to downstream and it hits point P_2. As a result, the box at P_2 must produce the same type of internal wave that will hit P_3 and so on. This "wave train" process means that the original internal wave from the canopy sill line will propagate downstream inside the body and the subsequent waves generated will be accumulated for a closed-end body. For a realistic fuselage-like body with many geometric corners, numerous internal waves generated by them will be accumulated downstream and will likely be further accentuated if two of these waves land on one single box. Clearly, these numerous internal wave-trains often degrade the (external) flowfield quality to an extent that the resulting flowfield solution becomes unacceptable.

On the basis of the preceding discussions, it should now be clear that many velocity discontinuities can be altogether present in the external velocity fields calculated by the constant source approach and that most of the velocity discontinuities not only will be spurious in their own right but also will produce unwanted repercussions on the rest of the configuration. For such method straightforward attempts to calculate supersonic flow field streamlines are likely to produce rather odd jagged shapes that become less smooth as the number of calculated points increases.

To minimize the undesirable effect caused by the internal spurious wave-train, it is apparent that techniques to improve continuity in the representation of both geometric and surface singularity variation are required. The PANAIR Code (Ref 3.30) solves the steady aerodynamics by a high order steady panel model. Linear source and quadratic doublet singularities are distributed over each body box and the continuity conditions of singularity distribution across adjacent boxes are imposed. The unknown steady source strength and doublet strength are solved by imposing Neumann and Dirichlet boundary conditions on each boxes. However, extending PANAIR's high order panel method to unsteady one is extremely complex and computationally expensive.

Instead of using a high order panel method, ZONA7 employs the so-called "integral-averaged boundary condition" to minimize the spurious waves resulted from the constant source singularity (Ref 3.32). The integral-arranged boundary condition is a wave minimization technique. It defines an averaged normal velocity $\overline{V}_n$ on each box by a sample integral average technique:

$$\overline{V}_n = \frac{1}{s_p} \iint_{s_p} \left(\vec{\nabla}\phi_o \cdot \vec{n} \right) ds_p \tag{3.71}$$

where s_p denotes the box area.

For steady aerodynamics, the integral-averaged boundary condition reads:

$$\overline{V}_n = -\left(\vec{V} \cdot \vec{n} \right) \tag{3.72}$$

Comparing Eq 3.72 with the steady boundary condition of Eq 3.28, it can be seen that Eq 3.28 is normally imposed at the control point whereas Eq 3.72 is satisfied over the box area. The averaged normal velocity $\overline{V}_n$ can be obtained by a four-point Gaussian Quadrature of Eq 3.71.

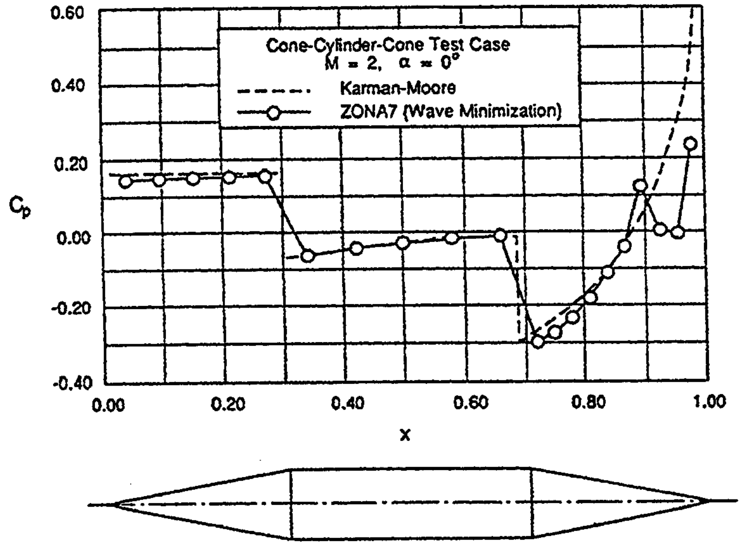

Fig 3.40 Cone-Cylinder-Cone at $M = 2.0$ and $\alpha = 0°$ Using ZONA7 with Wave Minimization

Fig 3.40 shows the results obtained by ZONA7 with the integral-averaged boundary condition (wave minimization technique) of the cone-cylinder-cone case at $M = 2.0$. Comparing to the one without wave minimization shown in Fig 3.37, it can be seen that the stability of the solution with the wave minimization technique is greatly improved.

It is found that the integral-averaged boundary condition works equally well for unsteady aerodynamics. This is done by applying Eq 3.71 to the unsteady boundary condition of Eq 3.23b. Thus, the integral-averaged boundary condition offers a technique that minimizes the spurious wave caused by the constant source singularity approach for both steady and unsteady supersonic aerodynamics.

3.11 Super-Inclined Boxes and Inlet Boxes

In a linearized supersonic flow formulation, the freestream Mach cone determines the region of influence. Typical supersonic panel methods generally work well if the body under consideration is fully immersed within this region of influence. However, when the supersonic freestream becomes higher and/or the body is relatively thick whereby a part of the body would be exposed outside of the zone of influence, most supersonic panel methods would cease to be applicable.

For boxes placed on the inlet surface (Fig 3.41a) or on the nose of a thick body (Fig 3.41b), the local angles of incidence on some boxes would be greater than the freestream Mach cone angle, this would render them lie outside of the freestream Mach cone. These boxes are called "super-inclined boxes" and they are the causes for numerical singularities in the supersonic aerodynamic influence coefficient computation.

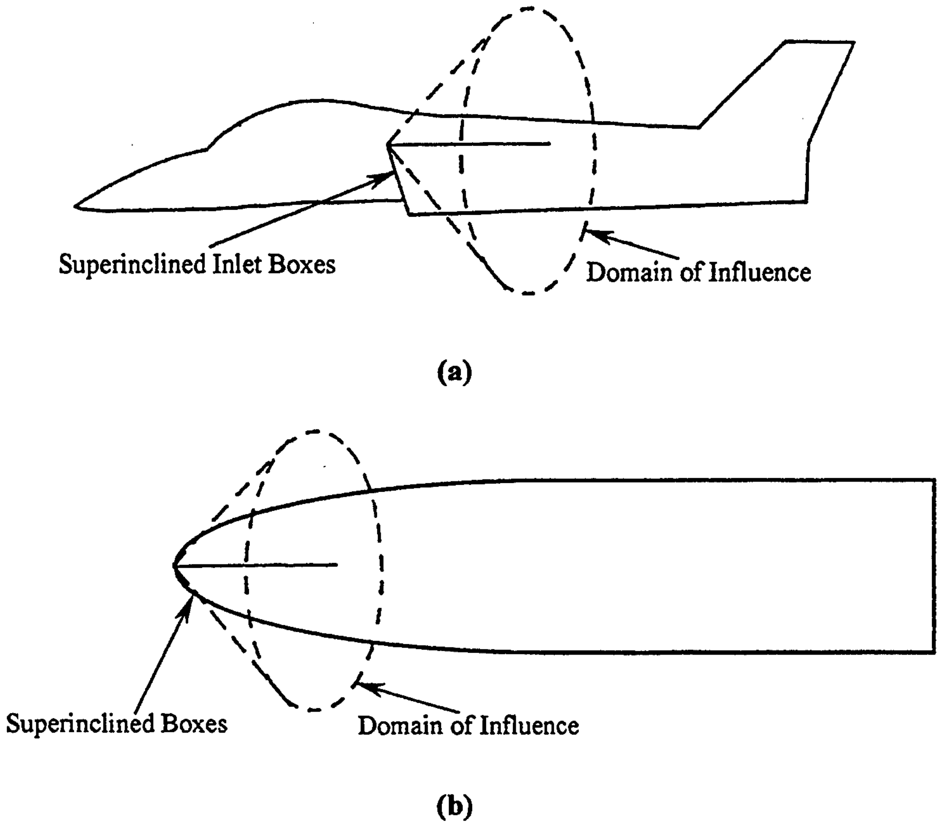

Fig 3.41 Superinclined Box (a) on Engine Inlet (b) on Thick Body

To circumvent this numerical singularity problem that is associated with super-inclined boxes in supersonic flow, we introduce a special treatment for the aerodynamic influence coefficient computation in ZONA7. This engineering treatment adopts the corresponding oblique shock angle for a cone (based on the Exact Euler Conical-Flow Solutions, e.g., Sims, Ref 3.33, 3.34) to substitute the Mach wave angle. The local cone angle for each superinclined box is measured by the angle between the freestream and the slope of the box. The corresponding oblique shock angle is used as a modified Mach wave angle to position a "Mach Wave" slightly ahead of the super-inclined boxes. It is this modified Mach angle that will determine the region of influence of the super-inclined boxes.

3.12 Treatment of Engine Inlets

ZONA6/7 can also include the aerodynamic computations for engine inlets. For body boxes on the inlet face, the boundary condition must be modified for the "flow-through" condition. This type of body boxes is called "inlet box".

Let A_c be the height of the stream tube containing the maximum mass flow which can enter the inlet, length A_o be the height of the stream tube actually entering the inlet, the mass flow ratio (*MFR*) is defined as:

$$MFR = \frac{A_o}{A_c} \tag{3.73}$$

For the inlet operating critically, no blockage occurs and the inlets are "flowing full". In this case A_o is equal to A_c and $MFR = 1$. For the subcritical flow condition, only the stream tube with height A_o enters the inlet. The remaining stream tube with height $(A_c - A_o)$ is spilled from the intake. For this case, *MFR* becomes less than 1. For a given mass flow ratio (*MFR*), the steady boundary condition expressed in Eq 3.28 can be modified for the inlet boxes, as:

$$\vec{\nabla}\phi_o \cdot \vec{n} = -\left(\vec{V}\cdot\vec{n}\right)\left(1 - MFR\right) \tag{3.74}$$

and the unsteady boundary condition becomes:

$$\vec{\nabla}\phi\cdot\vec{n} = \mathbf{F}_B\left(1 - MFR\right) \tag{3.75}$$

Regions OPEN and BLOCKED are determined by the intersections of the stream tubes and the box of the inlet. As such, the lengths of the two regions are proportional to the heights of the stream tubes, A_o and $(A_c - A_o)$, respectively. Thus, the ratio of the inlet area covered by OPEN boxes to the total inlet area reflects the mass flow ratio *MFR*, where *MFR* is determined by the intersection of the stream tubes and the inlet box.

The inlet in supersonic freestream usually requires the treatment of superinclined boxes (see Fig 3.41a). In ZONA7, the calculation of Aerodynamic Influence Coefficients (AIC) for an inlet box with respect to other boxes adopts the modified Mach angle substitution developed previously for superinclined boxes of thick bodies.

4.0 ZTAIC: UNSTEADY TRANSONIC AERODYNAMICS WITH STEADY PRESSURE INPUT

ZTAIC is ZONA's Transonic Aerodynamic Influence Coefficient method for generating unsteady transonic aerodynamics for lifting surface systems. With provided steady pressure distribution from CFD solutions or measured data on each wing section, ZTAIC generated transonic (modal) AIC's, which necessarily supports effective unsteady aerodynamics/aeroelastic computations. Hence, in addition to the ZONA6 input, the supplied wing-section steady pressures are required to be inputted by the user.

Unsteady subsonic and supersonic aerodynamic forces and moments can be well predicted by ZONA6 and ZONA7. But in the transonic flight regime these methods cease to be applicable due to the nonlinear compressibility and the presence of transonic shock waves. The nonlinear Transonic Small Disturbance Equation (TSDE) can be time-linearized with respect to the motion amplitude. This allows the formulation of a modal-based ZONA's Transonic Aerodynamic Influence Coefficient (TAIC) matrix method. In this way, ZTAIC generates unsteady transonic aerodynamic forces and moments that properly account for the transonic effects including shock oscillations up to the linear order in amplitude. The unique features of ZTAIC include:

- ZTAIC input requirement is nearly identical to these of ZONA6 and ZONA7 except the additional user-supplied steady pressure input.
- The user-supplied steady pressure input can be obtained either by wind tunnel measured data or a high level CFD solver. These steady input contains sufficient detail of the transonic shock structure; hence, the resulting unsteady pressures in terms of unsteady shock strength and location are found to be well predicted.
- ZTAIC does not require grid generation. The grid system for solving the unsteady transonic small disturbance equation is built in ZTAIC. ZTAIC can automatically optimize the mesh of the grid system according to given Mach number, oscillating frequency, and steady pressure input.
- ZTAIC generates a transonic *AIC* matrix using a Modal-based *AIC* (MAIC) approach. MAIC represents a frequency-domain aerodynamic transfer function whose definition is the same as that of ZONA6 and ZONA7.

In this section, we will discuss:

- *Background of ZTAIC*
- *Inverse airfoil design scheme based on the users supplied steady C_p input*
- *Time-domain unsteady transonic aerodynamic computational scheme of ZTAIC*
- *Transforming ZTAIC to the frequency-domain*
- *Modal AIC (MAIC) approach*

4.1 Background of ZTAIC

In the transonic flow regimes, the wing (body) thickness renders the problem nonlinear and the mean flow nonuniform (for an unsteady problem). Thus the current treatment of the unsteady transonic mostly adopts the Computational Fluid Dynamics (CFD) methodology. Currently there exists a number of well-practiced CFD unsteady transonic methods presumably ready for aeroelastic applications (e.g. CFL3D, ENS3DAE and ENSAERO, Refs 4.1, 4.2, 4.3). However, their acceptance by the aerospace industry for rapid analysis and design is still hampered by problems in grid generation, CFD/CSD interfacing and affordable computing time. For example, to perform a high-level (Navier-Stokes) CFD computation for a single wing structure flutter boundary would take days if not weeks of CPU time on a mainframe computer. Thus, if rendering such high-level CFD methods for flutter boundary prediction of a whole aircraft should take up much longer CPU time which will not be affordable for the industry. On the other hand, solving the unsteady TSDE equation using a lower-level CFD method such as CAP-TSD (Ref 4.4) should be computationally efficient. But CAP-TSD is confined by its self-generated steady-flow solution in that the TSD assumption would restrict its applicability to wings with thick-airfoil or supercritical-wing sections. If the viscous effect is not introduced in the steady mean flow of an unsteady TSD method such as CAP-TSD, then the resulting shock position and strength, and hence the flutter solutions would be invalidated.

Further attempts in an MDO environment have been somewhat discouraged by their incompatibility with structural FEM. Although current CFD efforts are directed towards meeting the FEM compatibility, questions of affordable computing time for each MDO cycle remain outstanding. Toward this end, we have re-examined the unsteady transonic aerodynamic methodology critically from the viewpoint of its FEM compatibility and its expediency for aeroelastic analysis and design applications. The result of this re-examination effort is the development of ZTAIC.

Since 1988, ZONA has been following up on the development of the Transonic Equivalent Strip (TES) method originally supported by NAVAIR/ONR (Refs 4.5, 4.6) for unsteady flow computation of arbitrary wing planforms. The TES method consists of two consecutive steps added to a given nonlinear Transonic Small Disturbance code such as ZTRAN (Ref 4.7); namely the chordwise mean flow correction and the spanwise phase correction. The chordwise mean flow correction is accomplished by an inverse airfoil design scheme incorporated in ZTRAN. The computational procedure require direct steady pressure input from other CFD codes or measured data. It does not require airfoil shape or grid generation. Meanwhile, all the mean-flow shock jumps are properly included in the resulting unsteady aerodynamics. Based on the TES concept, ZONA has further developed the ZONA Transonic Aerodynamic Influence Coefficient (ZTAIC) code by adopting a Model-based AIC (MAIC) procedure (Ref 4.8). ZTAIC has been successfully applied in a Multi-Disciplinary Optimization (MDO) software system for aeroelastic applications (Ref 4.9). Shown in Fig 4.1 is a flow chart presenting ZTAIC procedure for flutter analysis.

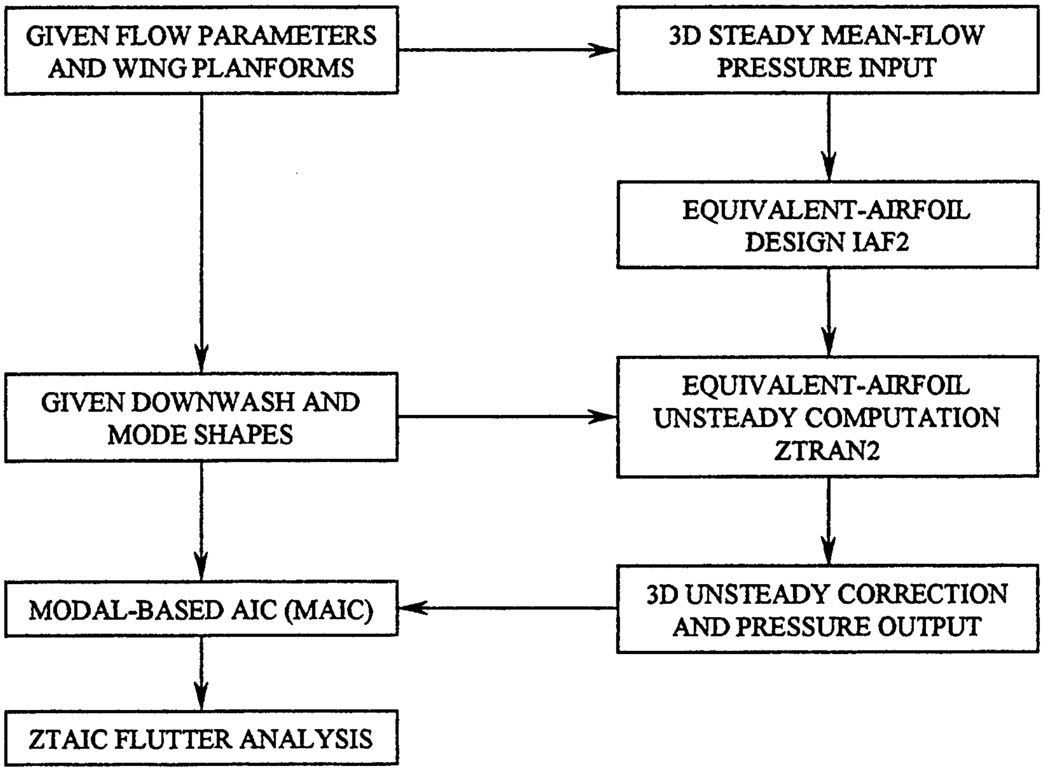
GIVEN FLOW PARAMETERS AND WING PLANFORMS
3D STEADY MEAN-FLOW PRESSURE INPUT
EQUIVALENT-AIRFOIL DESIGN IAF2
GIVEN DOWNWASH AND MODE SHAPES
EQUIVALENT-AIRFOIL UNSTEADY COMPUTATION ZTRAN2
MODAL-BASED AIC (MAIC)
3D UNSTEADY CORRECTION AND PRESSURE OUTPUT
ZTAIC FLUTTER ANALYSIS

Fig 4.1 Flow Chart of ZTAIC Computation Procedure

Results computed by ZTAIC have been validated with wind tunnel data for a number of wing planforms with various aspect ratios. These include:

Unsteady Pressures: Measured Data Input

- *The Lessing Wing (Ref 4.10)*

Fig 4.2a shows the Lessing Wing with a rectangular planform of aspect ratio 3.0 and width a 5 % thick parabolic arc airfoil section. Unsteady pressure magnitudes and phase angles are presented in Figs 4.2b and 4.2c for spanwise locations at $\eta = 0.5, 0.7$ and 0.9 ($\eta = 2y / b$). It is seen that the ZTAIC results correlate reasonably well with two sets of experimental data (1st and 2nd runs).

- *The LANN Wing (Ref 4.11)*

Fig 4.3 shows the dimensions of the LANN Wing Planform of aspect ratio 7.93 and a 12 % thick airfoil section as well as the in-phase and out-of-phase pressures of the LANN Wing with pitching axis at 62 % root chord. Throughout three spanwise locations considered ($\eta = 32.5$ %, 65 % and 95 %), the present results for the upper surface compare more favorably with NLR measured data that do the XTRAN3 results (Ref 4.12). Since subcritical flows are predicted for lower surfaces, the unsteady pressures do not contain the shock jump, as expected.

- *The F-5 Wing with Control Surface (Ref 4.13)*

Fig 4.4 compares in and out-of-phase pressures at two flap sections of F-5 wing at $M_\infty = 0.9$. Close agreements are found with XTRAN3S (Ref 4.14) results and the NLR measured data.

Flutter Results

- *The AGARD Standard 445.6 Wing (Ref 4.15)*

The 445.6 Wing planform, has an aspect ratio of 4 and a NACA 65A004 airfoil section. It has two structural models: the solid wing and the weakened wing. This is an ideal case to demonstrate ZTAIC's AIC capability. The aerodynamic shapes of these two models remain the same, but structurally they have two different sets of structural modes associated with the solid wing and the weakened wing. For this reason, the same modal *AIC* can be shared by both models. Hence, the modal *AIC* computed for the weakened wing can be saved allowing for a warm-start for the solid wing. Fig 4.5 presents the flutter results of the weakened wing. At a subsonic Mach number $M_\infty = 0.678$, the ZTAIC result is in good agreement with that of ZONA6, as expected. At other supercritical Mach numbers where $M_\infty = 0.9$ and 0.95, ZTAIC predicts a pronounced transonic dip which is comparable to that predicted by the CAP-TSD code.

Fig 4.6 presents the flutter results of the solid wing. The stored modal *AIC* from the weakened wing is warm-started here. Consequently the computing time for each flutter point requires only one minute, in contrast to the weakened wing case which requires five hours of CPU time for a flutter point on a SUN SPARC 20 workstation.

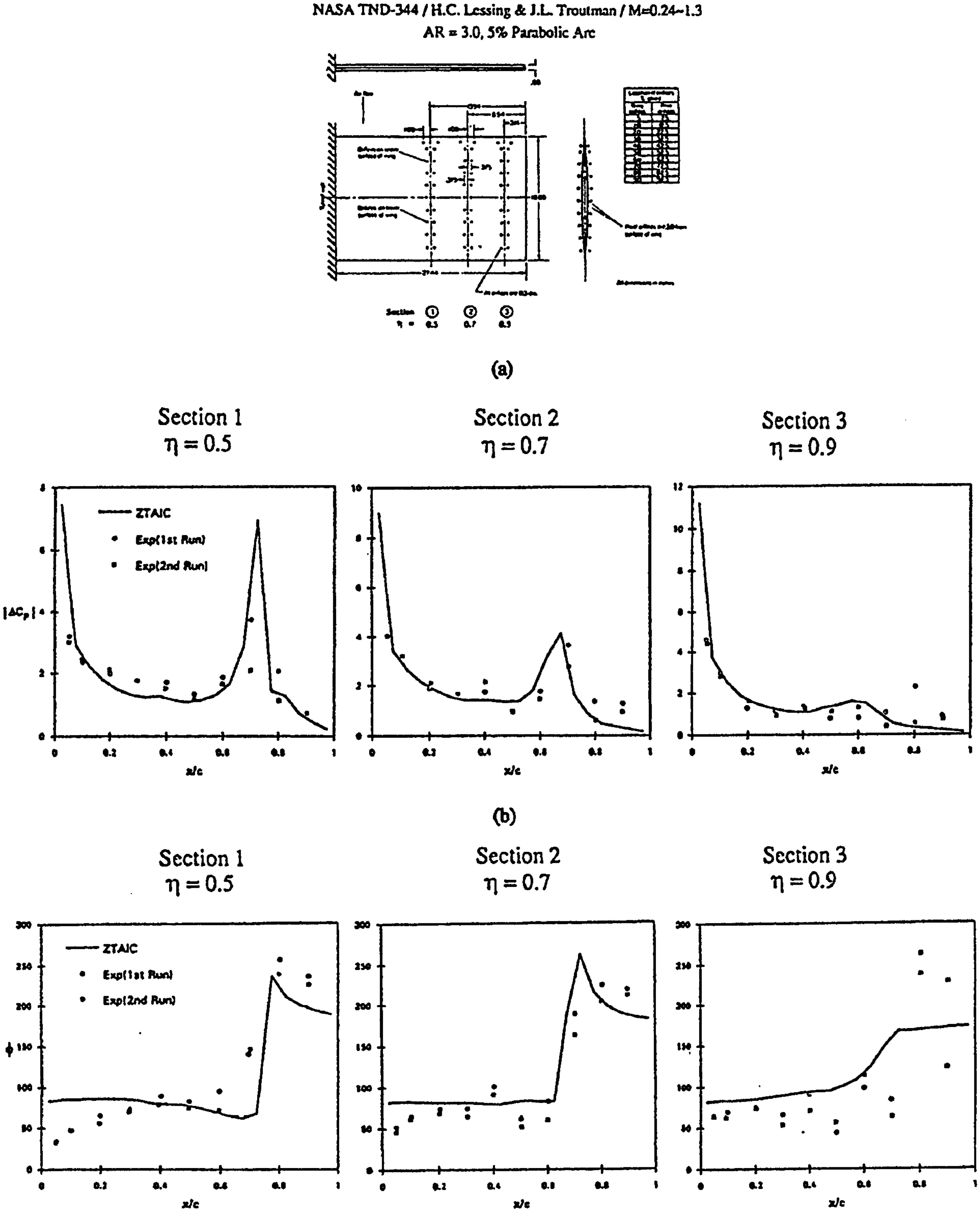

(a)

(b)

(c)

Fig 4.2 The Lessing Wing (a) Configuration (b) Magnitude of the First Bending (c) Phase Angle (in °) of the First Bending, $M = 0.9$, $k = 0.13$

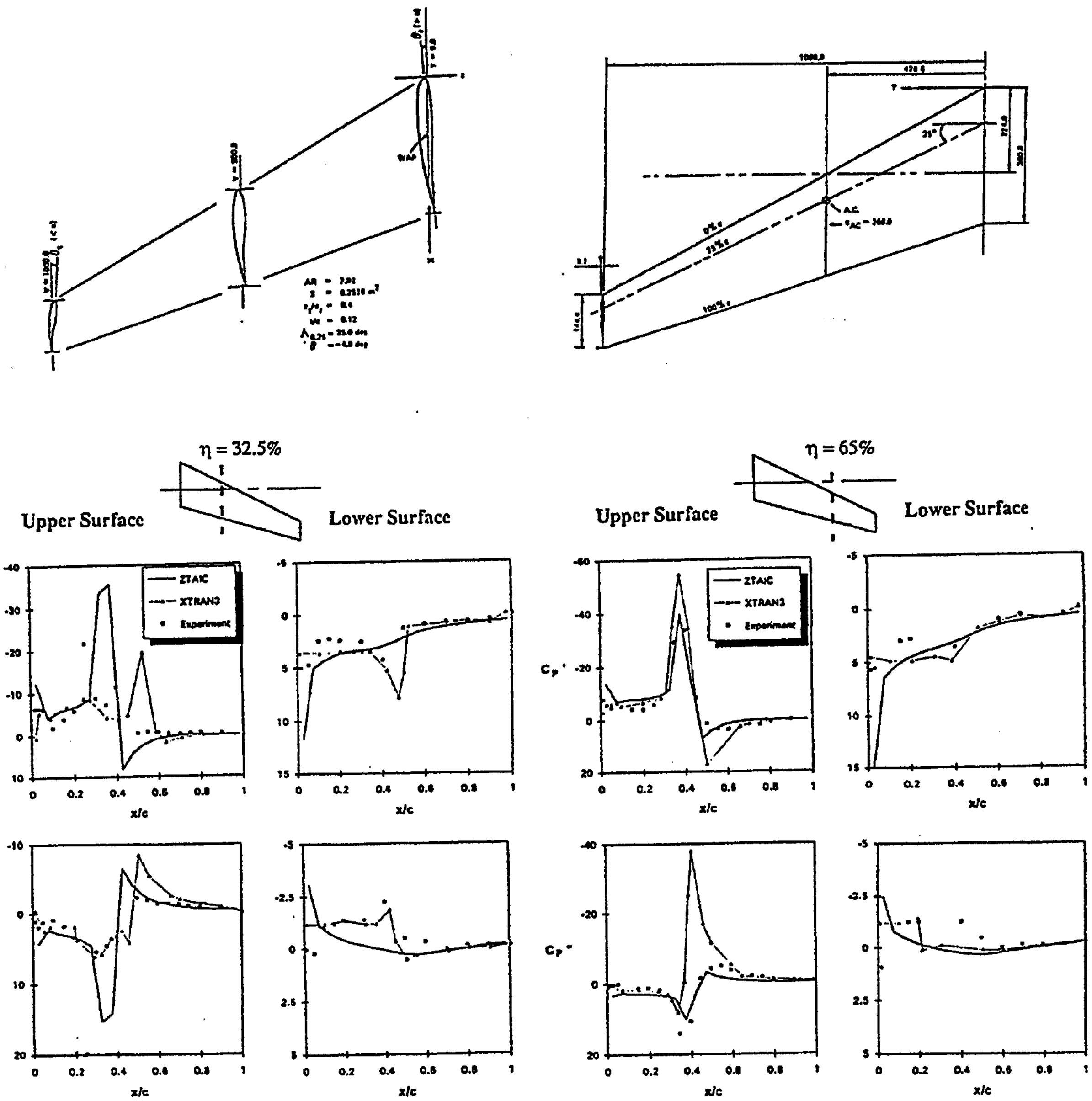

Fig 4.3 LANN Wing Comparison of In-Phase and Out-of Phase Pressures at Two Spanwise Locations: Pitching Oscillation About 62% Root-Chord at $M = 0.82$, $k = 0.205$

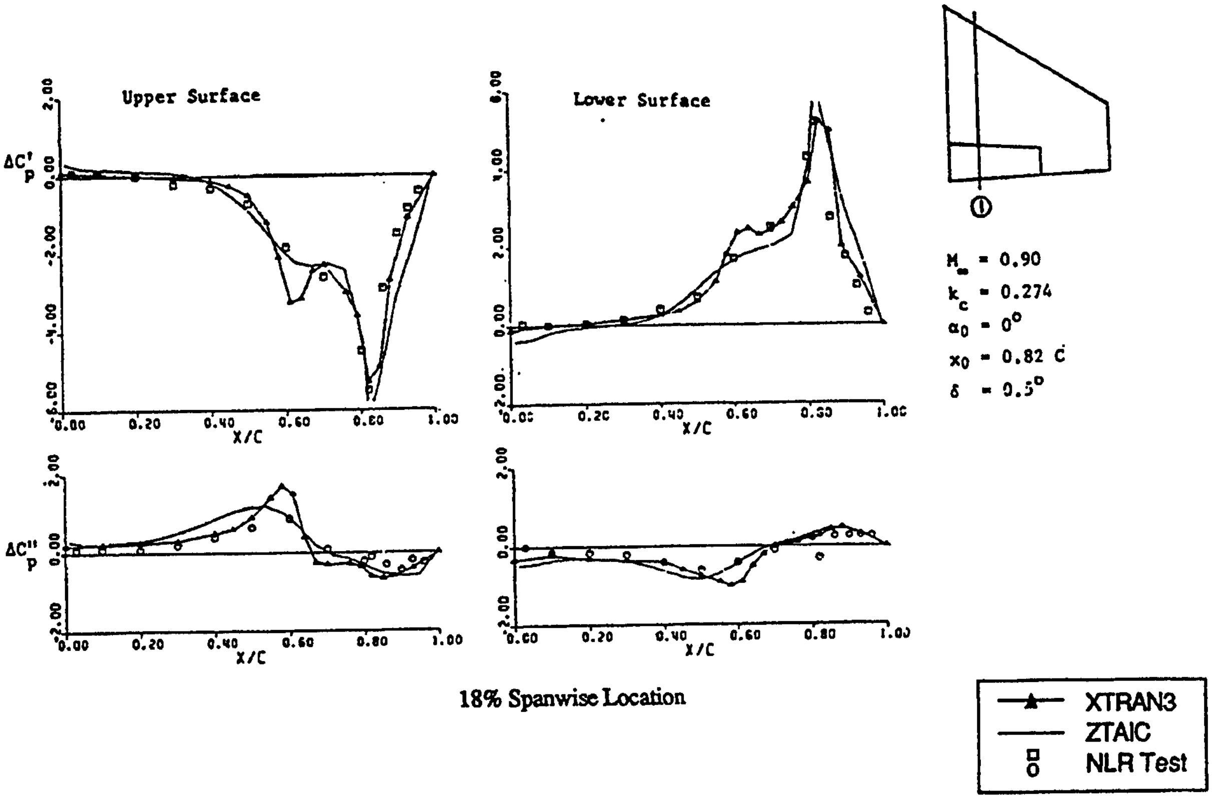

18% Spanwise Location

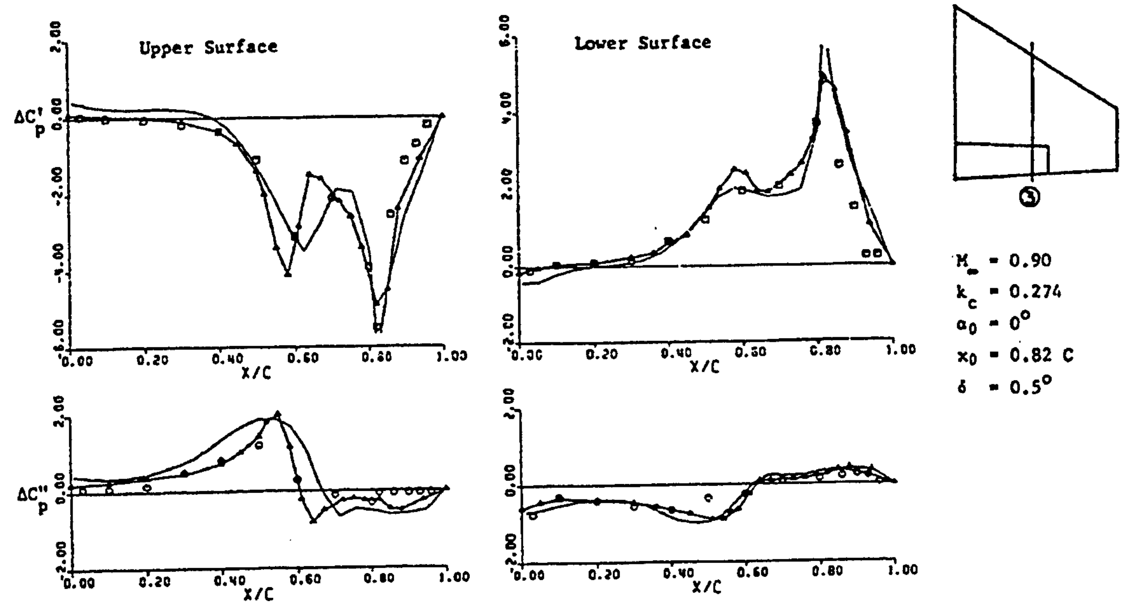

51% Spanwise Location

Fig 4.4 Northrop F-5 Wing with Oscillation Flap: Comparison of In-Phase and Out-of Phase Pressures with Hinge Line at 82% Chord at Sections 1 and 3, $M = 0.9$, $k = 0.274$

Test Cases		Wind Tunnel Data		ZONA6 --- (Linear)		ZTAIC △ (Nonlinear)		CAPTSD ◇ (Nonlinear)	
M	ρ (slug/ft³)	ωf (Hz)	Vf (ft/sec)	ωf (Hz)	Vf (ft/sec)	ωf (Hz)	Vf (ft/sec)	ωf (Hz)	Vf (ft/sec)
0.678	0.000404	17.98	759.1	19.81	766.0	19.30	761.0	19.2	768
0.900	0.000193	16.09	973.4	16.31	984.0	16.38	965.2	15.8	952
0.950	0.000123	14.50	1008.4	16.18	1192.0	13.46	944.0	12.8	956

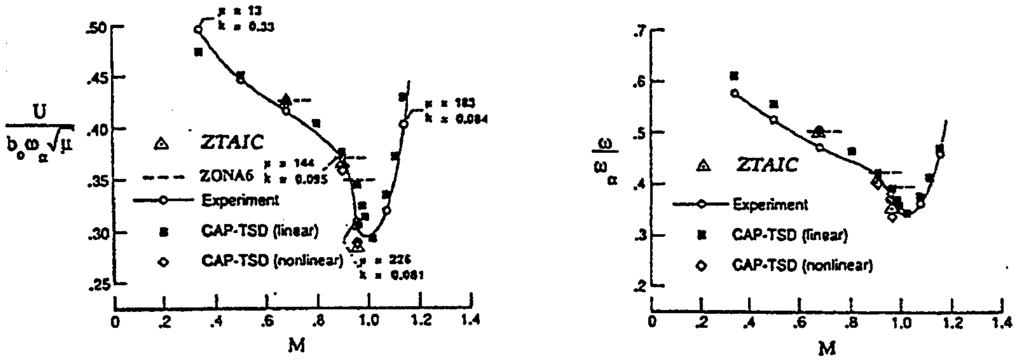

Fig 4.5 Comparison of Flutter Speed and Frequency of 445.6 Weakened Wing at $M = 0.678$, 0.90 and 0.95

Test Cases		Wind Tunnel Data*		ZONA6 (Linear)		ZTAIC** (Nonlinear)		CAPTSD* (Nonlinear)	
M	ρ (slug/ft³)	ωf (Hz)	Vf (ft/sec)	ωf (Hz)	Vf (ft/sec)	ωf (Hz)	Vf (ft/sec)	ωf (Hz)	Vf (ft/sec)
0.90	0.00357	27.00	452.0	26.75	439.0	25.71	418.0	25.8	435.0
0.95	0.00320	26.91	479.0	26.89	462.0	25.46	450.0	26.2	472.1

---

* Interpolated between Mach 0.87, 0.92 and 0.96.

** Restart Run Using AIC's of Weakened Wing (1 min cpu/case).

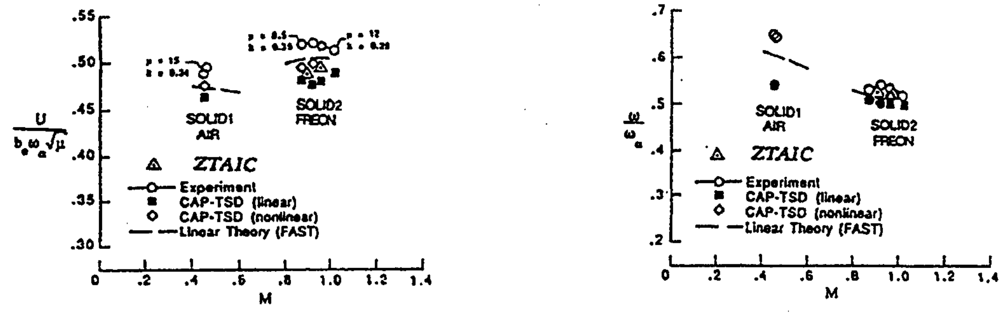

Fig 4.6 Comparison of Flutter Speed and Frequency of 445.6 Solid Wing at $M = 0.90$ and 0.95

4.2 The Chordwise Mean Flow and Spanwise Phase Correction Procedures

Governing Equations

The unsteady Transonic Small Disturbance (TSD) equation reads:

$$[(1 - M_\infty^2) - (\gamma + 1)M_\infty^2 \Phi_x]\Phi_{xx} + \Phi_{yy} + \Phi_{zz} - 2M_\infty^2 \Phi_{xt} - M_\infty^2 \Phi_{tt} = 0 \qquad (4.1)$$

Similar to Eq 3.2, the TSD potential Φ can be expressed in terms of the steady TSD potential ϕ_o and the time-linearized TSD potential ϕ_1 with respect to linear amplitude, i.e.:

$$\Phi = \phi_o(x,y,t) + \phi_1(x,y,z,t) \qquad (4.2)$$

where ϕ_o and ϕ_1 should satisfy the following equations, respectively.

$$[(1 - M_\infty^2) - (\gamma + 1)M_\infty^2 \phi_{ox}]\phi_{oxx} + \phi_{oyy} + \phi_{ozz} = 0 \qquad (4.3)$$

$$(1 - M_\infty^2)\phi_{1xx} + (\gamma + 1)M_\infty^2 (\phi_{ox}\phi_{1x})_x + \phi_{1yy} + \phi_{1zz} = 2M_\infty^2 \phi_{1xt} + M_\infty^2 \phi_{1tt} \qquad (4.4)$$

Eq 4.3 is the famous steady TSD equation due to von Karman. Eq 4.4 is the so-called time-linearized equation derived by Landahl (Unsteady Transonic Flow, Pergamon Press, 1961, Ref 4.16).

Notice that Eqs 4.3 and 4.4 are the transonic counterparts of Eqs 3.4 and 3.5 for subsonic/supersonic linearized formulation.

The premises of the Transonic Equivalent Strip (TSE) method (Ref 4.5) is to propose utilizing a two-dimensional TSD potential solver to solve Eq 4.4 in conjunction with a 3D linear potential solver such as ZONA6. LTRAN2 (Ref 4.17) was originally selected for this 2D solver. But ZONA's improved ZTRAN is to replace LTRAN2 in all our subsequent development. The governing 2D TSD equation is nothing more than a 2D version of Eq 4.1, viz.:

$$[(1 - M_\infty^2) - (\gamma + 1)M_\infty^2 \Phi_x]\Phi_{xx} + \Phi_{zz} = 2M_\infty^2 \Phi_{xt} + M_\infty^2 \Phi_{tt} \qquad (4.5)$$

The LTRAN2 of Ballhaus and Goorjian solves Eq 4.5 with two alternatives: the Harmonic Oscillation Method and the Indicial Method (Refs 4.17, 4.18). The latter method amounts to an expedient method of time linearization of Eq 4.5 directly by CFD means. Equivalently, their indicial method solves a 2D version of Eq 4.4, viz.:

$$(1 - M_\infty^2)\varphi_{1xx} + (\gamma + 1)M_\infty^2 (\varphi_{ox}\varphi_{1x})_x + \varphi_{1zz} = 2M_\infty^2 \varphi_{1xt} + M_\infty^2 \varphi_{1tt} \qquad (4.6)$$

where ϕ_o, the 2D steady TSD potential, satisfies the 2D Karman equation, i.e.:

$$[(1 - M_\infty^2) - (\gamma + 1)M_\infty^2 \varphi_{ox}]\varphi_{oxx} + \varphi_{ozz} = 0 \tag{4.7}$$

Boundary Conditions

On the mean surface of the wing planform, the potentials must satisfy the linearized tangency condition, i.e. at $z = 0$,

$$\begin{aligned} \phi_{oz} &= \tau T(x, y_i, 0) \\ \phi_{1z} &= \delta[H_x + H_t] \end{aligned} \tag{4.8}$$

where:
T is the wing airfoil-section thickness distribution at spanwise station y_i
H is the mode shape
τ is the thickness ratio
δ is the oscillation amplitude, and $\delta < \tau$.

The tangency condition along with the wake condition imposed here are the typical linearized boundary conditions, also adopted in the previous linearized subsonic and supersonic potential formulations. Hence, one assumes that ϕ_0 and ϕ_1 are decoupled throughout except the governing equation, Eq 4.4, itself. For TSD potentials φ_o and φ_1 of Eqs 4.6 and 4.7, they should satisfy the same boundary conditions as above except in the 2D sense.

TES Solution of Eq 4.4

Proposed earlier by Liu et al. (Ref 4.6) and further supported by Oyibo's Separability Principle for Full-Potential Transonic Solutions (Ref 4.19), a ϕ_1 solution of Eq 4.4 can be derived, i.e., at a spanwise location $y = y_i$,

$$\phi_1(x, y_i, z, t) = \varphi_{1_i}(x, z, t) \; F(y_i; \lambda_i) \tag{4.9}$$

where:
φ_1 is the 2D unsteady solution by ZTRAN at a spanwise location $y = y_i$
F is Oyibo's spanwise exponential decaying function
λ_i is the decaying parameter measured by the chordwise (2D) to the spanwise (3D) lift slope ratio.

Clearly, the same separability of ϕ_1 in Eq 4.9 showed also holds for ϕ_1 of Eq 3.5, i.e.:

$$\phi_1^{\ell}(x, y_i, z, t) = \varphi_1^{\ell}(x, z, t) \; G(y_i; \alpha_i) \tag{4.10}$$

where the superscript "ℓ" denotes the purely "linear" subsonic perturbed potential.

Pressure coefficients

The linearized unsteady pressure coefficient reads:

$$\Delta C_p = -2\,(\phi_{1x} + \phi_{1t}) \tag{4.11}$$

Again, Eq 4.11 holds in general for unsteady transonic potential ϕ_1 or φ_1 as well as for unsteady subsonic potential ϕ_1^{ℓ} or φ_1^{ℓ}. Combining Eqs 4.9, 4.10 and 4.11 yields the TES pressure relations for the correction procedure, i.e. at $y = y_i$:

$$\Delta C_{p_3}{}^{N} = \Delta C_{p_2}{}^{N}\, f_n(\Delta C_{p_3}{}^{\ell}, \Delta C_{p_2}{}^{\ell}) \cdot \exp\{(\lambda_i - \alpha_i)\, y_i\} \tag{4.12}$$

where superscripts N and ℓ denote transonic and subsonic unsteady pressures and $\Delta C_{p_3}{}^{N}$ and $\Delta C_{p_2}{}^{N}$ denote the 3D and 2D unsteady pressure, respectively. Hence, the proposed correction procedures for TES lies in the pressure relation given by Eq 4.12. The chordwise mean-flow correction is supplied by "injecting" the correct steady pressure input in $\Delta C_{p_2}{}^{N}$, which is to be computed by ZTRAN. Recall that steady pressure input is provided by measured data or by a high-level CFD solution. The way to "inject" this input into ZTRAN is accomplished by an inverse airfoil design (IAF2) scheme to be discussed in the next section. The spanwise phase correction is accomplished by providing the linear pressure distributions $\Delta C_{p_3}{}^{\ell}$ and $\Delta C_{p_2}{}^{\ell}$ in the function "f_n", whereas they are obtained from ZONA6 computation.

The exponential decaying parameters λ_i and α_i are measures of 3D to 2D lift curve slope ratios (for transonic and subsonic, respectively). For simplicity, the current TES procedure maintains at an approximated level where $\lambda_i = \alpha_i$.

Finally, the two correction procedures combined in Eq 4.12 have the physical meaning that: i) the chordwise correction accounts for reproducing the nonlinear structure of the three-dimensional mean flow, ii) the spanwise phase correction is responsible for the adjustment of the spanwise phase lag of the pressure according to an equivalent linear three-dimensional flow. Clearly, shock waves cannot be created or destroyed by any process of these corrections.

4.3 The Inverse Airfoil Design (IAF2) Scheme

It has been pointed out by Fung (Ref 4.20) and Lambourne (Ref 4.21), among others, that an accurate steady state with correct shock jump and locations is essential for correct unsteady aerodynamic computations. It is believed that TES in general should be adequate in handling the classical flutter analysis in the transonic regime, because its chordwise mean-flow correction could result in the proper shock position and strength including viscous effects. This correction procedure is made possible by adopting the externally provided steady pressure input from measured data or from high-level CFD computations. To "inject" the steady pressure input into ZTRAN of the TES method requires to build in an equivalent airfoil design procedure using an inverse design algorithm called IAF2. In doing so, a proper steady flowfield can be generated corresponding to the input steady pressure prescribed on the airfoil surface.

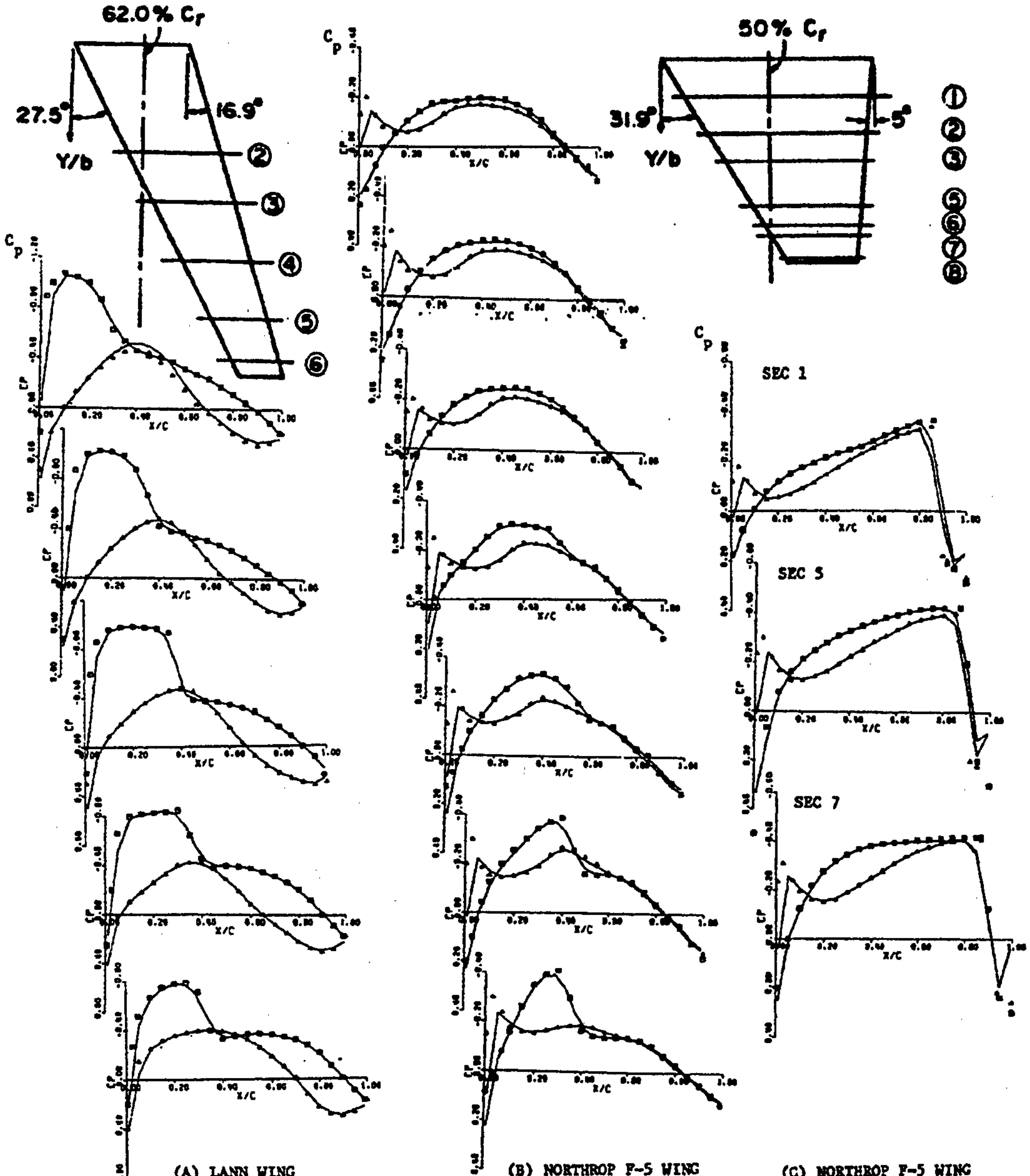

(A) LANN WING $M_\infty = 0.82$

(B) NORTHROP F-5 WING $M_\infty = 0.90$

(C) NORTHROP F-5 WING $M_\infty = 0.95$

Fig 4.7 Steady Pressure Inputs and Equivalent Airfoil Outputs at various Spanwise Locations (□ upper surface, Δ lower surface, —— presents TES data):

a) LANN Wing at Mean Incidence $\alpha_0 = 0.62°$, $M_\infty = 0.82$ (NLR Measured Data);

b) Northrop F-5 Wing at Mean Incidence $\alpha_0 = 0°$, $M_\infty = 0.90$ (NLR Measured Data);

c) Northrop F-5 Wing at Mean Incidence $\alpha_0 = 0°$, $M_\infty = 0.95$ (XTRAN3S-Ames Input)

Based on the user supplied steady pressure input, an Inverse Approximate Factorization scheme (IAF2) proposed by Fung and Chung (Ref 4.7) is adopted to perform an inverse airfoil design according to Eq 4.7. The velocity potential obtained from integrating the pressure on the slit representing an airfoil is known up to an arbitrary constant. To determine this constant, it is required that a closure condition is imposed, e.g. the resulting slope distribution being equivalent to a closed body. This constant a being updating during the numerical iteration process until a converged solution satisfying the closure requirement is obtained. Fig 4.7a and Fig 4.7b display the pressure inputs for upper and lower surface at $M_\infty = 0.82$ and 0.9 for the LANN and F-5 wings, respectively, based on the NLR measured data. The input data in general are shown by open symbols whereas the pressures computed by the IAF2 scheme by solid lines.

Fig 4.7c demonstrates the flexibility of the pressure input scheme using inverse airfoil design, in which the computed pressures by XTRAN3S of F-5 wing at M=0.95 is adopted as the steady pressure input. The strong shock close to the trailing edge in this case is considered a challenging case for an airfoil design code. As can be seen in Fig 4.7c, the present IAF2 showed excellent comparison between the XTRAN3S pressure input and the design output. Further studies in using the present IAF2 for pressure input/output verification showed the present scheme is indeed very robust and can generate accurate pressure flowfield associated with a wide class of transonic pressure input with transonic shock jumps.

4.4 Frequency-Domain Pressure Coefficient by Indicial Method

For 2D unsteady transonic computation, the ZTRAN code, similar to LTRAN2, also has two alternative methods, namely the harmonic oscillation method and a method based on a time linearized scheme proposed by Fung et al. (Ref 4.22). Most unsteady TSD codes like LTRAN2 and XTRAN3S generated their steady aerodynamics and pressures according to the steady TSDE. Unlike these methods, ZTRAN employs the inverse airfoil design to inject the externally provided steady pressure input and generate the corresponding steady computation. Thus, this steady pressure input procedure removes the mandatory usage of self-generated steady aerodynamics. Instead the steady pressure input can be supplied from the results of a high-level CFD computation or wind tunnel measured data. In this way, the inverse airfoil design scheme ensures that the nonlinear effects including shock structure and viscous effects are closely reproduced and properly incorporated into the follow-on unsteady aerodynamic computation scheme.

Both the harmonic oscillation scheme and the time-linearized scheme of ZTRAN yield the unsteady aerodynamic solution in time domain. The former scheme can be further linearized if the oscillatory amplitude is kept sufficiently small.

To achieve a sinusoidal oscillation solution (linearized), it is required to apply the following procedures. First, the aerodynamic-response solution is to be selected only after a few cycles of oscillation, when the transient solution is seen to be diminishing (or the response solution becomes closely periodic). Next, Fourier analysis is applied to the selected last-cycle response solution in which only the first harmonic component is retained, whereas all the higher harmonics are filtered through in this step. From the first-harmonic solution, the pressure magnitude and phase angle can be properly identified. This method for the first-harmonic solution works fine for the K and P-K flutter methods, except that each solution obtained corresponds to only one single frequency input, hence it tends to be computationally ineffective. For computational expediency, the indicial method is preferred.

The indicial method, first introduced by Tobak (Ref 4.23), offers a rapid procedure for converting the time-domain solution of a CFD code to the frequency domain. Normally, the objective of the indicial method is to obtain the "aeroelastic transfer function" of an aerodynamic quantity of interest in the frequency domain, i.e.:

$$\mathbf{H}(ik) = \mathcal{F}(H(T)) \tag{4.13}$$

where:

$$\mathcal{F}(\cdot) = \int_{-\infty}^{\infty} (\cdot)\, e^{-ikT}\, dT \tag{4.14}$$

is the Fourier transform of $(\cdot)$, $T = \dfrac{t\, V_\infty}{L}$ is the non-dimensional time and $\mathbf{H}$ denotes the aeroelastic transfer function of an aerodynamic quantity of interest such as C_p, C_L, ... etc.

Ballhaus and Goorjian (Ref 4.24) have demonstrated the applicability of the indicial method for transonic aerodynamics. However, the step function of the indicial method has numerical difficulties due to the evaluation of the Dirac delta function associated with the derivative of the step function at $t = 0$. Later, Seidel, Benett and Ricketts (Ref 4.25) introduced a pulse function method in the XTRAN3 code. The pulse function is defined as:

$$f(T) = e^{-W(T-T_c)^2} \tag{4.15}$$

where T_c is the non-dimensional time at which the maximum amplitude is reached and W represents the width of the pulse. The desired aeroelastic transfer function is then obtained by solving the following equation numerically:

$$\mathbf{H}(ik) = \frac{\mathcal{F}(X(T))}{\mathcal{F}(f(T))} \tag{4.16}$$

where $X(T)$ is the aeroelastic response subject to the pulse function $f(T)$.

Because the pulse function and its derivative are continuous, it removes the numerical difficulty. Eq 4.16 also suggests that the entire frequency-domain solution can be obtained by Fourier Transform on $X(T)$ and $f(T)$ in a post-processing sense. Therefore, instead of repeated computation for each frequency by the sinusoidal method, the pulse function method provides the entire frequency-domain unsteady aerodynamic solution with only a single unsteady aerodynamic computation, leading to a rapid procedure for frequency-domain solution.

4.5 Modal Aerodynamic Influence Coefficient (MAIC) Approach

A formal *AIC* matrix should contain purely aerodynamic information relevant to the governing equation. However, to generate this type of *AIC* from CFD methods such as the ZTRAN code remains a major undertaking. The validity of the MAIC approach is based on the assumption of the amplitude linearization principle that states: "*the linearization of the aerodynamics for an aeroelastic system in any flow regime can be assured if the modal amplitude is kept sufficiently small at all times*". In fact, this is equivalent to the principle of time linearization. This principle suggests that an expedient modal-based *AIC* procedure can be developed readily.

Consider a typical CFD computation procedure, in which the incremental pressure distribution is related to a given pre-defined baseline modal vector by:

$$\{\mathrm{C_p}\}_i = \mathcal{N}\{\phi\}_i \qquad i = 1, \ldots, m \tag{4.17}$$

where $\mathcal{N}$ is a nonlinear CFD operator that generates the incremental pressure due to a given baseline modal vector ϕ. For m number of baseline modal vectors, Eq 4.17 becomes a matrix equation:

$$[\mathbf{P}] = \mathcal{N}[\mathbf{H}] \tag{4.18}$$

where:

$$[\mathbf{P}] = [\{\mathrm{C_p}\}_i \cdots \{\mathrm{C_p}\}_m] \tag{4.19}$$

is defined as the incremental pressure matrix.

and:

$$[\Phi] = [\{\phi\}_i \cdots \{\phi\}_m] \tag{4.20}$$

is defined as the baseline modal matrix.

With the amplitude linearization principle imposed, the operator $\mathcal{N}$ can be approximated by a linearized operator $\mathcal{L}$. Thus:

$$[\mathbf{P}] = \mathcal{L}[\Phi] \tag{4.21}$$

The baseline modal matrix is defined as a set of displacement vectors that could be superimposed to closely represent the deformation of the structure. Let **h** be the structural deformation vector, the relation between *h* and the baseline modal matrix reads:

$$\{\mathbf{h}\} = [\Phi]\{\mathbf{a}\} \tag{4.22}$$

where **a**'s are the best-fit coefficients, to be determined by the following least squares procedure:

$$\{\mathbf{a}\} = [\ [[\Phi]^T [\Phi]]^{-1} [\Phi]^T\ ] \{\mathbf{h}\} \tag{4.23}$$

Let $\mathbf{C_p}$ be the incremental pressure vector due to the structural deformation h, then $\mathbf{C_p}$ can be related to $\mathbf{h}$ by the same linear operator:

$$\{\mathbf{C_p}\} = \mathcal{L}\{\mathbf{h}\} \tag{4.24}$$

Substituting Eq 4.22 into Eq 4.24 yields:

$$\{\mathbf{C_p}\} = \mathcal{L}[\Phi]\{\mathbf{a}\} \tag{4.25}$$

Combining Eqs 4.21, 4.23 and 4.25 gives a matrix that directly related the incremental pressure vector to the structural deformation h:

$$\{\mathbf{C_p}\} = [MAIC]\{\mathbf{h}\} \tag{4.26}$$

where:

$$[MAIC] = [\ [\mathbf{P}]\ [[\Phi]^T [\Phi]]^{-1} [\Phi]^T\ ] \tag{4.27}$$

is the sought modal-based *AIC* matrix.

The modal-based *AIC* approach is a general procedure which could be applied to any CFD codes. Chen et al demonstrated the MAIC approach in a transonic aeroelastic optimization problem (Ref 4.9). In Ref 4.9, the structural modes of the initial structure are defined as the baseline modal matrix. The modal-based *AIC* matrix is then constructed from the baseline modal matrix and their associated unsteady pressure matrix. The constructed modal-based matrix is computed once and reused in the structural optimization loop. In so doing, considerable saving in computer time is achieved.

The ZTAIC method requires a somewhat different type of MAIC matrix. For a stripwise unsteady transonic aerodynamic computation, only a 2D-baseline modal AIC matrix is needed. For high aspect ratio wing structures involving primarily spanwise bending and torsion deformations, 2D rigid pitch mode and 2D rigid plunge mode are used to represent the local structural deformation at each strip. For wing sections containing leading edge and trailing edge control surfaces, a 2D leading edge and 2D trailing edge modes are used to represent these control surfaces at the strip. For low aspect ratio wing planforms where chordwise bending deformation may occur, a 2D chordwise bending mode is introduced. Altogether, five modal vectors are used to define the 2D baseline modal matrix.

With the 2D baseline modal matrix in hand, the generation of the MAIC matrix for ZTAIC is a straight forward procedure. The formal AIC for relating the structural deformation to the aerodynamic forces can be obtained simply by multiplying the area of each aerodynamic boxes to the MAIC matrix. This gives:

$$\{\mathbf{F}_h\} = q_\infty [AIC]\{\mathbf{h}\} \tag{4.28}$$

where:

$$[AIC] = [\bar{n}][AREA][MAIC]$$

and:

$[AREA]$ is a diagonal matrix containing the area of each aerodynamic boxes.

$[\bar{n}]$ is a *K-set* by *J-set* matrix containing the normal vector components of each aerodynamic box. The exact expression of $[\bar{n}]$ can be found in Eq 3.62.

5.0 ZONA7U: UNIFIED HYPERSONIC/SUPERSONIC UNSTEADY AERODINAMICS FOR WING-BODY AIRCRAFT CONFIGURATION

ZONA7U extends the applicability of the lifting surface method of ZONA7 into the unified hypersonic and supersonic flight regime. The unsteady lifting surface option of ZONA7U (formerly ZONA51U) takes into account the nonlinear wing thickness effect and the flow rotationality effect due to strong shock waves, whereas these effects are neglected by the linear theory and overestimated by Piston theory. In addition to the ZONA7 input, only the wing-section profiles are required to be inputted by the user. In this section, we will discuss:

- *Background of ZONA7U*
- *Review of Piston theory and Third-Order theories*
- *Hypersonic Similitude*
- *Unified Hypersonic/Supersonic Lifting Surface method of ZONA7U*
- *AIC matrix of ZONA7U*

5.1 Background of ZONA7U

Exact unsteady supersonic three-dimensional (3D) linear theory has been sufficiently developed for the treatments of lifting surfaces, e.g. the ZONA7 method. Nonetheless, the lifting surface method incorporated in ZONA7 is confined to flat-plate wing sections, in which no thickness effect can be accounted for. But such a thickness effect at moderate to high supersonic Mach number is of practical importance, for it should usually lower the predicted flutter speed.

The lifting surface method of ZONA7U adopts the unified supersonic and hypersonic lifting surface method ZONA51U (Ref 5.1). ZONA51U combines the supersonic lifting surface method of ZONA51 with a nonlinear correction matrix E_{ij} based on Donov & Linnell's uniformly-valid higher-order hypersonic/supersonic scheme. For aeroelastic applications, ZONA51U has been applied to various wing planforms with thickness distributions. Some of these are shown as follows:

- *Rectangular Wing with Thickness Profile*

Fig 5.1 presents the variation of generalized aerodynamic forces (C_{L_α}) with reduced frequency k for an oscillating wedge ($\sigma = 10$) at $M = 3.0$. Results of ZONA51 and ZONA51U are compared with that of the Euler-Perturbed Euler Characteristics (PEC) method (Ref 5.2). Good correlation is found between the results of ZONA51U and the Euler-PEC solution. Substantial departures exist between the ZONA51 and ZONA51U results throughout the frequency range, indicating clearly the persistent nonlinear thickness effect.

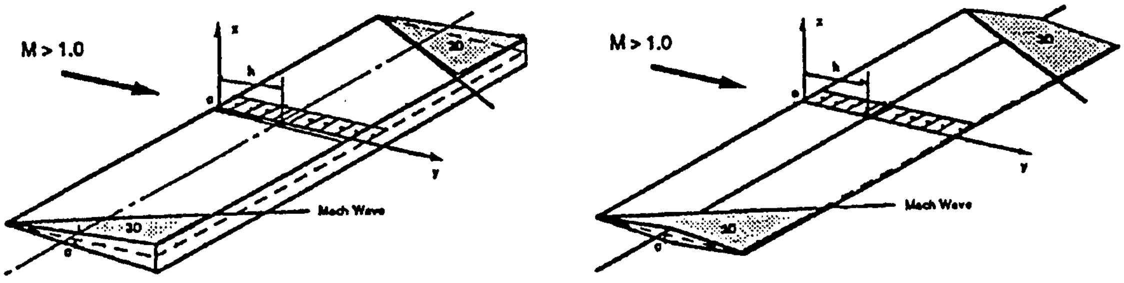

M > 1.0
x
h
o
y
Mach Wave
30
c
M > 1.0
x
h
o
y
Mach Wave
30
c

a) Wedge Profile

b) Diamond Profile

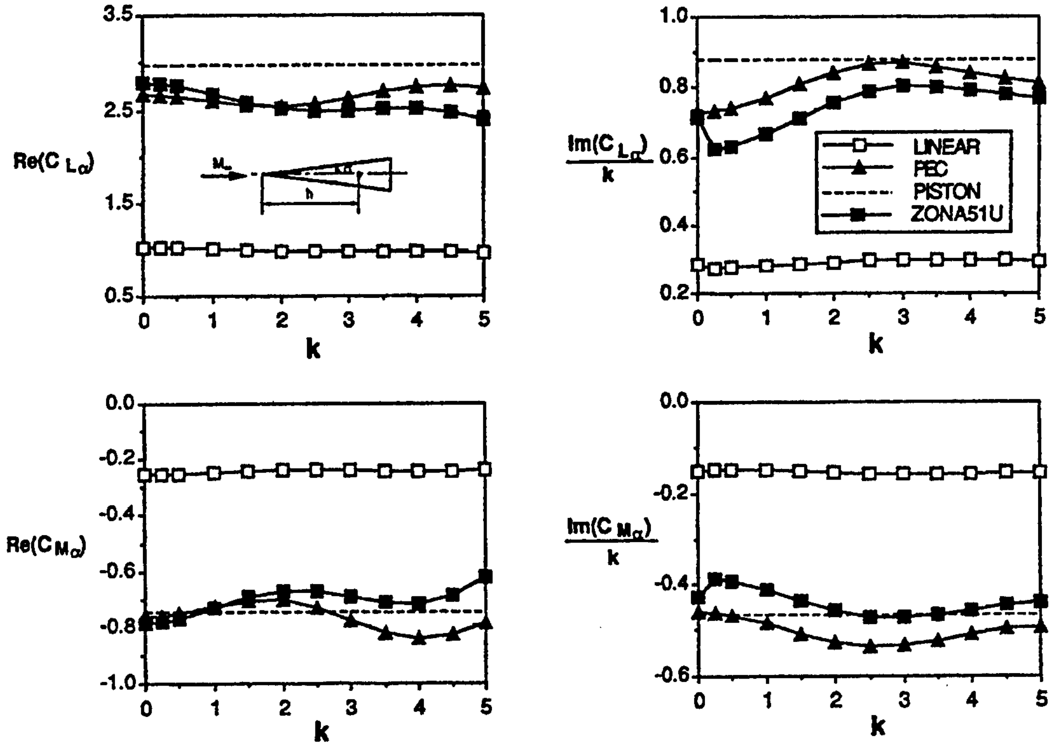

Fig 5.1 Stability Derivatives for an oscillating Wedge vs. Reduced Frequency: ($M = 3.0, h = 0.5c, \sigma = 10°$)

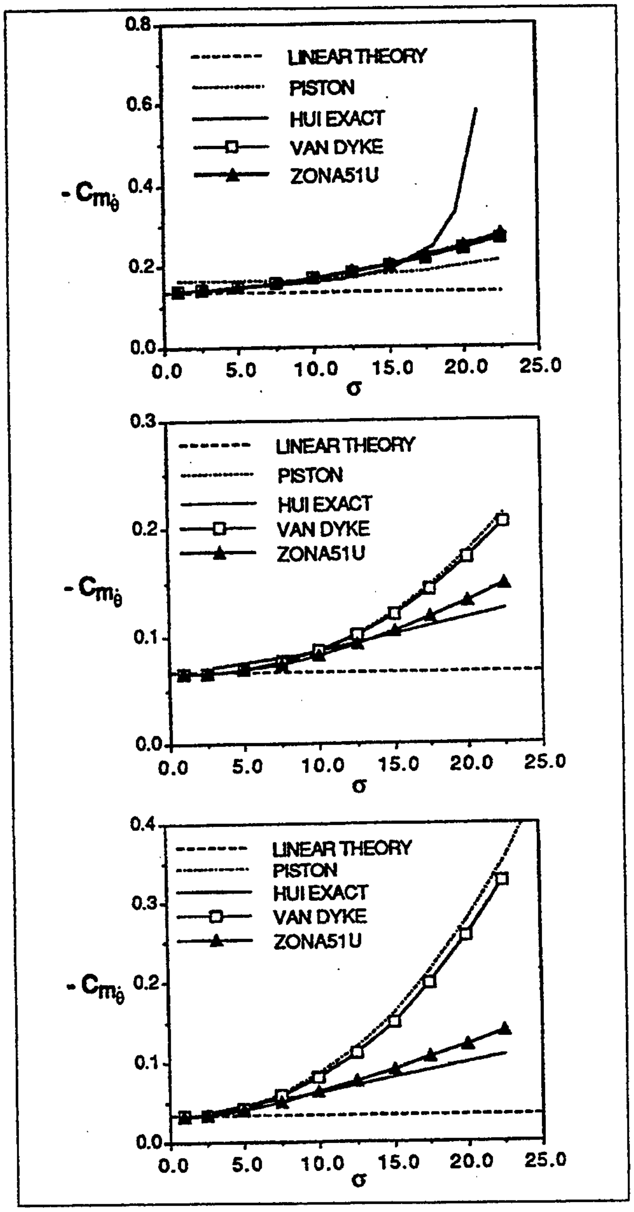

Fig 5.2 Damping-in-pitch $C_{m_{\dot\theta}}$ vs. Semiwedge Angle, $h = 0.5c$: $M =$ a) 5.0, b) 10.0

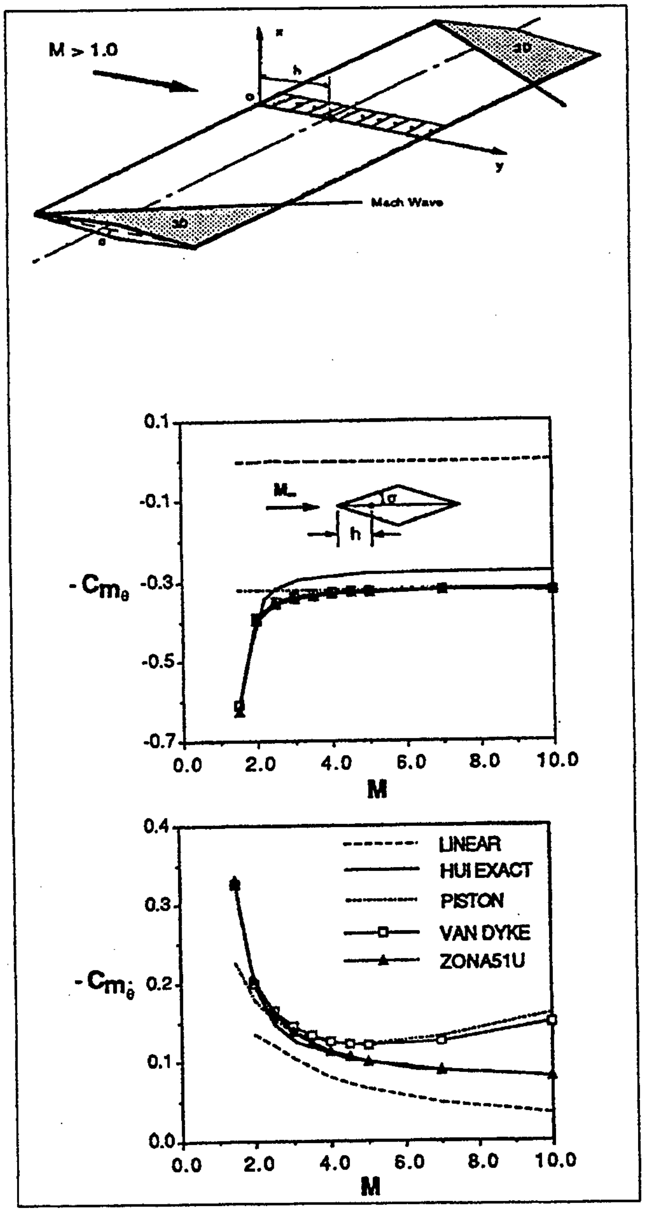

Fig 5.3 Stiffness Derivative C_{m_θ} and Damping-in-pitch Derivatives $C_{m_{\dot\theta}}$ vs. Semiwedge Angle, $h = 0.5c$: $M =$ a) 5.0, b) 10.0

Fig 5.2 presents the variation of damping-in-pitch derivative with wing thickness σ for a diamond airfoil section at $M = 2.0$, 5.0 and 10.0. For $M = 2.0$, nonlinear results of Van Dyke (Ref 5.3), Piston theory and ZONA51U agree well up to $\sigma = 15°$. When Mach number is increased to $M = 5.0$ and 10.0, all nonlinear results tend to over-predict the damping derivatives except that of ZONA51U. In fact, 51U yields results in close agreement with Hui's Exact Euler Solution (Euler-Hui, Ref 5.4) up to $\sigma = 15°$ for all Mach numbers considered. By contrast, the linear theory such as ZONA51 fails to account for the thickness effect.

Fig 5.3 presents the Mach number variation of the stiffness derivative and damping-in-pitch derivative for a diamond profile with thickness (σ=15°). It is seen that the ZONA51U results essentially follow the trend of the Euler-Hui solutions throughout the Mach range. Other nonlinear results begin to depart from the Euler solution around $M = 4.0$ and continue to diverge from it as the Mach number increases. In fact, among all of the above results, only results of ZONA51U and the Euler-Hui exact solution would correctly approach the Newtonian limit.

- *Panel Flutter*

Shown in Fig 5.4 are two flexible panels (membranes) mounted on both surfaces of a wedge (σ=2°). The motion of the oscillating panels is described by the assumed mode:

$$z = \varepsilon \sin\left(\frac{N\pi}{L}x\right) e^{ikt}$$

where $N = 2$ and ε is the amplitude of vibration.

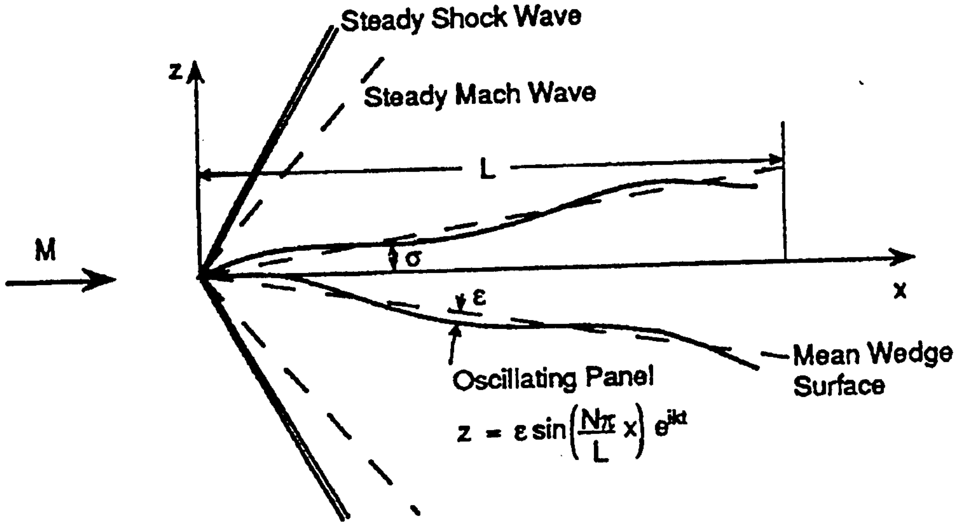

Fig 5.4 Oscillating Panels Mounted on a Wedge with Semi-Wedge Angle σ = 2°

Fig 5.5 presents the effect of reduced frequency on generalized aerodynamic forces for these vibrating panels at $M = 5.0$. Generalized Aerodynamic Forces (GAF) results in Q_{12}, based on the linear theory, Piston theory and ZONA51U are compared with the Euler-PEC solution. Similar to the earlier observation in the case of flap oscillation, ZONA51U in Fig 5.5 substantially improves the pressure magnitude over that of the linear theory. For the reason stated earlier, only slight improvement of the phase change is found in the present result. Once again, the results of Piston Theory show practically no phase change for all cases considered.

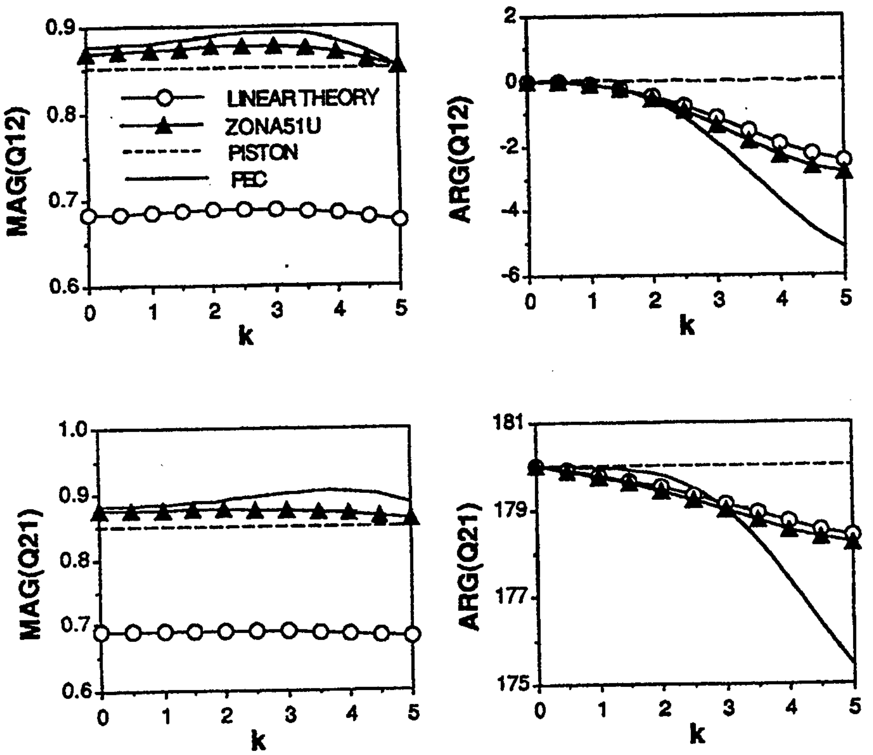

Fig 5.5 Effect of Reduced Frequency on Generalized Aerodynamic Forces for Oscillating Panels ($M = 5.0, \sigma = 2°, N = 2$)

- *SAAB Canard-Wing*

Shown in Fig 5.6 is the aerodynamic model of a SAAB Canard-Wing combination. Biconvex airfoil sections of 6% in thickness are assumed for both canard and wing. Two modes, the wing plunging and the canard pitching about its midchord, are considered.

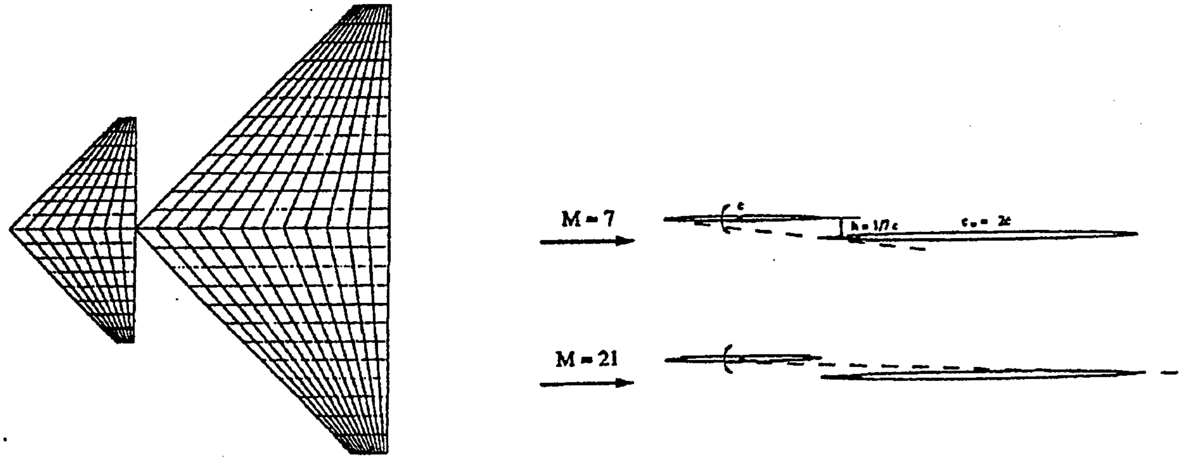

Fig 5.6 Paneling Scheme of SAAB Canard-Wing

In Fig 5.7, variation of generalized aerodynamic forces Q_{12} with Mach number is presented at three reduced frequencies, $k = 0.01$, 0.5 and 2.0. It is seen that the trends of Q_{12} due to ZONA51U is different from that of the linear theory in the hypersonic range (between $M = 5.0$ and $M = 20.0$) showing strong canard-wing aerodynamic interaction. This range is found to be related to the canard-wing dimensions. As can be seen from Fig 5.6, such interaction is expected to vanish when the hypersonic Mach number is increased up to $M = 21$, where the first Mach wave of canard detaches from the wing trailing edges.

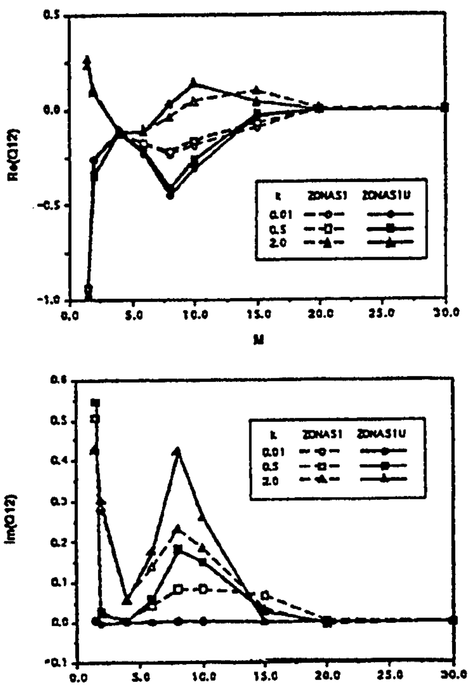

Fig 5.7 GAF Q_{12} of SAAB Canard-Wing vs. Mach Number: Mode 1 Wing Plunging and Mode 2 Canard Pitching about Midchord

- *Wing Flutter*

Two wing planforms are selected for performing flutter analysis using ZONA51U: a 70-degree delta wing and a 15-degree swept untapered wing.

- *70-Degree Delta Wing*

Fig 5.8a presents flutter boundaries for a 70-degree delta wing with a 6% thick diamond airfoil section computed by ZONA51U and Piston theory.

The flutter experiment was carried out at NASA Langley by Hanson and Levey (Ref 5.5). The wing model used was essentially a flat-plate. According to Ref 5.5, four measured modes are used in the present flutter analysis. Half of the delta planform is subdivided into 10 x 10 panels. The flutter boundary consists of the flutter points obtained for six Mach numbers ($M = 1.19$, 1.30, 1.64, 2.0, 2.25 and 3.0). Flutter results computed by CAP-TSD (Ref 5.6), Piston theory, ZONA51 and ZONA51U are compared with the measured data. Several observations on Fig 5.8a can be put forth:

- ZONA51U predicts flutter boundary that is more conservative than that of ZONA51 indicating that the thickness effect indeed reduces the supersonic flutter speed. Piston theory on the other hand tends to over-predict the flutter speeds.
- In fact, ZONA51U predicts the most conservative flutter boundary among all methods considered. Flutter boundary of CAP-TSD, on the other hand, appears to be the most non-conservative.

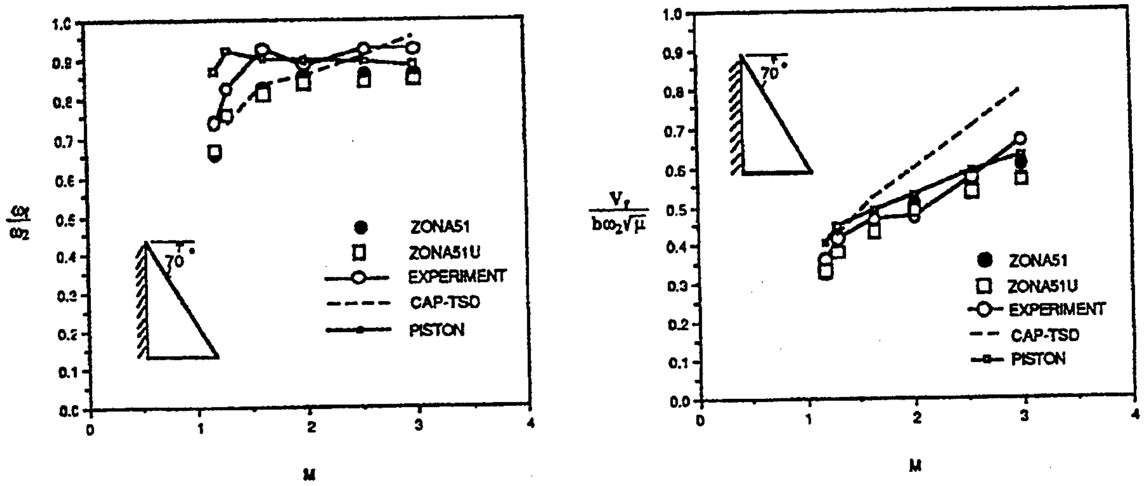

Fig 5.8a Flutter Speeds and Frequencies vs. Mach Number Predicted by Various Methods: 70° Delta Wing with and without Thickness

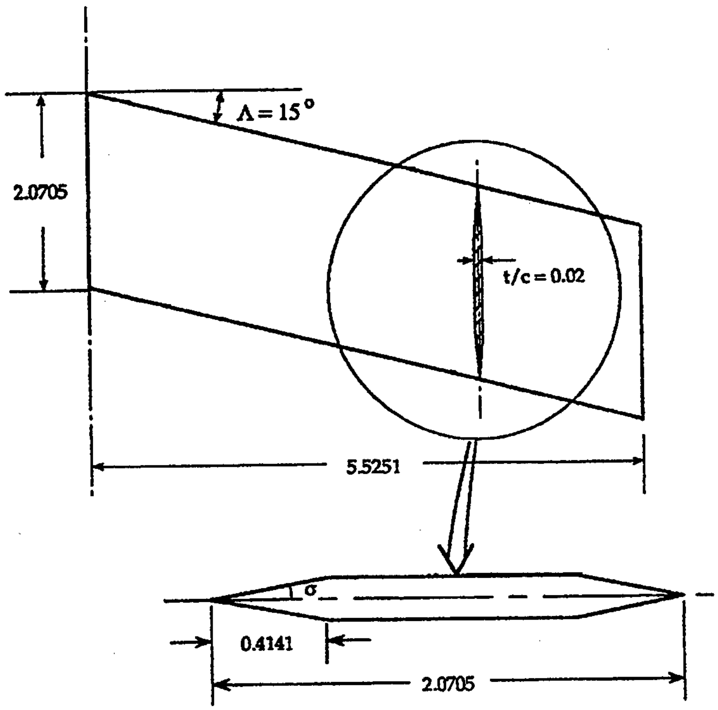

	$M = 1.3$		$M = 3.0$	
	V_f (ft/s)	f_f (Hz)	V_f (ft/s)	f_f (Hz)
Test [24]	1280	102	2030	146
Rodden [25]	1397	124	1913	149
ZONA51	1547	127	2159	148
ZONA51U	1487	124	2014	146

Fig 5.8b Flutter Speed and Flutter Frequency for a 15° Swept Untapered Wing (M = 1.3 and 3.0)

- *15-Degree Swept Untapered Wing*

Fig 5.8b presents two computed flutter points for a 15-degree swept untapered wing of aspect ratio $AR = 5.35$ at $M = 1.3$ and $M = 3.0$.

The flutter experiment was carried out at NASA Langley Field by Tuovila and McCarty (Ref 5.7). The wing model used is a cantilever wing with a 2% thick hexagonal airfoil section. According to Ref 5.7, eight modes generated by MSC/NASTRAN are used in the present flutter analysis. Half of the wing planform is subdivided into 10 x 10 panels.

Computed results of ZONA51, Rodden's method (Ref 5.8) (employing ZONA51), and ZONA51U are compared with test data of Tuovila and McCarty. Note that Rodden's method adopts coefficients from Van Dyke's theory and Piston theory and corrects upon results of ZONA51. While the predicted flutter speeds due to Rodden and ZONA51U are slightly non-conservative at $M = 1.5$, both are conservative at $M = 3.0$. Overall, the listed results confirms once again the impact of thickness on flutter speed. The linear theory, as computed by ZONA51, yields non-conservative flutter points at both Mach numbers.

5.2 Review of Piston Theory

Subsequent to the original publication of Lighthill (Ref 5.9), Ashley and Zartarian (Ref 5.10) first proposed the application of Piston Theory for flutter analysis and other aeroelastic applications. They found that the nonlinear thickness effect provided by the theory indeed results in a more conservative flutter boundary, which was validated by measured data. Based on a criterion that if any one of the conditions holds, namely:

$$M^2 >> 1, \qquad kM^2 >> 1 \qquad \text{or} \qquad k^2M^2 >> 1 \tag{5.1}$$

Landahl, Ashley and Mello-Christiansen (Ref 5.11) further established a consistent linearized Piston Theory. With this theory, they obtained an explicit flutter solution for a typical two dimensional wing section. The flutter speed according to their theory approaches those predicted by the exact linear theory (Ref 5.12) as the Mach number increases, whereas they tend to depart from the latter as the Mach number decreases toward unity.

Originally, Lighthill's Piston Theory accounts for the effect of the nonlinear thickness in the high Mach number range such that $M^2 >> 1$. It imposes the condition that the magnitude of the piston velocity never exceeds the speed of sound in the undisturbed fluid. The aerodynamics of this analogy is to state that:

$$M\delta < 1 \qquad \text{and} \qquad kM\delta < 1 \tag{5.2}$$

where δ is the thickness or oscillatory amplitude of the airfoil, whichever is the larger; and k is the reduced frequency defined as $k = \dfrac{\omega L}{U_\infty}$.

According to his large-Mach-number expansion theory, Landahl (Ref 5.13) pointed out that Piston Theory amounts to ignoring a second order term in his linear amplitude sequence. Hence, the valid range of Mach number for Piston Theory can be defined by the criterion:

$$\delta^{-1/3} < M < \delta^{-1} \qquad \text{and} \qquad M^2 >> 1 \tag{5.3}$$

In terms of Tsien's Hypersonic Similarity parameter (Ref 5.14) K, where $K = M\delta$, Eq 5.3 reads:

$$\delta^{2/3} < K < 1 \tag{5.4}$$

For a wedge of semi-angle σ=10°, K falls in the range of $0.31 < K < 1.0$. Inspection of results obtained in Fig 5.9 shows that the valid lower bound of the Mach numbers is really more restrictive than the above criterion so indicated, whereas the upper bound $K < 1$ is less restrictive.

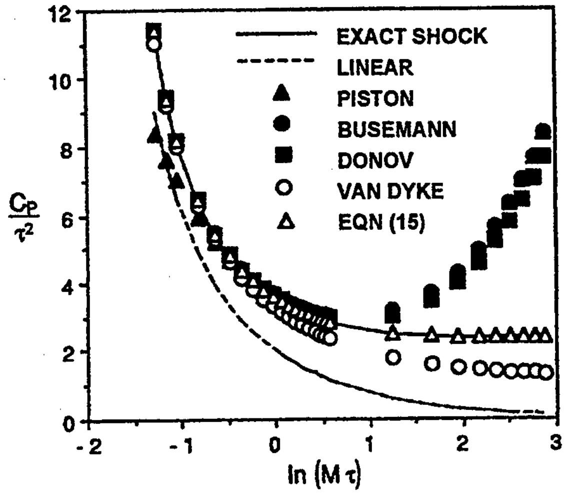

Fig 5.9 Surface Pressure of a Wedge According to Various Supersonic/Hypersonic Models: $\tau = \tan 10°$; $\gamma = 1.4$

While the condition $K < 1$ for Piston Theory may be somewhat relaxed to include regions near $K \approx 1.0$, the condition $kK < 1$ of Eq 5.2 is a rather stringent one. For unsteady hypersonic flow, if $K \approx O(1)$ then the reduced frequency k must be kept very small. The failure of Piston Theory in the moderate to high range of k is evidenced by the Panel Flutter results presented in the work of Chavez and Liu (Ref 5.2).

Following the suggestion of Morgen, Herchel and Runyan (Ref 5.15), Rodden and Farkes (Ref 5.16) have arrived at a generalized expression for the pressure coefficients, i.e.:

$$C_P = \frac{2}{M^2}\left[c_1\left(\frac{w}{a_o}\right) + c_2\left(\frac{w}{a_o}\right)^2 + c_3\left(\frac{w}{a_o}\right)^3\right] \tag{5.5}$$

where w represents the piston upwash.

For Piston Theory:

$$c_1 = 1, \qquad c_2 = \frac{\gamma+1}{4}, \qquad c_3 = \frac{\gamma+1}{12} \tag{5.6}$$

For Van Dyke's second order theory (Ref 5.17):

$$c_1 = \frac{M}{m}, \qquad c_2 = \frac{M^4(\gamma+1) - 4m^2}{4m^4} \tag{5.7}$$

where $m^2 = M^2 - 1$, and γ is the ratio of specific heats.

A modified Piston Theory is recommended to replace c_1 and c_2 of Eq 5.6 by that of Eq 5.7 rendering an extension to the lower Mach number region.

The c_1 and c_2 of Van Dyke in fact were first obtained by Busemann (Ref 5.18), in which he also included a third-order term based on a consistent expansion of the simple wave theory, i.e.:

$$c_3 = \frac{1}{6m^7}\left\{a_o M^8 + b_o M^6 + c_o M^4 + d_o M^2 + e_o\right\} \tag{5.8}$$

where:

$$a_o = \gamma + 1, \qquad b_o = 2\gamma^2 - 7\gamma - 5, \qquad c_o = 10(\gamma + 1)$$

$$d_o = -12, \qquad e_o = 8$$

Following Busemann, Donov (Refs 5.18, 5.19) further developed a comprehensive theory in which he obtains series expansion solution up to the fourth-order term accounting separately for the isentropic part and the rotational part due to simple wave and shock wave respectively. Here, Donov's third-order term including shock wave, also derived independently by Carafoli (Ref 5.20), reads:

$$c_3 = \frac{1}{6Mm^7}\left\{aM^8 + bM^6 + cM^4 + dM^2 + e\right\} \tag{5.9}$$

where:

$$a = 3\left(\frac{\gamma+1}{4}\right)^2, \qquad b = \frac{3\gamma^2 - 12\gamma - 7}{4}, \qquad c = \frac{9(\gamma+1)}{2}$$

$$d = -6, \qquad e = 4$$

In passing, it is noted that through a different approach Kahane and Lees (Ref 5.21) have obtained a correction term to c_3 of Eq 5.8 resulting in essentially the same c_3 as that Eq 5.9. Therefore, a consistent choice of C_P would be to adopt Donov's series and Busemann's series for flow compression and expansion respectively.

In the analysis that follows, we remain to adopt Lighthill's Piston Theory, Eq 5.6, in order to simplify the present approach.

For unsteady flow applications, Eq 5.6 is recast into the form of pressure differential of the upper and the lower wing surfaces, i.e. $\Delta C_P = C_{P_{lower}} - C_{P_{upper}}$, and the piston velocity w / U_∞ is represented by two terms, i.e. $w / U_\infty = w_o + w_1$, where w_o denotes the thickness distribution of the wing and w_1 the downwash. Thus, the total pressure differential $\Delta \overline{C}_P$ can be expressed as:

$$\Delta \overline{C}_P = \Delta C_{P_o} + \Delta C_P \tag{5.10}$$

and up to the third-order term:

$$\Delta C_{P_o} \cong \frac{2}{M^2} \sum_{n=1}^{3} c_n M^n \left(\Delta w_o\right)^{(n)} \tag{5.10a}$$

and:

$$\Delta C_P \cong \frac{4 w_1}{M^2} \sum_{n=1}^{3} n\, c_n M^n \left(\Delta \overline{w}_o\right)^{(n-1)} + \left(6 w_1^{\,2} \Delta w_o^{(1)} + 4 w_1^{\,3}\right) c_3 M \tag{5.10b}$$

where:

$$\begin{aligned} \left(\Delta w_o\right)^{(n)} &\equiv w_{o_{lower}}^{\;n} - w_{o_{upper}}^{\;n} \\ \left(\Delta \overline{w}_o\right)^{(n)} &\equiv \frac{w_{o_{lower}}^{\;n} + w_{o_{upper}}^{\;n}}{2} \end{aligned} \tag{5.10c}$$

For non lifting airfoil sections, where $\left(w_o\right)_l = \left(w_o\right)_{u'}$. Eq 5.10b reduces to the expression:

$$\Delta C_P = \frac{4}{M}\left[\left(c_1 + 2 c_2 M w_o + 3 c_3 M^2 w_o^{\,2}\right) w_1 + \left(c_3 M^2\right) w_1^{\,3} \right] \tag{5.11}$$

Substituting Eq 5.6 into Eq 5.11 and dropping the higher order terms in w_1 yields the linear amplitude version of Piston Theory as a special case, i.e.:

$$\Delta C_P = \left[\frac{4}{M} + 2\left(\gamma + 1\right) w_o + \left(\gamma + 1\right) M w_o^{\,2} \right] w_1 \tag{5.12}$$

We shall use the above expression to develop the Unified Lifting Surface Method.

5.3 Hypersonic Similarity for Thickness Effects

A classical Hypersonic Similarity (Ref 5.22) can be expressed as:

$$C_p = \frac{2}{M^2} fn(K,\gamma) \tag{5.13}$$

where:

$$fn = \frac{1}{\gamma}\left\{\left[1 + \frac{\gamma - 1}{2}K\right]^{\frac{2\gamma}{\gamma - 1}} - 1\right\} \tag{5.13a}$$

is the universal function due to the Prandtl-Meyer expansion, and:

$$fn = K^2\left\{\left[\left(\frac{\gamma+1}{4}\right)^2 + \frac{1}{K^2}\right]^{\frac{1}{2}} + \frac{\gamma+1}{4}\right\} \tag{5.13b}$$

is the universal function due to oblique shock waves, where $K = M\delta$ or $M\tau$.

Clearly, Eq 5.13a is the basis of Lighthill's Piston Theory and hence of Eq 5.5. Eq 5.13b was established by Tsien (Ref 5.14) and Linnell (Ref 5.23). When Eq 5.13b is expanded up to the third-order term, the coefficient c_3 corresponding to Eq 5.6 reads:

$$c_3 = \frac{(\gamma+1)^2}{32} \tag{5.14}$$

This is to say that the departure between Eqs 5.13a and 5.13b starts from the third-order term and the difference of which amounts to $\Delta c_3 = \frac{(3\gamma^2 - 2\gamma - 5)}{96} < 0$, representing the difference in rotationality due to shock wave.

It is desirable to extend the previous third-order theories into the hypersonic flow regime where $K \geq O(1)$. Close examination of them reveals that the C_p's of these third-order theories diverge drastically as K increases toward the Newtonian limit (Fig 5.9).

Second-order theories, on the other hand, usually result in one half the value of Newtonian pressure, whereas C_p of Linear theory vanishes at the Newtonian limit.

It is clear that Piston Theory does not yield the correct limit in the low supersonic end, nor does it approach the Newtonian limit in the hypersonic end. Fig 5.9 shows that Piston Theory has a limited valid range of *ln K* between roughly say –1 to at most 0.5 ($0.368 < K < 1.05$), for a wedge of semi-angle equal to 10°.

Clearly, the status of the previous third-order theories warrants further establishment of one that is uniformly valid and covers both the supersonic and hypersonic limits. In the present development we have established such a uniformly valid solution by means of a strained parameter technique in the unified supersonic-hypersonic domain. The resulting C_p's are two composite functions, one for the compression waves and the other for the expansion waves, which can be generally recast into a pseudosimilar form as:

$$\frac{C_P}{\tau^2} = f_c(K, \gamma; c_1, c_2, c_3) \tag{5.15}$$

provided that the coefficients c_1, c_2 and c_3 could be suitably chosen from the appropriate third-order theories.

5.4 Unified Supersonic/Hypersonic Lifting Surface Method of ZONA7U

The matrix equation for solving ΔC_p on wing-like components of ZONA7U can be expressed as:

$$\mathbf{w}_i = \mathbf{D}_{ij}\, \Delta C_{p_j} \tag{5.16}$$

where $\mathbf{w}_i$ is the downwash i^{th} wingbox due to structural oscillation $\{\mathbf{w}_i\} = \mathbf{F}_w$, $\mathbf{F}_w$ is expressed in Eq 3.26. $\mathbf{D}_{ij}$ is the normal velocity influence coefficients. $[\mathbf{D}_{ij}] = [NIC]_{WW}$, $[NIC]_{WW}$ is expressed in Eq 3.51 and ΔC_p is the unsteady pressure difference between the lower and upper surface of the ith wingbox.

It has been shown that in Ref 5.1 that a unified *NIC* matrix can be constructed by superposing a "nonlinear" matrix $\mathbf{E}_{ij}$ onto the matrix $\mathbf{D}_{ij}$ based on the principle of amplitude perturbation, i.e.

$$\mathbf{w}_i = [\mathbf{D}_{ij} + \mu_{ij}\, \mathbf{E}_{ij}]\Delta C_{P_j} \tag{5.17}$$

The matrix $\mathbf{E}_{ij}$ is "nonlinear" in the sense that it contains effects due to nonlinear functions in wing thickness τ or flow incidence α_o. These nonlinear effects include shock-induced rotationality or local flow expansions.

There are a number of approaches that could provide the $\mathbf{E}_{ij}$ matrix. For example, a stripwise solution could be provided by the Perturbed Euler Characteristic method (Euler-Pec method, Ref 5.2). However, the simplest and most expedient approach is to adopt the concept of Hayes-Lighthill's Piston theory. In so doing, it is required that $\mathbf{E}_{ij}$ be a diagonal matrix whose elements is related to two nonlinear functions in w_o:

$$\begin{aligned}\mathbf{E}_{ii}^{-1} &= f(w_o;\gamma,M,K) \\ &= g(w_o;\gamma,M,K)\end{aligned} \tag{5.18}$$

where w_o is the local thickness function at the ith wingbox, γ is the ratio of specific heat of gas and $K\,(=M\tau)$ is Tsien's hypersonic similarity parameter (Ref 5.14). The functions f and g are uniformly-valid solutions in the unified supersonic-hypersonic domain for compression and expansion surfaces, respectively. By means of strained coordinate technique (Ref 5.24), the function f is derived by matching the Newtonian impact solution with then Donov-Linell series for flow compression (Ref 5.19), and the function g with the Busemann-Lighthill series for flow expansion (Ref 5.18). Hence, the parameter μ_{ij} (Eq 5.17) is a local switching operator on $\mathbf{E}_{ij}$ for suitable adaptation of function f or g on each panel. It should be noted that Eq 5.17 contains piston theory as a special case, in which $\mathbf{D}_{ij} = 0$, $\mu_{ij} = 1$ and $\mathbf{E}_{ij}$ reduces to:

$$\mathbf{E}_{ii}^{-1} = g(w_o) = \frac{4}{M} + 2(\gamma+1)\,w_o + M(\gamma+1)\,w_o^{\,2} \tag{5.19}$$

As commented in Ref 5.1, Piston theory inherits two undesirable features. First, it is strictly one-dimensional model which provides no upstream influence whatsoever. Second, its applicability in Mach number range is ambiguous for it does not approach the Ackeret limit in the low supersonic end, nor does it approach the Newtonian limit in the hypersonic end. By contrast, the present unified solution contains both limits. In the Newtonian limit, where M approaches infinity and γ approaches unity simultaneously, $\mathbf{E}_{ij}$ reduces, as expected, to:

$$\begin{aligned}\mathbf{E}_{ii}^{-1} &= f(w_o) = 2\,w_o^{\,2} \quad \text{and} \\ \mathbf{E}_{ii}^{-1} &= g(w_o) = 0\end{aligned} \tag{5.20}$$

The inadequacy of Piston Theory can be seen in the case of an oscillating flap.

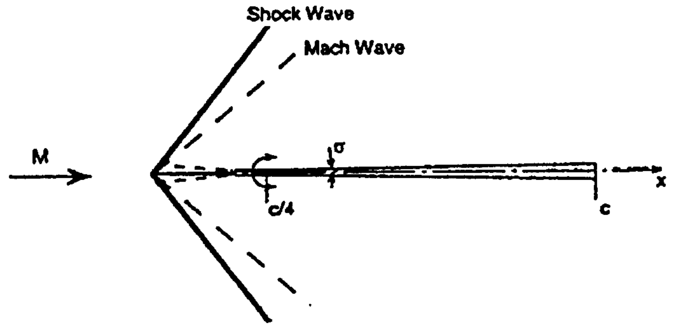

Fig 5.10 Oscillating Leading-Edge Flap os a Thin Wedge Airfoil: σ = 2°

Fig 5.10 shows an oscillating leading edge flap of thin wedge profile ($\sigma = 2$) with a hinge line located at the quarter chord. Fig 5.11 shows the magnitude and phase angle of the unsteady pressure along the profile at $M = 5.0$ and $k = 0.5$. The pressure magnitude on the flap predicted by ZONA 51U is in good agreement with Euler-Pec solution. However, the phase angle of ZONA51U follows essentially that of the linear theory, which disagrees with the Euler-Pec solution. This is expected in that the nonlinear functions *f* and *g* of Eq 5.18 only contribute to self-influenced elements of $\mathbf{E}_{ij}$, an inherent feature of Piston theory where $\mathbf{D}_{ij} = 0$, it essentially provides no phase change; hence, its prediction is inadequate for the present case.

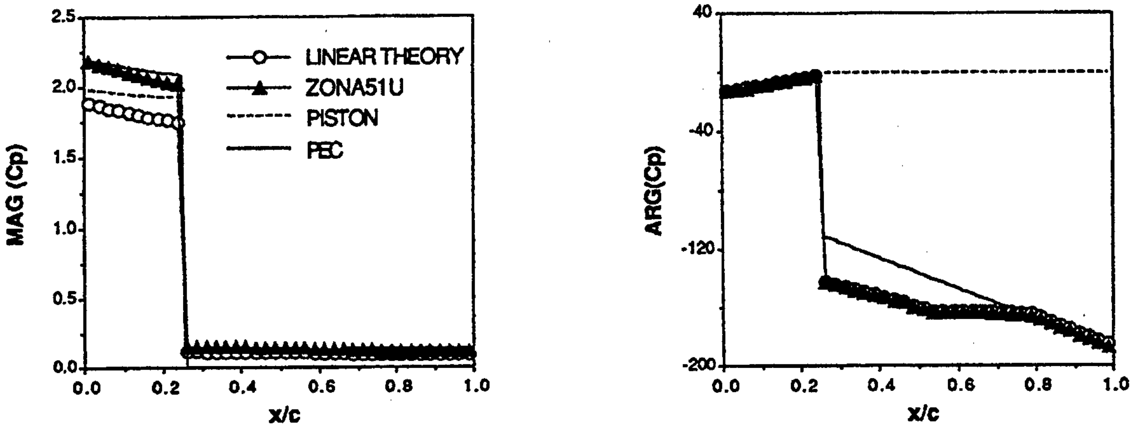

Fig 5.11 Unsteady Pressure Distribution for an Oscillating Leading Edge Flap with Hinge Line at Quarter Chord: ($M = 2.4$, $k = 0.5$, $\sigma = 3°$)

5.5 *AIC* Matrix of ZONA7U for Hypersonic Wing-Body Configuration

The inclusion of the nonlinear matrix $\mathbf{E}_{ij}$ in the $[NIC]_{\mathrm{WW}}$ matrix suggests that the total normal velocity influence coefficient matrix for wing-body configuration in Eq 3.49a can be modified as:

$$\begin{bmatrix} [NIC]_{\mathrm{BB}} & [NIC]_{\mathrm{WB}} \\ [NIC]_{\mathrm{BW}} & [NIC]_{\mathrm{WW}} + [\mu_{ij} \cdot \mathbf{E}_{ij}] \end{bmatrix} \begin{Bmatrix} \sigma \\ \Delta C_{\mathrm{p}} \end{Bmatrix} = \begin{Bmatrix} \mathbf{F}_{\mathrm{B}} \\ \mathbf{F}_{\mathrm{W}} \end{Bmatrix} \tag{5.21}$$

Since solving σ and ΔC_{p} in Eq 5.21 requires the matrix inversion of the modified *NIC*, the nonlinear matrix $\mathbf{E}_{ij}$ indeed gives a nonlinear relationship of ΔC_{p} and the thickness effect. Also, the procedures for *AIC* generation described in Sec 3 can be directly adopted for ZONA7U. This leads to the *AIC* matrix of ZONA7U to be in the same form of that of ZONA7.

6.0 SPLINE METHODS FOR SPLINE MATRIX GENERATION

Aeroelastic analysis, as an interdisciplinary problem, requires the coupling of the aerodynamic and structural responses. In practice, the requirements to generate the discretized models of these disciplines are subject to different engineering considerations. The grid of the discretized aerodynamic model is usually placed on the external surface, whereas that of the structural model is placed on the internal load-carry component. This gives rise to the data-transferred problem between two computational grid systems. This would amount to the proper transferal of the displacements computed in the structural grid to the aerodynamic grid and that of loads from the aerodynamic grid to the structural grid. The development of a suitable methodology for solving this type of data transferal problem is by no means a trivial task. In fact, such a methodology should be further developed as the aerodynamic and/or structural methods advance.

ZAERO resolves this data transferal problem by mean of providing a spline matrix that relates or interpolates the displacements at the structural finite element grid points to the control points of aerodynamic boxes. This spline matrix is generated by a spline module in ZAERO that contains four spline methods namely the beam spline method, infinite plate spline (IPS) method, thin-plate spline (TPS) method and the rigid-body attachment method. These four methods jointly assemble the total spline matrix **G** expressed in Eq 2.15, repeated below:

$$\mathbf{h} = \mathbf{G}\,\mathbf{x}$$

where **h** is the "interpolated" displacement vector at aerodynamic boxes, including the translational displacements and their slopes with respect to **x**. Specifically, **h** is in the order of *K-set* defined in Eq 3.60, repeated below:

$$\{\mathbf{h}\}_{K\text{-set}} = \left\{ \begin{matrix} \vdots \\ \left\{ \begin{matrix} h_x \\ h_y \\ h_z \\ h'_x \\ h'_y \\ h'_z \end{matrix} \right\}_i \\ \vdots \end{matrix} \right\}$$

where:

i represents the index of the ith aerodynamic box

G is the total spline matrix relating **h** to **x**

x is the displacement vector defined at the structural finite element grid points and $(\ )'$ denotes the derivatives of $(\ )$ with respect to $\left(\frac{x}{L}\right)$, L is the reference length.

Usually, each structural finite element grid point has six degrees of freedom (d.o.f.); namely T_1, T_2 and T_3 for translational displacement as well as R_1, R_2 and R_3 for rotational displacement along x, y and z directions. Thus, for n grid points there are 6 x n degrees of freedom. These 6 x n degrees of freedom are defined as *G-set* d.o.f. that can be expressed as:

$$\{\mathbf{x}\}_{G\text{-set}} = \left\{ \begin{matrix} \vdots \\ \left\{ \begin{matrix} T_1 \\ T_2 \\ T_3 \\ R_1 \\ R_2 \\ R_3 \end{matrix} \right\}_i \\ \vdots \end{matrix} \right\}$$

where i represents the index of the ith structural finite element grid point.

Once the spline matrix **G** is generated, the force transferal from the aerodynamic boxes to the structural finite element grid points (from *K-set* to *G-set*) can be achieved by the transpose of matrix **G**. This has been shown in Eq 2.16, repeated below:

$$\{\mathbf{F}_{\mathrm{a}}\}_{G\text{-set}} = [\mathbf{G}]^{\mathrm{T}}\ \{\mathbf{F}_{\mathrm{h}}\}_{K\text{-set}}$$

In this section, we will discuss the theoretical derivation of:

- *Infinite Plate Spline (IPS) method*
- *Thin-Plate Spline (TPS) method*
- *Beam Spline method*
- *Rigid-Body Attachment (RBA) method*
- *Matrix Assembly of the Total Spline Matrix*

6.1 The Infinite Plate Spline (IPS) Method

The IPS method was first proposed by Harder and Desmarais (Ref 6.1), which was a significant improvement over the two-dimensional (2D) interpolation method of Rodden (Ref 6.2). This development was motivated by the advent of lifting surface methods in aerodynamics at that time, which required a 2D interpolation method such as IPS. The 2D surface is defined as the plane of the lifting surface. Therefore, IPS is ideally suited for displacements and forces transferal of wing-like components. Today, IPS is one of the more popular method of interpolation used in aerospace industry.

Consider a set of N discrete structural grid points (x_i, y_i), for $i = 1, 2, \ldots, N$ lying within a 2D domain with Cartesian coordinates x and y. Each grid point defines the vertical position coordinate of the "deformed" surface. IPS solves the partial differential equation of equilibrium for an infinite plate with uniform thickness. The deformation of the infinite plate satisfies the given deflection $w_i(x_i, y_i)$ at the N structural grid points. Once the partial differential equation is solved, the deflection at other points, for instance the aerodynamic points, on the plate can be determined.

The governing equation of an infinite plate with bending stiffness reads:

$$D\nabla^4 W = q \tag{6.1}$$

where W is the plate deflection, D is the plate bending rigidity, and q is the distributed load on the plate. Introducing polar coordinates, $x = r\cos\theta$, $y = r\sin\theta$, so that ∇^4 in polar coordinates is given by:

$$\nabla^4 = \frac{1}{r}\frac{d}{dr}\left\{ r\frac{d}{dr}\left[\frac{1}{r}\frac{d}{dr}\left(r\frac{dw}{dr} \right) \right] \right\} \tag{6.2}$$

and considering the deflection due to a point load P at the origin of the coordinate system, a solution of Eq 6.1 can be written as:

$$W(r) = A + Br^2 + \left(\frac{P}{16\pi D} \right) r^2 \ln r^2 \tag{6.3}$$

where A and B are undetermined coefficients.

For N point loads at the given location (x_i, y_i), for $i = 1, 2, \ldots, N$ in the 2D space, the total deflection can be obtained by superimposing the fundamental solution of Eq 7.1 such that:

$$W(x,y) = \sum_{i=1}^{N} \left(A_i + B_i r_i^2 + F_i r_i^2 \ln r_i^2 \right) \tag{6.4}$$

where:

A_i, B_i and $F_i = \dfrac{P_i}{16\pi D}$ are undetermined coefficients,

and:

$$r_i^2 = (x - x_i)^2 + (y - y_i)^2$$

For the purpose of determining these undetermined coefficients one needs to use certain information about the solution. Harder and Desmarais showed that by expanding Eq 6.4 for large values of r, one obtains terms of order r^2, r, 1, $1/r$, etc., along with terms of order $r^2 \ln r^2$, $r \ln r^2$, $\ln r^2$, etc.:

$$W(r,\theta) = r^2 \ln r^2 \sum_{i=1}^{N} F_i + r^2 \sum_{i=1}^{N} B_i - 2r \ln r^2 \sum_{i=1}^{N} (x_i \cos\theta + y_i \sin\theta) F_i$$
$$- 2r \sum_{i=1}^{N} (x_i \cos\theta + y_i \sin\theta)(F_i + B_i) + \ln r^2 \sum_{i=1}^{N} (x_i^2 + y_i^2) F_i + \ldots \tag{6.5}$$

For removing the singularity at $r = \infty$, coefficients of the terms of order r^2, $r^2 \ln r^2$ and $r \ln r^2$ must vanish. This gives:

$$\sum_{i=1}^{N} F_i = 0 \tag{6.6}$$

$$\sum_{i=1}^{N} x_i F_i = 0 \tag{6.7}$$

$$\sum_{i=1}^{N} y_i F_i = 0 \tag{6.8}$$

$$\sum_{i=1}^{N} B_i = 0 \tag{6.9}$$

Here Eq 6.6 can be recognized as the discrete force equilibrium equation, which eliminates terms of order $r^2 \ln r^2$. Eqs 6.7 and 6.8 are discrete moment equilibrium equations and eliminate terms of order $r \ln r^2$. Finally, Eq 6.9, the physical significance of which is not clear, serves to eliminate terms of order r^2.

Eqs 6.6 through 6.9 result in linear deflection at infinity. For extrapolation, this implies that linear deflection of the aerodynamic points occurs only if they are located far from the domain of the structural grid points. A solution to the general spline problem, formed by superimposing solutions of Eq 6.1, is given by:

$$w(x,y) = a_o + a_1 x + a_2 y + \sum_{i=1}^{N} K_i(x,y) F_i \tag{6.10}$$

where:

$$K_i(x,y) = r_i^2 \ln r_i^2$$

$$r_i^2 = (x - x_i)^2 + (y - y_i)^2$$

where a_o, a_1 and a_2 are unknowns given by:

$$a_o = \sum_{i=1}^{N} \left[A_i + B_i \left(x_i^2 + y_i^2\right)\right] \tag{6.11}$$

$$a_1 = -2 \sum_{i=1}^{N} B_i \, x_i \tag{6.12}$$

$$a_2 = -2 \sum_{i=1}^{N} B_i \, y_i \tag{6.13}$$

Note that the $N+3$ unknowns in Eq 6.10 can be determined from application of side conditions found in Eqs 6.6 – 6.8 along with setting the deflection at the ith point to its known value W_i. Viz.,

$$W_i = a_o + a_1 x_i + a_2 y_i + \sum_{j=1}^{N} K_{ij} F_j \qquad \text{for } i = 1, 2, \ldots, N \tag{6.14}$$

where:

$$\begin{aligned} K_{ij} &= r_{ij}^2 \ln r_{ij}^2 \\ r_{ij}^2 &= (x_i - x_j)^2 + (y_i - y_j)^2 \end{aligned} \tag{6.15}$$

is the square of the distance between known points (x_i, y_i) and (x_j, y_j).

Eq 6.14 and the side conditions found in Eq 6.6 – 6.8 can now be expressed in matrix form as:

$$\{\mathbf{W}\} = [\mathbf{R}]\{\mathbf{a}\} + [\mathbf{K}_{ij}]\{\mathbf{F}\} \tag{6.16}$$

and:

$$[\mathbf{R}]^{\mathrm{T}} \{\mathbf{F}\} = 0 \tag{6.17}$$

where:

$$\{\mathbf{W}\} = \begin{Bmatrix} W_1 \\ W_2 \\ \vdots \\ W_N \end{Bmatrix}, \qquad \{\mathbf{F}\} = \begin{Bmatrix} F_1 \\ F_2 \\ \vdots \\ F_N \end{Bmatrix}$$
$$\{\mathbf{a}\} = \begin{Bmatrix} a_o \\ a_1 \\ a_2 \end{Bmatrix}, \qquad [\mathbf{R}] = \begin{bmatrix} \begin{Bmatrix} 1 \\ 1 \\ \vdots \\ 1 \end{Bmatrix} & \begin{Bmatrix} x_1 \\ x_2 \\ \vdots \\ x_N \end{Bmatrix} & \begin{Bmatrix} y_1 \\ y_2 \\ \vdots \\ y_N \end{Bmatrix} \end{bmatrix} \tag{6.18}$$

Thus, the deflection W_i, for $i = 1, 2, \ldots, N$ can be determined using Eqs 6.16 and 6.17 along with the above definitions. Combining Eqs 6.16 and 6.17 gives:

$$\left\{\begin{matrix} 0 \\ 0 \\ 0 \\ w_1 \\ w_2 \\ \cdots \\ w_N \end{matrix}\right\} = \begin{bmatrix} 0 & 0 & 0 & 1 & \cdots & 1 \\ 0 & 0 & 0 & x_1 & \cdots & x_N \\ 0 & 0 & 0 & y_1 & \cdots & y_N \\ 1 & x_1 & y_1 & 0 & \cdots & K_{1N} \\ 1 & x_2 & y_2 & K_{21} & \cdots & K_{2N} \\ \cdots & \cdots & \cdots & \cdots & \cdots & \cdots \\ 1 & x_N & y_N & K_{N1} & \cdots & 0 \end{bmatrix} \left\{\begin{matrix} a_0 \\ a_1 \\ a_2 \\ P_1 \\ P_2 \\ \cdots \\ P_N \end{matrix}\right\} = [\mathbf{C}][\mathbf{P}] \qquad (6.19)$$

The interpolation to any point in the 2D plane is then achieved by evaluating $w(x, y)$ from Eq 6.10 at the desired points. Thus, for a given aerodynamic point (x_k, y_k), its displacement is:

$$\mathbf{h}(x_k, y_k) = (1,\ x_k,\ y_k,\ K_{k,1},\ K_{k,2},\ \ldots,\ K_{k,n})\ [\mathbf{C}]^{-1} \left\{\begin{matrix} 0 \\ 0 \\ 0 \\ w_1 \\ w_2 \\ \vdots \\ w_n \end{matrix}\right\} \qquad (6.20)$$

and its streamwise slopes is:

$$\mathbf{h}'(x_k, y_k) = (0,\ -1,\ 0,\ DK_{k,1},\ DK_{k,2},\ \ldots,\ DK_{k,n})\ [\mathbf{C}]^{-1} \left\{\begin{matrix} 0 \\ 0 \\ 0 \\ w_1 \\ w_2 \\ \vdots \\ w_n \end{matrix}\right\} \qquad (6.21)$$

where:

$$DK_{k,i} = -\frac{\partial K_{k,i}}{\partial x_k} = -2\left(x_i - x_k\right)\left(1 + \ln r_{k,i}^{\ 2}\right)$$

Eqs 6.20 and 6.21 can be rewritten as:

$$\mathbf{h}(x_k, y_k) = [\mathbf{s}_k] \begin{Bmatrix} w_1 \\ w_1 \\ \vdots \\ w_n \end{Bmatrix} \tag{6.22}$$

and:

$$\mathbf{h}'(x_k, y_k) = [D\mathbf{s}_k] \begin{Bmatrix} w_1 \\ w_1 \\ \vdots \\ w_n \end{Bmatrix} \tag{6.23}$$

where $[\mathbf{s}_k]$ and $[D\mathbf{s}_k]$ are resulted from the matrix multiplications in Eqs 6.22 and 6.23, respectively, but with the first three columns of $[\mathbf{C}]^{-1}$ being removed.

The solutions of $\mathbf{h}(x_k, y_k)$ and $\mathbf{h}'(x_k, y_k)$ exist only if the matrix **C** is non-singular. The singularity in matrix **C** occurs when:

- all structural grid points are aligned along a line. This is obvious since a line fails to define a plane.
- two or more than two structural grid points have the same *x* and *y* location.

To perform the IPS method, it is required that all structural grid points and aerodynamic points are located on the same plane. This plane is called "spline plane". Normally, the plane of the lifting surface (or the mean plane of the wing-like component) is selected as the spline plane. However, for structural grid points located in 3D space, these structural grid points may not be necessarily located on the plane. In this case, it is required to project the structural grid points onto the spline plane along the normal direction of the spline plane. This can be done by transforming the structural grid point locations to a local coordinates whose *x-y* plane coincide with the spline plane.

Singularity in matrix **C** appears in case two structural grid points shear the same x and y locations on their projected position, even if their original positions in the 3D space are not the same. Therefore, in this kind of situation, one of the two grid points must be excluded from the selection of the structural grid points.

Another important concept needed to be addressed here is that the IPS method is a scalar operator. This is to say that for a given set of normal displacements at structural grid points the IPS method results the displacements at the aerodynamic points only along the normal direction of the spline plane. For instance, the deflection W in Eq 6.1 represents the normal displacement at structural grid point. Therefore, the deflection $\mathbf{h}$ in Eq 6.20 at aerodynamic point is also the normal displacement. However, for the deflection along other directions one finds out that the IPS method can be applied in the same way as that of the normal displacements. Let u be the streamwise deflections and v be the lateral deflections, Eq 6.1 can be rewritten as:

$$D\nabla^4 u = q \tag{6.24}$$

$$D\nabla^4 v = q \tag{6.25}$$

This time, D is not the plate bending rigidity but represents some in-plane flexural rigidity. Solving Eqs 6.24 and 6.25 results the solutions that are identical to Eqs 6.22 and 6.23 but with W replaced by u for streamwise displacement and by v for lateral displacement. This also indicates that for 6 d.o.f. at each structural finite element grid points, namely, T_1, T_2, T_3 of translational displacements and R_1, R_2, R_3 for rotational displacements, Eqs 6.22 and 6.23 can be generalized as:

$$\begin{Bmatrix} h_x \\ h_y \\ h_z \\ h'_x \\ h'_y \\ h'_z \end{Bmatrix}_k = \begin{bmatrix} [\mathbf{s}_k] & 0 & 0 & 0 & 0 & 0 \\ 0 & [\mathbf{s}_k] & 0 & 0 & 0 & 0 \\ 0 & 0 & [\mathbf{s}_k] & 0 & 0 & 0 \\ [D\mathbf{s}_k] & 0 & 0 & 0 & 0 & 0 \\ 0 & [D\mathbf{s}_k] & 0 & 0 & 0 & 0 \\ 0 & 0 & [D\mathbf{s}_k] & 0 & 0 & 0 \end{bmatrix} \begin{Bmatrix} \{\mathbf{T}_1\} \\ \{\mathbf{T}_2\} \\ \{\mathbf{T}_3\} \\ \{\mathbf{R}_1\} \\ \{\mathbf{R}_2\} \\ \{\mathbf{R}_3\} \end{Bmatrix} \tag{6.26}$$

The zero matrices associated with $\{\mathbf{R}_1\}$, $\{\mathbf{R}_2\}$ and $\{\mathbf{R}_3\}$ in the right hand side of Eq 6.26 are resulted from the IPS formulation which does not involve the structural rotational displacements.

Applying Eq 6.26 for M aerodynamic points by letting the index k be $\mathrm{k} = 1, 2, \ldots, M$ yields:

$$\{\mathbf{h}\} = [\mathbf{G}_{\mathrm{IPS}}]\{\mathbf{x}\} \tag{6.27}$$

where:

$$\{\mathbf{h}\} = \begin{Bmatrix} \vdots \\ \begin{Bmatrix} h_x \\ h_y \\ h_z \\ h'_x \\ h'_y \\ h'_z \end{Bmatrix}_k \\ \vdots \end{Bmatrix} \qquad \mathrm{k} = 1, 2, \ldots, M \tag{6.28}$$

$$\{\mathbf{x}\} = \begin{Bmatrix} \{\mathbf{T}_1\} \\ \{\mathbf{T}_2\} \\ \{\mathbf{T}_3\} \\ \{\mathbf{R}_1\} \\ \{\mathbf{R}_2\} \\ \{\mathbf{R}_3\} \end{Bmatrix} \tag{6.29}$$

and:

$$[\mathbf{G}_{\mathrm{IPS}}] = \begin{bmatrix} [\mathbf{s}_k] & 0 & 0 & 0 & 0 & 0 \\ 0 & [\mathbf{s}_k] & 0 & 0 & 0 & 0 \\ 0 & 0 & [\mathbf{s}_k] & 0 & 0 & 0 \\ [D\mathbf{s}_k] & 0 & 0 & 0 & 0 & 0 \\ 0 & [D\mathbf{s}_k] & 0 & 0 & 0 & 0 \\ 0 & 0 & [D\mathbf{s}_k] & 0 & 0 & 0 \end{bmatrix} \qquad \mathrm{k} = 1, 2, \ldots, M \tag{6.30}$$

Thus, $[\mathbf{G}_{\mathrm{IPS}}]$ represents an IPS method generated spline matrix that interpolates the displacements of the 6 d.o.f. at N structural grid points to the displacements along x, y, z directions as well as their streamwise slopes at M aerodynamic points.

Finally, some important remarks about the IPS method are summarized below:

- The spline matrix becomes singular when two or more than two structural grid points shear the same x and y location of their projection position on the spline plane.
- The spline matrix is singular if all structural grid points are aligned along a line.
- Linear extrapolation occurs only if the aerodynamic points are far from the domain of the structural points. Otherwise, distortions or oscillations may appear in the extrapolated regions.
- The IPS method is a scalar operator. For a given set of displacements along one direction, the IPS method does not recover displacements along other directions.

6.2 The Thin-Plate Spline (TPS) Method

The TPS method (Ref 6.3) is a generalization of the IPS method by incorporating some three-dimensional aspects. TPS provides a means to characterize an irregular surface by using functions that minimize an energy functional. The derivation is entirely analogous with the IPS method with the addition of the third coordinate. Eq 6.4 becomes:

$$W(x, y, z) = \sum_{i=1}^{N} \left(A_i + B_i\, r_i^2 + F_i\, r_i^2 \ln r_i^2 \right) \tag{6.31}$$

where:

$$r_i^2 = (x-x_i)^2 + (y-y_i)^2 + (z-z_i)^2$$

The boundary conditions at infinity are similar to these of IPS but with the addition moments in the third axis:

$$\sum B_i = \sum F_i = \sum x_i F_i = \sum y_i F_i = \sum z_i F_i \tag{6.32}$$

Expanding Eq 6.31 for large r, terms of order $r^2 \ln r^2$, r^2 and $r \ln r^2$ can be eliminated by applying the boundary conditions expressed in Eq 6.32. This leads to:

$$w(x,y,z) = a_o + a_1 x + a_2 y + a_3 z + \sum_{i=1}^{N} K_i(x,y,z) F_i \tag{6.33}$$

where:

$$K_i(x,y) = r_i^2 \ln r_i^2$$

In order to solve the unknown coefficients, one can introduce a matrix notation such that Eqs 6.32 and 6.33 become:

$$\begin{aligned} \{\mathbf{W}\} &= [\mathbf{R}]\{\mathbf{a}\} + [\mathbf{K}_{ij}]\{\mathbf{F}\} \\ [\mathbf{R}]^{\mathrm{T}}\{\mathbf{F}\} &= 0 \end{aligned} \tag{6.34}$$

where:

$$\mathbf{K}_{ij} = r_{ij}^2 \ln r_{ij}^2$$

and:

$$r_{ij}^2 = (x_j - x_i)^2 + (y_j - y_i)^2 + (z_j - z_i)^2$$

The matrix **R** is:

$$[\mathbf{R}] = \left[\begin{Bmatrix} 1 \\ 1 \\ \vdots \\ 1 \end{Bmatrix} \begin{Bmatrix} x_1 \\ x_2 \\ \vdots \\ x_N \end{Bmatrix} \begin{Bmatrix} y_1 \\ y_2 \\ \vdots \\ y_N \end{Bmatrix} \begin{Bmatrix} z_1 \\ z_2 \\ \vdots \\ z_N \end{Bmatrix} \right] \tag{6.35}$$

$$\{\mathbf{W}\} = \begin{Bmatrix} W_1 \\ W_2 \\ \vdots \\ W_N \end{Bmatrix}, \qquad \{\mathbf{a}\} = \begin{Bmatrix} a_o \\ a_1 \\ a_2 \\ a_3 \end{Bmatrix}, \qquad \{\mathbf{F}\} = \begin{Bmatrix} F_1 \\ F_2 \\ \vdots \\ F_N \end{Bmatrix} \tag{6.36}$$

For a given coordinates of the N structural grid points, Eq 3.34 becomes:

$$\begin{Bmatrix} \{0\} \\ \{\mathbf{W}\} \end{Bmatrix} = \begin{bmatrix} [0] & [\mathbf{R}]^{T} \\ [\mathbf{R}] & [\mathbf{K}_{ij}] \end{bmatrix} \begin{Bmatrix} \{\mathbf{a}\} \\ \{\mathbf{F}\} \end{Bmatrix} = [\mathbf{C}] \begin{Bmatrix} \{\mathbf{a}\} \\ \{\mathbf{F}\} \end{Bmatrix} \tag{6.37}$$

The interpolation to any point in the 3D space is then achieved by evaluating $w(x, y, z)$ of Eq 6.33 at the desired point. Thus, for a given aerodynamic point (x_k, y_k, z_k), its displacement is:

$$\mathbf{h}(x_k, y_k, z_k) = (1,\ x_k,\ y_k,\ z_k,\ K_{k,1},\ K_{k,2},\ \ldots,\ K_{k,n})\ [\mathbf{C}]^{-1} \begin{Bmatrix} \{0\} \\ \{\mathbf{W}\} \end{Bmatrix} \tag{6.38}$$

and its streamwise slopes is:

$$\mathbf{h}'(x_k, y_k, z_k) = (0,\ -1,\ 0,\ 0,\ DK_{k,1},\ DK_{k,2},\ \ldots,\ DK_{k,n})\ [\mathbf{C}]^{-1} \begin{Bmatrix} \{0\} \\ \{\mathbf{W}\} \end{Bmatrix} \tag{6.39}$$

where:

$$DK_{k,i} = -\frac{\partial K_{k,i}}{\partial x_k} = -2\left(x_i - x_k\right)\left(1 + \ln r_{k,i}{}^{2}\right)$$

Eqs 6.38 and 6.39 can be rewritten as:

$$\mathbf{h}(x_k, y_k, z_k) = [\mathbf{s}_k]\ \{\mathbf{W}\} \tag{6.40}$$

and:

$$\mathbf{h}'(x_k, y_k, z_k) = [D\mathbf{s}_k]\ \{\mathbf{W}\} \tag{6.41}$$

where $[\mathbf{s}_k]$ and $[D\mathbf{s}_k]$ are resulted from the matrix multiplication in Eqs 6.38 and 6.39, respectively, but with the first four columns of $[\mathbf{C}]^{-1}$ being removed.

Unlike the IPS method, TPS does not require a spline plane. Therefore, TPS can be considered as a 3D spline method that performs the interpolation based on a set of structural points located in a 3D space.

Similar to IPS, the TPS method has several restrictions:

- The matrix [C] in Eq 6.37 is singular if two structural grid points have the same x, y and z locations.
- The matrix [C] is singular if all structural grid points are located on the same plane. In this case, the sub-matrix [**R**] becomes singular that leads to a singular matrix of [**C**].

TPS is also a scalar operator. Similar to IPS, Eq 6.41 can be generalized into a spline matrix such that:

$$\{\mathbf{h}\} = [\mathbf{G}_{\mathrm{TPS}}]\{\mathbf{x}\} \tag{6.42}$$

where $\{\mathbf{h}\}$ and $\{\mathbf{x}\}$are the same as Eqs 6.28 and 6.29, respectively, and $[\mathbf{G}_{\mathrm{TPS}}]$ has the same form as Eq 6.30.

Since there is no requirement of spline plane, for interpolation of displacements at 3D structural grid points, TPS outperforms the IPS method. However, if all structural grid points are on the same plane, the TPS method breaks down. In theory, for this kind of situation the formulation of TPS can be reduced to that of IPS. But such a reduction is not straight forward. Therefore, in practice, the IPS method should not be treated as a special case of TPS. Thus, for all structural grid point on the same plane, the use of that IPS method is suggested.

6.3 The Beam Spline Method

It is often that a high aspect ratio wing structure is modeled by a beam-type finite elements along the elastic axis of the wing, or a body by beam-type finite elements along the center line of the body. On the other hand, the aerodynamic boxes of the wing-like and body-like components in the aerodynamic model are generally located in a 3D space. The Beam Spline Method is designed to specially handle this kind of spline problem.

The Beam Spline Method solves the partial differential equation of equilibrium for an infinite beam with uniform bending and torsion stiffness. For bending deflections, it satisfies the given displacements and slopes at the N structural grid points. For torsion, it satisfies the given twists. The N structural grid points are assumed to be located along a line called the "spline axis". In the present formulation of the Beam Spline Method, the spline axis is defined as the y axis of a user specified local coordinate system.

After the unknowns of the infinite beam equation are determined, the displacements and slopes at the aerodynamic points can be obtained by rigid connections between the beam and the aerodynamic points (see Fig 6.1). To derive the solution of the infinite beam equation, it is required first to transform all structural grid points and aerodynamic points into the spline axis coordinate system. This can be done by computing a transformation matrix $[\mathbf{T}_s]$ such that:

$$\begin{Bmatrix} x' \\ y' \\ z' \end{Bmatrix} = [\mathbf{T}_s] \begin{Bmatrix} x \\ y \\ z \end{Bmatrix} \tag{6.43}$$

where:

x', y' and z' are a local coordinate system whose y' axis is the spline line

and:

x , y and z are the basic coordinate system whose x axis is parallel to the streamwise direction.

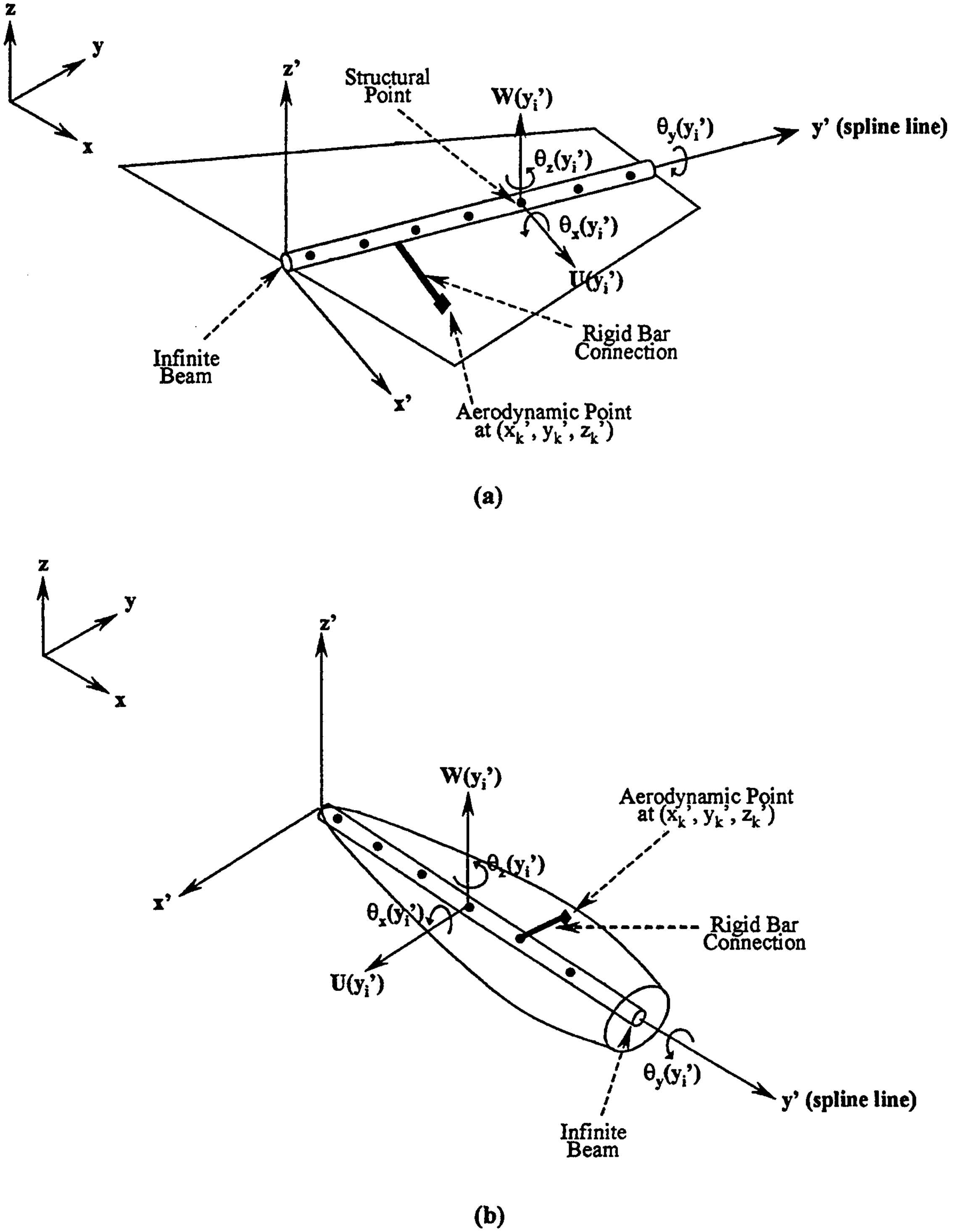

z
y
x
z'
Structural Point
$W(y_i')$
$\theta_y(y_i')$
y' (spline line)
$\theta_z(y_i')$
$\theta_x(y_i')$
$U(y_i')$
Rigid Bar Connection
Infinite Beam
x'
Aerodynamic Point at (x_k', y_k', z_k')
(a)
z
y
x
z'
$W(y_i')$
Aerodynamic Point at (x_k', y_k', z_k')
$\theta_z(y_i')$
x'
$\theta_x(y_i')$
Rigid Bar Connection
$U(y_i')$
$\theta_y(y_i')$
y' (spline line)
Infinite Beam
(b)

Fig 6.1 Spline Axis Coordinate System (a) Spline Axis Along the Elastic Axis of Wing-Like Component (b) Spline Axis Along the Center Line of Body-Like Component

Bending Stiffness About the x' Axis

The partial equation of an infinite beam with constant bending stiffness about x' axis reads:

$$E\,I\,\frac{d^4W}{dy^4} = q - \frac{dM}{dy'} \tag{6.44}$$

where:

W is the beam deflection parallel to the z' axis

$E\,I$ represents the bending stiffness

q is a distributed transverse load

and:

M is a distributed moment

For N structural grid points located along the beam, the solution is found by superimposing the fundamental solutions:

$$W(y') = a_o + a_1\,y' + \sum_{i=1}^{N}\left(-\frac{M_i\,(y'-y'_i)\,|\,y'-y'_i\,|}{4\,E\,I} + \frac{P_i\,|\,y'-y'_i\,|^3}{12\,E\,I} \right) \tag{6.45}$$

$$\theta_x(y') = \frac{dW}{dy'} = a_1 + \sum_{i=1}^{N}\left(-\frac{M_i\,|\,y'-y'_i\,|}{2\,E\,I} + \frac{P_i\,(y'-y'_i)\,|\,y'-y'_i\,|}{4\,E\,I} \right) \tag{6.46}$$

Applying Eqs 6.45 and 6.46 for the given W and θ_x at N structural grid points and imposing the boundary condition at infinity for linear function of W:

$$\sum P_i = 0 \tag{6.47}$$

$$\sum (\,y'_i\,P_i + M_i\,) = 0 \tag{6.48}$$

gives:

$$\left\{ \begin{matrix} \{0\} \\ \{\mathbf{W}\} \\ \{\theta_x\} \end{matrix} \right\} = \begin{bmatrix} [0] & R_1^{\mathrm{T}} & R_2^{\mathrm{T}} \\ R_1 & A_{11} & A_{21} \\ R_2 & A_{21} & A_{22} \end{bmatrix} \left\{ \begin{matrix} \{\mathbf{a}\} \\ \{\mathbf{P}\} \\ \{\mathbf{M}\} \end{matrix} \right\} = [\mathbf{C}] \left\{ \begin{matrix} \{\mathbf{a}\} \\ \{\mathbf{P}\} \\ \{\mathbf{M}\} \end{matrix} \right\} \tag{6.49}$$

where:

$$\{\mathbf{W}\} = \begin{Bmatrix} W_1 \\ W_2 \\ \vdots \\ W_N \end{Bmatrix}, \quad \{\theta_{\mathrm{x}}\} = \begin{Bmatrix} \theta_{\mathrm{x}_1} \\ \theta_{\mathrm{x}_2} \\ \vdots \\ \theta_{\mathrm{x}_N} \end{Bmatrix}, \quad \{\mathbf{a}\} = \begin{Bmatrix} a_o \\ a_1 \end{Bmatrix},$$

$$\{\mathbf{P}\} = \begin{Bmatrix} P_1 \\ P_2 \\ \vdots \\ P_N \end{Bmatrix}, \quad \{\mathbf{M}\} = \begin{Bmatrix} M_1 \\ M_2 \\ \vdots \\ M_N \end{Bmatrix}$$

$$\mathbf{R}_1{}^{\mathrm{T}} = \begin{bmatrix} 1 & 1 & \cdots & 1 \\ y_1' & y_2' & \cdots & y_N' \end{bmatrix}, \qquad \mathbf{R}_2{}^{\mathrm{T}} = \begin{bmatrix} 0 & 0 & \cdots & 0 \\ 1 & 1 & \cdots & 1 \end{bmatrix}$$

$$\mathbf{A}_{11} = \frac{1}{12\,EI} \begin{bmatrix} \eta_{11}{}^3 & \eta_{21}{}^3 & \cdots & \eta_{N1}{}^3 \\ -\eta_{12}{}^3 & \eta_{22}{}^3 & \cdots & \eta_{N2}{}^3 \\ \vdots & \vdots & & \vdots \\ -\eta_{1N}{}^3 & -\eta_{2N}{}^3 & \cdots & \eta_{NN}{}^3 \end{bmatrix}$$

$$\mathbf{A}_{21} = \frac{1}{4\,EI} \begin{bmatrix} \eta_{11}{}^2 & -\eta_{21}{}^2 & \cdots & -\eta_{N1}{}^2 \\ \eta_{12}{}^2 & \eta_{22}{}^2 & \cdots & -\eta_{N2}{}^2 \\ \vdots & \vdots & & \vdots \\ \eta_{1N}{}^2 & \eta_{2N}{}^2 & \cdots & \eta_{NN}{}^2 \end{bmatrix}$$

$$\mathbf{A}_{22} = \frac{1}{2\,EI} \begin{bmatrix} \eta_{11} & -\eta_{21} & \cdots & -\eta_{N1} \\ \eta_{12} & \eta_{22} & \cdots & -\eta_{N2} \\ \vdots & \vdots & & \vdots \\ \eta_{1N} & \eta_{2N} & \cdots & \eta_{NN} \end{bmatrix}$$

and:

$$\eta_{ij} = (y_i' - y_j')$$

For a given aerodynamic point $(x_{\mathrm{k}},\ y_{\mathrm{k}},\ z_{\mathrm{k}})$ exactly located at the beam so that $x_{\mathrm{k}} = z_{\mathrm{k}} = 0$, the interpolated displacement $\mathbf{W}(0, y_{\mathrm{k}}, 0)$ can be obtained by evaluating $\mathbf{W}(y')$ of Eq 6.45 at the desired point:

$$\mathbf{W}(0, y_{\mathrm{k}}, 0) = \left(1,\ y'_{\mathrm{k}},\ \frac{|\eta_{\mathrm{k1}}|^3}{12\,EI},\ \frac{|\eta_{\mathrm{k2}}|^3}{12\,EI},\ \cdots,\ \frac{|\eta_{\mathrm{k}N}|^3}{12\,EI},\ -\frac{\eta_{\mathrm{k1}}\,|\eta_{\mathrm{k1}}|}{4\,EI},\right.$$

$$\left. -\frac{\eta_{\mathrm{k2}}\,|\eta_{\mathrm{k2}}|}{4\,EI},\ \cdots,\ -\frac{\eta_{\mathrm{k}N}\,|\eta_{\mathrm{k}N}|}{4\,EI} \right) [\mathbf{C}]^{-1} \begin{Bmatrix} \{0\} \\ \{\mathbf{W}\} \\ \{\theta_{\mathrm{k}}\} \end{Bmatrix} \tag{6.50}$$

$$\frac{d\mathbf{W}}{dy'_{\mathrm{k}}}(0, y_{\mathrm{k}}, 0) = \left(0,\ 1,\ \frac{\eta_{\mathrm{k1}}\,|\eta_{\mathrm{k1}}|}{4\,EI},\ \frac{\eta_{\mathrm{k2}}\,|\eta_{\mathrm{k2}}|}{4\,EI},\ \cdots,\ \frac{\eta_{\mathrm{k}N}\,|\eta_{\mathrm{k}N}|}{4\,EI},\ -\frac{|\eta_{\mathrm{k1}}|}{2\,EI},\right.$$

$$\left. -\frac{|\eta_{\mathrm{k2}}|}{2\,EI},\ \cdots,\ -\frac{|\eta_{\mathrm{k}N}|}{2\,EI} \right) [\mathbf{C}]^{-1} \begin{Bmatrix} \{0\} \\ \{\mathbf{W}\} \\ \{\theta_{\mathrm{k}}\} \end{Bmatrix} \tag{6.51}$$

$$\frac{d^2\mathbf{W}}{dy'^{\,2}_{\mathrm{k}}}(0, y_{\mathrm{k}}, 0) = \left(0,\ 0,\ \frac{|\eta_{\mathrm{k1}}|}{2\,EI},\ \frac{|\eta_{\mathrm{k2}}|}{2\,EI},\ \cdots,\ \frac{|\eta_{\mathrm{k}N}|}{2\,EI},\ -\frac{\mathrm{sign}(\eta_{\mathrm{k1}})}{2\,EI},\right.$$

$$\left. -\frac{\mathrm{sign}(\eta_{\mathrm{k2}})}{2\,EI},\ \cdots,\ -\frac{\mathrm{sign}(\eta_{\mathrm{k}N})}{2\,EI} \right) [\mathbf{C}]^{-1} \begin{Bmatrix} \{0\} \\ \{\mathbf{W}\} \\ \{\theta_{\mathrm{k}}\} \end{Bmatrix} \tag{6.52}$$

Eqs 6.50, 6.51 and 6.52 can be simplified and rewritten as:

$$\mathbf{W}(0, y'_{\mathrm{k}}, 0) = [\mathbf{s}_{\mathrm{k}} \quad \mathbf{R}_{\mathrm{k}}] \begin{Bmatrix} \{\mathbf{W}\} \\ \{\theta_{\mathrm{x}}\} \end{Bmatrix} \tag{6.53}$$

$$\frac{d\mathbf{W}}{dy'_{\mathrm{k}}}(0, y'_{\mathrm{k}}, 0) = [D\mathbf{s}_{\mathrm{k}} \quad D\mathbf{R}_{\mathrm{k}}] \begin{Bmatrix} \{\mathbf{W}\} \\ \{\theta_{\mathrm{x}}\} \end{Bmatrix} \tag{6.54}$$

$$\frac{d^2\mathbf{W}}{dy'^{\,2}_{\mathrm{k}}}(0, y'_{\mathrm{k}}, 0) = [C\mathbf{s}_{\mathrm{k}} \quad C\mathbf{R}_{\mathrm{k}}] \begin{Bmatrix} \{\mathbf{W}\} \\ \{\theta_{\mathrm{x}}\} \end{Bmatrix} \tag{6.55}$$

where:

$[\mathbf{s}_{\mathrm{k}} \quad \mathbf{R}_{\mathrm{k}}]$, $[D\mathbf{s}_{\mathrm{k}} \quad D\mathbf{R}_{\mathrm{k}}]$, $[C\mathbf{s}_{\mathrm{k}} \quad C\mathbf{R}_{\mathrm{k}}]$ are resulted from the matrix multiplications in Eqs 6.50, 6.51 and 6.52, respectively, but with the first two columns of $[\mathbf{C}]^{-1}$ being removed.

Bending Stiffness About the z' Axis

The partial equation of an infinite beam with constant bending stiffness about the z' axis reads:

$$EI\ \frac{d^4\mathbf{U}}{dy'^4} = q - \frac{dM}{dy'} \tag{6.56}$$

where **U** is the beam deflection parallel to the x' axis.

The equivalence of Eq 6.56 and Eq 6.44 suggests that the solution of Eq 6.44 can be adopted for Eq 6.56. Thus, Eqs 6.53, 6.54 and 6.55 can be rewritten as the solutions for **U**:

$$\mathbf{U}(0,y'_k,0) = \begin{bmatrix}\mathbf{s}_k & \mathbf{R}_k\end{bmatrix}\begin{Bmatrix}\{\mathbf{U}\}\\ \{\theta_z\}\end{Bmatrix} \tag{6.57}$$

$$\frac{d\mathbf{U}}{dy'_k}(0,y'_k,0) = \begin{bmatrix}D\mathbf{s}_k & D\mathbf{R}_k\end{bmatrix}\begin{Bmatrix}\{\mathbf{U}\}\\ \{\theta_z\}\end{Bmatrix} \tag{6.58}$$

$$\frac{d^2\mathbf{U}}{dy'^2_k}(0,y'_k,0) = \begin{bmatrix}C\mathbf{s}_k & C\mathbf{R}_k\end{bmatrix}\begin{Bmatrix}\{\mathbf{U}\}\\ \{\theta_z\}\end{Bmatrix} \tag{6.59}$$

Torsion Stiffness About the y' Axis

The equation of infinite beam with constant torsion stiffness reads:

$$GJ\left(\frac{d\theta_y{}^2}{dy^2}\right) = -\mathbf{M}_{y'} \tag{6.60}$$

where:

θ_y is the twist about y'

$\mathbf{M}'_y$ is a distributed torque.

For N structural grid points located along the beam, the solution of Eq 6.60 is:

$$\theta_y(y') = \left[1, -\frac{|y'_1-y'|}{2GJ}, -\frac{|y'_2-y'|}{2GJ}, \ldots, -\frac{|y'_N-y'|}{2GJ}\right]\begin{Bmatrix}a\\ \{\mathbf{M}_{y'}\}\end{Bmatrix} \tag{6.61}$$

The equilibrium condition requires:

$$\sum \mathbf{M}_{y'} = 0 \tag{6.62}$$

Applying Eq 6.61 for the twists at N structural grid points and imposing the equilibrium condition yield:

$$\begin{Bmatrix} 0 \\ \{\theta_y\} \end{Bmatrix} = \begin{bmatrix} 0 & 1 & 1 & \cdots & 1 \\ 1 & 0 & -\frac{|\eta_{21}|}{2GJ} & \cdots & -\frac{|\eta_{N1}|}{2GJ} \\ \vdots & & & & \\ 1 & -\frac{|\eta_{N1}|}{2GJ} & -\frac{|\eta_{N2}|}{2GJ} & \cdots & 0 \end{bmatrix} \begin{Bmatrix} a \\ \{\mathbf{M}_{y'}\} \end{Bmatrix} \tag{6.63}$$

$$= [\mathbf{C}] \begin{Bmatrix} a \\ \{\mathbf{M}_{y'}\} \end{Bmatrix}$$

For a given aerodynamic point $(0, y'_k, 0)$ at the beam, the interpolated twist is:

$$\theta_y(0, y'_k, 0) = [\mathbf{T}_{r_k}]\,\{\theta_y\} \tag{6.64}$$

where:

$[\mathbf{T}_{r_k}]$ is resulted from the combination of Eq 6.61 and Eq 6.63.

Displacement of Aerodynamic Point in 3D Space

The displacement of a given aerodynamic point (x'_k, y'_k, z'_k) in 3D space is obtained by assuming a rigid bar connecting the point and the beam. This leads to:

$$\begin{Bmatrix} u \\ v \\ w \end{Bmatrix}_k = \left[\mathbf{G}_1(\mathbf{s}_k, \mathbf{R}_k, D\mathbf{s}_k, D\mathbf{R}_k, \mathbf{T}_{r_k}, x_k, z_k)\right]\{\mathbf{x}'\} \tag{6.65}$$

$$\begin{Bmatrix} \frac{du}{dx'_k} \\ \frac{dv}{dx'_k} \\ \frac{dw}{dx'_k} \end{Bmatrix}_k = \left[\mathbf{G}_2(D\mathbf{s}_k, D\mathbf{R}_k, \mathbf{T}_{r_k})\right]\{\mathbf{x}'\} \tag{6.66}$$

$$\begin{Bmatrix} \frac{du}{dy'_k} \\ \frac{dv}{dy'_k} \\ \frac{dw}{dy'_k} \end{Bmatrix}_k = \left[\mathbf{G}_3(D\mathbf{s}_k, D\mathbf{R}_k, C\mathbf{s}_k, C\mathbf{R}_k, x_k, z_k)\right]\{\mathbf{x}'\} \tag{6.67}$$

$$\begin{Bmatrix} \dfrac{du}{dz'_{\mathrm{k}}} \\ \dfrac{dv}{dz'_{\mathrm{k}}} \\ \dfrac{dw}{dz'_{\mathrm{k}}} \end{Bmatrix}_{\mathrm{k}} = \left[\mathbf{G}_4(D\mathbf{s}_{\mathrm{k}}, D\mathbf{R}_{\mathrm{k}}, \mathbf{T}_{\mathrm{s_k}}) \right] \{\mathbf{x}'\} \tag{6.68}$$

where:

$$\{\mathbf{x}'\} = \begin{Bmatrix} \{\mathbf{u}\} \\ \{\mathbf{v}\} \\ \{\mathbf{w}\} \\ \{\theta_{\mathrm{x}}\} \\ \{\theta_{\mathrm{y}}\} \\ \{\theta_{\mathrm{z}}\} \end{Bmatrix} \tag{6.69}$$

and:

$\mathbf{G}_1$, $\mathbf{G}_2$, $\mathbf{G}_3$ and $\mathbf{G}_4$ can be derived from Eqs 6.53 to 6.55, Eqs 6.57 to 6.59, and 6.60 as well as with a rigid bar connecting the aerodynamic point $(x'_{\mathrm{k}}, y'_{\mathrm{k}}, z'_{\mathrm{k}})$ to the beam.

Transformation from Spline Axis Coördinate to Basic Coordinates

Eqs 6.65 to 6.69 are derived in the spline axis coordinates. The transformation matrix $[\mathbf{T}_{\mathrm{s}}]$ relating the spline axis coordinates to the basic coordinates is defined in Eq 6.43. Therefore, Eq 6.69 can be transformed to T_1, T_2, T_3 and R_1, R_2, R_3 of the given displacements defined in the basic coordinates by:

$$\{\mathbf{x}'\} = \begin{bmatrix} [\mathbf{T}_{\mathrm{s}}] & 0 \\ 0 & [\mathbf{T}_{\mathrm{s}}] \end{bmatrix} \{\mathbf{x}\} \tag{6.70}$$

where $\{\mathbf{x}\}$ is expressed in Eq 6.29.

The interpolated displacement u, v and w can be transformed to h_{x}, h_{y} and h_{z} by:

$$\begin{Bmatrix} h_{\mathrm{x}} \\ h_{\mathrm{y}} \\ h_{\mathrm{z}} \end{Bmatrix}_{\mathrm{k}} = [\mathbf{T}_{\mathrm{s}}]^{\mathrm{T}} \begin{Bmatrix} u \\ v \\ w \end{Bmatrix}_{\mathrm{k}} \tag{6.71}$$

Substituting Eqs 6.70 and 6.71 into Eq 6.65 yields:

$$\begin{Bmatrix} h_x \\ h_y \\ h_z \end{Bmatrix}_k = [\mathbf{T}_s]^T \, [\mathbf{G}_1] \begin{bmatrix} [\mathbf{T}_s] & 0 \\ 0 & [\mathbf{T}_s] \end{bmatrix} \{\mathbf{x}\} \tag{6.72}$$

The streamwise slopes can be derived from:

$$\begin{aligned} h'_x &= \frac{\partial h_x}{\partial x} = \frac{\partial h_x}{\partial x'}\frac{\partial x'}{\partial x} + \frac{\partial h_x}{\partial y'}\frac{\partial y'}{\partial x} + \frac{\partial h_x}{\partial z'}\frac{\partial z'}{\partial x} \\ h'_y &= \frac{\partial h_y}{\partial y} = \frac{\partial h_y}{\partial x'}\frac{\partial x'}{\partial y} + \frac{\partial h_y}{\partial y'}\frac{\partial y'}{\partial y} + \frac{\partial h_y}{\partial z'}\frac{\partial z'}{\partial y} \\ h'_z &= \frac{\partial h_z}{\partial z} = \frac{\partial h_z}{\partial x'}\frac{\partial x'}{\partial z} + \frac{\partial h_z}{\partial y'}\frac{\partial y'}{\partial z} + \frac{\partial h_z}{\partial z'}\frac{\partial z'}{\partial z} \end{aligned} \tag{6.73}$$

Substituting Eqs 6.66 to 6.69 and combining the resultant equation with Eq 6.72 yield a spline matrix relating the 6 d.o.f. displacements at N structural grid points. Repeating this process for M aerodynamic points by letting the index k vary from 1 to M gives:

$$\{\mathbf{h}\} = [\mathbf{G}_{\text{Beam}}]\{\mathbf{x}\} \tag{6.74}$$

where:

$\{\mathbf{h}\}$ and $\{\mathbf{x}\}$ are defined in Eqs 6.28 and 6.29, respectively,

and:

$[\mathbf{G}_{\text{Beam}}]$ is a $6 \times M$ spline matrix generated by the beam spline method.

Some important remarks about the Beam Spline Method are discussed as follows:

- One of the basic assumptions of the Beam Spline Method is that all structural grid points are located along the spline axis. Errors may be introduced if some of the grid points are off the axis.
- Similar to the IPS and TPS methods, the spline matrix becomes singular if two structural grid points are coincided at their projected position at the spline axis.
- Linear extrapolation occurs only if the aerodynamic points are far away from the domain of the structural points. Otherwise, distortions or oscillations may appear in the extrapolation regions.

6.4 The Rigid-Body Attachment (RBA) Method

The Rigid-Body Attachment (RBA) method is developed for the cases where no structural model exists for a particular aerodynamic component. For example, an underwing store may be modeled as a point mass in the structural finite element model, but its surface may be represented by a detailed aerodynamic panel model. Since no information of the structural connectivity between the point mass and the store surface is given, it is assumed that all aerodynamic points are attached to the point mass by a rigid body. For a given aerodynamic point located at x_k, y_k, z_k, its displacements can be expressed as:

$$\begin{Bmatrix} h_x \\ h_y \\ h_z \end{Bmatrix}_k = \begin{bmatrix} 1 & 0 & 0 & 0 & (z_k - z) & -(y_k - y) \\ 0 & 1 & 0 & -(z_k - z) & 0 & (x_k - x) \\ 0 & 0 & 1 & (y_k - y) & -(x_k - x) & 0 \end{bmatrix} \begin{Bmatrix} T_1 \\ T_2 \\ T_3 \\ R_1 \\ R_2 \\ R_3 \end{Bmatrix} \tag{6.75}$$

and its streamwise slopes are:

$$\begin{Bmatrix} h'_x \\ h'_y \\ h'_z \end{Bmatrix}_k = \begin{bmatrix} 0 & 0 & 0 & 0 & 0 & 0 \\ 0 & 0 & 0 & 0 & 0 & -1 \\ 0 & 0 & 0 & 0 & 1 & 0 \end{bmatrix} \begin{Bmatrix} T_1 \\ T_2 \\ T_3 \\ R_1 \\ R_2 \\ R_3 \end{Bmatrix} \tag{6.76}$$

where x, y and z are the location of the structural grid point to which the aerodynamic points are attached.

Applying Eqs 6.75 and 6.76 for M aerodynamic points by letting the index k be $k = 1, 2, \ldots, M$ yields:

$$\{\mathbf{h}\} = [\mathbf{G}_{\text{RBA}}]\{\mathbf{x}\} \tag{6.77}$$

where:

$\{\mathbf{h}\}$ and $\{\mathbf{x}\}$ are defined in Eqs 6.28 and 6.29, respectively,

and:

$[\mathbf{G}_{\text{RBA}}]$ is a 6 x M by 6 spline matrix generated by the Rigid-Body Attachment method.

Since there is no matrix inversion involved in the Rigid-Body Attachment method, $[\mathbf{G}_{\text{RBA}}]$ cannot be singular. Unsatisfactory results of the Rigid-Body Attachment method is usually caused by the over-simplified finite element model. For instance, using the transposed of $[\mathbf{G}_{\text{RBA}}]$ for the force transferal from aerodynamic points to the structural point implies that the entire aerodynamic forces on the aerodynamic component are lumped at a single structural point. This will create a highly concentrated load on the structure which may not be realistic. To avoid this kind of problem, it is suggested to refine the structural finite element model by introducing more grid points and using other spline methods such as TPS.

6.5 Matrix Assembly of the Total Spline Matrix

The generation of the total spline matrix that relates the displacements at the structural *G-set* d.o.f. to the aerodynamic *K-set* d.o.f. is performed on a component-by-component basis. The selection of the spline methods depends on the type of the component in the aerodynamic model (i.e. wing-like or body-like components) and the type of elements (beam or plate element) in the structural finite element model. Within each component, the use of several splines is also allowed. For example, a model may use the beam spline method for the inboard section, the TPS method for the outboard section and the IPS method for the aileron of a wing-like component. Separation into sub-regions of a component allows discontinuous slopes (e.g. along the wing-aileron hingeline) and discontinuous displacements (e.g. along the inboard and outboard edges of ailerons). Therefore, the spline matrices generated by different spline methods on different sub-regions are the sub-matrices of the total spline matrix. Eq 6.78 shows an example of such sub-matrix arrangement:

$$\{\mathbf{h}\} = \begin{bmatrix} [\mathbf{G}_{\mathrm{IPS}}] & \cdots & 0 & \cdots & 0 \\ \vdots & & \vdots & & \vdots \\ 0 & \cdots & [\mathbf{G}_{\mathrm{TPS}}] & \cdots & 0 \\ \vdots & & \vdots & & \vdots \\ [\mathbf{G}_{\mathrm{IPS}}] & \cdots & 0 & \cdots & 0 \\ 0 & \cdots & 0 & \cdots & [\mathbf{G}_{\mathrm{RBA}}] \end{bmatrix} \{\mathbf{x}\} \tag{6.78}$$

The degrees of freedom in $\{\mathbf{h}\}$ and $\{\mathbf{x}\}$ are grouped based on the aerodynamic and structural points, respectively, involved in each spline. Therefore, it is required to rearrange the rows and columns of the total spline matrix in Eq 6.78 according to the *K-set* and *G-set* degrees of freedom of the aerodynamic model and structural finite element model, respectively.

Finally, it should be noted that some of the degrees of freedom in the structural finite element model could be specified in local coordinate systems. It is these coordinate systems that define the displacement vectors computed by the structural finite element method. Therefore, a final transformation of $\{\mathbf{x}\}$ for these degrees of freedom is required. Let $[\mathbf{T}_m]$ be a transformation matrix that relates the local to the basic coordinate systems, then the spline matrix becomes the total such that:

$$\{\mathbf{h}\}_{K-set} = [\mathbf{G}]\, \{\bar{\mathbf{x}}\}_{G-set} \tag{6.79}$$

where:

$$[\mathbf{G}] = [\bar{\mathbf{G}}]\, [\mathbf{T}_{\mathrm{m}}]$$

$\bar{\mathbf{x}}$ is the structural displacements defined

$$\{\mathbf{x}\} = [\mathbf{T}_{\mathrm{m}}]\, \{\bar{\mathbf{x}}\}$$

and:

$[\bar{\mathbf{G}}]$ is the total spline matrix for structural displacement defined in basic coordinates.

7.0 FLUTTER SOLUTION TECHNIQUES

ZAERO provides flutter solutions for aeroelastic analysis. Several flutter methods are included in ZAERO. In this section, we will discuss the solution technique of various flutter methods. These methods include:

- *the K-method*
- *the P-K method*
- *the g-method*

Technical merits and theoretical validity of each method will also be discussed.

In Sec 2, we have derived the flutter matrix equation in the Laplace domain (Eq 2.9) in terms of the generalized mass matrix, **M**, generalized stiffness matrix **K**, and the generalized aerodynamic force matrix **Q**. Eq 2.9 reads, repeated below:

$$\left[s^2 \mathbf{M} + \mathbf{K} - q_\infty \mathbf{Q}(\frac{sL}{V}) \right] \mathbf{q} = 0 \tag{7.1}$$

Introducing a non-dimensional Laplace parameter p defined in Eq 2.23, repeated below:

$$p = \frac{sL}{V} = (\gamma k + ik) \tag{7.2}$$

where k is the reduced frequency defined in Eq 2.13, repeated below:

$$k = \frac{\omega L}{V}$$

ω is the harmonic oscillatory frequency

L is the reference length

V is the velocity of undisturbed flow

then Eq 7.1 becomes:

$$\left[\left(\frac{V}{L}\right)^2 \mathbf{M}^2 p^2 + \mathbf{K} - q_\infty \mathbf{Q}(p) \right] \mathbf{q} = 0 \tag{7.3}$$

Eq 7.3 is the so-called p-method equation. It is the desired equation for flutter analysis since its solution can provide the true damping of the aeroelastic system. However, because most of the unsteady aerodynamic methods, including ZONA6, ZONA7, ZTAIC and ZONA7U, are formulation in the reduced frequency domain (k domain) by assuming simple harmonic motion, the unsteady aerodynamic forces generated by these methods are strictly valid only at zero-damping condition. This implies that using the reduced-frequency domain unsteady aerodynamic forces (k-domain $\mathbf{Q}(ik)$) in the flutter equation, the solution is valid only at the stability boundary (the on-set of flutter). Therefore, for reliable damping prediction in the complete velocity range of interest, approximation technique for flutter solution are required.

7.1 The *K*-Method

The basic equation for flutter analysis by the K-method is expressed in Eq 2.22, repeated below:

$$[-\omega^2 \mathbf{M} + (1 + ig_s)\mathbf{K} - q_\infty \, \mathbf{Q}(ik)]\mathbf{q} = 0 \qquad (7.4)$$

Eq 7.4 is obtained by replacing p by ik in Eq 7.3, where ig_s is the added artificial complex structural damping that is proportional to the stiffness.

The introduction of ig_s was first proposed by Theodorsen (Ref 7.1) for the purpose of sustaining the assumed harmonic motion. Since the dynamic pressure q_∞ can be written as:

$$q_\infty = \frac{1}{2}\rho V^2 = \frac{1}{2}\rho\left(\frac{\omega L}{k}\right)^2 \qquad (7.5)$$

where ρ is the air density.

The K-method equation can be obtained by substituting Eq 7.5 into 7.4 and dividing the resultant equation by ω^2:

$$\left[\mathbf{M} + \frac{\rho}{2}\left(\frac{L}{k}\right)^2 \mathbf{Q}(ik) - \lambda \mathbf{K}\right]\mathbf{q} = 0 \qquad (7.6)$$

where:

$$\lambda = \frac{(1+ig_s)}{\omega^2}$$

is the complex eigenvalue of Eq 7.6.

If rigid body modes exist, Eq 7.6 cannot be solved directly since it contains some trivial solutions associated with the rigid body modes. Therefore, it is necessary to eliminate these trivial solutions by partitioning Eq 7.6 into rigid body and elastic modes:

$$\left[\begin{bmatrix} \mathbf{M}_{rr} & 0 \\ 0 & \mathbf{M}_{ll} \end{bmatrix} + \frac{1}{2}\rho\left(\frac{L}{k}\right)^2 \begin{bmatrix} \mathbf{Q}_{rr} & \mathbf{Q}_{rl} \\ \mathbf{Q}_{lr} & \mathbf{Q}_{ll} \end{bmatrix} - \lambda \begin{bmatrix} 0 & 0 \\ 0 & \mathbf{K}_{ll} \end{bmatrix}\right] \begin{Bmatrix} \mathbf{q}_r \\ \mathbf{q}_l \end{Bmatrix} = 0 \qquad (7.7)$$

where the subscripts r and l denote the rigid body modes and the elastic modes, respectively.

Since:

$$\{\mathbf{q}_r\} = -\overline{\mathbf{M}}_{rr}^{-1}\,\overline{\mathbf{M}}_{rl}\,\{\mathbf{q}_l\}$$

Eq 7.7 can be reduced to:

$$[[-\overline{\mathbf{M}}_{lr}\,\overline{\mathbf{M}}_{rr}^{-1}\,\overline{\mathbf{M}}_{rl} + \overline{\mathbf{M}}_{ll}] - \lambda[\mathbf{K}_{ll}]]\{\mathbf{q}_l\} = 0 \qquad (7.8)$$

where:

$$\overline{\mathbf{M}}_{lr} = \frac{1}{2}\rho\left(\frac{L}{k}\right)^2 \mathbf{Q}_{lr}$$

$$\overline{\mathbf{M}}_{rr} = \mathbf{M}_{rr} + \frac{1}{2}\rho\left(\frac{L}{k}\right)^2 \mathbf{Q}_{rr}$$

$$\overline{\mathbf{M}}_{rl} = \frac{1}{2}\rho\left(\frac{L}{k}\right)^2 \mathbf{Q}_{rl}$$

$$\overline{\mathbf{M}}_{ll} = \mathbf{M}_{ll} + \frac{1}{2}\rho\left(\frac{L}{k}\right)^2 \mathbf{Q}_{ll}$$

To solve for the eigenvalue λ , it is required to perform the unsteady aerodynamic computations at several given reduced frequencies. These reduced frequencies are defined here as the "reduced frequency list". $\mathbf{Q}(ik)$ are generated at a given Mach number of interest for each reduced frequency. For a given air density ρ, the eigenvalue of Eq 7.6 in terms of λ's are solved in the complete reduced frequency list. For n structural modes, there are n eigenvalues corresponding to n modes at each reduced frequency. The flutter frequency ω_f , the airspeed V_f , and artificial damping g_s are given by:

$$\omega_f = \frac{1}{\sqrt{\mathrm{Re}(\lambda)}}$$

$$g_s = \omega_f^{\,2}\,\mathrm{Im}(\lambda) \qquad (7.9)$$

$$V_f = \frac{\omega_f\, L}{k}$$

Fig 7.1 depicts a typical K-method results of the AGARD 445.6 wing (Ref 7.2) with 4 structural modes and 15 set of $\mathbf{Q}(ik)$ ranging from $k = 0.001$ to $k = 0.5$ computed by ZONA6. The K-

method is performed at a given Mach number and presented in terms of velocity vs. frequency diagram (*V-f* diagram) and velocity vs. damping diagram (*V-g* diagram).

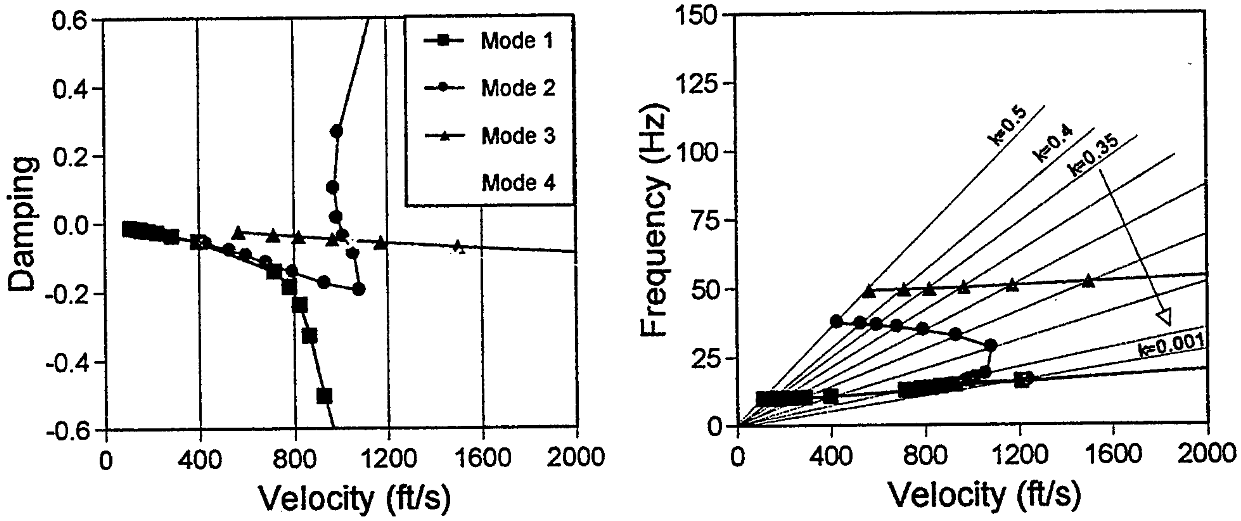

Fig 7.1 AGARD 445.6 *K*-Method Flutter Results (ZONA6), $M = 0.9$, $\rho = 0.000193$ slug/ft^3

The *V-g* diagram shows that the damping of mode 2 crosses the zero damping axis at V_f = 1000/sec indicating a flutter boundary of the wing structure. The *V-f* diagram of Fig 7.1 clearly depicts the numerical procedure of the *K*-method. At each reduced frequency, the flutter frequencies of all structural modes are located along a radial line that starts from the origin. The *K*-method solves the eigenvalues of the flutter equation, usually from the highest to the lowest frequencies in the reduced frequency list. This will give their corresponding flutter velocities generally from the low speeds to high speeds.

Since the *K*-method's numerical procedure requires only a straightforward complex eigenvalue analysis of each reduced frequency, its solution technique is efficient and robust. However, several drawbacks discussed below make the *K*-method a less attractive method for flutter analysis.

- The solution is valid only at g_s =0. Other non-zero damping values are artificial and may not have significant physical meaning.
- The frequencies and velocities are computed at a given pair of Mach number and air density. This implies that the flutter boundary computed by the *K*-method generally is not a "matched point" solution in that the flutter velocity, $V_f \neq M a_\infty$. The matched point solution can be achieved only by performing the flutter analysis at various air densities iteratively until the condition of $V_f = M a_\infty$ is satisfied.
- Sometimes the frequency and damping values "loop" around themselves and yield multi-value frequency and damping as a function of velocity. This gives difficulty in tracting the eigenvalue in the reduced frequency list.
- The term $\frac{1}{k}$ involved in Eq 7.6 indicates that the *K*-method cannot generate flutter solution at $k = 0$. This is the reason why the *K*-method excludes the rigid body modes from its flutter

equation. The failure at $k = 0$ also implies that the *K*-method cannot predict the divergence speed instability; an important aeroelastic instability problem.

7.2 The *P-K* Method

Since its applicability for flutter method analysis was first proposed by Irwin and Guyett (Ref 7.3) in 1965, the *P-K* method has been widely adopted by aeroelasticians as the primary tool for finding flutter solutions. Hassig (Ref 7.4) has given a detailed description of the superiority of the *P-K* method over the *K*-method. In Ref 7.4, the equation of the *P-K* method reads:

$$\left[\left(\frac{V^2}{L^2}\right)\mathbf{M}\,p^2 + \mathbf{K} - \frac{1}{2}\rho V^2\,\mathbf{Q}(ik)\right]\{\mathrm{q}\} = 0 \tag{7.10}$$

For simplicity, Eq 7.10 excludes the structural modal damping matrix, but it can be easily included. p is the non-dimensional Laplace parameter and can be expressed as:

$$p = g + ik \tag{7.11}$$

where:

$g = \gamma k$

γ is the transient decay rate coefficient.

The *P-K* method is an approximate method of finding a rate-of-decay of type solution. It is a mathematically inconsistent formulation since the eigenvalues p is expressed as damped sinusoidal motion while the $\mathbf{Q}(ik)$ term is obtained based on the undamped simple harmonic motion. However, it is generally believed that the *P-K* method gives a good approximation of the *p*-method.

Rodden (Ref 7.5) modified Hassig's *P-K* method equation by adding an aerodynamic damping matrix into Eq 7.10. The modified *P-K* method equation reads:

$$\left[\frac{V^2}{L^2}\mathbf{M}\,p^2 + \mathbf{K} - \frac{1}{2}\rho V^2\frac{\mathbf{Q}^{\mathrm{I}}}{k}p - \frac{1}{2}\rho V^2\,\mathbf{Q}^{\mathrm{R}}\right]\{\mathrm{q}\} = 0 \tag{7.12}$$

where:

$\mathbf{Q}^{\mathrm{R}}$ and $\mathbf{Q}^{\mathrm{I}}$ are the real part and imaginary part of $\mathbf{Q}(ik)$, i.e.:

$$\mathbf{Q}(ik) = \mathbf{Q}^{\mathrm{R}} + i\,\mathbf{Q}^{\mathrm{I}} \tag{7.13}$$

By substituting $p = g + ik$ into the third term of Eq 7.12, this equation can be rewritten as:

$$\left[\left(\frac{V^2}{L^2}\right)\mathbf{M}p^2 + \mathbf{K} - \frac{1}{2}\rho V^2 \frac{\mathbf{Q}^{\mathrm{I}}}{k} g - \frac{1}{2}\rho V^2\, \mathbf{Q}(ik)\right]\{\mathrm{q}\} = 0 \tag{7.14}$$

By comparing Eq 7.14 to Eq 7.10, it is clearly seen that the extra term:

$$-\frac{1}{2}\rho V^2 \frac{\mathbf{Q}^{\mathrm{I}}}{k} g$$

is the added aerodynamic damping matrix. Eq 7.12 is solved at several given values of V and ρ, for complex roots p associated with modes of interest. This is accomplished by an iterative procedure that matches the reduced frequency k to the imaginary part of p for every structural mode. This iterative procedure is called the reduced frequency "lining-up" process (Ref 3.3) which requires the repeated interpolation of $\mathbf{Q}(ik)$ from these of the reduced frequency list.

Fig 7.2 shows the *P-K* solutions of the AGARD 445.6 wing described in Sec 7.1 at six given velocities from 700 to 1200 ft/sec with intervals of 100 ft/sec. The damping and frequency values at each given velocity are presented in the *V-g* and *V-f* diagrams in Fig 7.2.

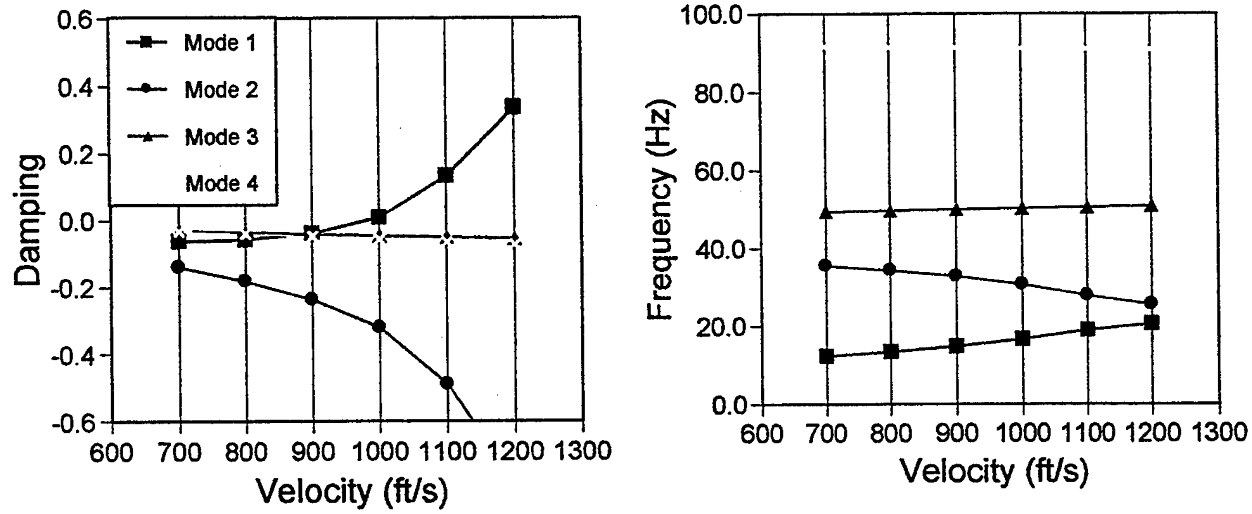

Fig 7.2 AGARD 445.6 *P-K* Method Flutter Results (ZONA6), $M = 0.9$, $\rho = 0.000193$ slug/ft^3

Comparing Fig 7.2 to Fig 7.1, it can be seen that the *P-K* method yields "well-behaved" damping and frequency curves; no "loop" problem occurs. The predicted V_{f} and ω_{f} at zero damping agree very well with these of the *K*-method. The well-behaved damping and frequency curves are believed to be more realistic than these of the *K*-method. Also, for the present AGARD 445.6 case, the *P-K* method predicts a flutter mode associated with the first mode as opposite to the second mode by the *K*-method.

A more meaningful contrast of the tow methods can be seen when the divergence speed instability occurs. Fig 7.3 shows the *V-g* and *V-f* diagrams of the *K*-method and the *V-g* and *V-f* diagrams of a jet transport wing (Ref 7.6) with 10 modes at $M = 0$. Both methods predict a flutter speed V_f at 1050 ft/sec. This is expected since at zero damping both methods reduce to the same equation.

A significant difference does occur when a divergence speed instability appears at 1651 ft/sec. This divergence speed instability is evident by its associated zero frequency. The *V*-*g* curve of the bending mode predicted by the *K*-method approaches the zero damping axis perpendicularly but doe not cross it. The corresponding damping cure of the *P*-*K* method has a discontinuity but it develops the divergence speed instability. It is believed that this discontinuity is associated with the occurrence of an aerodynamic lag root. In the next section, we will discuss the physical significance of the aerodynamic lag root.

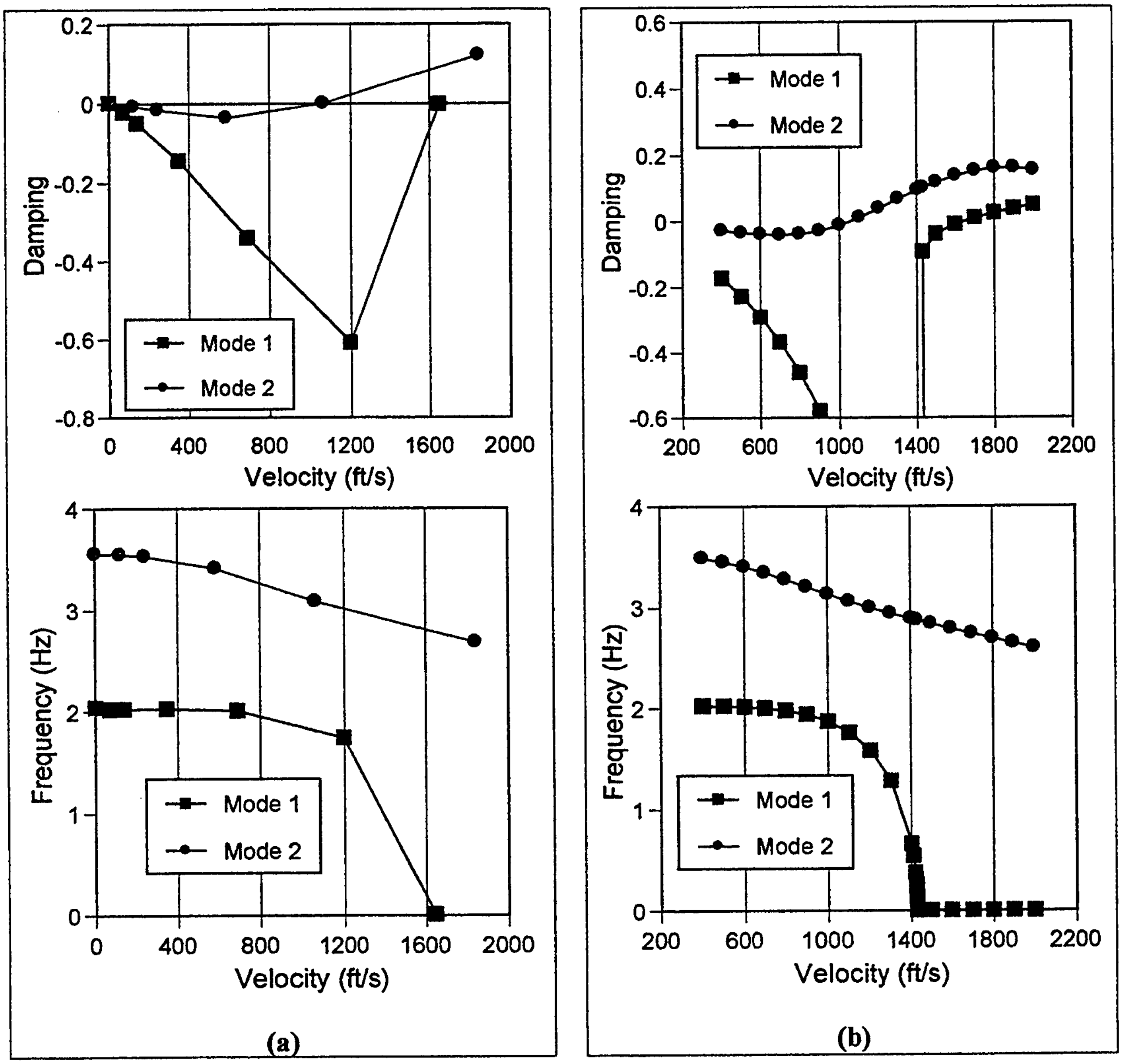

(a) (b)

Fig 7.3 Jet Transport Wing at M=0.0 at Sea Level using: (a) *K-Method* (b) *P-K* Method

Another principal advantage of the cure of the *P-K* method is that it produces results directly for given values of velocity and air density pairs. This allows the cure of the *P-K* method to provide the matched point solution in that the given velocity and air density satisfy $V_f = M\,a_\infty$. However, in the next section, we will show that the added aerodynamic damping matrix in Eq 7.12 is valid only at small k or for linearly varying $\mathbf{Q}(ik)$. For highly nonlinear $\mathbf{Q}(ik)$, the *P-K* method may produce unrealistic root.

7.3 The *g*-Method

By utilizing a damping perturbation method, Chen (Ref 7.7) suggested that a first order damping term can be included in the flutter equation. This first order damping term is rigorously derived from the Laplace domain aerodynamic, leading to a flutter solution technique called the "g-method".

Formulation of the g-Method

The basic assumption of the *g*-method lies in the existence of an analytic function of $\mathbf{Q}(p) = \mathbf{Q}(g+ik)$, where $g = \gamma k$ so that $\mathbf{Q}(p)$ can be expanded along the imaginary axis (i.e., $g = 0$) for small g by means of a damping perturbation method:

$$\mathbf{Q}(p) \approx \mathbf{Q}(ik) + g\left.\frac{\partial \mathbf{Q}(p)}{\partial g}\right|_{g=0}, \qquad \text{for } g \ll 1 \tag{7.15}$$

The second term on the right hand side of Eq 7.15 is generally not available from the k-domain unsteady aerodynamic methods. However, due to analytic continuation, it can be replaced by:

$$\left.\frac{\partial \mathbf{Q}(p)}{\partial g}\right|_{g=0} = \left.\frac{\partial \mathbf{Q}(p)}{\partial (ik)}\right|_{g=0} = \frac{d\mathbf{Q}(ik)}{d(ik)} = \mathbf{Q}'(ik) \tag{7.16}$$

Eq 7.16 is valid in the complete p-domain except along the negative real axis in subsonic flow (Ref 7.8). This implies that $\mathbf{Q}'(ik)$ can be computed from $\mathbf{Q}(ik)$ by a central differencing scheme, except at $k = 0$. At $k = 0$, a forward differencing scheme is employed to accommodate the discontinuity of $\mathbf{Q}(ik)$ along the negative real axis. Substituting Eq 7.16 into Eq 7.15 yields the approximated p-domain solution of $\mathbf{Q}(p)$ in terms of k and for small g:

$$\mathbf{Q}(p) \approx \mathbf{Q}(ik) + g\,\mathbf{Q}'(ik) \tag{7.17}$$

Substituting Eq 7.17 into Eq 7.3 yields the *g*-method equation:

$$\left[\left(\frac{V^2}{L^2}\right)\mathbf{M}\,p^2 + \mathbf{K} - \frac{1}{2}\rho V^2\,\mathbf{Q}'(ik)\,g - \frac{1}{2}\rho V^2\,\mathbf{Q}(ik)\right]\{\mathrm{q}\} = 0 \tag{7.18}$$

At $g = 0$, both the g-method and the *P-K* method reduce to the same form. This indicates that both methods will provide the same flutter boundary for zero damping. For non-zero *g*, comparing Eq 7.18 to Eq 7.14, it can be seen that the difference between the *P-K* method equation and the *g*-method equation lies in the terms $\mathbf{Q}^{I}/k$ in Eq 7.14 and $\mathbf{Q}'(ik)$ in Eq 7.18. In fact, $\mathbf{Q}^{I}/k$ is a special case of $\mathbf{Q}'(ik)$. This can be shown as follows:

Expanding $\mathbf{Q}(ik)$ about $ik = 0$ by Taylor's expansion gives:

$$\mathbf{Q}(ik) = \mathbf{Q}(0) + ik\,\mathbf{Q}'(0) + \frac{1}{2}(ik)^2\,\mathbf{Q}''(0) + \ldots \qquad (7.19)$$

Since all $\mathbf{Q}''(0)$ are real, $\mathbf{Q}(ik)$ can be split into the real and imaginary parts. It reads:

$$\mathbf{Q}(ik) = \mathbf{Q}^{R} + i\,\mathbf{Q}^{I} \qquad (7.20)$$

where:

$$\mathbf{Q}^{R} = \mathbf{Q}(0) - \frac{1}{2}k^2\,\mathbf{Q}''(0) + \ldots \qquad (7.21)$$

and:

$$\mathbf{Q}^{I} = k\,\mathbf{Q}'(0) - \frac{1}{6}k^3\,\mathbf{Q}'''(0) + \ldots \qquad (7.22)$$

Dividing Eq 7.22 by k gives the term $\mathbf{Q}^{I}/k$ in Eq 7.14 as:

$$\frac{\mathbf{Q}^{I}}{k} = \mathbf{Q}'(0) - \frac{1}{6}k^2\,\mathbf{Q}'''(0) + \ldots \qquad (7.25)$$

Differentiating Eq 7.19 with respect to ik gives the term $\mathbf{Q}'(ik)$ in Eq 7.18 as:

$$\mathbf{Q}'(ik) = \mathbf{Q}'(0) + ik\,\mathbf{Q}''(0) + \ldots \qquad (7.26)$$

Comparison of Eq 7.23 with Eq 7.24 shows that the equality of $\mathbf{Q}^{I}/k$ and $\mathbf{Q}'(ik)$ exists only if $\mathbf{Q}(ik)$ is a linear function of k or at $k = 0$. This proves that the added aerodynamic damping matrix in Eq 7.14 is valid only if one of the above conditions is satisfied. In fact, if $\mathbf{Q}(ik)$ is highly nonlinear, the *P-K* method may produce unrealistic roots due to the error from the differences between Eq 7.23 and Eq 7.24.

Solution Algorithm of the g-Method

Substituting $p = g + ik$ into Eq 7.18 yields a second-order linear system in terms of g:

$$[g^2\,\mathbf{A} + g\,\mathbf{B} + \mathbf{C}]\{\mathrm{q}\} = 0 \qquad (7.25)$$

where:

$$\mathbf{A} = \left(\frac{V}{L}\right)^2 \mathbf{M}$$

$$\mathbf{B} = 2\,ik\left(\frac{V}{L}\right)^2 \mathbf{M} - \frac{1}{2}\rho V^2\, \mathbf{Q}'(ik) + \left(\frac{V}{L}\right)\mathbf{Z}$$

$$\mathbf{C} = -k^2\left(\frac{V}{L}\right)^2 \mathbf{M} + \mathbf{K} - \frac{1}{2}\rho V^2\, \mathbf{Q}(ik) + ik\left(\frac{V}{L}\right)\mathbf{Z}$$

Here, Eq 7.25 is formally called the *g*-Method equation. For completeness, in Eq 7.25, we have included a modal structural damping matrix **Z**. The solutions of Eq 7.25 exist when Im(*g*) = 0. To search for this condition, we first rewrite Eq 7.25 in a state space form:

$$[\mathbf{D} - g\,\mathbf{I}]\{\mathbf{X}\} = 0 \tag{7.26}$$

where:

$$\mathbf{D} = \begin{bmatrix} \mathbf{0} & \mathbf{I} \\ -\mathbf{A}^{-1}\mathbf{C} & -\mathbf{A}^{-1}\mathbf{B} \end{bmatrix} \tag{7.27}$$

Next, a reduced-frequency-sweep technique is introduced. This technique searches for the condition Im(*g*) = 0 and solves for the eigenvalues of **D** in term of *g*; starting from $k = 0$, incrementally increasing *k* by Δk, and ending at $k_{\max}$ ($k_{\max}$ is the highest value in the reduced frequency list of the unsteady aerodynamic computations). The reduced frequency-sweep technique searches for the sign change of the imaginary part of the eigenvalues between *k* and $|k + \Delta k|$. If this occurs, the condition of Im(*g*) = 0 can be obtained by a linear interpolation in *k* for the appropriate frequency range. Then the flutter frequency ω_f and damping 2γ are computed by:

$$\omega_f = k\left(\frac{V}{L}\right) \tag{7.27}$$

$$2\gamma = 2\frac{\mathrm{Re}(g)}{k} \tag{7.28}$$

For $k = 0$, an alternative form of Eq 7.28 is used (Ref 7.9):

$$2\gamma = \frac{\mathrm{Re}(g)\left(\dfrac{L}{V}\right)}{\ln(2)} \tag{7.29}$$

One of the issues in performing the reduced frequency-sweep technique is the eigenvalue tracking from *k* to $|k + \Delta k|$. In order to monitor the sign change of eigenvalues, it is required that the eigenvalues are lined up at each k and $|k + \Delta k|$. Using the regular sorting scheme by comparing the differences of the eigenvalues at $|k + \Delta k|$ to those at k is certainly not robust and requires small Δk values that may be costly. This eigenvalue tracking issue can be resolved by means of a predictor-corrector scheme.

Predictor-Corrector Scheme for Eigenvalue Tracking

The predictor predicts the eigenvalues at $|k + \Delta k|$ by a linear extrapolation from the eigenvalues and their derivatives at k:

$$g_p(k + \Delta k) = g(k) + \Delta k \frac{dg}{dk} \tag{7.30}$$

where g_p is defined as the predicted eigenvalue. $\frac{dg}{dk}$ can be obtained by using the orthogonality property of the left and right eigenvectors of Eq 7.26. This leads to:

$$\frac{dg}{dk} = \frac{\left(\mathbf{Y}^T \frac{d\mathbf{D}}{dk} \mathbf{X}\right)}{\mathbf{Y}^T\mathbf{X}} \tag{7.31}$$

where **Y** and **X** are the left and right eigenvectors of Eq 7.26, respectively, and:

$$\frac{d\mathbf{D}}{dk} = \begin{bmatrix} 0 & 0 \\ -\mathbf{A}^{-1}\frac{d\mathbf{C}}{dk} & -\mathbf{A}^{-1}\frac{d\mathbf{B}}{dk} \end{bmatrix} \tag{7.32}$$

Once g_p is given by the predictor, g_p is used as the baseline eigenvalues for sorting the computed eigenvalues at $|k + \Delta k|$, defined as g_c. The maximum norm of the error between g_p and g_c for all eigenvalues is also computed. If it exceeds a certain level, the predictor could potentially introduce incorrect eigenvalue tracking results due to rapid changes of the eigenvalues. In this case, the corrector is activated.

The corrector reduces the size of Δk by a factor, for instance 100, and recomputes g_p and g_c at $\left(k + \frac{\Delta k}{100}\right)$ as well as the maximum norm of the error. This process repeats until the maximum norm of the error is below a certain level. However, numerical experience shows that when the corrector is activated, this condition can be satisfied by reducing the size of Δk only once. Therefore, the corrector normally would not increase the computational time significantly. It serves only as a fail-safe scheme.

At $k = k_{\max}$, $\frac{dg}{dk}$ is also used to search for the condition Im(g) = 0 at $k > k_{\max}$ by a linear extrapolation. Thus, the reduced-frequency-sweep technique offers a scheme that could find all real roots of Eq 7.25 in the complete reduced frequency domain.

At this point, the issue of the number of real roots that could exist in Eq 7.25 is discussed. For n structural modes, the *P-K* method and *K*-method normally provide only n roots of the flutter equation. However, as indicated by Ref 26, the number of roots could exceed the number of the structural modes if the aerodynamic lag roots appear. For instance, if the exact Theodorsen function is used, the number of aerodynamic lag roots that would appear is infinite. As one can see, unlike the *P-K* and *K*-methods, the reduced frequency-sweep technique employed by the present *g*-method potentially gives an unlimited number of roots. The inclusion of all activated aerodynamic lag roots could provide important physical interpretations of the flutter solution.

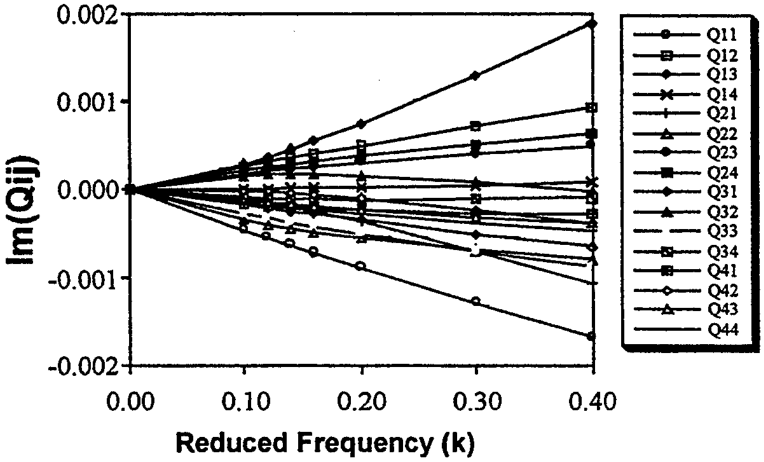

Fig 7.4 Generalized Aerodynamic Forces vs. Reduced Frequency of the 15° Sweptback Wing at $M = 0.45$, 4 Modes

Comparison Between the g-Method and the P-K Method

- *The 15-Degree Sweptback Wing at $M = 0.45$*

This test case is denoted as HA145E in Ref 3.3. Four structural modes are used for flutter analysis. The imaginary parts of the 4 x 4 generalized aerodynamic forces matrix (denoted as $\mathbf{Q}_{ij}$) vs. k are presented in Fig 7.4. Since Im($\mathbf{Q}_{ij}$) are all nearly linear that gives a close equality of Eq 7.23 and Eq 7.25, the agreement between the damping computed by the *P-K* method and the g-method is expected. Fig 7.5 shows the damping vs. velocity diagram (*V-g* diagram) and the flutter frequency vs. velocity diagram (*V-f* diagram) computed by both methods. Good agreement between these methods is obtained except the g-method predicts one extra aerodynamic lag root (represented by the crosses in Fig 2). This aerodynamic lag root becomes active at $V = 550$ ft/sec with stable damping but its frequency remains zero. Since the number of roots computed by the *P-K* method is restricted to be the same as the number of the structural modes, at $V = 600$ ft/sec the *P-K* method's reduced frequency "lining-up" process skips the bending mode and obtains the aerodynamic lag root; this creates a discontinuity of the damping associated with the bending mode in the v-g diagram (represented by the opened triangles). By contrast, the g-method gives a continuous damping curve of the bending mode (represented by the solid triangles) and a discontinuity in the damping curve of the aerodynamic lag root (the crosses) at $V = 550$ ft/sec.

In order to investigate how the g-method obtains the aerodynamic lag root, the search history in terms of eigenvalues vs. k for the reduced frequency-sweep technique is presented in Fig 7.6 for $V = 500$ ft/sec and Fig 7.7 for $V = 650$ ft/sec. Since there are 4 structural modes, the state space form of Eq 7.26 provides 8 eigenvalues. At $V = 500$ ft/sec the imaginary parts (Im(g)) of these 8 eigenvalues provide four zero crossings (marked by the opened circles in Fig 7.6). These four zero crossings represent the four roots of the four structural modes.
It is noted that the zero crossing of the first eigenvalue is obtained by extrapolation from the eigenvalue and its derivative at $k = k_{\max}$. At $V = 650$ ft/sec Im(g) of the seventh eigenvalue becomes zero at $k = 0$ which corresponds to the occurrence of the aerodynamic lag root. This can be seen clearly in the expanded view of Im(g) at small k (at the upper right corner of Fig 7.7). The real part of this eigenvalue (Re(g)) at $k = 0$ has a negative value (Fig 7.7) that indicates this aerodynamic lag root is stable; however, the expanded view shows a potential coupling between the aerodynamic lag root and the sixth eigenvalue since the zero crossing of the sixth eigenvalue already occurs at small k. This indicates an instability may appear at a higher velocity.

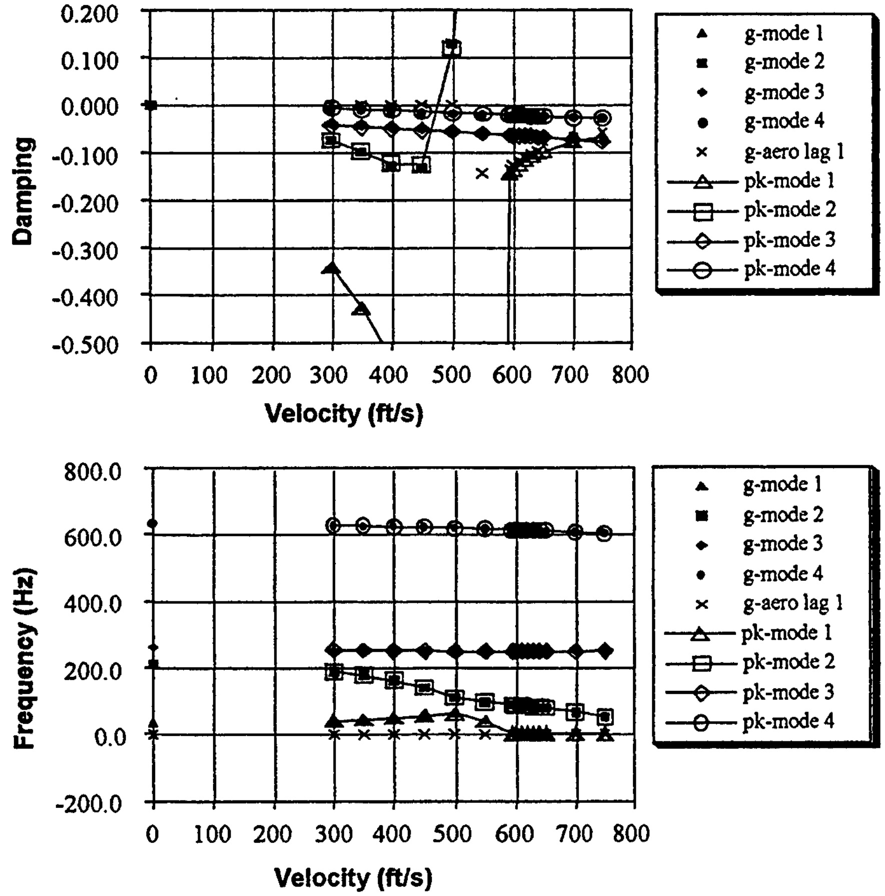

Fig 7.5 ***V-g*** **and** ***V-f*** **Diagrams of the 15° Sweptback Wing at** $M = 0.45$

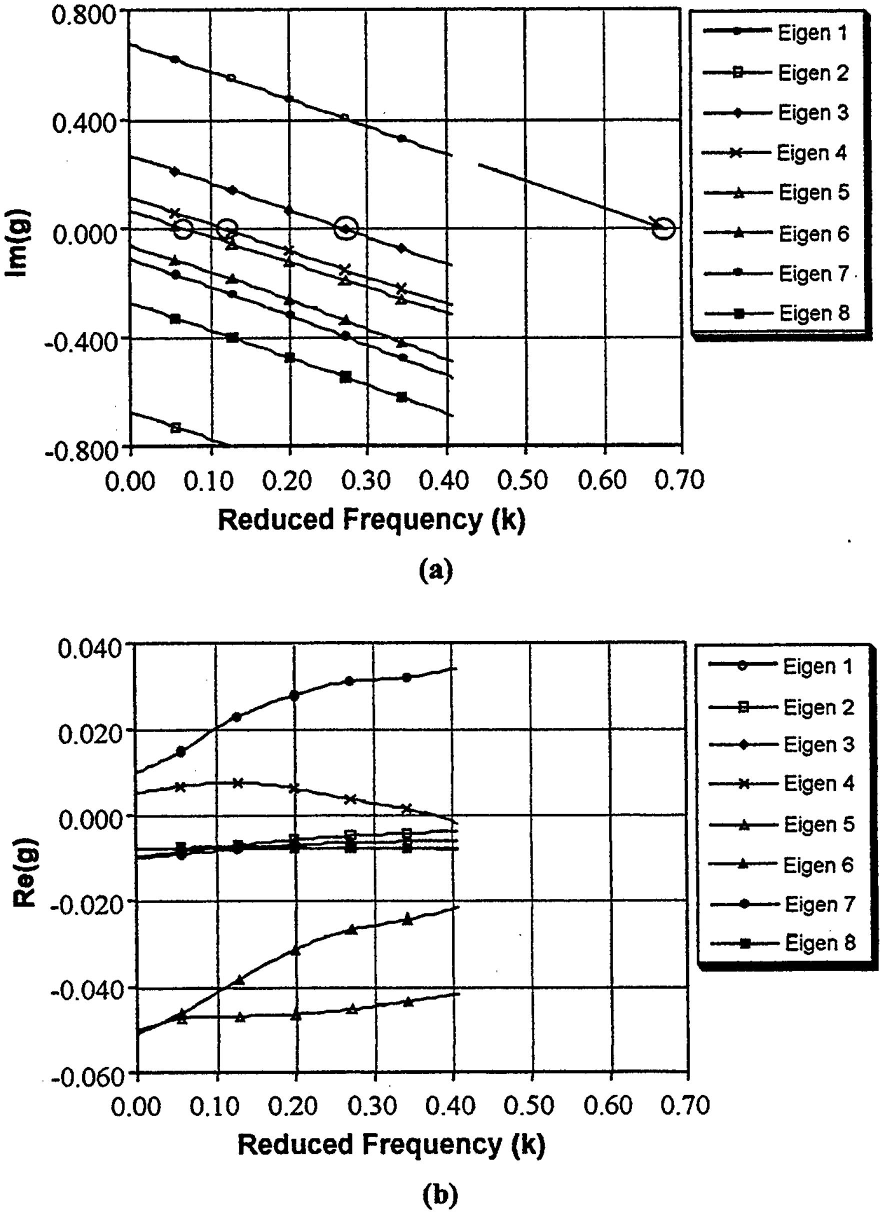

Fig 7.6 Search History of the Reduced Frequency-Sweep Technique at *V* = 500 ft/sec, (a) Imaginary Damping and (b) Real Damping

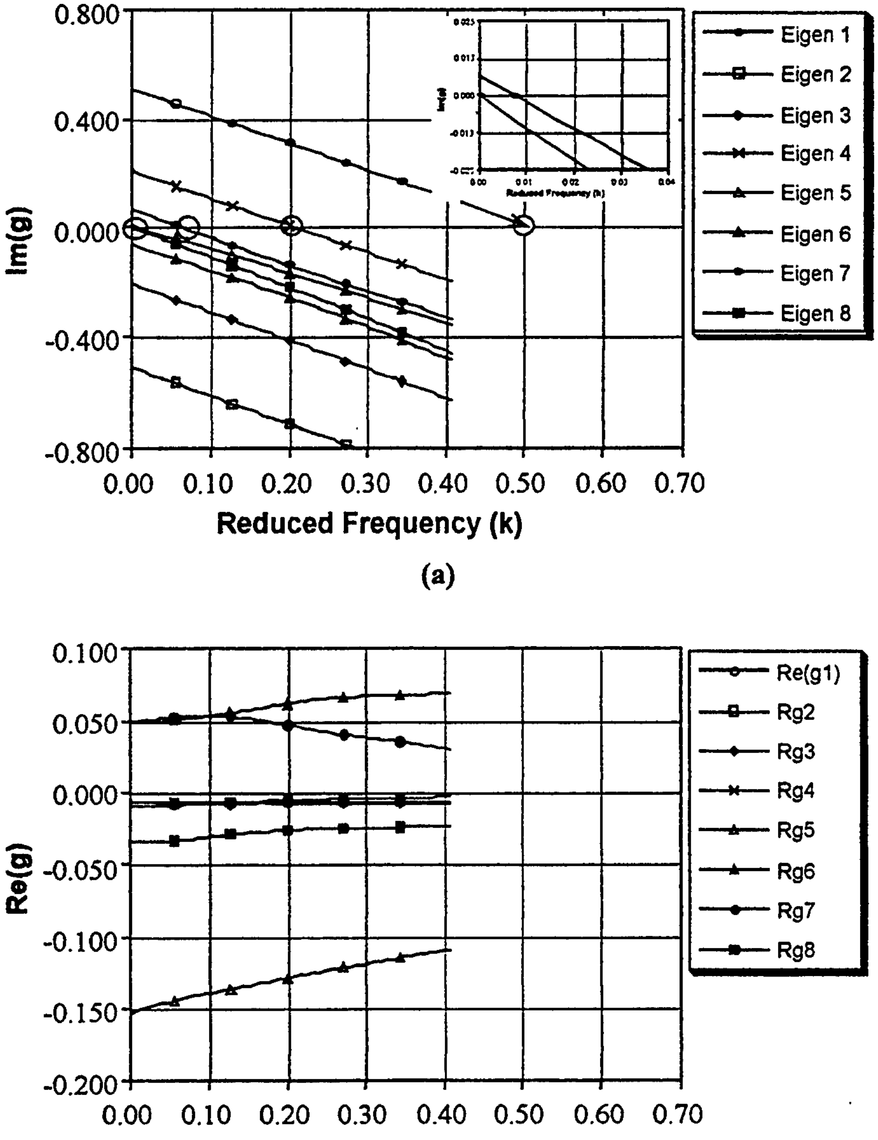

(a)

(b)

Fig 7.7 Search History of the Reduced Frequency-Sweep Technique at *V* = 600 ft/sec

- *Jet Transport Wing at M = 0.0 with 10 Modes*

This test case has been discussed in Sec 7.2. Ten structural modes are used for flutter analysis but only the results of the first bending and torsion modes are presented in the *V-g* and *V-f* diagrams shown in Fig 7.8. Two types of instability are predicted by both the *P-K* method and the g-method: a flutter speed at *V* = 1056 ft/.sec and a divergence speed at *V* = 1651 ft/.sec. This agreement is expected since at $g = 0$ the flutter equation of both methods reduce to the same form. Three aerodynamic lag roots are obtained by the *g*-method and their frequencies are all zero throughout the velocity range of interest. Both of the first and second aerodynamic lag roots become active at the same speed (V = 1400 ft/sec). After this speed, the second aerodynamic lag root forms a super-stable mode but at this speed the damping of the first aerodynamic lag root jumps suddenly from zero to – 0.1 then gradually crosses the zero-damping axis, forming a divergence type of instability at *V* = 1651 ft/sec. At this divergence speed, the third aerodynamic lag root becomes active and suddenly jumps to a high value of unstable damping (Fig 7.8). This is an interesting phenomenon because it indicates that this divergence speed could be a bifurcation point. Determining the third aerodynamic lag root is bifurcated from the first aerodynamic lag root or originates on its own needs further investigation.

Similarly to the first test case, the damping curve of the bending mode computed by the *P-K* method has a discontinuity while that of the *g*-method remains a smooth curve. The damping curve of the torsion mode computed by both methods are in excellent agreement. The frequency curves of the two structural modes computed by both methods also in good agreement except for the absence of the three aerodynamic lag roots of the *P-K* method.

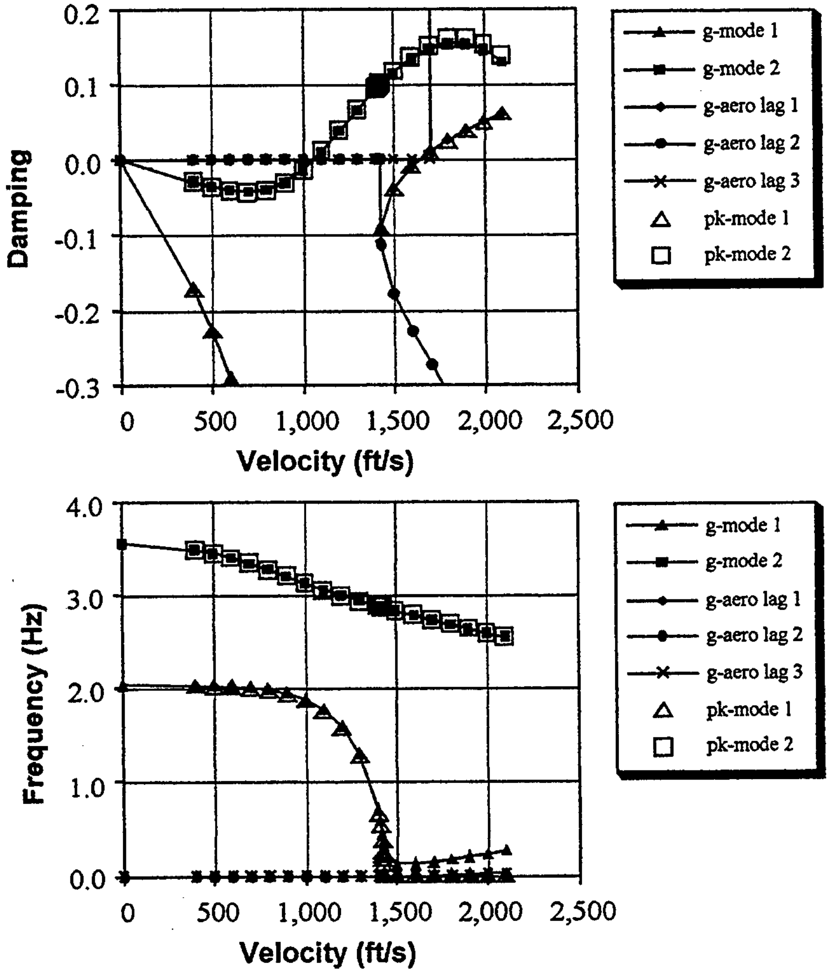

Fig 7.8 ***V-g*** **and** ***V-f*** **Diagrams of the BAH Wing,** ***M*** **= 0.0, 10 Modes**

- *Two Degrees of Freedom Airfoil at M = 0.0*

This test case is adopted from Ref 7.10 and is derived from the case denoted as HA145A in Ref 3.3 but with the fuselage grid point being constrained. The center of gravity is located at 37% chord. Fig 7.9 presents the variations of the 2 x 2 $\mathbf{Q}_{ij}$ vs. k. In this case, Fig 7.9 shows that the imaginary parts of $\mathbf{Q}_{ij}$ is not linear. Therefore, some difference in flutter results between the *P-K* method and the *g*-method is expected. First, for clarity, the *V-g* diagram computed by the *g*-method alone is presented in Fig 7.10. Two aerodynamic lag roots are found. Again, it seems that the second aerodynamic lag root is bifurcated from the first one at $V = 210$ ft/sec where a divergence instability occurs. The comparison of the damping and flutter frequencies between the *P-K* method and the *g*-method is shown in Fig 7.11; however, for clarity, the second aerodynamic lag root is not repeatedly shown. In Fig 7.11 the results computed by the transient method are also presented. The transient method is based on a time-domain unsteady aerodynamic method, therefore it can be considered as a p-method. All of the three methods predict the same instabilities: a divergence instability at $V = 210$ ft/sec and a flutter instability at $V = 250$ ft/sec. The damping curves of the first and second modes computed by the *g*-method correlate well with those of the transient method. But, again, the *P-K* method gives a discontinuous damping curve of the first mode.

For the case of the center of gravity moved to 45% chord, the *V-g* diagram shown in Fig 12.a indicates that the flutter instability (at $V = 170$ ft/sec) occurs before the divergence instability (at V=225 ft/sec). Again, this is well predicted by all three methods. The frequency curves in the *V-f* diagram (Fig 12.b) computed by the g-method show a similar trend as those of the transient method. But the curves of the *P-K* method are discontinuous at $V = 100$ ft/sec where an aerodynamic lag root appears (not obtained by the transient method but well captured by the *g*-method). This results a poor correlation of the *V-f* curves obtained by the *P-K* method with the other two methods.

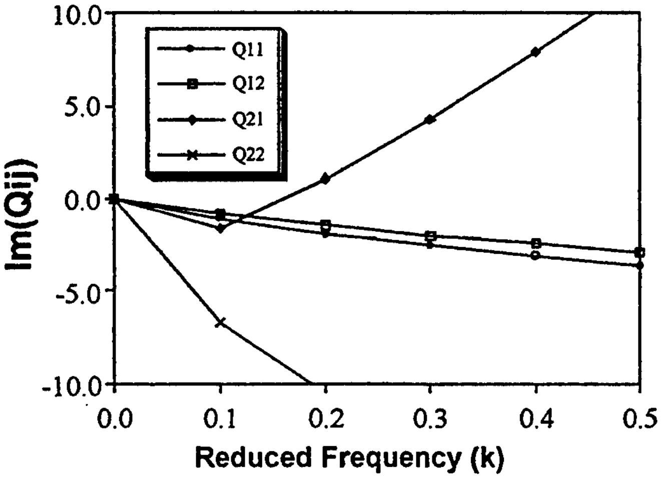

Fig 7.9 Generalized Forces of 2 D.O.F. Airfoil, C.G. @ 37% Chord (HA145A1), $M = 0.0$, 2 Modes

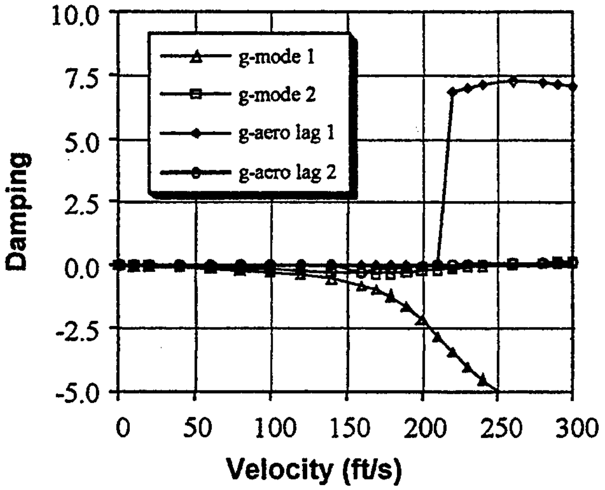

Fig 7.10 2 D.O.F. Airfoil, C.G. @ 37% Chord (HA145A1), $M = 0.0$, 2 Modes

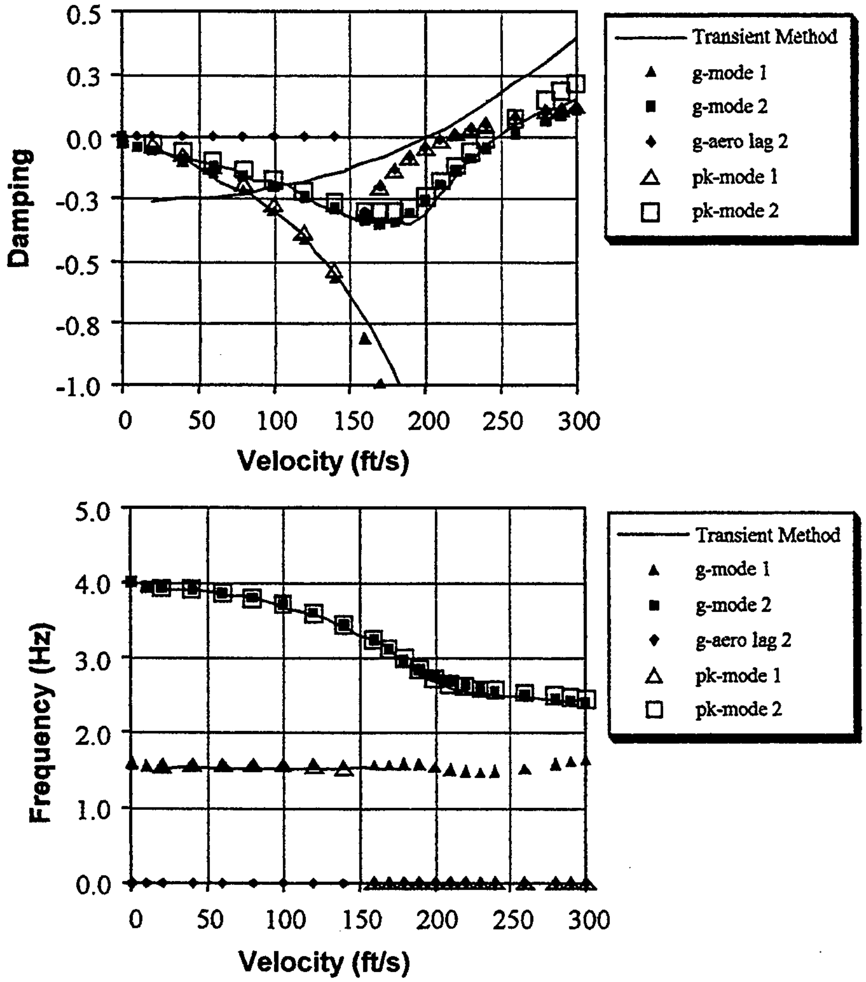

Fig 7.11 Damping and Frequency vs. Velocity of 2 D.O.F. Airfoil, C.G. @ 37% Chord (HA145A1), $M = 0.0$, 2 Modes

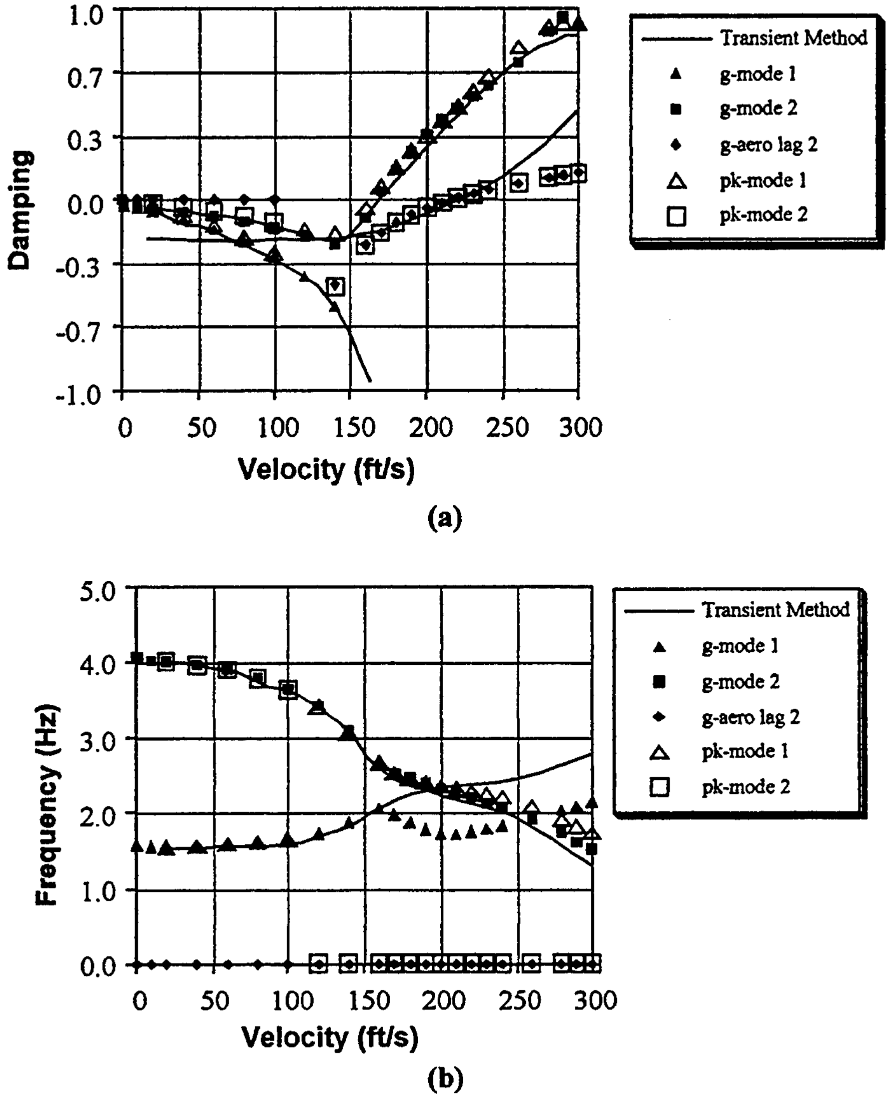

Fig 7.12 Damping and Frequency vs. Velocity of 2 D.O.F. Airfoil, C.G. @ 45% Chord (HA145A2), $M = 0.0$, 2 Modes

- *Three Degrees of Freedom Airfoil at M = 0.0*

This test case is denoted as HA145A in Ref 3.3. A fuselage free-free plunge mode is added in the above two degrees of freedom case. The *V-g* and *V-f* diagrams for the case of the center of gravity located at 37% chord are shown in Fig 7.13 and those for 45% chord are in Fig 7.14. For both cases, the so-called "dynamic divergence" (Ref 7.11) occurs and its speeds and frequencies are well predicted by all three methods: the *P-K* method, the *g*-method, and the transient method. Both the *g*-method and the transient method capture one aerodynamic lag root (in the 45% chord case, the *g*-method obtains a second lag root but it becomes active at the dynamic divergence speed and is not discussed here). Unlike the restrained structures of all previous test cases where the frequency of the lag roots remains zero, the aerodynamic lag root of the present unrestrained structure 'takes off' from the zero-frequency axis then couples with the bending mode. This coupling of the lag root and bending mode forms a "dynamic divergence" instability.

As indicated by Ref 7.11, this dynamic divergence has a non-zero frequency and could be defined as a low-frequency flutter instability. On the other hand, the *P-K* method generated lag root somehow refuses to 'take off' from the zero-frequency axis. This problem of the *P-K* method is probably due to the fact that since $\mathbf{Q}_{ij}$ of the present test case is nonlinear, the *P-K* method is valid only at $k = 0$ for non-zero damping. This $k = 0$ condition restricts the frequency of the lag root from being a non-zero value and results in a poor correlation in the *V-f* diagram with the other two methods.

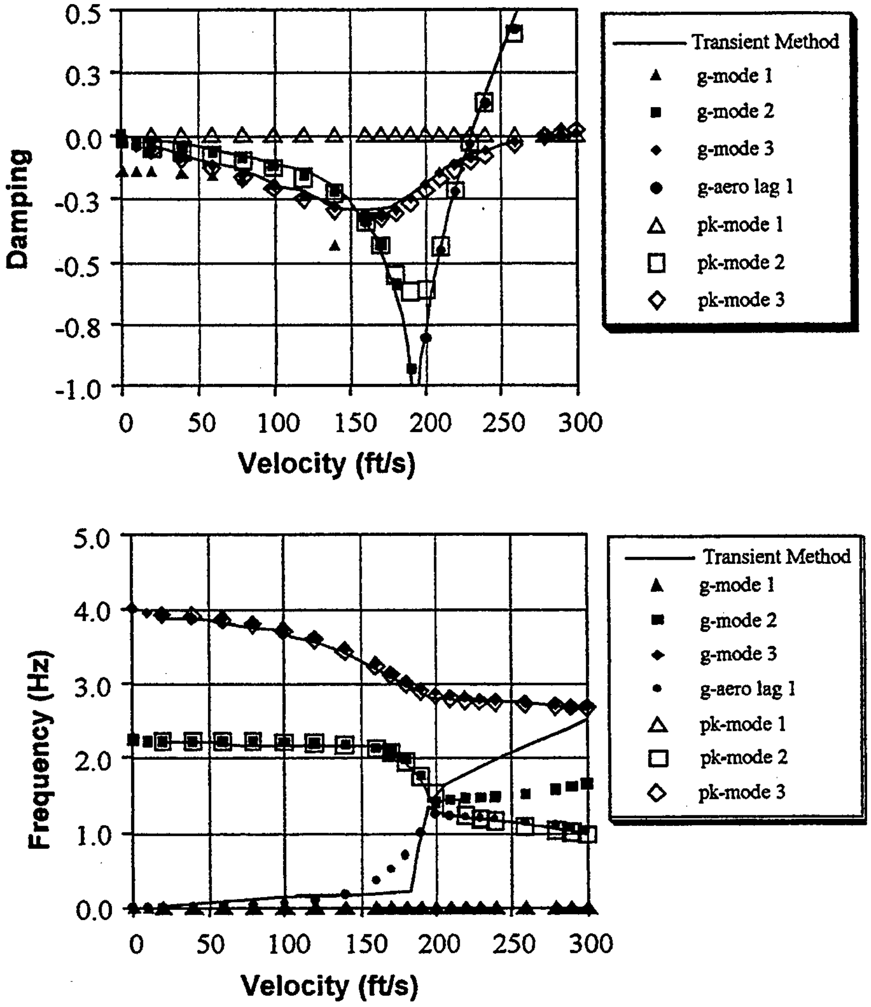

Fig 7.13 Damping and Frequency vs. Velocity of 3 D.O.F. Airfoil, C.G. @ 37% Chord (HA145A2), $M = 0.0$, 3 Modes

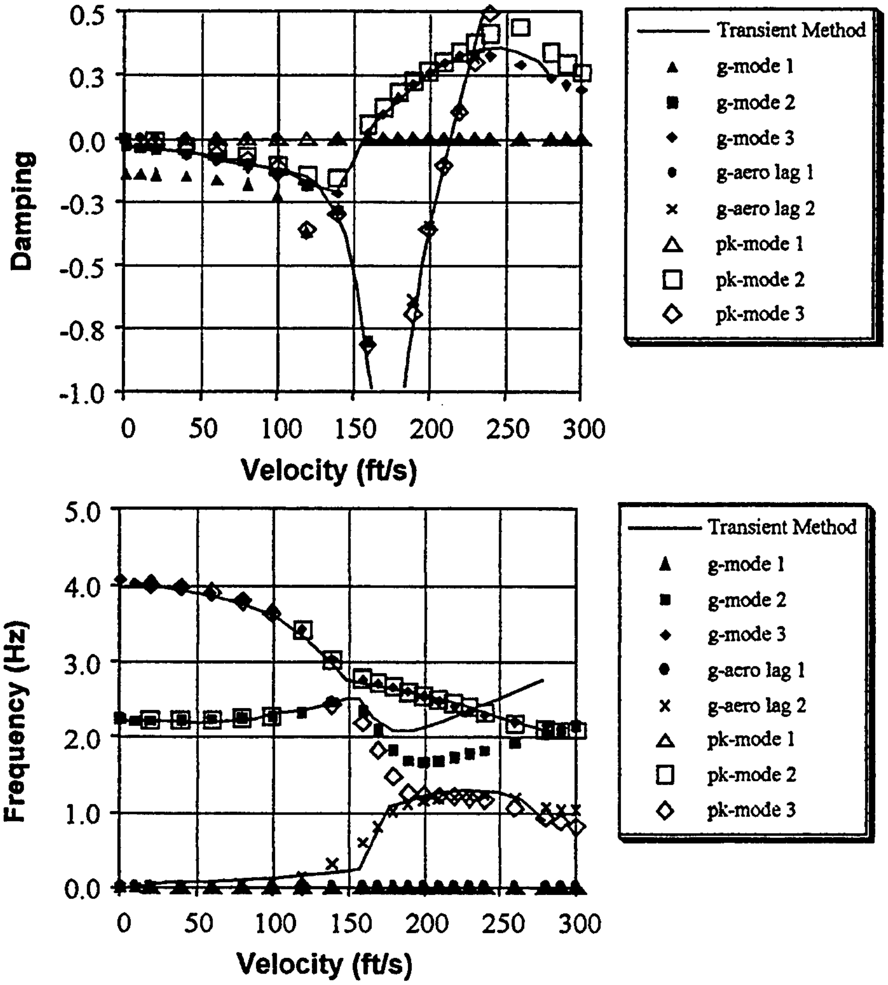

Fig 7.14 Damping and Frequency vs. Velocity of 3 D.O.F. Airfoil, C.G. @ 45% Chord (HA145A2), $M = 0.0$, 3 Modes

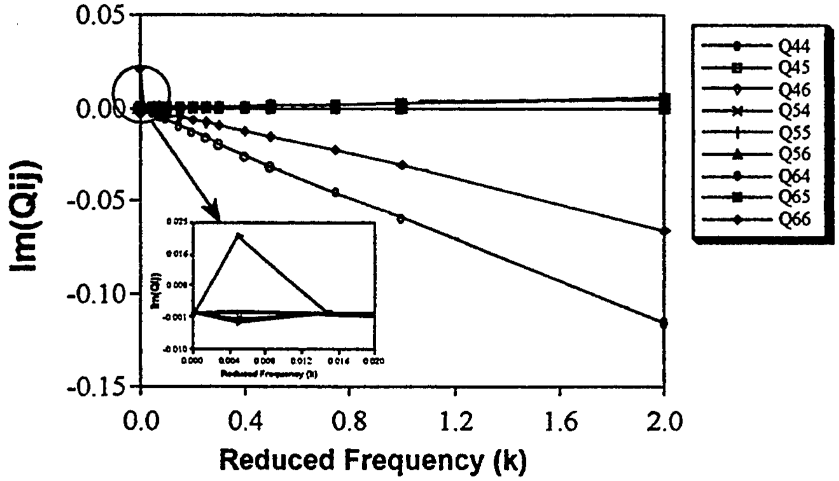

Fig 7.15 Johnson Configuration Generalized Aerodynamic Forces, M=0.84, 17 Modes

- *The Johnson Configuration at M = 0.84 with 17 Modes*

This test case is adopted from Ref 7.12. The Johnson configuration has three rigid body modes and 14 elastic modes. The imaginary parts of $\mathbf{Q}_{ij}$ vs. k for i and j = 4, 5 and 6 presented in Fig 7.15 show that spikes occur at small k. The cause of the spikes is probably due to poor aerodynamic modeling; but this is not an issue to be discussed here. Since $\mathbf{Q}_{ij}$ are highly nonlinear, a large difference between the results obtained from the *P-K* method and the *g*-method is anticipated. In fact, in this case the *P-K* method breaks down (Ref 7.12) and its results are totally unreliable. It is believed that the break-down of the *P-K* method is caused by the unrealistic roots produced by the nonlinear $\mathbf{Q}_{ij}$. In order to validate the g-method result, the *K*-method is used for comparison.

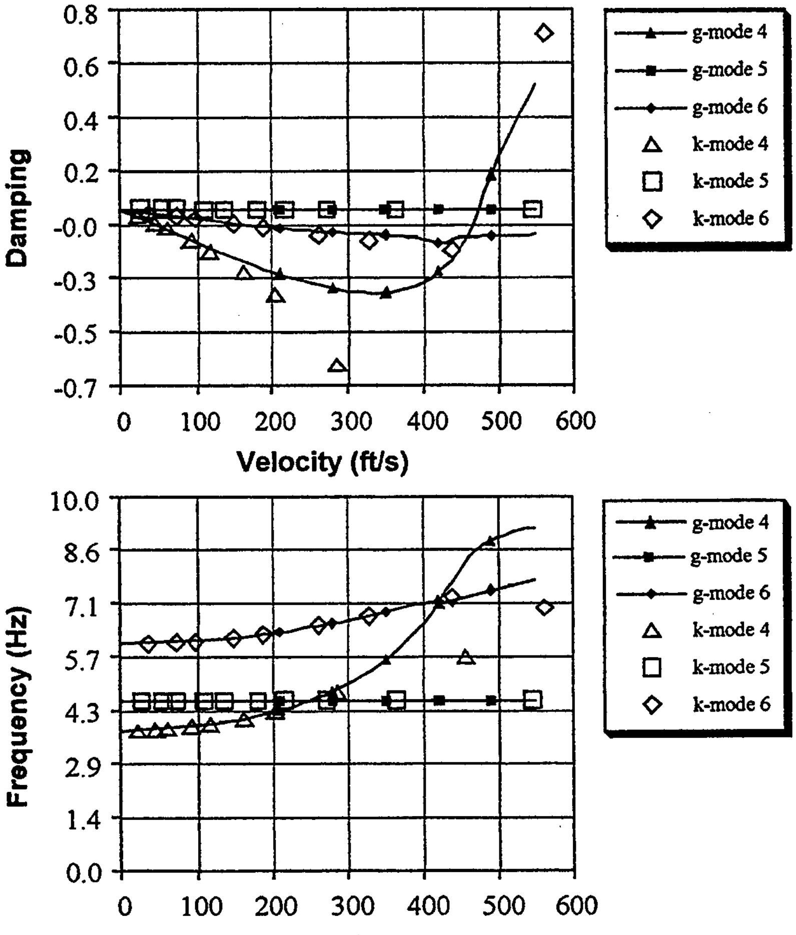

Fig 7.16 Damping and Frequency vs. Velocity of Johnson Configuration, M = 0.84, 17 Modes

There are 13 aerodynamic lag roots obtained by the *g*-method. Due to the spikes at small k, some of them become active even at very low speed. These lag roots are not presented here. Fig 7.16 shows the *V-g* and *V-f* diagrams obtained by the *K*-method and the *g*-method for the first three elastic modes; denoted as mode 4, 5, and 6. It can be seen that both methods predict the same flutter boundary around $V = 470$ ft/sec. The good agreement between the *K*-method and the g-method indicates the robustness of the g-method's solution algorithm.

It is generally believed that the *K*-method is only valid at the $g = 0$ condition. The present work also proves that the *P-K* method is valid at the conditions of $g = 0$, $k = 0$, or $\frac{d^n\mathbf{Q}}{dk^n} = 0$, where $n > 1$. The *g*-method generalizes the *K*-method and the *P-K* method. It is valid for all k and up to the first order of g. This first order term of g is rigorously derived from $\mathbf{Q}(p)$ by a damping perturbation method.

The present work also provides a theoretical foundation for the *g*-method that can be used to estimate the error of large damping (beyond the first order assumption) due to the truncation of the higher order terms of g. However, based on the formulation of the *g*-method, adding higher order terms in g seems to be straightforward.

REFERENCES

Chapter 1

1.1 Johnson, E.H. and Venkayya, V.B., "Automated Structural Optimization System (ASTROS), Theoretical Manual," AFWAL-TR-88-3028, Vol. 1, Dec. 1988.

1.2 Chen, P.C., Liu, D.D., Sarhaddi, D., Striz, A.G., Neill, D.J. and Karpel, M., "Enhancement of the Aeroservoelastic Capability in ASTROS," STTR Phase I Final Report, WL-TR-96-3119, Sep. 1996.

1.3 Chen, P.C., Sarhaddi, D., Liu, D.D. and Karpel, M., "A Unified Unsteady Aerodynamic Influence Coefficient Approach for Aeroelastic/Aeroservoelastic and MDO Applications," AIAA 97-1181-CP, Kissimmee, FL, Apr. 7-10, 1997.

1.4 Chen, P.C., Sarhaddi, D., Liu, D.D., Karpel, M., Striz, A.G. and Jung, S.Y., "A Unified Unsteady Aerodynamic Module for Aeroelastic, Aeroservoelastic and MDO Applications," CEAS, Vol. 2, Rome, Italy, Jun. 17-20, 1997.

1.5 Chen, P.C. and Jadic, I., "CFD/CSD Interfacing via an Innovative Structural Boundary Element Method," AIAA-97-1088CP, Kissimmee, FL, Apr. 7-10, 1997.

1.6 Albano, E. and Rodden, W.P., "A Doublet-Lattice Method for Calculating Lift Distributions on Oscillating Surfaces in Subsonic Flows," AIAA Journal, Vol. 7, Feb. 1969, pp. 279-285.

1.7 Rodden, W.P., Giesing, J.P. and Kalman, T.P., "New Method for Nonplanar Configurations," *AGARD Conference Proceedings*, CP-80-71, Pt. II, No. 4, 1971.

1.8 Chen, P.C., Lee, H.W. and Liu, D.D., "Unsteady Subsonic Aerodynamics for Bodies and Wings with External Stores Including Wake Effort," Journal of Aircraft, Vol. 30, No. 5, Sep.-Oct. 1993, pp. 618-628.

1.9 Chen, P.C. and Liu, D.D., "Unsteady Supersonic Computation of Arbitrary Wing-Body Configurations Including External Stores," Journal of Aircraft, Vol. 27, No. 2, Feb. 1990, pp. 108-116.

1.10 Liu, D.D., "Computational Transonic Equivalent Strip Method for Applications to Unsteady 3D Aerodynamics," AIAA-83-0261, Reno, NV, Jan. 10-13, 1983.

1.11 Liu, D.D., Kao, Y.F. and Fung, K.Y., "An Efficient Method for Computing Unsteady ransonic Aerodynamics of Swept Wings with Control Surfaces," AIAA-85-4058, Oct. 1985.

1.12 Chen, P.C., Sarhaddi, D. and Liu, D.D., "Transonic AIC Approach for Aeroelastic and MDO Applications," presented at the Euromech Colloquium 349 at DLR , Göttingen, Germany, Sept. 16-18, 1996.

1.13 Liu, D.D., Yao, Z.X., Sarhaddi, D. and Chavez, F., "From Piston Theory to a Unified Hypersonic-Supersonic Lifting Surface Method," Journal of Aircraft, Vol. 34, No. 3, May-June 1997, pp. 304-312.

1.14 Liu, D.D., Chen, P.C., Yao, Z.X. and Sarhaddi, D., "Recent Advances in Lifting Surface Methods," the Aeronautical Journal of the Royal Aeronautical Society, Vol. 100, No. 958, Oct. 1996, pp. 327-339.

1.15 Chen, P.C. and Liu, D.D., "A Harmonic Gradient Method for Unsteady Supersonic Flow Calculations," Journal of Aircraft, Vol. 22, No. 5, May 1985, pp. 371-379.

1.16 Karpel, M., Moulin, B. and Striz, A.G., "Development of the Aerodynamic / Aeroservoelastic Modules in ASTROS," Aeroservoelastic Discipline in ASTROS, Theoretical Manual, Vol. III, Feb. 1999.

1.17 Karpel, M., "Time-Domain Aeroservoelastic Modeling Using Weighted Unsteady Aerodynamic Forces," *J. Guidance, Control and Dyn.*, Vol. 13, No. 1, 1990, pp. 30-37.

1.18 Karpel, M. and Strull, E., "Minimum-State Unsteady Aerodynamic Approzimation with Flexible Constraints," International Forum on Aeroelasticity and Structural Dynamics, Manchester, UK, Jun. 1995, pp. 66.1-66.8.

Chapter 3

3.1 Chen, P.C. and Liu, D.D., "A Harmonic Gradient Method for Unsteady Supersonic Flow Calculations," Journal of Aircraft, Vol. 22, No. 5, May 1985, pp. 371-379.

3.2 Liu, D.D., James, D.K., Chen, P.C. and Pototzky, A.S., "Further Studies of Harmonic Gradient Method for Supersonic Aeroelastic Applications," Journal of Aircraft, Vol. 28, No. 9, pp. 598-605.

3.3 Rodden, W.P. and Johnson, E.H., "MSC/NASTRAN Aeroelastic Analysis User's Guide Version 68," The MacNeal-Schwendler Corporation Publication, 1994.

3.4 Jordan, P.F., "Aerodynamic Flutter Coefficients for Subsonic, Sonic and Supersonic Flow (Linear Two-Dimensional Theory)," British Aeronautical Research Council, London, ARCTR R&M 2932, 1957.

3.5 Lee, B.H.K., "Flutter Analysis of the CF-18 Aircraft at Supersonic Speeds," Journal of Aircraft, Vol. 26, No. 6, Jun. 1989, pp. 588-590.

3.6 Burkhart, T.H., "Numerical Application of Evvard's Supersonic Wing Theory to Flutter Analysis," AIAA Paper 80-0741, 1980.

3.7 Johnson, E.H., Rodden, W.P., Chen, P.C. and Liu, D.D., "Comment on Canard-Wing Interaction in Unsteady Supersonic Flow," Journal of Aircraft, Vol. 29, No. 4, 1992, p. 744.

3.8 Stark, V.J.E., "Canard-Wing Interaction in Unsteady Supersonic Flow," Journal of Aircraft, Vol. 19, No. 10, 1989, pp. 951-952.

3.9 Hounjet, M.H.L., "Improved Potential Gradient Method to Calculate Airloads on Oscillating Supersonic Interfering Surfaces," Journal of Aircraft, Vol. 19, No. 5, 1982, pp. 390-399.

3.10 Stark, V.J.E., "Calculation of Aerodynamic Forces on Two Oscillating Finite Wings at Low Supersonic Mach Numbers," Rept. SAAB TN-53, SAAB Scania AB, Linköping, Sweden, 1964.

3.11 Markowitz, J. and Isakson, G., "FASTOP-S: A Strength, Deflection and Flutter Optimization Program for Metallic and Composite Structures," Air Force Flight Dynamics Lab., Wright-Patterson AFB, OH, AFFDL-TR-78-50, May 1978.

3.12 Cunningham, A.M., Jr., "Oscillatory Supersonic Kernel Function Method for Interfering Surface," Journal of Aircraft, Vol. 11, No. 11, 1974, pp. 664-670.

3.13 Ashley, H. and Zartarian, G., "Piston-Theory – A New Aerodynamics Tool for the Aeroelastician," Journal Aeronautic Science, Vol. 23, No. 12, 1956, pp. 1109-1118.

3.14 Bennett, R.M., Bland, S.R., Batina, J.T., Gibbons, M.D. and Mabey, D.G., "Calculation of Steady and Unsteady Pressure on Wings at Supersonic Speeds with a Transonic Small-Disturbance Code," AIAA Paper 87-0851, April 1987; also Journal of Aircraft, Vol. 28, No. 3, 1991, pp. 175-180.

3.15 Chen, P.C. and Liu, D.D., "Unsteady Supersonic Computations of Arbitrary Wing-Body Configurations Including External Stores," Journal of Aircraft, Vol. 27, No. 2, February 1990, pp. 108-116.

3.16 Garcia-Fogeda, P. and Liu, D.D., "A Harmonic Potential Panel Method for Flexible Bodies in Unsteady Supersonic Flow," AIAA Paper 86-007, 1986; also Journal of Aircraft, Vol. 24, Dec. 1987, pp. 833-840.

3.17 Loving, D.L. and Eastbrooks, B.B., "Transonic-Wing Investigation in the Langley 8-Foot High-Speed Tunnel at High Subsonic Mach numbers and a Mach Number of 1.2," NACA RM L51F07, Sep. 1951.

3.18 Tijdeman, J. et al., "Transonic Wind-Tunnel Tests on an Oscillating Wing with External Stores; Part I-IV, the Wing with Tip Store," Air Force Flight Dynamics Laboratory, Wright-Patterson AFB, OH, AFDL-TR-78-194, May 1979.

3.19 Chen, P.C., Lee, H.W. and Liu, D.D., "Unsteady Subsonic Aerodynamics for Bodies and Wings with External Stores Including Wake Effect," Journal of Aircraft, Vol. 30, No.5, Sept.-Oct. 1993, pp. 618-628.

3.20 Bennekers, B., Roos, R. and Zwaan, R.J., "Calcon of Aerodynamics Loads on Oscillating Wing/Store Combinations in Subsonic Flow," AGARD Specialists Meeting on Wing-with-Stores Flutter, CP-162, Paper 4, Munich, Germany, 1974.

3.21 Rodden, W.P., Giesing, J.P. and Kalman, T.P., "New Development and Applications of the Subsonic Doublet-Lattice Method for Nonplanar Configurations," AGARD Conf. Proc. No. 80-71, Part II, No. 4, 1971.

3.22 Liu, D.D., Chen, P.C., Yao, Z.X. and Sarhaddi, D., "Recent Advances in Lifting Surface Methods," The Aeronautical Journal, Royal Aeronautical Society, Vol. 100, No. 998, Oct. 1996, pp. 327-339.

3.23 Theodorsen, T., "General Theory of Aerodynamic Instability and the Mechanism of Flutter," NACA Report No. 496, 1940.

3.24 Miles, J.W., "Potential Theory of Unsteady Supersonic Flow," Cambridge Univ. Press, London, 1959.

3.25 Morino, L. and Tseng, K., "Time-Domain Green's Function Method for Three-Dimensional Nonlinear Subsonic Flows," AIAA Paper No. 78-1204, 1978.

3.26 Freedman, M.I. and Tseng, K., "A First-Order Time-Domain Green's Function Approach to Supersonic Unsteady Flow," NACA CR-17228, April 1985.

3.27 Garcia-Fogeda, P. and Liu, D.D., "Analysis of Unsteady Aerodynamics for Elastic Bodies in Supersonic Flow," Journal of Aircraft, Vol. 24, No. 12, 1987, pp. 833-840.

3.28 Garcia-Fogeda, P. and Liu, D.D., "Supersonic Aeroelastic Applications of Harmonic Potential Panel Method to Oscillating Flexible Bodies," Journal of Spacecraft and Rockets, Vol. 25, No. 4, 1988, pp. 271-277.

3.29 Garcia-Fogeda, P., Chen, P.C. and Liu, D.D., "Unsteady Supersonic Flow Calculations for Wing-Body Combinations Using Harmonic Gradient Method," AIAA Journal, Vol. 28, No. 4, 1990, pp. 635-641.

3.30 Magnus, A.E. and Epton, M.A., "PANAIR – A Computer Program for Predicting Subsonic or Supersonic Linear Potential Flows About Arbitrary Configurations Using a Higher Order Panel Method, Vol. I – Theory Document," NASA-CR-3251, 1980.

3.31 von Karman, T. and Moore, N.B., "The Resistance of Slender Bodies," *Trans. ASME 54*, pp. 303-310.

3.32 Marchank, W.R., Crowley, J.A. and Mariand, D., "Development of a Supersonic Panel Program, Phase II: Development Within the Warton MkII CFM System of Version I of a Lifting Supersonic Panel Program," Ae456, 1984, British Aerospace, Warton Division.

3.33 Sims, J.L., "Tables for Supersonic Flow Around Right Circular Cones at Zero Angle of Attack," NASA SP-3004, 1964.

3.34 Sims, J.L., "Tables for Supersonic Flow Around Right Circular Cones at Small Angle of Attack," NASA SP-3007, 1964.

Chapter 4

4.1 Anderson, W.K., Thomas, J.L. and Van Leer, B., "Comparison of Finite Volume Flux Vector Splittings for the Euler Equations," AIAA Journal, Vol. 24, No. 9, 1986, pp. 1453-1460.

4.2 Schuster, D.M., Vadyak, J. and Atta, E., "Flight Loads Prediction Methods for Fighter Aircraft," WRDC-TR-89-3104, Nov. 1989.

4.3 Guruswamy, G.P., "Navier-Stokes Computations on Swept-Tapered Wings, Including Flexibility," AIAA Paper 90-1152, Apr. 1990.

4.4 Batina, J.T., "Unsteady Transonic Small-Disturbance Theory Including Entropy and Vorticity Effects," Journal of Aircraft, Vol. 26, No. 6, June 1989, p. 531.

4.5 Liu, D.D., "Computational Transonic Equivalent Strip Method for Applications to Unsteady 3D Aerodynamics," AIAA 21st Aerospace Science Meeting, Reno, NV., January 10-13, 1983, AIAA Paper No. 83-0261.

4.6 Liu, D.D., Kao, Y.F. and Fung, K.Y., "An Efficient Method for Computing Unsteady Transonic Aerodynamics of Swept Wings with Control Surfaces," Journal of Aircraft, Vol. 25, No. 1, January 1988.

4.7 Fung, K.Y. and Chung, A., "Computations of Unsteady Transonic Aerodynamics Using Prescribed Steady Pressures," Journal of Aircraft, Vol. 20, no. 12, December 1983, pp. 1058-1061.

4.8 Chen, P.C., Sarhaddi, D. and Liu, D.D., "Transonic AIC Approach for Aeroelastic and MDO Applications," presented at the Euromech Colloquium 349 at DLR , Göttingen, Germany, Sept. 16-18, 1996.

4.9 Chen, P.C., Sarhaddi, D. and Liu, D.D., "A Unified Unsteady Aerodynamic Module for Aeroelastic and MDO Applications," presented at AGARD Structures and Material Panel, Alborg, Denmark, Oct. 13-17, 1997.

4.10 Lessing, H.C., Troutman, J.L. and Menees, G.P., "Experimental Determination on a Rectangular Wing Oscillating in the First Bending Mode for Mach Numbers from 0.24 to 1.30," NASA TND-33, December 1960.

4.11 Malone, J.B. and Ruo, S.Y., "LANN Wing Test Program: Acquisition and Application of Unsteady Transonic Data for Evaluation of Three-Dimensional Computational Methods," AFWAL-TR-83-3006, Feb. 1983.

4.12 Guruswamy, P. and Goorjian, P.M., "An Efficient Coordinate Transformation Technique for Unsteady Transonic Aerodynamic Analysis of Low-Aspect-Ratio Wings," AIA Paper 84-0872, 1984.

4.13 Persoon, A.J., Roos, R. and Schippers, P., "Transonic and Low Supersonic Wind-Tunnel Tests on a Wing with Inboard Control Surface," AFWAL-TR-80-3146, Dec. 1980.

4.14 Sotomayer, W.A. and Borland, C.J., "Numerical Computation of Unsteady Transonic Flow about Wings and Flaps," AIAA Paper 85-1712, 1985.

4.15 Yates, E.C., "AGARD Standard Aeroelastic Configurations for Dynamic Response I-Wing 445.6," AGARD Report No. 765.

4.16 Landahl, M.T., *Unsteady Transonic Flow*, Pergamon Press, 1961, Ch. 1,

4.17 Ballhaus, W.F. and Goorjian, P.M., "Implicit Finite-Difference Computations of Unsteady Transonic Flows about Airfoils, AIAA Journal, Vol. 15, No. 12, Dec. 1977, pp. 1728-1735.

4.18 Ballhaus, W.F. and Goorjian, P.M., "Computation of Unsteady Transonic Flows by the Indicial Method," AIAA Journal, Vol. 16, No. 2, Feb. 1978, pp. 117-124.

4.19 Oyibo, G.A., "Formulation of Three Dimensional Hodograph Method and Separable Solutions for Nonlinear Transonic Flows," AIAA Journal, Vol. 28, No. 10, pp. 1745-1750.

4.20 Fung, K.Y., "A Simple, Accurate and Efficient Algorithm for Unsteady Transonic Flow," Recent Advances in Numerical Methods in Fluid Dynamics, edited by W.G. Habashi, Pineridge Press, Swansea, U.K., 1984.

4.21 Lambourne, N.C., " Experimental Techniques in Unsteady Aerodynamics," Special Course on Unsteady Aerodynamics, AGARD Report 679, Jun. 18, 1980, pp. 10.1-10.26.

4.22 Fung, K.Y., Yu, N.J. and Seebass, A.R., "Small Unsteady Perturbations in Transonic Flows," AIAA Journal, No. 16, 1978, pp. 815-822.

4.23 Tobak, M., "On the Use of Indicial Function Concept in the Analysis of Unsteady Motions of Wings and Wing-Tail Combinations," NACA Report 1188, 1954.

4.24 Ballhaus, W.F. and Goorjian, P.M., "Computation of Unsteady Transonic Flows by the Indicial Method," AIAA Journal, Vol. 16, No. 2, Feb. 1978, pp. 117-124.

4.25 Seidel, D.A., Bennett, R.M. and Whitlow, W., Jr., "An Exploratory Study of Finite-Difference Grids Transonic Unsteady Aerodynamics," AIAA Paper 83-0503, Jan. 1983.

Chapter 5

5.1 Liu, D.D., Yao, Z.X., Sarhaddi, D. and Chavez, F., "Piston Theory Revisited and Further Applications," ICAS Paper 94-2.8.4, presented at the 19th Congress of the International Council of the Aeronautical Sciences, Sep. 1994.

5.2 Chavez, F.R. and Liu, D.D., "A Unified Hypersonic/Supersonic Method for Aeroelastic Applications Including Shock-Unsteady Wave Interaction," AIAA Paper, 93-1317, Apr. 1993.

5.3 Van Dyke, M.D., "A Study of Second-Order Supersonic Flow Theory," NACA Report 1081, 1952.

5.4 Hui, W.H., "Unified Unsteady Supersonic/Hypersonic Theory of Flow Past Double Wedge Airfoils," Journal of Applied Mathematics and Physics, ZAMP, Vol. 34, No. 4, pp. 458-488, 1983.

5.5 Hanson, P.W. and Levey, G.M., "Experimental and Calculated Results of a Flutter Investigation of Some Very Low Aspect-Ratio Flat-Plate Surface at Mach Numbers from 0.62 to 3.0," NASA TN D-2038, 1963.
5.6 Bennett, R.M., Bland, S.R., Batina, J.T., Gibbons, M.D. and Mabey, D.G., "Calculation of Steady and Unsteady Pressure on Wings at Supersonic Speeds with a Transonic Small-Disturbance Code," Journal of Aircraft, 28(3), 1991, pp. 175-180.
5.7 Tuovila, W.J. and McCarty, J.L., "Experimental Flutter Results for Cantilever-Wing Models at Mach Numbers up to 3.0," NACA RM L55E11, 1955.
5.8 Rodden, W.P., "Correction Factors for Supersonic Thickness Effects," MSC/NASTRAN-WPR-3, Apr. 1, 1991.
5.9 Lighthill, M.J., "Oscillating Airfoils at High Mach Number," Journal of Aeronautical Sciences, Vol. 20, No. 6, Jun. 1953, pp. 402-406.
5.10 Ashley, H. and Zartarian, G., "Piston Theory – A New Aerodynamic Tool for the Aeroelastician," Journal of Aeronautical Sciences, Vol. 23, No. 12, 1956, pp. 1109-1118.
5.11 Landahl, M., Mello-Christensen, E.L. and Ashley, H., "Parametric Studies of Viscous and Nonviscous Unsteady Flows," O.S.R. Technical Report 55-13, 1955.
5.12 Garrick, I.E. and Rubinow, S.I., "Flutter and Oscillating Air Force Calculations for an Airfoil in a Two-Dimensional Supersonic Flow," NACA Report 846, 1946.
5.13 Landahl, M., "Unsteady Flow Around Thin Wings at high Mach Numbers," Journal of Aeronautical Sciences, Vol. 24, No. 1, Jan. 1957, pp. 33-38.
5.14 Tsien, H.S., "Similarity Laws of Hypersonic Flows," Journal of Mathematics & Physics, Vol. 25, 1946, pp. 247-251.
5.15 Morgan, H.G., Huckel, V. and Runyan, H.L., "Procedure for Calculating Flutter at high Supersonic Speed Including Camber Deflections and Comparisons with Experimental Results," NACA TN 4335, Sep. 1958.
5.16 Rodden, W.P., Farkas, E.F., Malcolm, H.A. and Kliszewski, A.M., "Aerodynamic Influence Coefficients from Piston Theory: Analytical Development and Computational Procedure," Aerospace Corporation Report No. TDR-169 (3230-11) TN-2, Aug. 1962.
5.17 Van Dyke, M.D, "A Study of Second-Order Supersonic Flow Theory," NACA Report 1081, 1952.
5.18 Busemann, A., "Aerodynamischer Auftrieb bei Überschallgeschwindigkeit," Luftfahrtforschung, Vol. 12, 1935, p. 210.
5.19 Donov, A.E., "A Flat Wing with Sharp Edges in A Supersonic Stream," NACA TM-1394, 1956, Translation of Izvestiia-Akademia, NAUK, USSR, 1939.
5.20 Carafoli, E., "High-Speed Aerodynamics," Editura Technica, Bucharest, 1968, pp. 374-375.
5.21 Kahane, A. and Lees, L., "The Flow at the Rear of a Two-Dimensional Supersonic Airfoil," Journal of Aeronautical Sciences, Vol. 15, 1948, pp. 167-170.
5.22 Liepmann, H.W. and Roshko, A., "Elements of Gas Dynamics," John Wiley & Sons, New York, NY, 1957.
5.23 Linnell, R.D., "Two-Dimensional Airfoils in Hypersonic Flow," Journal of Aeronautical Sciences, Vol. 16, 1948, pp. 22-30.
5.24 Lighthill, M.J., "A Technique for Rendering Approximate Solutions to Physical Problems Uniformly Valid," Phil. Mag., 40, pp. 1179-1201.

Chapter 6

6.1 Harder, R.L. and Desmarais, R.N., "Interpolation Using Surface Splines," AIAA Journal, Vol. 9, No. 2, 1972, pp. 189-191.

6.2 Rodden, W.P., "Further Remarks on Matrix Interpolation of Flexibility Influence Coefficients," Journal of Aerospace Sciences, Vol. 26, Nov. 1959, pp. 760-761.

6.3 Duchon, J., "Splines Minimizing Rotation-Invariant Semi-Norms in Sobolev Spaces," Constructive Theory of Functions of Several Variables, edited by W. Schempp and K. Zeller, Springer, Oberwolfach, Germany, 1976, pp. 85-100.

Chapter 7

7.1 Theodorsen, T., "General Theory of Aerodynamic Instability and the Mechanism of Flutter," NACA Report 496, 1935.

7.2 Yates, E.C., Jr., Land, N.S. and Foughner, J.T., Jr., "Measured and Calculated Subsonic and Transonic Flutter Characteristics of a 45° Sweptback Wing Planform in Air and in Freon-12 in the Langley Transonic Dynamics Tunnel," NASA TN-D-1616, Mar. 1963.

7.3 Irwin, C.A. and Guyett, P.R., "The Subcritical Response and Flutter of a Swept Wing Model," Technical Report 65186, Royal Aircraft Establishment, Farnborough, U.K., Aug. 1965.

7.4 Hassig, H.J., "An Approximate True Damping Solution of the Flutter Equation by Determinant Iteration," Journal of Aircraft, Vol. 8, No. 11, Nov. 1971.

7.5 Rodden, W.P., Harder, R.L. and Bellinger, E.D., "Aeroelastic Addition to NASTRAN," NASA CR 3094, 1979.

7.6 Rodden, W.P. and Stahl, B., "A Strip Method for Prediction of Damping in Subsonic Wind Tunnel and Flight Flutter Test," Journal of Aircraft, Vol. 6, No. 1, Jan.-Feb. 1969, pp. 9-17.

7.7 Chen, P.C., "A Damping Perturbation Method for Flutter Solution: The g-Method," International Forum on Aeroelasticity and Structural Dynamics, Hampton, VA, Jun. 22-25, 1999.

7.8 Stark, V.J., "General Equations of Motion for an Elastic Wing and Method of Solution," AIAA Journal, Vol. 22, No. 8, Aug. 1984.

7.9 Rodden, W.P., "Handbook for Aeroelastic Analysis," Vol. 1, MSC/NASTRAN Version 65.

7.10 Rodden, W.P. and Bellinger, E.D., "Aerodynamic Lag Functions, Divergence and the British Flutter Method," Journal of Aircraft, Vol. 19, No. 7, Jul. 1982.

7.11 Rodden, W.P. and Bellinger, E.D., "Unrestrained Aeroelastic Divergence in a Dynamic Stability Analysis," Journal of Aircraft, Vol. 19, No. 9, Sep. 1982.

7.12 Johnson, E.H., "MSC/NASTRAN User's Guide for Aeroelastic Analysis," presented at Aerospace Flutter and Dynamics Council, Seattle, WA, May 19, 1995.